Personalized Electromechanical Modeling of the Human Heart

Challenges and Opportunities for the Simulation of Pathophysiological Scenarios

Zur Erlangung des akademischen Grades eines

DOKTORS DER INGENIEURWISSENSCHAFTEN (Dr.-Ing.)

von der KIT-Fakultät für Elektrotechnik und Informationstechnik des

Karlsruher Instituts für Technologie (KIT)

angenommene

DISSERTATION

von

Tobias Gerach, M.Sc.

geb. in Spaichingen

Tag der mündlichen Prüfung:	12.05.2022
Hauptreferent:	Priv.-Doz. Dr.-Ing. Axel Loewe
1. Korreferent:	Prof. Dr. rer. nat. Christian Wieners
2. Korreferent:	Prof. Dr. rer. nat. Olaf Dössel

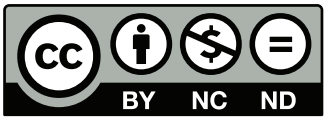

Abstract

Mathematical models of the human heart are evolving to become a cornerstone of precision medicine and support clinical decision making by providing a powerful tool to understand the mechanisms underlying pathophysiological conditions. Due to the complexity of the heart, these models require a detailed description of physical processes that interact on different spatial and temporal scales ranging from nanometers to centimeters and from nanoseconds to seconds, respectively. From a mathematical perspective, this poses a variety of challenges such as developing robust numerical schemes for the solution of the model in space and time and parameter identification based on patient specific measurements. In this work, a detailed mathematical description of the electromechanically coupled multi-scale model of the human heart is presented, including the propagation of electrical excitation, large scale deformations, and a model of the circulatory system.

Starting from state-of-the-art models of membrane kinetics and active force generation based on human physiology, an atrial and ventricular model of cardiac excitation-contraction coupling is developed and parameterized to match observations from single cell experiments. Furthermore, a segregated and staggered numerical scheme to solve the electromechanically coupled model of the whole heart is established based on already existing software and used to investigate the effects of mechano-electric feedback during sinus rhythm. The numerical results showed that mechano-electric feedback on the cellular level has an impact on the mechanical behavior of the heart due to changes in the active force generation by modulating the interaction between calcium and the binding units of troponin C. Including the effect of deformation on the diffusion of the electrical signal had no significant effect.

To verify the different components of the modeling framework, specific problems are designed to cover the most important aspects of electrophysiology and mechanics. Additionally, these problems are used to assess how spatial and temporal discretization affect the numerical solution. The results show that spatial and temporal discretization of the electrophysiology problem dictate the limitations of numerical accuracy while the mechanics problem is more vulnerable to locking effects due to the choice of tetrahedral finite elements.

The model is further used to investigate how a dispersion of fiber stress into the sheet and sheetnormal directions changes mechanical biomarkers of the left ventricle. In an idealized model of the left ventricle, additional stress in the sheetnormal direction promoted a more physiological contraction with respect to ejection fraction, longitudinal shortening, wall thickening, and rotation. However, numerical results using the whole heart model revealed contradicting results compared to the idealized left ventricle.

In a second project, in vivo measurements of electromechanical parameters in 30 patients suffering from heart failure with reduced ejection fraction and left bundle branch block were integrated into the left ventricular model to shed light on the clinical hypothesis that local electromechanical alterations change the left ventricular rotation pattern. Simulation results could not verify this hypothesis and showed no correlation between the electromechanical parameters and rotation.

Next, the impact of standard ablation strategies for the treatment of atrial fibrillation on cardiovascular performance is evaluated in a four-chamber heart model. Due to the scars in the left atrium, the electrical activation and stiffness of the myocardium was altered resulting in a reduction of atrial stroke volume that depends linearly on the amount of inactivated tissue. Additionally, atrial pressure was increased depending on the stiffness of the scar tissue and ventricular function was only affected slightly.

Finally, pathological mechanisms related to heart failure in patients with dilated cardiomyopathy are introduced into the whole heart model one by one to differentiate their individual contribution. The numerical results showed that cellular remodeling, especially the one affecting electrophysiology, is mainly responsible for the poor mechanical activity of the heart in patients with dilated cardiomyopathy. Furthermore, structural remodeling and an increased stiffness of the myocardium as well as adaptations of the circulatory system were necessary to replicate in vivo observations.

In conclusion, this work presents a numerical framework for the approximation of electromechanical whole heart models including the circulatory system. The framework was verified with the use of simple problem definitions, validated using magnetic resonance imaging data, and used to answer clinical questions that would otherwise be impossible to address in real world scenarios.

Zusammenfassung

Mathematische Modelle des menschlichen Herzens entwickeln sich zu einem Eckpfeiler der personalisierten Medizin. Sie sind ein nützliches Instrument und helfen klinischen Entscheidungsträgern die zugrundeliegenden Mechanismen von Herzkrankheiten zu erforschen und zu verstehen. Aufgrund der Komplexität des Herzens benötigen derartige Modelle allerdings eine detaillierte Beschreibung der physikalischen Prozesse, welche auf verschiedenen räumlichen und zeitlichen Skalen miteinander interagieren. Aus mathematischer Perspektive stellen vor allem die Entwicklung robuster numerischer Methoden für die Lösung des Modells in Raum und Zeit sowie die Identifizierung von Parametern aus patientenspezifischen Messungen eine Herausforderung dar. In dieser Arbeit wird ein detailliertes mathematisches Modell vorgestellt, welches ein vollgekoppeltes Multiskalenmodell des menschlichen Herzens beschreibt. Das Modell beinhaltet unter anderem die Ausbreitung des elektrischen Signals und die mechanische Verformung des Herzmuskels sowie eine Beschreibung des Herz-Kreislauf-Systems.

Basierend auf dem neusten Stand der Technik wurden Modelle der Membrankinetik sowie der Entwicklung der aktiven Kraft zu einem einheitlichen Modell einer Herzmuskelzelle zusammengeführt. Dieses beschreibt die elektromechanische Kopplung in Herzmuskelzellen der Vorhöfe und der Herzkammern basierend auf der Physiologie im Menschen und wurde mit Hilfe von experimentellen Daten aus einzelnen Zellen neu parametrisiert. Um das elektromechanisch gekoppelte Modell des menschlichen Herzens lösen zu können, wurde ein gestaffeltes Lösungsverfahren entwickelt, welches auf bereits existierenden Softwarelösungen der Elektrophysiologie und Mechanik aufbaut. Das neue Modell wurde verwendet, um den Einfluss elektromechanischer Rückkopplungseffekte auf das Herz im Sinusrhythmus zu untersuchen. Die Simulationsergebnisse zeigten, dass elektromechanische Rückkopplungseffekte auf zellulärer Ebene einen wesentlichen Einfluss auf das mechanische Verhalten des Herzens haben. Dahingegen hatte die Verformung des Herzens nur einen geringen Einfluss auf den Diffusionskoeffizienten des elektrischen Signals.

Um die verschiedenen Komponenten der Simulationssoftware zu verifizieren, wurden spezielle Probleme definiert, welche die wichtigsten Aspekte der Elektrophysiologie und der Mechanik abdecken. Zusätzlich wurden diese Probleme dazu verwendet, den Einfluss von räumlicher und zeitlicher Diskretisierung auf die numerische Lösung zu bewerten. Die Ergebnisse zeigten, dass Raum- und Zeitdiskretisierung vor allem für das elektrophysiologische Problem die limitierenden Faktoren sind, während die Mechanik hauptsächlich anfällig für volumenversteifende Effekte ist.

Weiterhin wurde das Modell verwendet, um zu untersuchen, wie sich eine Verteilung der Faserspannung auf den gesamten Herzmuskel auf die Funktion der linken Herzkammer auswirkt. Hierzu wurde zusätzlich eine Spannung in die Normalenrichtungen der Fasern einer idealisierten linken Herzkammer angewandt. Es zeigte sich, dass insbesondere eine Spannung senkrecht zu den Faserschichten zu einer physiologischeren Kontraktion der Kammer führte. Allerdings konnten diese Ergebnisse auf einem ganzen Herzen nicht vollständig bestätigt werden.

In einem zweiten Projekt wurde mit Hilfe eines Modells der linken Herzkammer untersucht, wie sich das Rotationsmuster der Kammer unter Modifikation der lokalen elektromechanischen Eigenschaften verändert. Hierzu wurden in vivo Daten elektromechanischer Parameter von 30 Patienten mit Herzversagen und Linksschenkelblock in das Modell integriert, simuliert und ausgewertet. Die Ergebnisse konnten die klinisch aufgestellte Hypothese nicht bestätigen und es zeigte sich keine Korrelation zwischen den elektromechanischen Parametern und dem Rotationsverhalten.

Die Auswirkungen von standardisierten Ablationsstrategien zur Behandlung von Vorhofflimmern in Bezug auf die kardiovaskuläre Leistung wurde in einem Modell des ganzen Herzens untersucht. Aufgrund der Narben im linken Vorhof wurde die elektrische Aktivierung und die Steifigkeit des Herzmuskels verändert. Dies führte zu einem reduzierten Auswurfvolumen, welches in direktem Zusammenhang mit dem inaktiven Gewebe steht. Abhängig von der Steifigkeit der Narben hat sich zusätzlich der Druck im linken Vorhof erhöht. Die linke Herzkammer war nur wenig beeinflusst.

Zu guter Letzt wurden schrittweise pathologische Mechanismen in das Herzmodell integriert, welche in Zusammenhang mit Herzversagen stehen und in Patienten mit dilatativer Kardiomyopathie zu beobachten sind. Die Simulationen zeigten, dass vor allem zelluläre Veränderungen bezüglich der elektrophysiologischen Eigenschaften für die schlechte mechanische Aktivtät des Herzens verantwortlich sind. Weiterhin zeigte sich, dass strukturelle Veränderungen der Anatomie und die erhöhte Steifigkeit des Herzmuskels und die damit einhergehenden Anpassungen des Herz-Kreislauf-Systems nötig sind, um in vivo Messungen zu reproduzieren.

In dieser Arbeit wurde eine Simulationsumgebung vorgestellt, welche die Berechnung der elektromechanischen Aktivität des Herzens und des Herz-Kreislauf-Systems ermöglicht. Die Simulationsumgebung wurde mit Hilfe von einfachen Beispielen verifiziert und unter Einbeziehung von Daten aus der Magnetresonanztomographie validiert. Zu guter Letzt wurde die Simulationsumgebung genutzt, um klinische Fragen zu beantworten, welche andernfalls im Dunkeln blieben.

Danksagung

Ich bin zutiefst dankbar für all die Erfahrungen die ich die letzten Jahre in meiner Zeit am IBT machen durfte. Egal ob auf Konferenzen, gemeinsamen Reisen oder sonstigen Freizeitaktivitäten, ich hatte immer eine Menge Spaß und habe einige sehr gute Freundschaften geschlossen.

Zu aller erst möchte ich mich bei Prof. Olaf Dössel bedanken. Er hat es mir ermöglicht den Sprung aus der Geophysik zu wagen und ohne jegliche Vorkenntnisse in die Forschung der Herzmodellierung einzutauchen. Weiterhin möchte ich ein riesen Dankeschön an Dr. Axel Loewe aussprechen. Er hat es geschafft mich immer wieder in die richtige Bahn zu lenken und hat sich auch immer Zeit dafür genommen, um gemeinsam Lösungen für die zahlreich aufgetauchten Probleme zu finden. Es war für mich unglaublich spannend und auch lehrreich die Arbeitsgruppe wachsen zu sehen und auch zu ihrer Entwicklung beitragen zu können. Ein herzliches Dankeschön geht auch an Prof. Wieners, der dieses Projekt von Anfang an begleitet hat.

Allen Kollegen des IBT möchte ich für die tolle Zusammenarbeit und Unterstützung danken. Besonders bedanken möchte ich mich bei: Steffen, für die großartigen Ratschläge und Softwaretools ohne die diese Arbeit nicht möglich gewesen wäre; Ekaterina, für die endlose Geduld mit mir und für die wunderbare Zusammenarbeit; Jorge & Laura, für die schönen Erfahrungen während unserer gemeinsamen Reisen; Deborah, dafür, dass du immer ein offenes Ohr für mich hast; Larissa, Albert und Stephanie, für die tolle Arbeit die ihr in euren Abschlussarbeiten geleistet habt.

Vielen Dank auch an Carmen und Lorena. Ihr beide habt mir vor allem in den letzten Wochen des Schreibens immer wieder den Tag versüßt und mich zum Lachen gebracht. Auch wenn ich mich manchmal einfach nur im „Nappierenstuhl“ ausruhen wollte.

Danke auch an Jonathan Fröhlich und Laura Lindner. Wenn mich meine Mathematik Kenntnisse mal wieder im Stich gelassen haben, konnte ich mich auf euch verlassen.

Zu guter Letzt, möchte ich meiner Familie für die jahrelange Unterstützung danken, die mir das Studium und somit die Promotion überhaupt erst ermöglicht hat. Besonders meinem Opa Fritz möchte ich für das nie endende Interesse an meiner Arbeit danken.

Contents

Abstract . . . . . **i**

Zusammenfassung . . . . . **iii**

Danksagung . . . . . **v**

Abbreviations . . . . . **xi**

1 Introduction **1**
1.1 Objectives of the Thesis 2
1.2 Structure of the Thesis 2

I Fundamentals **5**

2 Anatomy & Physiology of the Human Heart **7**
2.1 Anatomy & Structure of the Heart 7
2.2 Cardiac Excitation, Conduction, and Contraction 9
2.3 Phases of the Cardiac Cycle 10

3 Modeling Cardiac Function **13**
3.1 Modeling Cardiac Electrophysiology 13
3.2 Modeling Active Force Generation 15
3.3 Modeling Cardiac Mechanics 17
3.4 Modeling the Circulatory System 19

II Electromechanical Modeling of the Whole Heart **23**

4 Generating a Four Chamber Heart Model **25**
4.1 Fiber Generation in the Atria and Ventricles 26
4.2 Defining Universal Ventricular Coordinates 28
4.3 Bullseye Polar Representation of the Ventricles 28

5 Electromechanical Model of the Whole Heart **31**
5.1 Modeling the Electromechanical Response of Cardiac Muscle Cells 31

5.2 Mechano-Electric Feedback . . . 33
5.3 The Coupled 3D-0D Whole Heart Problem . . . 34
5.4 Numerical Results for the Coupled 3D-0D Whole Heart Problem . . . 46
5.5 Discussion . . . 60

III Reproducible Verification of Model Components 65

6 Electrophysiology . . . 67
6.1 Problem Definition . . . 67
6.2 Results . . . 68

7 Mechanics . . . 73
7.1 Problem Definition . . . 73
7.2 Results . . . 74

8 Electromechanics . . . 77
8.1 Problem Definition . . . 77
8.2 Results . . . 79

IV Analysis of Left Ventricular Mechanics 81

9 Orthotropic Active Contraction in the Ventricles . . . 83
9.1 Materials and Methods . . . 84
9.2 Results . . . 87
9.3 Discussion . . . 91

10 Analysis of Left Ventricular Rotation in Heart Failure Patients . . . 93
10.1 Materials and methods . . . 94
10.2 Results . . . 98
10.3 Discussion . . . 102

V Modeling Pathological Scenarios in the Whole Heart 107

11 Standard Ablation Strategies for the Treatment of Atrial Fibrillation . . . 109
11.1 Materials and Methods . . . 111
11.2 Results . . . 114
11.3 Discussion . . . 122

12 Electromechanical Remodeling During Heart Failure in DCM . . . 125
12.1 Adaptations to the Electromechanical Heart Model . . . 126
12.2 Results . . . 133
12.3 Discussion . . . 138

VI Final Remarks **149**

13 Conclusion & Outlook **151**

A Determination of Rayleigh Damping Parameters **153**

B Derivation of the Passive Contribution to the 2nd Piola-Kirchhoff Stress . . . **155**

C Analysis of MRI Data for the Purpose of Validation **159**

D Numerical Integration – Gaussian Quadrature Rules **165**

References **167**

List of Publications and Supervised Theses **189**

Abbreviations

$\mathcal{A}$	sarcomere models
$\mathcal{C}$	circulatory system model
$\mathcal{E}$	monodomain model
$\mathcal{E}_{\text{LAT}}$-$\mathcal{MC}$	minimally coupled electromechanics model with precomputed LAT
$\mathcal{I}$	ionic model
$\mathcal{IA}$	electromechanical model of a cardiac muscle cell
$\mathcal{IAE}$	electrophysiology model
$\mathcal{IAE}$-$\mathcal{MC}$	fully coupled electromechanics model without MEF
$\mathcal{IAE}_{\text{MEF}}$-$\mathcal{MC}$	fully coupled electromechanics model with MEF
$\mathcal{M}$	mechanics model
$\mathcal{MC}$	3D-0D mechanics model
0D	zero-dimensional
3D	three-dimensional
AF	atrial fibrillation
AHA	American Heart Association
AL	anterior line
AV	aortic valve
AVN	atrioventricular node
AVPD	atrioventricular plane displacement
BB	Bachmann's bundle
BL	posterior box lesion
CRN	Courtemanche-Ramirez-Nattel
CS	coronary sinus
CT	crista terminalis
CV	conduction velocity
DCM	dilated cardiomyopathy
DoF	degrees of freedom
ED	end-diastole
EDPVR	end-diastolic pressure-volume relationship
EDV	end-diastolic volume
EF	ejection fraction
ES	end-systole
ESPVR	end-systolic pressure-volume relationship

ESV	end-systolic volume
FEM	finite element method
HF	heart failure
HFrEF	heart failure with reduced ejection fraction
HIS	bundle of His
IVC	inferior vena cava
L17	Land
LA	left atrium
LAT	local activation time
LBBB	left bundle branch block
LDRBM	Laplace-Dirichlet-Rule-Based-Method
LEMD	local rotational electromechanical delay
LGE-MRI	late gadolinium enhanced magnetic resonance imaging
LPV	left pulmonary veins
LV	left ventricle
MEF	mechano-electric feedback
MIL	mitral isthmus line
MRI	magnetic resonance imaging
MV	mitral valve
ODE	ordinary differential equation
ORd	O'Hara-Rudy-dynamic
PA	pulmonary artery
PM	pectinate muscle
PV	pulmonary valve
PVI	pulmonary vein isolation
PVR	pressure-volume relation
RA	right atrium
RFA	radio frequency ablation
RL	roof line
RPV	right pulmonary veins
RV	right ventricle
SAC	stretch activated current
SAN	sinoatrial node
SV	stroke volume
SVC	superior vena cava
TEMD	total rotational electromechanical delay
TTP	ten-Tusscher-Panfilov
TV	tricuspid valve

Chapter 1

Introduction

Cardiovascular diseases are the biggest contributors to the mortality and morbidity in the European Union, affecting millions of people every year [1]. While diagnostic tools and therapeutic options continuously improve and more data become available to researchers, the treatment of diseases such as ischemic heart disease or atrial fibrillation remains difficult due to the highly complex nature of the human heart and cardiovascular system. Evidently, the complex mechanisms underlying these pathophysiological conditions are notoriously difficult to evaluate in the clinical environment due to ethical and technical limitations. Computational models of the human heart have the ability to overcome these limitations and provide a valuable tool for clinical research and practice [2]. Already today, these models can improve diagnosis [3], risk stratification [4], therapy planning [5, 6], and intraprocedural support [7]. Furthermore, the vision of providing therapies customized to each individual patient heavily relies on mechanistic models to build a digital twin based on our knowledge of physiology and the fundamental laws of physics on the one hand and measured characteristics of the individual patient on the other hand [8].

Modeling cardiac function is a highly complex task. During a single heart beat electrochemical processes on the scale of single cells initiate a chain of events that lead to a coordinated depolarization and contraction of the heart to pump blood throughout the entire body. The mathematical models associated with these events are therefore required to handle vastly different scales in space and time as well as different physics. Due to these challenges, mathematical models typically focused on the local behavior of the heart including ventricular [9–13] or atrial [14–16] studies. Only recently and only a small part of the cardiac modeling community started to extent their models to the whole heart [17–20].

Another aspect of such a complex model is the parameterization of all its components. With personalized heart models in mind, this is ideally done using patient-specific measurements. However, the majority of parameters can only be measured by invasive procedures, estimated indirectly, or not at all due technical limitations. Hence, efficient workflows are necessary to gain as much information as possible and incorporate them into digital twin models. Anatomically accurate heart models based on imaging data are created using (semi-)automatic workflows [21–23]. To make these heart models comparable to each other, universal coordinate systems have been proposed for the atria [24] and the ventricles [25, 26].

Furthermore, we can build on already existing pipelines for the personalization of passive mechanical behavior of the heart [27, 28], ventricular afterload models [9], and cardiac electrophysiology based on electrocardiograms [29–32] or electroanatomical mapping [33, 34].

1.1 Objectives of the Thesis

The main objective of this thesis is to develop an electromechanically coupled model of a personalized human heart and to study the influence of excitation contraction coupling and mechano-electric feedback in healthy and pathological scenarios. Specifically, this thesis tries to reach the following milestones to achieve a better understanding of the mechanisms that drive the human heart:

- Establish models of atrial and ventricular cardiomyocytes based on human data that are able to express cardiac excitation-contraction coupling.
- Develop a simulation framework to efficiently and robustly couple cardiac electrophysiology and cardiac mechanics on the tissue level based on already existing software.
- Verify the developed framework to confirm that the model is correctly implemented and accurate with respect to the conceptual idea of the model.
- Investigate how different levels of electromechanical coupling influence the response of the individual core models.
- Create a personalized four chamber model of a human heart including circulation and validate the model using magnetic resonance imaging (MRI) data and data from literature.
- Use the model to answer clinically relevant questions.

1.2 Structure of the Thesis

This thesis is organized according to the following structure.

Part I outlines the fundamental knowledge this thesis builds upon.

- **Chapter 2** is a short introduction to the physiology and anatomy of the human heart. The process of converting an electrical signal into a mechanical force mediated by calcium and how this electrical signal propagates through the myocardium is described. Furthermore, a timeline of the phases of the cardiac cycle is given.
- **Chapter 3** introduces state of the art mathematical models of cardiac electrophysiology, mechanics, and the circulatory system.

Part II introduces the mathematical framework of the electromechanically coupled four chamber heart model. Parts of this Chapter were originally published in [35].

- **Chapter 4** provides the spatially discretized anatomical representation of the heart of a healthy human volunteer that is used in the reference simulations. Furthermore, pre-processing steps such as the fiber generation in the ventricles and atria and the computation of ventricular coordinates are presented. Additionally, the polar bullseye representation of the ventricles is introduced.
- **Chapter 5** details the adaptations made to the mathematical model to achieve electromechanical coupling on the cellular and tissue scale. Furthermore, the method for the numerical approximation of this system of equations is presented. Coupling on the cellular level was part of the Bachelor thesis of Stephanie Appel [36] and was previously published in [37].

Part III defines problems with the purpose to provide simulation setups that can be used to verify the correctness of the framework.

- In **Chapter 6**, solutions to a previously established benchmark [38] with different spatial and temporal discretizations are presented.
- **Chapter 7** takes a look at spatial convergence of the mechanical core model in an idealized left ventricle based on an established benchmark [39].
- In **Chapter 8**, a new benchmark for the electromechanically coupled model is proposed.

Part IV provides two simulation studies that focus on the mechanics of the left ventricle (LV).

- **Chapter 9** analyzes the effects of an orthotropically applied active stress tensor on standard clinical biomarkers of the LV. This Chapter is based on results originally published in [40].
- In **Chapter 10**, data from electroanatomical mapping and late gadolinium enhanced magnetic resonance imaging (LGE-MRI) of 30 patients are integrated into a left ventricular model. The conducted simulations are analyzed with respect to the rotational behavior of the LV and a clinical hypothesis is rebutted. The results of this Chapter were previously published in [41].

Part V explores the possibility of using the mathematical model of the whole heart to study pathological scenarios.

- **Chapter 11** provides a simulation study with the intent of evaluating the impact of standard ablation strategies for atrial fibrillation on overall cardiovascular performance.
- **Chapter 12** details the steps of modeling heart failure in an artificial scenario of dilated cardiomyopathy (DCM) including cellular and anatomical remodelling. This Chapter is based on the Master thesis by Albert Dasí [42].

Finally, **Part VI** draws a conclusion with respect to the specific research goals this thesis tried to answer and gives guidance to further improve the models in future studies.

PART I

FUNDAMENTALS

Chapter 2

Anatomy & Physiology of the Human Heart

This chapter outlines the basic concepts of the anatomy and physiology of the human heart, which are required to understand the content of this thesis, and is mostly based on the freely available book "Anatomy & Physiology" [43].

2.1 Anatomy & Structure of the Heart

The heart is the central organ of the cardiovascular system that pumps blood into the rest of the body nearly three billion times throughout a standard human lifetime. It is located in between the lungs within the thoracic cavity otherwise known as the mediastinum, where it is separated from the surrounding tissue by the pericardial sac. The posterior surface of the heart (also called the base of the heart) is attached to the superior vena cava (SVC), the inferior vena cava (IVC), the aorta, and the pulmonary artery (PA). At its most inferior point, the apex, the heart is deviated to the left of the mediastinum.

The heart is divided into four chambers: the left atrium (LA) and the left ventricle (LV) as well as the right atrium (RA) and the right ventricle (RV). These four chambers connect two distinct circuits called the pulmonary and systemic circuits to form the human circulatory system (Fig. 2.1, left panel). Deoxygenated blood is pumped into the PA by the RV before it branches into the many capillaries of the pulmonary circuit in the lungs. Here, the carbon dioxide in the blood is replaced with oxygen and transported back to the heart through the pulmonary veins. This highly oxygenated blood enters the heart via the LA to the LV, which in turn distributes the blood out of the aorta into the systemic circuit. After supplying the body with oxygen and nutrients, the blood returns to the RA through smaller veins that ultimately converge into the IVC and SVC. Finally, the blood in the RA is transferred actively or passively into the RV to close the circuit.

The walls of the four heart chambers are structured in three distinct layers of dissimilar thickness: the epicardium on the outside, the endocardium on the inside, and the myocardium

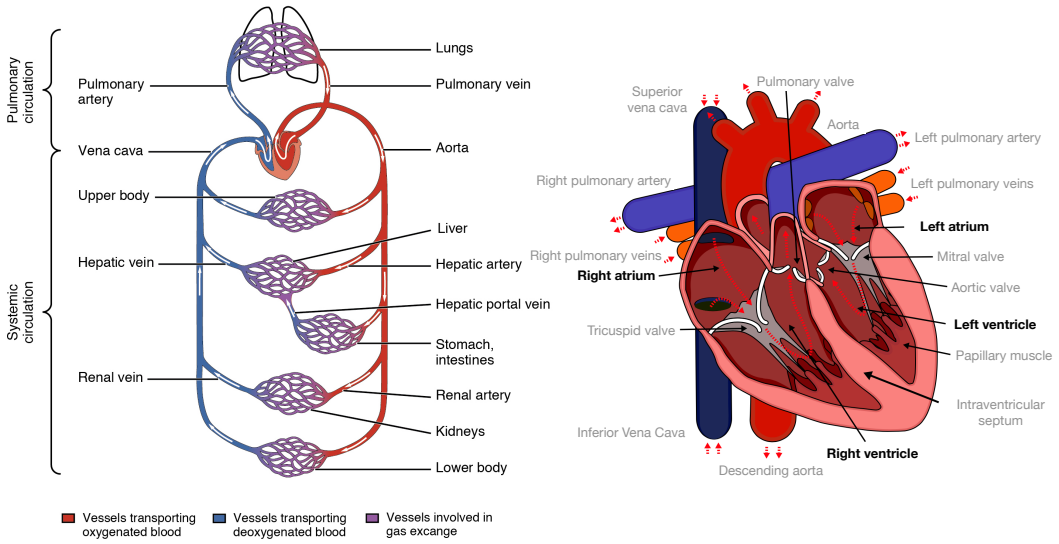

Figure 2.1: System of the human blood circulation. Blood flows from the RA to the RV, where it is pumped into the pulmonary circuit. After oxygenation in the lungs, the blood returns to the heart into the LA. From here, blood enters the LV, which pumps it into the systemic circuit. Following a gas exchange in the systemic capillaries, blood returns to the RA and the cycle is repeated. Modified from [43, 44], license: CC BY 4.0.

in between. The myocardium is the thickest of the three layers and is mainly composed of muscle cells, embedded in a framework of collagenous fibers, blood vessels and nerves. The muscle cells are organized in sheets. Individual sheets are held together by collagen [45, 46]. This microstructure is the source of the anisotropic properties of the myocardium. In the ventricles, the orientation of the muscle fibers and sheets varies throughout the wall and forms a complex, helical pattern (Fig. 2.2, right panel). During ventricular contraction, the helical arrangement of the muscle fibers results in a twisting motion, or torsion, of the ventricles, which greatly supports the ejection of blood from the chambers.

Cardiac muscle cells, or cardiomyocytes, are similar to skeletal muscle cells in terms of their internal architecture: they are striated muscles composed of individual myofibrils with alternating patterns of dark A bands and light I bands due to the precise alignment of sarcomeres along the length of the cell (Fig. 2.2, bottom left panel). T tubules that penetrate from the sarcolemma into the cell are found only at the connections between the sarcomeres, the Z discs, where they conduct the electrical impulse to the interior of the cell. Sarcomeres, the smallest contractile units of the heart, consist of a thin filament (composed of actin, troponin, and tropomyosin) and a thick filament (composed of myosin).

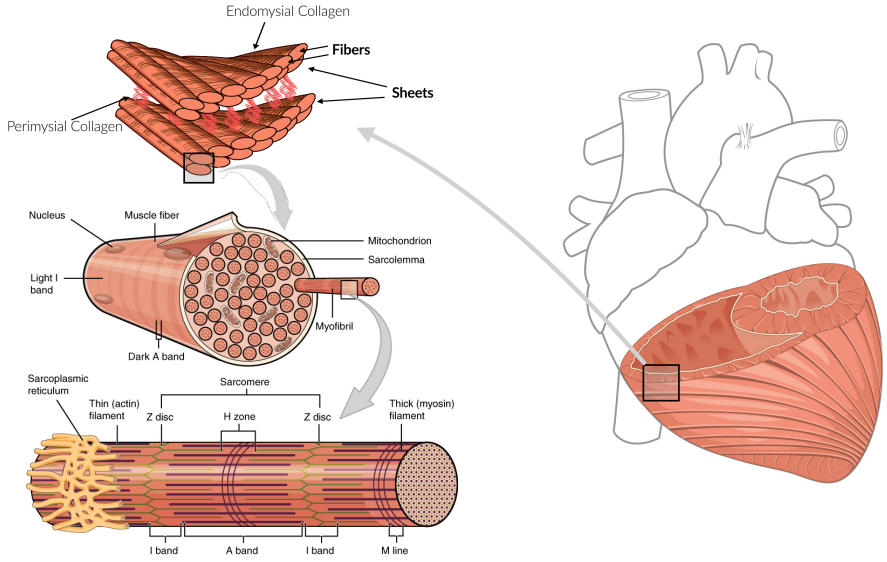

Figure 2.2: Multiscale structure of the myocardium. Modified from [43, 44], license: CC BY 4.0.

2.2 Cardiac Excitation, Conduction, and Contraction

Besides the contractile cells of the myocardium, which constitute the majority of atrial and ventricular tissue, there is a second type of cell with the main responsibility to initiate and propagate electrical impulses throughout the heart in a coordinated manner. These types of cells can be found in the sinoatrial node (SAN), the Bachmann's bundle (BB), the atrioventricular node (AVN), the bundle of His (HIS), and the Purkinje fibers [47]. Together, these specialized cells form the conduction system of the heart (Fig. 2.3). All types of myocytes have in common that they are excitable. The term excitable refers to the ability of the cell to be electrically excited, resulting in the generation of an action potential following the all-or-none principle. The time course of the cardiac action potential is the result of a complex process of active and passive ion exchange through the membrane of the cell. Ion movement and thus the action potential are considerably different between pacemaker and contractile cells (Fig. 2.3). Pacemaker cells contain ion channels that allow a slow influx of sodium ions into the cell, resulting in a slow depolarization and the capability of spontaneously generating electrical impulses. Contractile cells, however, need to be electrically excited by a neighboring cell through distinct connections, so called gap junctions. After reaching a certain threshold voltage, sodium ions rapidly flow through the membrane and depolarize the cell. As soon as the sodium gates close again, L-type voltage-gated calcium channels are opened during the plateau phase of the action potential. The flow of calcium into the cell initiates the release of more calcium from the sarcoplasmic reticulum

through ryanodine receptors. Through the sudden increase of the intracellular calcium concentration, calcium ions bind to troponin C to uncover the binding sites on actin such that the myosin heads of the thick filament can attach to the thin filament - a process called crossbridge cycling. As a consequence, the two filaments start to slide over each other leading to the shortening and thickening of the myocyte. The resulting tension is proportional to the intracellular calcium concentration and lasts until the troponin C bound calcium is removed via ATPase (adenosine triphosphatase, a class of enzymes that catalyze the decomposition of adenosine triphosphate into adenosine diphosphate and a free phosphate ion) enzymes to induce relaxation. This process of converting an electrical stimulus into a mechanical force is called excitation-contraction coupling [47]. Furthermore, the tension that is produced by the sarcomere depends on the degree of overlap of the thin and thick filaments. Maximal tension is produced at a sarcomere length of 2.2 µm. In shorter or longer cells, tension will be decreased, since the calcium sensitivity of troponin C depends on the length of the cell. This mechanism forms the basis for the so-called Frank Starling law [48], which describes an increase in stroke volume (SV) in response to an increase in end-diastolic volume (EDV).

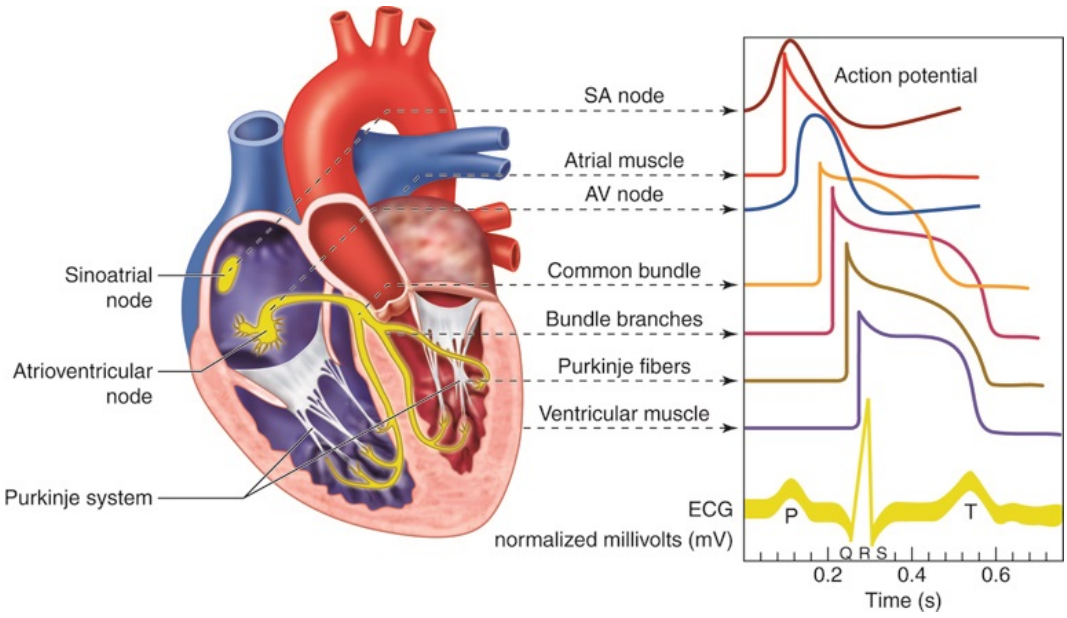

Figure 2.3: Schematic of the cardiac conduction system and associated action potentials in the different structures. From anatomytool.org, licence: CC BY-NC-SA 4.0.

2.3 Phases of the Cardiac Cycle

The cardiac cycle can be divided into a period of contraction when blood is pumped out of the chambers and a period of relaxation during which the chambers are actively or passively

filled with blood. These two periods are called systole and diastole, respectively. Illustrating the events of the cardiac cycle is possible in different ways. In the Wiggers diagram, the pressure and volume of the chambers and optionally the great vessels are related to time. An example of a Wiggers diagram including left ventricular volume and pressure as well as left atrial and aortic pressure is shown in Figure 2.4 together with a typical trace of an electrocardiogram (ECG).

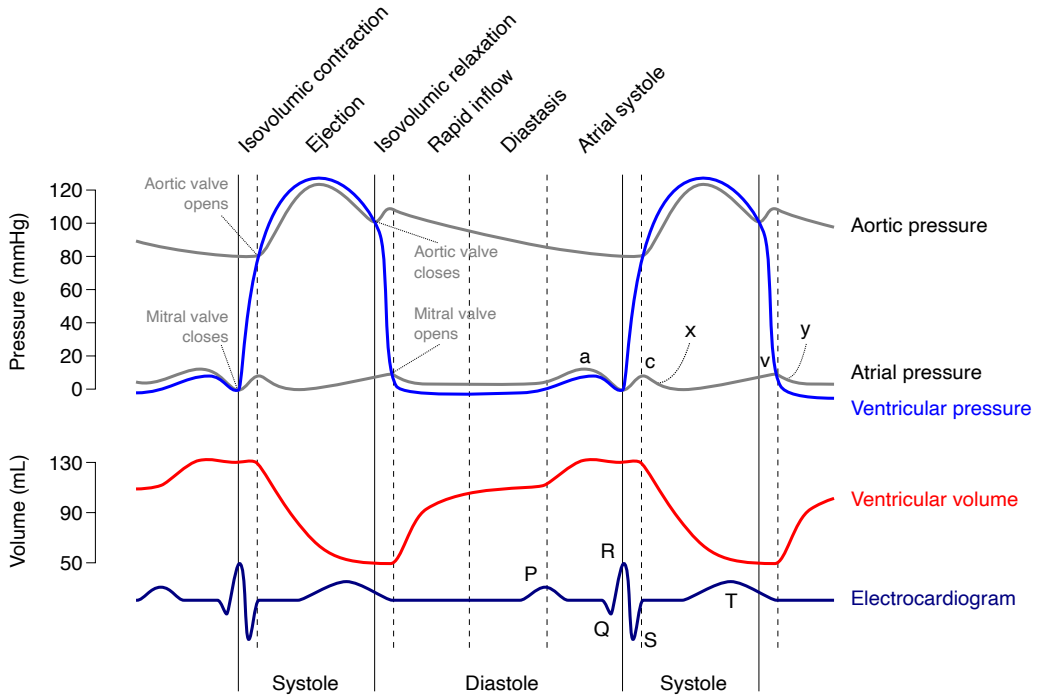

Figure 2.4: Cardiac cycle visualized by the Wiggers diagram of the LV. Modified from commons.wikimedia.org, original by Daniel Chang, license: CC BY-SA 2.5.

In the following, the events of the cardiac cycle will be explained with respect to ventricular systole and diastole: Ventricular systole may be conveniently divided into two phases. The first phase is called *isovolumetric contraction* since the volume of blood in the ventricles remains constant while the pressure increases and all valves are closed. The rising pressure in the ventricles pushes the atrioventricular valves slightly into the atria, which can be observed as a rise in atrial pressure denoted as the c-wave. In the second phase, ventricular pressure rises above the pressure in the systemic and pulmonary circuits and the semilunar valves open due to the *ejection* of blood from the ventricles. Meanwhile, the atria start to relax, which can be observed as a short decrease in pressure (x-descent) before the movement of the atrioventricular plane towards the apex results in a passive filling of the atria from the vena cavae and the pulmonary veins (v-wave). The amount of ejected blood from the ventricles is called SV and is the same for the left and right side even though the pressure on

the left side is remarkably higher than the one on the right side. The volume of blood that remains in the ventricles at the end of this phase is called end-systolic volume (ESV).

Ventricular relaxation, or diastole, begins as soon as the pressure in the ventricles drops below the pressure in the aorta and the PA and the semilunar valves close. For a short period of time, the ventricular volume stays constant which is why this period is named *isovolumetric relaxation*. *Early diastole* begins as soon as the ventricular pressure drops below the atrial pressure and the atrioventricular valves open. Due to the *rapid inflow* of blood into the ventricles, the pressure in all chambers drops slightly (y-descent) until the ventricles are fully relaxed and equilibrium is reached. The following period of time is called *diastasis* since it separates early diastole from atrial systole. It is the time when the movement and activity of the heart is at its minimum. The end of ventricular diastole coincides with *atrial systole* and can be observed by an increase in atrial and ventricular pressure (a-wave). The contraction of the atria, also called atrial kick, can contribute between 10% and 40% to ventricular SV depending on heart rate and age.

A second way of analyzing the events of the cardiac cycle are pressure-volume loops (PV-loop) or in particular the pressure-volume relation (PVR) of the chambers. Figure 2.5 shows an ideal PV-loop of the LV with almost rectangular shape, depicting the four major phases of the cardiac cycle: isovolumetric contraction, ejection, isovolumetric relaxation, and filling. This way of illustrating the cardiac cycle is particularly interesting since it can easily be analyzed with regard to pathologies such as heart failure and many other diseases. An example for this are the end-systolic pressure-volume relationship (ESPVR) and end-diastolic pressure-volume relationship (EDPVR), which characterize systolic and diastolic properties of the LV, respectively. An extensive overview of the clinical implications of invasive pressure-volume analysis is given in Bastos et al. [49].

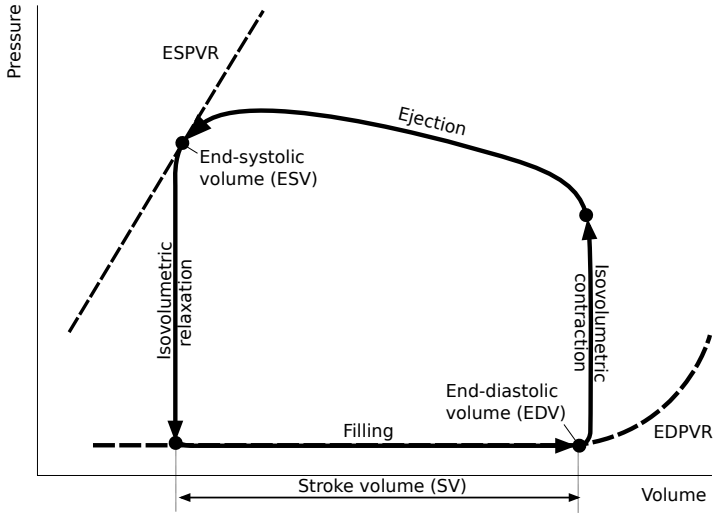

Figure 2.5: Cardiac cycle visualized by a pressure-volume-loop of the LV. Dashed lines illustrate the EDPVR and ESPVR.

Chapter 3

Modeling Cardiac Function

This chapter deals with the mathematical models that describe the physiological processes in a human heart. Specifically, it addresses the equations that are required to model the process of ion transportation through the cell membrane and the rise of an action potential, which propagates throughout the myocardium and results in the contraction of muscle fibers. For each of the core components of this mathematical model, methods based on current literature are presented and discussed with relevance to this thesis. The mathematical notation used throughout the thesis is adopted from current literature regarding cardiac modeling to ensure better comparability.

3.1 Modeling Cardiac Electrophysiology

Electrophysiological activity of the heart arises from complex electro-chemical processes at different spatial scales [50, 51]. At the finest scale, the electrical activity is the result of the flow of ions through specialized ionic channels embedded in the cell membrane. The membrane of a cardiomyocyte is permeable to multiple ionic species. Ion transport is not restricted to the passive flow of ions based on concentration gradients between the intra- and extracellular space. The total electric current across the membrane is given by the sum of electric currents associated with the respective number of ionic species N:

$$I_{\text{ion}} = \sum_{k=1}^{N} I_k \,, \tag{3.1}$$

where, according to Hodgkin and Huxley [52], the current of a single ionic species is given by

$$I_k = g_k \Big(\prod_{j=1}^{n_{\mathbf{w}}} w_j^{p_{j,k}} \Big) \Big(V_{\text{m}} - E_k \Big) \,, \tag{3.2}$$

with the membrane conductance g_k, the transmembrane voltage V_{m}, and the Nernst potential E_k, while $p_{j,k}$ quantifies the influence of channel j on the ionic species k. The dynamic behavior of opening and closing the ion channels is driven by the transmembrane voltage,

hence $n_{\mathbf{w}}$ gating variables

$$\frac{\mathrm{d}w_j}{\mathrm{d}t} = \frac{w_j^{\infty}(V_{\mathrm{m}}) - w_j}{\tau_j} \quad \text{for} \quad j = 1, \ldots, n_{\mathbf{w}}\,, \tag{3.3}$$

were introduced. The classic Hodgkin-Huxley model [52] only contains three ionic currents (sodium, potassium, and leakage current). More modern models not only encompass additional descriptions of ionic currents but also track the dynamics of ion concentrations in a set of variables denoted as $\mathbf{q}$. Therefore, in the most general sense, an ionic model ($\mathcal{I}$) can be described by

$$(\mathcal{I}) \begin{cases} \frac{\partial \mathbf{w}}{\partial t} - \mathbf{G}_{\mathbf{w}}(V_{\mathrm{m}}, \mathbf{w}, \mathbf{q}) &= \mathbf{0}\,, \\ \frac{\partial \mathbf{q}}{\partial t} - \mathbf{G}_{\mathbf{q}}(V_{\mathrm{m}}, \mathbf{w}, \mathbf{q}) &= \mathbf{0}\,, \end{cases} \tag{3.4}$$

where $\mathbf{w}$ and $\mathbf{q}$ collect the gating variables and ion concentrations, respectively, and $\mathbf{G}_{\mathbf{w}}$ and $\mathbf{G}_{\mathbf{q}}$ are suitably defined functions. The model of a single cardiac cell is completed by relating the transmembrane voltage V_{m} to the ionic currents. Assuming the cell membrane acts like a capacitor in parallel with a resistor, this relation is given by

$$C_{\mathrm{m}} \frac{\partial V_{\mathrm{m}}}{\partial t} + I_{\mathrm{ion}}(V_{\mathrm{m}}, \mathbf{w}, \mathbf{q}) + I_{\mathrm{app}}(t) = 0\,, \tag{3.5}$$

where C_{m} denotes the membrane capacitance and I_{app} is an externally applied stimulus current. As outlined in Chapter 2.2, primary cell types all have a slightly different function and thus different shapes of action potentials (Fig. 2.3). To account for these differences, each cell type has to be represented by a different ionic model [47], which results in differences in the term I_{ion}. An extensive collection of ionic models can be found on the website of the IUPS Physiome Project [1].

Moving on to a larger scale model of tissue electrophysiology, Eq. (3.5) is not sufficient anymore since cardiac cells are not electrically isolated from each other. They are connected by gap junctions that allow an exchange of ions between cells. Representing the microscopic details of these small structures on the tissue scale is difficult if not impossible. However, a suitable mathematical model, the so-called *bidomain model* [53–55], can be derived if the microstructure of the myocardium is homogenized in terms of muscle fibers that are organized in sheets. The bidomain model is generally considered as the most accurate representation of cardiac electrophysiology. However, it is computationally expensive and is not relevant for most applications. For this reason, many computational modeling studies refer to the *monodomain model*, which is a valid reduction of the bidomain model when an equal anisotropy ratio of the tissue is assumed. Given a computational domain $\Omega_0 \subset \mathbb{R}^3$ and a time interval $t \in (0, T]$, the monodomain model ($\mathcal{E}$) reads

$$(\mathcal{E}) \begin{cases} \beta \left[C_{\mathrm{m}} \frac{\partial V_{\mathrm{m}}}{\partial t} + I_{\mathrm{ion}}(V_{\mathrm{m}}, \mathbf{w}, \mathbf{q}) + I_{\mathrm{app}}(t) \right] = \nabla \cdot (\mathbf{D} \nabla V_{\mathrm{m}}) & \text{in} \quad \Omega_0\,, \\ (\mathbf{D} \nabla V_{\mathrm{m}}) \cdot \mathbf{N} = 0 & \text{on} \quad \partial\Omega_0\,, \end{cases} \tag{3.6}$$

[1] https://models.physiomeproject.org/cellml

where β is the membrane surface-to-volume ratio, $\mathbf{D}$ the diffusion tensor, and $\mathbf{N}$ the outer surface normal. To account for the anisotropy of cardiac tissue due to its structure (Chapter 2.1), a local frame of reference $(\mathbf{f}_0, \mathbf{s}_0, \mathbf{n}_0)$ is introduced at each point $\mathbf{X} \in \Omega_0$, consisting of the three orthogonal vectors that represent the direction of the fibers, sheets, and the sheet normals, respectively [46]. This reference frame is incorporated into the conductivity tensor by means of

$$\mathbf{D} = \sigma_f \mathbf{f}_0 \otimes \mathbf{f}_0 + \sigma_s \mathbf{s}_0 \otimes \mathbf{s}_0 + \sigma_n \mathbf{n}_0 \otimes \mathbf{n}_0 \,, \tag{3.7}$$

where σ_i is half of the harmonic mean of the intra- and extracellular conductivity in the three principal directions $i \in [f, s, n]$. Since it is much more likely to measure conduction velocity (CV) in clinical scenarios than conductivity (e.g., [34, 56]), Costa et al. [57] proposed an automated parameterization strategy to find optimal conductivity values for a given CV.

Most of the time, the external stimulus current I_{app} is given by a predefined protocol typically defined in a region $\Omega_{\text{stim}} = \Omega_{\text{SAN}} \cup \Omega_{\text{HPS}}$ as

$$I_{\text{app}}(t) = \begin{cases} A & \text{in} \quad \Omega_{\text{SAN}} \times (0, \tau] \,, \\ A & \text{in} \quad \Omega_{\text{HPS}} \times (t_{\text{AVN}}, t_{\text{AVN}} + \tau] \,, \\ 0 & \text{otherwise} \quad , \end{cases} \tag{3.8}$$

depending on the duration τ and the amplitude A of the stimulus as well as the conduction delay introduced by the atrioventricular node (AVN) t_{AVN}. The area of the stimulus Ω_{stim} mimics the major components of the cardiac conduction system (Fig. 2.3) to start atrial and ventricular depolarization. Specifically, Ω_{SAN} defines the location of the sinoatrial node (SAN) exit site at the junction of the right atrial appendage and the superior vena cava (SVC) [58]. Properly activating the ventricles is not as trivial due to the conduction of the depolarization wave through the AVN, the His-Purkinje system (HPS), and finally the ventricular myocardium. Therefore, different methods to define Ω_{HPS} have emerged in literature. One approach is to define sites of earliest activation based on experimental measurements [59] in combination with a thin, fast conducting endocardial layer to model the effect of the HPS [60–62]. More accurately, the HPS can be modeled explicitly [63–66] or implicitly by capturing the electrical activation at the Purkinje muscle junctions based on electrogram measurements [32, 67–72]. Both methods have proven to be able to accurately reproduce patient specific electrocardiogram measurements [32, 62]. However, the setup of a dedicated HPS is typically more complex.

3.2 Modeling Active Force Generation

The active contraction of the heart muscle is a direct consequence of the interaction between the proteins actin and myosin on the thin and thick filaments of the sarcomere [73–75]. Recalling Chapter 2.2, this interaction is the result of several electro-mechano-chemical processes on the subcellular level involving the increase of the intracellular calcium concentration $[\text{Ca}^{2+}]_{\text{i}}$ as the result of the depolarization of the cell and subsequent binding of

Ca^{2+} ions to the regulatory units consisting of troponin and tropomyosin. This enables the formation of crossbridges to generate force by consuming energy that is stored in the form of ATP. Additionally, these microscopic processes include other regulatory mechanisms that – on a macroscopic scale – give rise to the Frank-Starling effect [48, 75]. The amount of active tension T_a that is developed by a single sarcomere is dependent on two variables: the intracellular calcium concentration $[Ca^{2+}]_i$ and the sarcomere length SL. While the relationship between the maximal isometric force T_a^{iso} and calcium can be described by the famous Hill equation [76–79], an increase of SL will increase the force at maximal calcium saturation and enhance calcium sensitivity of the regulatory units (Fig. 3.1 (a); [80]). Furthermore,

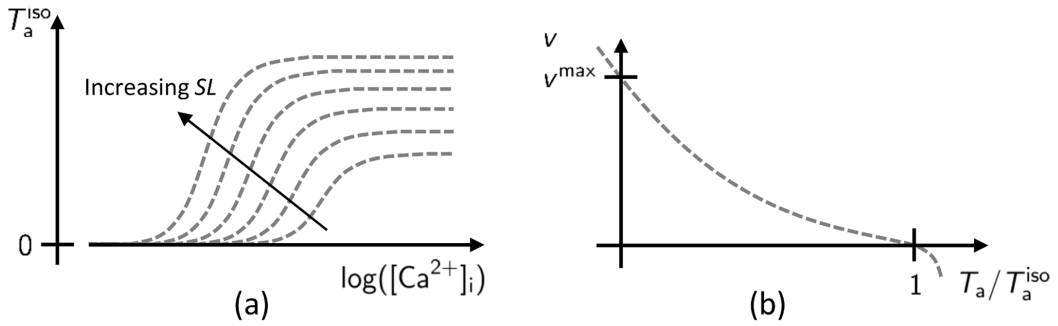

Figure 3.1: Representation of the steady-state force-calcium relationship (a) and the force-velocity relationship (b). Modified from [80], license: CC BY 4.0

muscle tension is regulated by the rate $v = -\frac{\partial}{\partial t}\,\mathrm{SL}/\mathrm{SL}_0$ at which the sarcomere changes its length, the so-called force-velocity curve (Fig. 3.1 (b)). Hill [76] discovered that the force-velocity curve is defined by a maximal velocity v^{max} at which the generated tension is zero [73, 75].

To capture all these mechanistic effects in a detailed mathematical model is inherently difficult and linked to large computational costs associated with the numerical schemes required to solve such models. Nevertheless, a lot of attempts were made in the past years to derive models that are able to capture the aforementioned mechanisms of force generation in organ level simulations. All of these models can be categorized into the following groups:

- Phenomenological models that focus on the development of active tension T_a by fitting experimental data to simple mathematical equations. These models may or may not include some form of dependence on the sarcomere length SL. However, they do not include calcium mediated activation and rely on explicit activation times to signal the start of contraction. Consequently, these models cannot adapt to a change in heart rate without re-parameterization. Due to their inherent simplicity, models from this category are easy to adapt to patient specific data and are therefore often used in cardiac multiscale simulations. Examples for models that fall into this category are given in [81–85].

- More complex models are typically motivated by physical principles and include the thin filament kinetics and a description of crossbridge cycling. The majority of models that fall into this category adopt the mean-field approach to model sarcomere dynamics by a single regulatory unit and a single crossbridge based on a Markov chain model with a finite number of states [14, 86–94]. An even higher complexity is reached in spatially explicit models [80, 95–99]. These include multiple continuous-time Markov chains to model the end-to-end interactions inside the sarcomere. Recently, artificial neural networks were used to reduce the computational effort required for one of these models to make it usable in multiscale simulations [100].

To summarize, with the exception of Markov chain models, sarcomere models ($\mathcal{A}$) can be written in the form

$$(\mathcal{A}) \quad \frac{\partial \mathbf{s}}{\partial t} - \mathbf{G}_{\mathbf{s}}(\mathbf{s}, [\mathrm{Ca}^{2+}]_{\mathrm{i}}, \lambda, \frac{\partial \lambda}{\partial t}) = \mathbf{0} \quad \text{in} \quad \Omega_0\,, \tag{3.9}$$

where $\mathbf{s}\colon (0,T] \times \Omega_0 \to \mathbb{R}^{n_{\mathbf{s}}}$ are the state variables associated with thin filament kinetics and crossbridge cycling, $\mathbf{G}_{\mathbf{s}}$ are suitably defined functions, and $\lambda = \mathrm{SL}/\mathrm{SL}_0$ is the normalized sarcomere length further denoted as the stretch ratio, or simply stretch.

3.3 Modeling Cardiac Mechanics

Under normal conditions, the heart undergoes large deformations during the contraction and relaxation phases of the cardiac cycle. The associated displacement of the myocardium can be found by relating the strain of the tissue with the stress generated by the contraction of myocytes together with the pressure that is exerted onto the endocardium by the blood inside the chambers. This is done in the framework of continuum mechanics [101, 102].

Considering a continuous body $\Omega_0 \subset \mathbb{R}^3$ in its reference configuration, a deformation map $\varphi\colon (0,T] \times \Omega_0 \to \mathbb{R}^3$ can be defined that relates the reference coordinates $\mathbf{X} \in \Omega_0$ to the current coordinates $\mathbf{x} \in \Omega$ such that $\mathbf{x} = \varphi(\mathbf{X},t)$ at time t. Next, the displacement field of the body is defined by $\mathbf{d}(\mathbf{X},t) = \varphi(\mathbf{X},t) - \mathbf{X}$ together with the deformation gradient $\mathbf{F}(\mathbf{X},t) = \nabla\varphi(\mathbf{X},t) = \mathbb{1} - \nabla\mathbf{d}$. The deformation map is injective and orientation preserving, i.e. its Jacobian satisfies $J = \det\mathbf{F} > 0$.

By Newton's second law, the force acting on a body has to be balanced by the time derivative of its momentum, which is described by the linear momentum equation

$$\rho_0 \frac{\partial^2 \mathbf{d}}{\partial t^2} - \nabla \cdot (\mathbf{F}\mathbf{S}) = \mathbf{0} \quad \text{in} \quad \Omega_0\,, \tag{3.10}$$

where ρ_0 is the body's density and $\mathbf{S}$ is the second Piola-Kirchhoff stress tensor.

To complete the model, suitable initial and boundary conditions together with a constitutive law to model the passive material properties have to be specified. Passive material properties of the myocardium are assumed to be hyperelastic and quasi-incompressible. As a consequence, the second Piola-Kirchhoff stress $\mathbf{S}$ can be defined by a stored strain

energy density function Ψ after introducing the right Cauchy-Green tensor $\mathbf{C} = \mathbf{F}^{\mathsf{T}}\mathbf{F}$ and the Green-Lagrange strain tensor $\mathbf{E} = \frac{1}{2}(\mathbf{C} - \mathbb{1})$:

$$\mathbf{S} = 2\frac{\partial \Psi(\mathbf{C})}{\partial \mathbf{C}} = \frac{\partial \Psi(\mathbf{E})}{\partial \mathbf{E}}. \tag{3.11}$$

Different constitutive laws have been introduced and used in the context of cardiac modeling. Due to the presence of fibers in cardiac tissue, these constitutive laws account for anisotropy by imposing a different elastic response along the directions of fibers $\mathbf{f}_0$, sheets $\mathbf{s}_0$, and sheet-normals $\mathbf{n}_0$. Some are referred to as transverse isotropic [103, 104] due to their symmetric response in the transverse plane. Others are considered orthotropic [105–107] due to their three orthogonal preferential directions. Recently, specialized constitutive laws for myocardial scars [108] and viscoelastic materials [109] have been proposed. Others consider the myocardium to be compressible during systole [110, 111] due to the blood perfusion of the myocardium. Purely passive tissue is typically modeled as a rubber-like Neo-Hookean model. The models considered in this thesis and their derivation of the 2nd Piola-Kirchhoff stress can be found in Appendix B (Eqs. (B.10), (B.12), (B.15)).

To account for the active stress generated during cardiac contraction, $\mathbf{S}$ is additively decomposed into an active ($\mathbf{S}_\mathrm{a}$) and a passive ($\mathbf{S}_\mathrm{p}$) component such that

$$\mathbf{S}(\mathbf{d}, T_\mathrm{a}(\mathbf{s}, \mathbf{F})) = \mathbf{S}_\mathrm{p} + \mathbf{S}_\mathrm{a} \tag{3.12}$$

$$= 2\frac{\partial \Psi(\mathbf{C})}{\partial \mathbf{C}} + T_\mathrm{a}(\mathbf{s}, \mathbf{F})\frac{\mathbf{f}_0 \otimes \mathbf{f}_0}{\lambda_\mathrm{f}^2}, \tag{3.13}$$

with T_a being the contractile force introduced in Section 3.2 and $\lambda_\mathrm{f} = (\mathbf{F}\mathbf{f})^{\mathsf{T}}(\mathbf{F}\mathbf{f})$ is the fiber stretch calculated from the deformation gradient. Active stress is modeled by upscaling the microscopic force T_a generated by cardiac muscle fibers to the tissue level. Thus, expressing it in terms of an internal stress that acts in the first principal direction of the tissue, namely the fibers $\mathbf{f}_0$. By nature, active stress is only added in atrial and ventricular tissue. Alternatively to the active stress approach (3.12), it is possible to prescribe an active strain to model mechanical activation [112–114]. However, the active stress approach is the most used method in cardiac mechanics and is the only method considered in this thesis.

The model is complemented by physiologically motivated boundary conditions. First, the deformation of the heart is physiologically restricted by the pericardial sac and other surrounding tissues such as the lungs, diaphragm, sternum and ribs, as well as the aorta and other vessels. Including pericardial boundary conditions in the model has been shown to help reproduce atrioventricular plane displacement (AVPD) observed in clinical measurements [13, 20, 115, 116]. Until now, the most accurate representation of the pericardium was proposed by Fritz et al. [20]. They model the interaction between the pericardium and myocardium as a frictionless contact problem using a penalty formulation that acts as a force on the epicardium and an elastic body surrounding the heart. However, this method is computationally rather expensive due to the need of solving the adhesive interaction problem. A more simple method that is used in the majority of cardiac mechanics studies for its ease of use in both

whole heart and (bi-)ventricular scenarios are generalized Robin boundary conditions. Here, the myocardial-pericardial interaction is modeled using the elastic potential of a linear spring with either constant [115] or spatially varying [116, 117] spring stiffness.

Finally, normal stress boundary conditions are imposed on the endocardium of the left ventricle (LV), right ventricle (RV), left atrium (LA), and right atrium (RA) to model the pressure exerted by the blood in these four chambers. This process is described in more detail in Chapter 3.4.

To summarize, the cardiac mechanics model ($\mathcal{M}$) is described by a system of equations which reads

$$(\mathcal{M}) \begin{cases} \rho_0 \frac{\partial^2 \mathbf{d}}{\partial t^2} - \nabla \cdot (\mathbf{F}\mathbf{S}(\mathbf{d}, T_\mathrm{a}(\mathbf{s}, \mathbf{F}))) = \mathbf{0} & \text{in} \quad \Omega_0\,, \\ \mathbf{F}\mathbf{S}(\mathbf{d}, T_\mathrm{a}(\mathbf{s}, \mathbf{F}))\mathbf{N} = \mathbf{f}^{\mathrm{epi}} & \text{on} \quad \Gamma_0^{\mathrm{epi}}\,, \\ \mathbf{F}\mathbf{S}(\mathbf{d}, T_\mathrm{a}(\mathbf{s}, \mathbf{F}))\mathbf{N} = -p_\mathrm{C}(t) J \mathbf{F}^{-\mathsf{T}}\mathbf{N} & \text{on} \quad \Gamma_0^{\mathrm{endo}}\,, \end{cases} \tag{3.14}$$

where $\mathbf{f}^{\mathrm{epi}}$ is the force acting on the epicardial surface Γ_0^{epi} of the heart, $p_\mathrm{C}(t)$ is the pressure inside the cardiac chamber C acting on the endocardial surface Γ_0^{endo}, and $\mathbf{N}$ is the surface normal vector.

3.4 Modeling the Circulatory System

The main function of the heart is to pump blood through the body. During each heart beat, blood flows through the heart, the pulmonary and the systemic circuit in a cyclic manner while interacting with the myocardium and the valves. Most accurately, this is described as a fluid-structure interaction (FSI) problem. Only a few cardiac simulation frameworks have been proposed that solve the FSI system [18, 50, 118, 119] with a mutual focus on the LV or the great vessels. More commonly, zero-dimensional (0D) lumped parameter models of the circulatory system are used to replace the need of using an FSI model. For whole heart simulations, a 0D closed-loop model [12, 120–123] is necessary to reproduce the full cardiac cycle. The model needs to be coupled to the mechanical system [124–130] such that the volume consistency of the three-dimensional (3D) and 0D models is guaranteed.

In this thesis, the circulatory system model developed during S. Schuler's Master's thesis [130, 131] is used, which was first published in [35]. The systemic and pulmonary circulation are each represented by a three-element Windkessel model. A description of the pressure gradient across the atrioventricular and semilunar valves is included based on Garcia et al. [132] with dynamic opening and closing of the valves [133]. Briefly, the circulatory system model ($\mathcal{C}$) is given by

$$(\mathcal{C}) \quad \frac{\mathrm{d}\mathbf{c}(t)}{\mathrm{d}t} - \mathbf{G}_\mathbf{c}(t, \mathbf{c}(t), \mathbf{p}(t)) = \mathbf{0} \quad \text{in} \quad (0, T]\,, \tag{3.15}$$

where $\mathbf{c}\colon (0,T] \to \mathbb{R}^{16}$ are the state variables

$$\begin{aligned} \mathbf{c} = &(V_{\mathrm{LV}}, V_{\mathrm{SysArt}}, V_{\mathrm{SysVen}}, V_{\mathrm{RA}}, V_{\mathrm{RV}}, V_{\mathrm{PulArt}}, V_{\mathrm{PulVen}}, V_{\mathrm{LA}}, Q_{\mathrm{AV}}, Q_{\mathrm{TV}}, Q_{\mathrm{PV}}, Q_{\mathrm{MV}}, \\ &\eta_{\mathrm{AV}}, \eta_{\mathrm{TV}}, \eta_{\mathrm{PV}}, \eta_{\mathrm{MV}})^{\mathsf{T}}\,, \end{aligned}$$

associated with the chamber and vessel volumes V, the blood flow Q through the atrioventricular and semilunar valves, and the current state of the valves η. $\mathbf{G_c}$ conveniently collects the r.h.s. of the ordinary differential equations (ODEs) and $\mathbf{p}\colon (0,T] \to \mathbb{R}^8$ contains the pressure values in all compartments of the circulatory system

$$\mathbf{p} = (p_{\mathrm{LV}}, p_{\mathrm{SysArt}}, p_{\mathrm{SysVen}}, p_{\mathrm{RA}}, p_{\mathrm{RV}}, p_{\mathrm{PulArt}}, p_{\mathrm{PulVen}}, p_{\mathrm{LA}})^{\mathsf{T}}.$$

The system of ODEs is given by

$$\begin{cases} \frac{\mathrm{d}V_{\mathrm{LV}}}{\mathrm{d}t} = Q_{\mathrm{MV}} - Q_{\mathrm{AV}}, & \frac{\mathrm{d}V_{\mathrm{SysArt}}}{\mathrm{d}t} = Q_{\mathrm{AV}} - Q_{\mathrm{SysPer}}, \\ \frac{\mathrm{d}V_{\mathrm{SysVen}}}{\mathrm{d}t} = Q_{\mathrm{SysPer}} - Q_{\mathrm{SysVen}}, & \frac{\mathrm{d}V_{\mathrm{RA}}}{\mathrm{d}t} = Q_{\mathrm{SysVen}} - Q_{\mathrm{TV}}, \\ \frac{\mathrm{d}V_{\mathrm{RV}}}{\mathrm{d}t} = Q_{\mathrm{TV}} - Q_{\mathrm{PV}}, & \frac{\mathrm{d}V_{\mathrm{PulArt}}}{\mathrm{d}t} = Q_{\mathrm{PV}} - Q_{\mathrm{PulPer}}, \\ \frac{\mathrm{d}V_{\mathrm{PulVen}}}{\mathrm{d}t} = Q_{\mathrm{PulPer}} - Q_{\mathrm{PulVen}}, & \frac{\mathrm{d}V_{\mathrm{LA}}}{\mathrm{d}t} = Q_{\mathrm{PulVen}} - Q_{\mathrm{MV}}, \\ L\frac{\mathrm{d}Q_{\mathrm{VT}}}{\mathrm{d}t} = \Delta p_{\mathrm{net}} - B|Q_{\mathrm{VT}}|Q_{\mathrm{VT}}, & \\ \frac{\mathrm{d}\eta_{\mathrm{VT}}}{\mathrm{d}t} = \begin{cases} K_o(1-\eta_{\mathrm{VT}})\Delta p_{\mathrm{net}} & \text{if} \quad \Delta p_{\mathrm{net}} > 0, \\ K_c \eta_{\mathrm{VT}} \Delta p_{\mathrm{net}} & \text{if} \quad \Delta p_{\mathrm{net}} \le 0, \end{cases} & \end{cases} \tag{3.16}$$

where $B = \frac{\rho_{\mathrm{Blood}}}{2A_{\mathrm{Eff}}^2}$ is the Borda-Carnot resistance, $L = \frac{6.28\rho_{\mathrm{Blood}}}{\sqrt{A_{\mathrm{Eff}}}}$ is the inertance, ρ_{Blood} is the density of blood, and Δp_{net} is the difference in pressure across the atrioventricular and semilunar valves $\mathrm{VT} \in \{\mathrm{AV}, \mathrm{TV}, \mathrm{PV}, \mathrm{MV}\}$. The rate of opening and closing of the valves is given by the coefficients K_o and K_c. The effective valve area A_{Eff} depends on the state of the valve and is given by

$$A_{\mathrm{Eff}}(t) = A_{\mathrm{Ref}} \frac{s(t)}{1-s(t)} \quad \text{using} \quad s(t) = (M_{\max} - M_{\min})\eta_{\mathrm{VT}}(t) + M_{\min}, \tag{3.17}$$

with the reference area A_{Ref} of the valve and the minimum and maximum area ratio, $M_{\min}$ and $M_{\max}$, respectively. For the pulmonary and systemic circulation, the blood flow is given by

$$Q_{\mathrm{SysPer}} = \frac{\frac{V_{\mathrm{SysArt}}}{C_{\mathrm{SysArt}}} - p_{\mathrm{SysVen}}}{R_{\mathrm{SysPer}}}, \qquad Q_{\mathrm{SysVen}} = \frac{p_{\mathrm{SysVen}} - p_{\mathrm{RA}}}{R_{\mathrm{SysVen}}}, \tag{3.18}$$

$$Q_{\mathrm{PulPer}} = \frac{\frac{V_{\mathrm{PulArt}}}{C_{\mathrm{PulArt}}} - p_{\mathrm{PulVen}}}{R_{\mathrm{PulPer}}}, \qquad Q_{\mathrm{PulVen}} = \frac{p_{\mathrm{PulVen}} - p_{\mathrm{LA}}}{R_{\mathrm{PulVen}}}, \tag{3.19}$$

with the resistances R, compliances C, and the pressures defined by

$$p_{\mathrm{SysArt}} = \frac{V_{\mathrm{SysArt}} - V^0_{\mathrm{SysArt}}}{C_{\mathrm{SysArt}}} + Q_{\mathrm{SysArt}} R_{\mathrm{SysArt}}, \qquad p_{\mathrm{SysVen}} = \frac{V_{\mathrm{SysVen}} - V^0_{\mathrm{SysVen}}}{C_{\mathrm{SysVen}}}, \tag{3.20}$$

$$p_{\mathrm{PulArt}} = \frac{V_{\mathrm{PulArt}} - V^0_{\mathrm{PulArt}}}{C_{\mathrm{PulArt}}} + Q_{\mathrm{PulArt}} R_{\mathrm{PulArt}}, \qquad p_{\mathrm{PulVen}} = \frac{V_{\mathrm{PulVen}} - V^0_{\mathrm{PulVen}}}{C_{\mathrm{PulVen}}}. \tag{3.21}$$

Unstressed systemic and peripheral volumes are denoted by a superscript 0. The pressure values p_{C} with $\mathrm{C} \in \{\mathrm{LV}, \mathrm{RV}, \mathrm{LA}, \mathrm{RA}\}$ are required for the Neumann boundary condition in Eq. (3.14) and are computed iteratively at each time step. In the first iteration $i = 0$ of each

time step t_n of the mechanical system ($\mathcal{M}$), the pressure p_C is extrapolated from the previous 5 time steps using a 4th order Adams-Bashforth scheme:

$$p_\mathrm{C}^{n,0} = p_\mathrm{C}^{n-1} + \Delta t_n \left(\frac{55}{24} \frac{\Delta p_\mathrm{C}^{n-1}}{\Delta t_{n-1}} - \frac{59}{24} \frac{\Delta p_\mathrm{C}^{n-2}}{\Delta t_{n-2}} + \frac{37}{24} \frac{\Delta p_\mathrm{C}^{n-3}}{\Delta t_{n-3}} - \frac{9}{24} \frac{\Delta p_\mathrm{C}^{n-4}}{\Delta t_{n-4}} \right), \tag{3.22}$$

with $\frac{\Delta p_\mathrm{C}^k}{\Delta t_k} = \frac{p_\mathrm{C}^k - p_\mathrm{C}^{k-1}}{t_k - t_{k-1}}$, $k \in \mathbb{N}$. If there are not enough pressure values available for extrapolation (i.e. $n < 5$), the pressure is simply increased $p_\mathrm{C}^{n,0} = p_\mathrm{C}^{n-1} + 1\,\mathrm{Pa}$. For the sake of brevity, the four chamber pressures are now denoted $\mathbf{p}_\mathrm{C} = (p_\mathrm{LV}, p_\mathrm{RV}, p_\mathrm{LA}, p_\mathrm{RA})^\mathsf{T}$. During consequent iterations $0 < i \leq 10$, the residual $\mathbf{r}_\mathrm{C} \colon \mathbb{R}^4 \to \mathbb{R}^4$ for all chambers

$$\mathbf{r}_\mathrm{C}(\mathbf{p}_\mathrm{C}^{n,i}) = (r_\mathrm{LV}, r_\mathrm{RV}, r_\mathrm{LA}, r_\mathrm{RA})^\mathsf{T},$$

with $r_\mathrm{C} = \left| V_\mathrm{C}^\mathrm{3D} - V_\mathrm{C}^\mathrm{0D} \right|$ is used to update $\mathbf{p}_\mathrm{C}$ by a quasi-Newton method [134]:

$$\mathbf{p}_\mathrm{C}^{n,i} = \mathbf{p}_\mathrm{C}^{n,i-1} - \mathbf{C}_i^{-1} \mathbf{r}_\mathrm{C}(\mathbf{p}_\mathrm{C}^{n,i}), \tag{3.23}$$

where $\mathbf{C}_i$ is the compliance matrix determined by

$$\mathbf{C}_i^{-1} = \mathbf{C}_{i-1}^{-1} + \left(\triangle \mathbf{p}_\mathrm{C}^{n,i} - \mathbf{C}_{i-1}^{-1} \triangle \mathbf{r}_\mathrm{C}^{n,i} \right) \frac{\triangle (\mathbf{p}_\mathrm{C}^{n,i})^\mathsf{T} \mathbf{C}_{i-1}^{-1}}{\triangle (\mathbf{p}_\mathrm{C}^{n,i})^\mathsf{T} \mathbf{C}_{i-1}^{-1} \triangle \mathbf{r}_\mathrm{C}^{n,i}}, \qquad \mathbf{C}_0^{-1} = \mathbb{1},$$

with $\triangle \mathbf{p}_\mathrm{C}^{n,i} = \mathbf{p}_\mathrm{C}^{n,i} - \mathbf{p}_\mathrm{C}^{n,i-1}$, $\triangle \mathbf{r}_\mathrm{C}^{n,i} = \mathbf{r}_\mathrm{C}(\mathbf{p}_\mathrm{C}^{n,i}) - \mathbf{r}_\mathrm{C}(\mathbf{p}_\mathrm{C}^{n,i-1})$. Typically, this method satisfies the volume-consistency constraint

$$\begin{cases} V_\mathrm{LV}^\mathrm{3D}(\mathbf{d}(t), \mathbf{p}_\mathrm{C}(t)) = V_\mathrm{LV}^\mathrm{0D}(\mathbf{c}(t), \mathbf{p}(t)) & \text{in} \quad (0,T], \\ V_\mathrm{RV}^\mathrm{3D}(\mathbf{d}(t), \mathbf{p}_\mathrm{C}(t)) = V_\mathrm{RV}^\mathrm{0D}(\mathbf{c}(t), \mathbf{p}(t)) & \text{in} \quad (0,T], \\ V_\mathrm{LA}^\mathrm{3D}(\mathbf{d}(t), \mathbf{p}_\mathrm{C}(t)) = V_\mathrm{LA}^\mathrm{0D}(\mathbf{c}(t), \mathbf{p}(t)) & \text{in} \quad (0,T], \\ V_\mathrm{RA}^\mathrm{3D}(\mathbf{d}(t), \mathbf{p}_\mathrm{C}(t)) = V_\mathrm{RA}^\mathrm{0D}(\mathbf{c}(t), \mathbf{p}(t)) & \text{in} \quad (0,T], \end{cases} \tag{3.24}$$

with a tolerance of $\|\mathbf{r}_\mathrm{C}\|_\infty < \varepsilon \leq 1 \times 10^{-7}\,\mathrm{mL}$ in 2 to 3 iterations. Compared to the modified Newton method proposed by Kerckhoffs et al. [125], this reduces the required iterations by a factor of 2 [131]. However, especially during the first time steps the quasi-Newton update might not be sufficient in which case a standard Newton method is applied and the compliance matrix is calculated using the Jacobian $\mathbf{C} = \frac{\mathrm{d}\mathbf{r}_\mathrm{C}}{\mathrm{d}\mathbf{p}_\mathrm{C}}$ after successively perturbing one chamber at a time.

PART II

ELECTROMECHANICAL MODELING OF THE WHOLE HEART

Chapter 4

Generating a Four Chamber Heart Model

The geometric model used throughout this thesis is based on magnetic resonance imaging (MRI) data of a 32-year-old healthy volunteer provided by Heidelberg University Hospital. The dataset was acquired using a 1.5 T MR tomography system (Philips Medical Systems) and consists of a static whole heart image at diastasis as well as time resolved MRI in 2-, 3-, and 4-chamber long axis view and 12 time resolved short axis slices with a 10 mm spacing. In previous works [44], endocardial and epicardial boundaries of the myocardial wall were segmented and labeled manually from the static whole heart image to create the atrial and ventricular domains. Valves, truncated vessels, and the pericardium were created using the workflow described by Kovacheva, E. [135]. Previous versions of this model were rather coarse [20, 131, 135], which presented limitations when a higher degree of anatomical detail was required. Additionally, the mesh had unreasonable element quality especially in regions with sharp edges, e.g. transitions between materials. During large deformations, low quality elements are prone to inversion under nearly incompressible conditions, causing simulations to fail. Therefore, the reference model was adapted and improved using the following strategy:

1. Obtain solutions to the Laplace equation $\nabla^2\Psi = 0$ with Dirichlet boundary conditions at the endocardium and epicardium, such that an arbitrary isovalue can be defined to split the myocardial wall in half.
2. Obtain an explicit mesh at this isovalue using the level-set discretization implemented in the software MMG [136].
3. If necessary connect, fix, and improve the explicit mesh using mesh manipulation tools such as Blender, Meshtool [137], or vmtk [138].
4. Remesh the volume and optimize mesh quality using Gmsh [139]. The explicit surface generated in steps 1 to 3 ensures a minimum of two elements throughout the myocardium.

Next, solutions to the Laplace equation were used to redefine materials in the heart domain Ω_0 as described by Kovacheva [135]. As shown in Figure 4.1, the heart was labeled and partitioned into left ventricle (LV), right ventricle (RV), left atrium (LA), right atrium (RA), tricuspid valve (TV), mitral valve (MV), pulmonary valve (PV), aortic valve (AV), pulmonary veins, superior vena cava (SVC), inferior vena cava (IVC), orifices to close the atrial cavities, and the pericardium. The pericardium was further divided into basal and apical sections and its thickness was chosen arbitrarily and does not only represent the pericardial sac but al surrounding tissues.

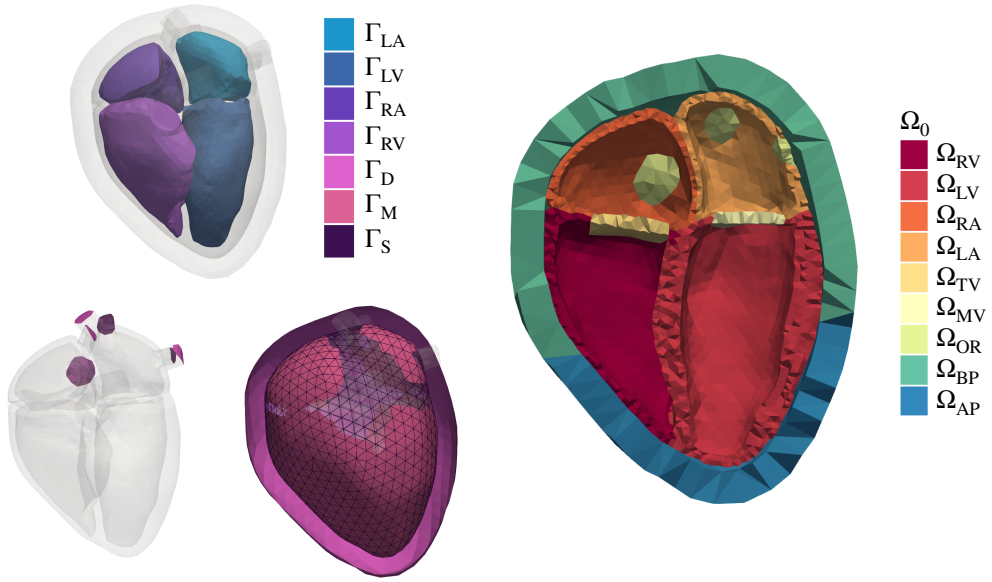

Figure 4.1: Labeled heart model after rediscretization. Visualized on the left are the surfaces required for the boundary conditions of the coupled problem described in Chapter 5. The slave surface Γ_S is shown as a wiremesh and the outer surface of the surrounding tissue is clipped. On the right, the heart was clipped in the long axis four-chamber view to reveal the labeled materials of the reference domain Ω_0. Due to the clip, PV, AV, pulmonary veins, SVC, and IVC are not visible.

4.1 Fiber Generation in the Atria and Ventricles

To capture the highly anisotropic characteristics of myocardial tissue, a fiber and sheet architecture was incorporated into the model. Recovering patient-specific fiber and sheet orientation is possible through diffusion tensor MRI [140]. However, this kind of imaging data are only available from ex vivo measurements and is extremely time consuming if acquired in vivo and thus, Laplace-Dirichlet-Rule-Based-Methods (LDRBMs) are used to define fiber and sheet orientations in the ventricles [141–144] and atria [144, 145]. Nevertheless, information about the transmural distribution of fiber and sheet angles from observations [146, 147] can

be used to parametrize LDRB methods to specify fiber and sheet angles at the endocardium and epicardium (α_{endo},α_{epi}, β_{endo},β_{epi}).

For the ventricles, a method based on Bayer et al. [141] was applied. The original algorithm was adapted by Schuler, S.[1] [148] to eliminate a discontinuity of the fibers in the free walls and to yield a fiber rotation that is proportional to the transmural Laplace solution. The helix angle α of the fibers in the ventricular wall transitions from about -60° to -90° on the epicardium to about 20° to 60° on the endocardium [146, 149]. Therefore, the following setup was used in this thesis:

$$\alpha_{\text{endo}} = 60^\circ, \quad \alpha_{\text{epi}} = -60^\circ, \quad \beta_{\text{endo}} = -65^\circ, \quad \beta_{\text{epi}} = 25^\circ,$$

which results in the reference frame $(\mathbf{f}_0, \mathbf{s}_0, \mathbf{n}_0)$ shown in Figure 4.2.

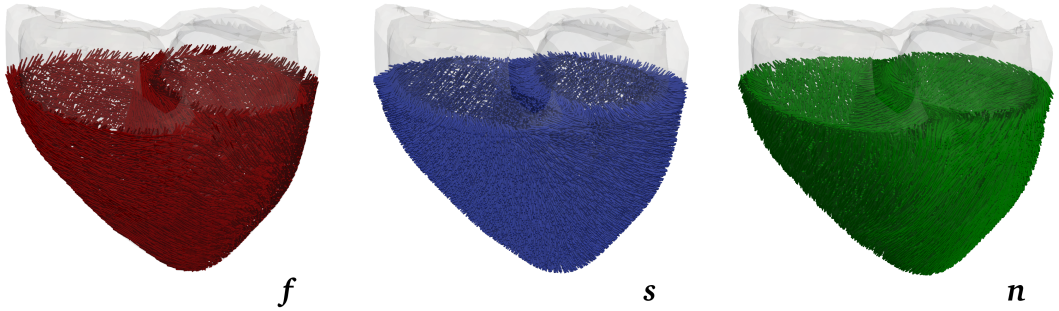

Figure 4.2: Fiber **f**, sheet **s**, and sheet-normal **n** orientation in the left and right ventricle.

The atrial fiber orientation **f** in this work is based on 22 seed points that define anatomical landmarks used to calculate numerous paths which split the atria in regions with distinct fiber orientation [145, 150][2]. Since this method only creates a fiber field, sheet and sheet-normal orientations have to be calculated separately. The sheet vectors were calculated based on the norm of the gradient of the solution to the Laplace equation $\nabla^2\Psi = 0$ between the endocardium and epicardium with the boundary conditions

$$\Psi = \begin{cases} 0 & \text{on} \quad \Gamma_{\text{endo}}, \\ 1 & \text{on} \quad \Gamma_{\text{epi}}, \end{cases}$$

with $\mathbf{s} = \|\nabla\Psi\|$ and the sheet-normal orientation was calculated using $\mathbf{n} = \frac{\mathbf{f}\times\mathbf{s}}{\|\mathbf{f}\times\mathbf{s}\|}$. Furthermore, this method automatically creates explicit inter-atrial connections that are essential to the cardiac conduction system. However, the Bachmann's bundle (BB), coronary sinus (CS), as well as middle and upper posterior connections are added to the outside of the mesh which causes problems in the electromechanically coupled heart model since they are very likely to flip during large mechanical deformations. To alleviate this issue, explicit representations

[1] https://github.com/KIT-IBT/LDRB_Fibers
[2] https://github.com/KIT-IBT/RESILIENT

of these inter-atrial connections in the existing myocardium are created using the following workflow: First, the shortest path $\mathbf{p}(\mathbf{X})$ on the surface Γ_{atria} between the exit sites of the inter-atrial connections in the right and left atrium is calculated using the fast marching method [151, 152][3]. Next, the existing fiber orientation $\mathbf{f}(\mathbf{X})$ is recalculated to follow the direction of the path using the relation

$$\mathbf{f}(\mathbf{p}_i) = \begin{cases} \frac{p_{i+1}-p_i}{\|p_{i+1}-p_i\|} & \text{if} \quad 0 \leq i < n\,, \\ \frac{p_i-p_{i-1}}{\|p_i-p_{i-1}\|} & \text{if} \quad i = n\,, \end{cases}$$

where n is the number of points along the path. Finally, the path is dilated by tagging each point $\mathbf{X}_C$ in the volume Ω_{atria} that resides within a sphere of radius 2.5 mm around the points of the path $\mathbf{p}(\mathbf{X})$.

4.2 Defining Universal Ventricular Coordinates

Universal coordinate systems are used in various applications that may benefit from a description of the local position of the heart. As an example, typical applications may include a standardized visualization and regional evaluation of cardiac data or the transfer of data between different imaging modalities. Recently, different universal coordinate systems have been proposed for the ventricles [25, 153] and atria [24]. Throughout this thesis, the method developed by Schuler et al. [153][4] is used to define universal ventricular coordinates which will be used for multiple purposes, e.g. a reproducible definition of the cardiac conduction system in the ventricles.

To define the universal coordinate system (a, m, r, v) with the apicobasal (a), transmural (m), rotational (r), and transventricular (v) coordinates, the ventricles are first truncated below the right ventricular outflow tract using a plane that is perpendicular to the long axis of the heart. Moreover, the resulting domain has to be tagged at the base, the epicardium, the LV, and the RV. The tags and the resulting coordinates are shown in Figure 4.3.

4.3 Bullseye Polar Representation of the Ventricles

Besides universal ventricular and atrial coordinates, there is another way to visualize and evaluate regional data especially in the ventricles. This approach divides the LV into 17 segments according to the American Heart Association (AHA) [154] and is commonly used in clinical practice and typically implemented directly into the proprietary software of MRI machines. However, the RV is not covered by this segmentation since it is rather

[3] Toolbox Fast Marching: https://www.mathworks.com/matlabcentral/fileexchange/6110-toolbox-fast-marching

[4] https://github.com/KIT-IBT/Cobiveco

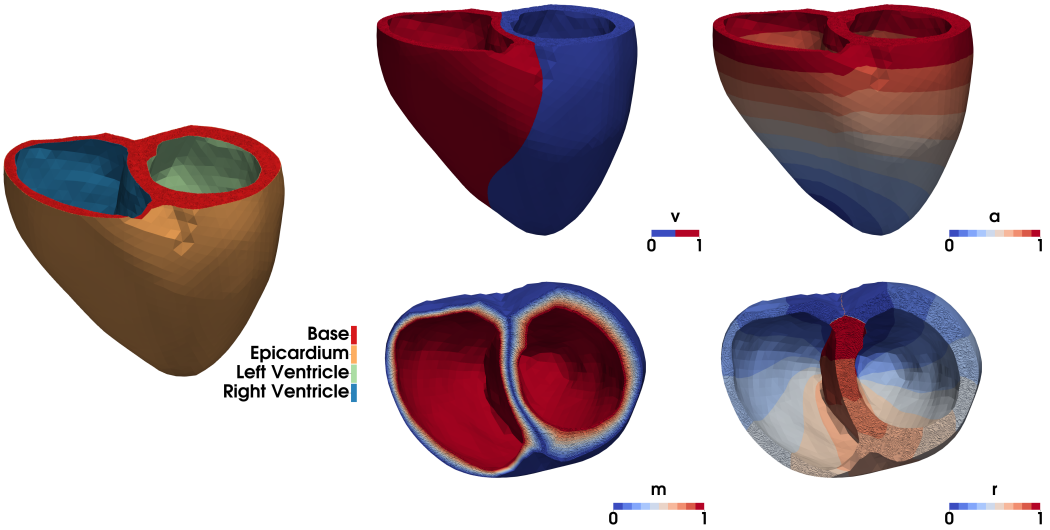

Figure 4.3: Universal coordinate system for the ventricles. On the left, the required tags for the method in [153] are shown. On the right, the coordinate system defined by the apicobasal (a), transmural (m), rotational (r), and transventricular (v) coordinates is shown.

difficult to properly establish a clear segmentation of the right ventricular epicardium in MRI measurements. Since a visualization of data on highly individualized left ventricular anatomies in three-dimensional (3D) can be quite cumbersome, a polar representation of these 17 segments in 2D is typically used, the so-called bullseye plot. The segmentation of the LV in our 3D geometry is shown in Figure 4.4 alongside the corresponding bullseye representation with the standardized nomenclature.

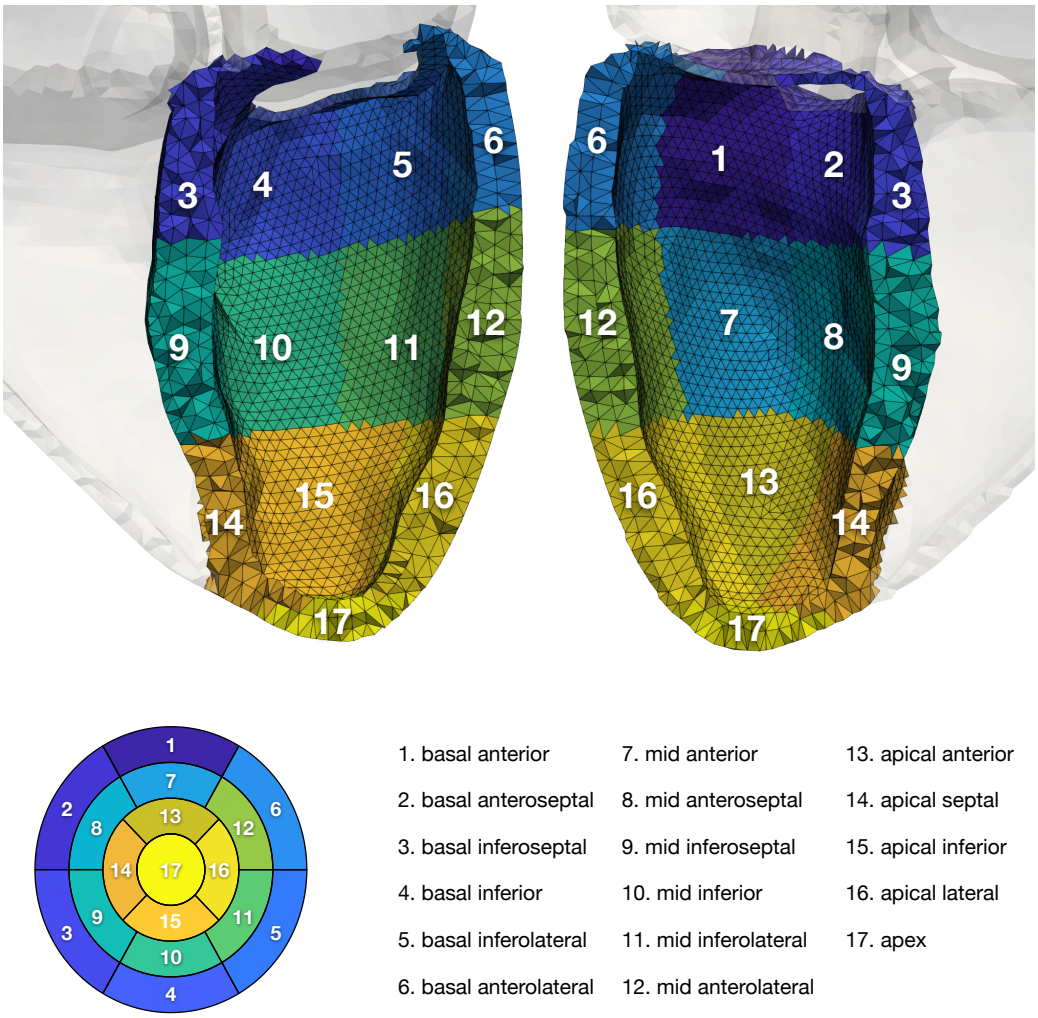

1. basal anterior
2. basal anteroseptal
3. basal inferoseptal
4. basal inferior
5. basal inferolateral
6. basal anterolateral
7. mid anterior
8. mid anteroseptal
9. mid inferoseptal
10. mid inferior
11. mid inferolateral
12. mid anterolateral
13. apical anterior
14. apical septal
15. apical inferior
16. apical lateral
17. apex

Figure 4.4: Division of the LV according to the AHA in the heart geometry (top) and visualized as a bullseye plot (bottom).

Chapter 5

Electromechanical Model of the Whole Heart

This section is based on the publications [35, 37] and some passages have been quoted verbatim.

In this chapter, the fully coupled electromechanics model with MEF ($\mathcal{IAE}_{\text{MEF}}$-$\mathcal{MC}$) is introduced. First, an electromechanical model of a cardiac muscle cell ($\mathcal{IA}$) is established by combining ionic membrane models of the atria and ventricles with a suitable physics based sarcomere model. Next, geometrically mediated MEF mechanisms are introduced to the tissue level of electrophysiology. Finally, the complete system of equations is formulated and the numerical approximation scheme is discussed.

5.1 Modeling the Electromechanical Response of Cardiac Muscle Cells

Throughout the heart, cardiac cells are differentiated into sinoatrial node (SAN) cells, atrioventricular node (AVN) cells, Purkinje fiber cells, atrial cells, and ventricular cells. Since all of these cells have a slightly different function, their action potential and thus the make up of the ionic current is different as well. The model presented in Chapter 4 only has an explicit representation of atrial and ventricular myocardium. Therefore, suitable models for these cell types have to be chosen. In this thesis, atrial myocardium is defined using the model of Courtemanche-Ramirez-Nattel (CRN) [155]. For the ventricles, the O'Hara-Rudy-dynamic (ORd) model [156] is used. In case of the ORd model, the modifications to the h- and j-gate as proposed by [157, 158] were implemented. Active tension development is represented by a recent model for human cardiac contraction proposed by Land (L17) [94]. It consists of a system of ODEs in the form of Eq. (3.9). Bidirectional coupling between the models of electrophysiology ($\mathcal{I}$) and active stress ($\mathcal{A}$) is established by replacing the algebraic formulation of the troponin buffer in the CRN and ORd models by the evolution of calcium bound to troponin from the L17 model. Therefore, the ion concentration $\mathbf{q}$ depends

on the stretch λ and Equation (3.4) extends to

$$\frac{\partial \mathbf{q}}{\partial t} - \mathbf{G}_{\mathbf{q}}(V_{\mathrm{m}}, \mathbf{w}, \mathbf{q}, \lambda) = \mathbf{0} \quad \text{in} \quad \Omega_0 \times (0,T]\,. \tag{5.1}$$

The components of (5.1) for the intracellular concentration of calcium ions $[\mathrm{Ca}^{2+}]_{\mathrm{i}}$ change to

$$\begin{aligned}\frac{\partial [\mathrm{Ca}^{2+}]_{\mathrm{i}}}{\partial t} = {} & \frac{1}{1+\frac{[\mathrm{CMDN}]_{\max} K_{\mathrm{CMDN}}}{([\mathrm{Ca}^{2+}]_{\mathrm{i}}+K_{\mathrm{CMDN}})^2}} \\ & \cdot \left[\frac{2I_{\mathrm{NaCa}} - I_{\mathrm{p,Ca}} - I_{\mathrm{Ca,L}} - I_{\mathrm{b,Ca}}}{2FV_{\mathrm{i}}} + \frac{V_{\mathrm{up}}(I_{\mathrm{up,leak}} - I_{\mathrm{up}}) + I_{\mathrm{rel}} V_{\mathrm{rel}}}{V_{\mathrm{i}}} - \frac{\partial [\mathrm{Ca}^{2+}]_{\mathrm{TRPN}}}{\partial t} \right],\end{aligned} \tag{5.2}$$

for the CRN model and

$$\begin{aligned}\frac{\partial [\mathrm{Ca}^{2+}]_{\mathrm{i}}}{\partial t} = {} & \frac{1}{1+\frac{[\mathrm{CMDN}]_{\max} K_{\mathrm{CMDN}}}{([\mathrm{Ca}^{2+}]_{\mathrm{i}}+K_{\mathrm{CMDN}})^2}} \\ & \left[-(I_{\mathrm{pCa}} + I_{\mathrm{Cab}} - 2I_{\mathrm{NaCa}}) \frac{A_{\mathrm{cap}}}{2F v_{\mathrm{myo}}} - J \frac{v_{\mathrm{nsr}}}{v_{\mathrm{myo}}} + J_{\mathrm{Ca}} \frac{v_{\mathrm{ss}}}{v_{\mathrm{myo}}} - \frac{\partial [\mathrm{Ca}^{2+}]_{\mathrm{TRPN}}}{\partial t} \right],\end{aligned} \tag{5.3}$$

for the ORd model with

$$\frac{\partial [\mathrm{Ca}^{2+}]_{\mathrm{TRPN}}}{\partial t} = [\mathrm{TRPN}]_{\max} \frac{\partial \mathrm{CaTRPN}}{\partial t}\,, \tag{5.4}$$

$$\frac{\partial \mathrm{CaTRPN}}{\partial t} = k_{\mathrm{TRPN}} \left[\left(\frac{[\mathrm{Ca}^{2+}]_{\mathrm{i}}}{[\mathrm{Ca}^{2+}]_{\mathrm{T50}}(\lambda)} \right)^{n_{\mathrm{TRPN}}} (1 - \mathrm{CaTRPN}) - \mathrm{CaTRPN} \right]. \tag{5.5}$$

TRPN is a component of $\mathbf{q}$ and represents the fraction of troponin C units with calcium bound to its regulatory binding site in the L17 model, $[\mathrm{TRPN}]_{\max}$ is the maximum concentration of troponin in the myoplasm, and $[\mathrm{Ca}^{2+}]_{\mathrm{T50}}(\lambda)$ is the length-dependent sensitivity to intracellular calcium given by

$$[\mathrm{Ca}^{2+}]_{\mathrm{T50}}(\lambda) = [\mathrm{Ca}^{2+}]^{\mathrm{ref}}_{\mathrm{T50}} + \beta_1 (\min(\lambda, 1.2) - 1)\,, \tag{5.6}$$

where β_1 is a constant that captures the change in calcium sensitivity. The above modifications are introduced in [159, 160] for the ORd model. Parameters or equations not defined specifically are adopted from the original models.

Originally, the active stress model by Land et al. was developed and driven by experimentally measured human calcium transients (CaT) for the atria [14] and ventricles [94], respectively. Due to differences in the CaTs of the two models used in this study compared to the ones used by Land et al. [14, 94], a re-parameterization of the tension model is necessary to achieve a physiologically correct active tension development. This is done by first identifying calcium-sensitive parameters in the L17 model and how these parameters affect the following characteristics of the force curve: diastolic tension (DT), force of contraction (FOC), duration of tension development (DTD), time to peak tension (TPT) and relaxation time from peak tension down to 50 % (RT_{50}) and 95 % (RT_{95}), respectively (Fig. 5.1). Then, the data is compared to experimental values from literature that was measured in single cell experiments of atrial and ventricular myocardium.

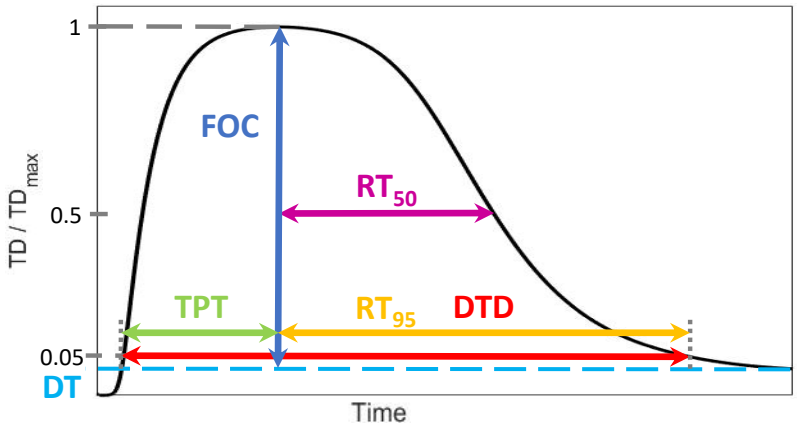

Figure 5.1: Schematic of the characteristics of a force curve. Reprinted with permission from [37].

5.2 Mechano-Electric Feedback

Besides from the electromechanical coupling mechanisms on the cellular level discussed in the previous section, MEF mechanisms can affect tissue level electrophysiology as well. In the past, electrophysiology in terms of the monodomain equation (3.6) was calculated on a fixed domain. However, several electrophysioloical alterations due to MEF have been reported, including a change in action potential duration, a decrease in resting membrane potential, stretch-induced depolarizations, and changes in intercellular conduction through gap junctions [161]. To reproduce these effects, the electrophysiology has to be evaluated on the deformed geometry, which makes a coupling to the tissue mechanics model (3.14) necessary [50, 159, 162, 163]. This can be achieved by introducing the deformation tensor $\mathbf{F}$ into the monodomain equation by pulling back into the material formulation [112]:

$$\beta \left[C_\mathrm{m} \frac{\partial}{\partial t}(V_\mathrm{m} J) + J(I_\mathrm{ion}(V_\mathrm{m}, \mathbf{w}, \mathbf{q}) + I_\mathrm{app}(t)) \right] = \nabla \cdot (J \mathbf{F}^{-1} \mathbf{D} \mathbf{F}^{-\mathsf{T}} \nabla V_\mathrm{m}) \,. \tag{5.7}$$

Since we assume a nearly incompressible material ($J = \det \mathbf{F} \approx 1$), the influence of the deformation on the time derivative of V_m and the ionic currents can be neglected. The diffusion tensor $\mathbf{D}_0$ in the reference configuration relates to the one in the material configuration $\mathbf{D}$ by

$$\mathbf{D}_0 = J \mathbf{F}^{-1} \mathbf{D} \mathbf{F}^{-\mathsf{T}} = J \left(\sigma_f \frac{\mathbf{f}_0 \otimes \mathbf{f}_0}{\lambda_f^2} + \sigma_s \frac{\mathbf{s}_0 \otimes \mathbf{s}_0}{\lambda_s^2} + \sigma_n \frac{\mathbf{n}_0 \otimes \mathbf{n}_0}{\lambda_n^2} \right) . \tag{5.8}$$

Notably, this means the conductivities σ^0, if measured in the fixed domain, are related to the ones in the deformed domain by means of

$$\sigma_f^0 = J \frac{\sigma_f}{\lambda_f^2}, \quad \sigma_s^0 = J \frac{\sigma_s}{\lambda_s^2}, \quad \sigma_n^0 = J \frac{\sigma_n}{\lambda_n^2} \,. \tag{5.9}$$

Furthermore, the existence of stretch-activated currents I_sac was first confirmed by Guharay and Sachs [164]. Different models were developed to describe the current $I_\mathrm{sac}(V_\mathrm{m}, \lambda)$ carried

by these channels including selective and nonselective variants [165–170]. For now, stretch activated currents are neglected. However, their influence on the cellular electrophysiology is evaluated in more detail in Chapter 12.

5.3 The Coupled 3D-0D Whole Heart Problem

For a time $t \in (0,T]$ in the reference domain Ω_0, the $\mathcal{IAE}_{\text{MEF}}$-$\mathcal{MC}$ model reads

$$
\begin{cases}
\dfrac{\partial \mathbf{w}}{\partial t} - \mathbf{G}_{\mathbf{w}}(V_{\text{m}}, \mathbf{w}, \mathbf{q}) = \mathbf{0} & \text{in } \Omega_0\,, & \text{(5.10a)}\\
\dfrac{\partial \mathbf{q}}{\partial t} - \mathbf{G}_{\mathbf{q}}(V_{\text{m}}, \mathbf{w}, \mathbf{q}, \lambda) = \mathbf{0} & \text{in } \Omega_0\,, & \text{(5.10b)}\\
\dfrac{\partial \mathbf{s}}{\partial t} - \mathbf{G}_{\mathbf{s}}(\mathbf{s}, [\text{Ca}^{2+}]_{\text{i}}, \lambda, \dfrac{\partial \lambda}{\partial t}) = \mathbf{0} & \text{in } \Omega_0\,, & \text{(5.10c)}\\
\beta \left[C_{\text{m}} \dfrac{\partial V_{\text{m}}}{\partial t} + I_{\text{ion}}(V_{\text{m}}, \mathbf{w}, \mathbf{q}) + I_{\text{app}}(t) \right] = \nabla \cdot (J\mathbf{F}^{-1}\mathbf{D}\mathbf{F}^{-\mathsf{T}} \nabla V_{\text{m}}) & \text{in } \Omega_0\,, & \text{(5.10d)}\\
(J\mathbf{F}^{-1}\mathbf{D}\mathbf{F}^{-\mathsf{T}} \nabla V_{\text{m}}) \cdot \mathbf{N} = 0 & \text{on } \partial\Omega_0\,, & \text{(5.10e)}\\
\rho_0 \dfrac{\partial^2 \mathbf{d}}{\partial t^2} - \nabla \cdot (\mathbf{F}\mathbf{S}(\mathbf{d}, T_{\text{a}}(\mathbf{s}, \mathbf{F}))) = \mathbf{0} & \text{in } \Omega_0\,, & \text{(5.10f)}\\
\mathbf{F}\mathbf{S}(\mathbf{d}, T_{\text{a}}(\mathbf{s}, \mathbf{F}))\mathbf{N} = \mathbf{f}^{\text{M}} & \text{on } \Gamma_0^{\text{M}}\,, & \text{(5.10g)}\\
\mathbf{F}\mathbf{S}(\mathbf{d}, T_{\text{a}}(\mathbf{s}, \mathbf{F}))\mathbf{N} = \mathbf{f}^{\text{S}} & \text{on } \Gamma_0^{\text{S}}\,, & \text{(5.10h)}\\
\mathbf{F}\mathbf{S}(\mathbf{d}, T_{\text{a}}(\mathbf{s}, \mathbf{F}))\mathbf{N} = -p_{\text{LV}} J\mathbf{F}^{-\mathsf{T}}\mathbf{N} & \text{on } \Gamma_0^{\text{LV}}\,, & \text{(5.10i)}\\
\mathbf{F}\mathbf{S}(\mathbf{d}, T_{\text{a}}(\mathbf{s}, \mathbf{F}))\mathbf{N} = -p_{\text{RV}} J\mathbf{F}^{-\mathsf{T}}\mathbf{N} & \text{on } \Gamma_0^{\text{RV}}\,, & \text{(5.10j)}\\
\mathbf{F}\mathbf{S}(\mathbf{d}, T_{\text{a}}(\mathbf{s}, \mathbf{F}))\mathbf{N} = -p_{\text{LA}} J\mathbf{F}^{-\mathsf{T}}\mathbf{N} & \text{on } \Gamma_0^{\text{LA}}\,, & \text{(5.10k)}\\
\mathbf{F}\mathbf{S}(\mathbf{d}, T_{\text{a}}(\mathbf{s}, \mathbf{F}))\mathbf{N} = -p_{\text{RA}} J\mathbf{F}^{-\mathsf{T}}\mathbf{N} & \text{on } \Gamma_0^{\text{RA}}\,, & \text{(5.10l)}\\
\mathbf{d} = \mathbf{0} & \text{on } \Gamma_0^{\text{D}}\,, & \text{(5.10m)}\\
\dfrac{\mathrm{d}\mathbf{c}}{\mathrm{d}t} - \mathbf{G}_{\mathbf{c}}(t, \mathbf{c}, p_{\text{LV}}, p_{\text{RV}}, p_{\text{LA}}, p_{\text{RA}}) = \mathbf{0}\,, & & \text{(5.10n)}\\
V_{\text{LV}}^{\text{3D}}(\mathbf{d}) = V_{\text{LV}}(\mathbf{c})\,, & & \text{(5.10o)}\\
V_{\text{RV}}^{\text{3D}}(\mathbf{d}) = V_{\text{RV}}(\mathbf{c})\,, & & \text{(5.10p)}\\
V_{\text{LA}}^{\text{3D}}(\mathbf{d}) = V_{\text{LA}}(\mathbf{c})\,, & & \text{(5.10q)}\\
V_{\text{RA}}^{\text{3D}}(\mathbf{d}) = V_{\text{RA}}(\mathbf{c})\,, & & \text{(5.10r)}
\end{cases}
$$

where the model unknowns are the transmembrane voltage $V_{\text{m}}\colon (0,T] \times \Omega_0 \to \mathbb{R}$, the vector of gating variables $\mathbf{w}\colon (0,T] \times \Omega_0 \to \mathbb{R}^{n_{\mathbf{w}}}$, the vector of ionic concentrations $\mathbf{q}\colon (0,T] \times \Omega_0 \to \mathbb{R}^{n_{\mathbf{q}}}$, the mechanical displacement $\mathbf{d}\colon (0,T] \times \Omega_0 \to \mathbb{R}^3$, the state variables of the active stress model $\mathbf{s}\colon (0,T] \times \Omega_0 \to \mathbb{R}^{n_{\mathbf{s}}}$, the state variables of the circulatory system model $\mathbf{c}\colon (0,T] \times \Omega_0 \to \mathbb{R}^{n_{\mathbf{c}}}$, and finally, the pressure $p_{\text{C}}\colon (0,T] \to \mathbb{R}$ in the left ventricle (LV), the right ventricle (RV), the left atrium (LA) and the right atrium (RA) for the compartments $\text{C} \in \{\text{LV}, \text{RV}, \text{LA}, \text{RA}\}$. The system of equations is complemented by initial values given in

$\Omega_0 \times 0$:

$$V_\mathrm{m} = V_\mathrm{m}^0, \quad \mathbf{w} = \mathbf{w}^0, \quad \mathbf{q} = \mathbf{q}^0, \quad \mathbf{d} = \mathbf{d}^0, \quad \mathbf{s} = \mathbf{s}^0, \quad \mathbf{c} = \mathbf{c}^0, \quad p_\mathrm{C} = p_\mathrm{C}^0 \,. \tag{5.11}$$

Equations (5.10a)-(5.10e) represent the monodomain equation including geometrically mediated MEF coupled to the cellular excitation-contraction models CRN+L17 ($n_\mathbf{w} = 15,\ n_\mathbf{q} = 5,\ n_\mathbf{s} = 7$) in the atria and ORd+L17 ($n_\mathbf{w} = 32,\ n_\mathbf{q} = 8,\ n_\mathbf{s} = 7$) in the ventricles. For the ORd model, the endo and mid variants are used.

Conductivity values in the atria were tuned in a simple geometry according to [57] to achieve physiological conduction velocities (CVs). Anisotropy ratios were chosen in agreement with Loewe et al. [171]. The resulting initial time to complete atrial depolarization $T_\mathrm{cAD,init}$ was above 120 ms and thus further adjusted using the formula from [172]

$$\sigma_\mathrm{adapt} \approx \sigma_\mathrm{init} \left(\frac{T_\mathrm{cAD,init}}{\mathrm{PWD}} \right)^2 , \tag{5.12}$$

to achieve a P-wave duration PWD of 100 ms. Ventricular conductivities were parameterized to result in CVs of 800 mm/s, 600 mm/s, and 400 mm/s in longitudinal, transversal, and normal directions, respectively. All values for the parameterization of the monodomain equation can be found in Table 5.1.

Table 5.1: Parameters for the electrophysiological model.

Parameter	Value	Unit	Description
$(\sigma_\mathrm{f}, \sigma_\mathrm{s}, \sigma_\mathrm{n})$	$(0.3108, 0.2020, 0.1087)$	S/m	conductivities in ventricular myocardium
$(\sigma_\mathrm{f}, \sigma_\mathrm{s}, \sigma_\mathrm{n})$	$(0.7415, 0.4819, 0.2595)$	S/m	conductivities in SE-layer
$(\sigma_\mathrm{f}, \sigma_\mathrm{s}, \sigma_\mathrm{n})$	$(0.7655, 0.0842, 0.0842)$	S/m	conductivities in atrial myocardium
$(\sigma_\mathrm{f}, \sigma_\mathrm{s}, \sigma_\mathrm{n})$	$(3.914, 0.0861, 0.0861)$	S/m	conductivities in Bachmann's bundle (BB)
$(\sigma_\mathrm{f}, \sigma_\mathrm{s}, \sigma_\mathrm{n})$	$(3.0927, 0.0618, 0.0618)$	S/m	conductivities in pectinate muscle (PM)
$(\sigma_\mathrm{f}, \sigma_\mathrm{s}, \sigma_\mathrm{n})$	$(2.3678, 0.0852, 0.0852)$	S/m	conductivities in crista terminalis (CT)
$(\sigma_\mathrm{f}, \sigma_\mathrm{s}, \sigma_\mathrm{n})$	$(0.0859, 0.0859, 0.0859)$	S/m	conductivities in isthmus
β	140000	1/m	membrane surface-to-volume ratio
C_m	0.01	F/m^2	membrane capacitance
t_AVN	0.150	s	atrio-ventricular conduction delay
BCL	1.2	s	basic cycle length ($= 1/$heartrate)

The external stimulus current is applied by a protocol that is summarized in Eq. (3.8). To choose the domain Ω_stim, sites of earliest activation have to be defined. In the atria, this is the most common SAN exit site at the junction of the right atrial appendage and the superior vena cava (SVC) [58]. Conduction between the left and right atrium is only possible via Bachmann's bundle (BB), a middle and upper posterior inter-atrial connection, and the coronary sinus (CS). Otherwise, the tissue was isolated in the middle of the septal wall through an electrically isolated layer. For the ventricles, two different strategies are employed: The first models the His-Purkinje system (HPS) by stimulating circular areas at positions that represent common sites of earliest activation in the ventricles and were chosen based on

Table 5.2: Setup of he His-Purkinje system models shown in Figure 5.2.

Fascicle model								
		Values						
		Cobiveco coordinates				Others		
Description	Parameter	a	m	r	v	δ_m	δ_{rad}	$t_{AVN} + t_a$
Early activation sites	$\mathbf{r}_{lv,pf}$	0.55	1	0.04	0	0.05	3 mm	176 ms
	$\mathbf{r}_{lv,af}$	0.85	1	0.57	0	0.05	3 mm	169 ms
	$\mathbf{r}_{lv,sf}$	0.40	1	0.70	0	0.05	3 mm	174 ms
	$\mathbf{r}_{rv,sf}$	0.75	1	0.87	1	0.05	3 mm	174 ms
	$\mathbf{r}_{rv,mod}$	0.75	1	0.4	1	0.05	3 mm	175 ms
SE-layer	s_m	-	[0.82 1]	-	-	-	-	-

PMJ model		
Description	Parameter	Value
Conduction velocity	CV	$1200\,\mathrm{mm\,s^{-1}}$
Node-to-node distance	d_N	2 mm
Atrial distance	$d_{A,lv}$	4 mm
	$d_{A,rv}$	0 mm

observations by Durrer et al. [59] and simulation results obtained in [60, 62]. The activation pattern includes three sites of earliest activation in the LV (anterior fascicle $\mathbf{r}_{lv,af}$, posterior fascicle $\mathbf{r}_{lv,pf}$, septal fascicle $\mathbf{r}_{lv,sf}$) and two in the RV (septal fascicle $\mathbf{r}_{rv,sf}$ and moderator band fascicle $\mathbf{r}_{rv,mod}$). The local coordinates of each root $\mathbf{r}$ is given in terms of universal coordinates (Chapter 4.2) in Table 5.2. This method only works in conjunction with a thin, fast-conducting subendocardial layer (SE) to mimic the effect of the HPS. Alternatively, starting from the same root locations as in the fascicle model, a dedicated Purkinje system is grown [32] with a minimal node-to-node distance d_N as shown in Figure 5.2b). The stimulus locations are the terminal ends of each branch of the Purkinje tree, the so-called Purkinje-muscle junctions (PMJ). The activation time t_a at the individual PMJs is determined using the fast marching algorithm [151] to solve the Eikonal equation $CV\sqrt{\nabla t_a \mathbf{D} \nabla t_a} = 1$ with a conduction velocity of $CV = 1200\,\mathrm{mm\,s^{-1}}$.

The passive behavior of the myocardium ($\Omega_{RV}, \Omega_{LV}, \Omega_{RA}, \Omega_{LA}$) is modeled by the constitutive law of Usyk et al. [103, 106] given by the strain energy function Eq. (B.12). The parameters of this model were determined using the method proposed by Kovacheva et al. [27] to match the empirical left ventricular EDPVR of Klotz et al. [173]. The rest of the domain ($\Omega_{TV}, \Omega_{MV}, \Omega_{AV}, \Omega_{PV}, \Omega_{OR}, \Omega_{BP}, \Omega_{AP}$) is modeled as an isotropic Neo-Hookean material according to the strain energy function Eq. B.10. All mechanical parameters are listed in Table 5.3.

The mechanical effect of the tissue surrounding the heart is modeled by Eqs. (5.10g) and (5.10h) as in Fritz et al. [20], which assumes a frictionless and permanent contact between the epicardium and the pericardium using a penalty formulation. For this purpose, the so called master (Γ_0^M) and slave (Γ_0^S) surfaces are defined as a contact interface. The force acting on the master surface is given by $\mathbf{f}^M = k_{epi} g(\mathbf{x}) \mathbf{n}$ with the penalty parameter $k_{epi} = 10^7\,\mathrm{Pa\,m^{-1}}$, the gap function $g(\mathbf{x})$, and the current surface normal vector $\mathbf{n}$. For the slave surface, the

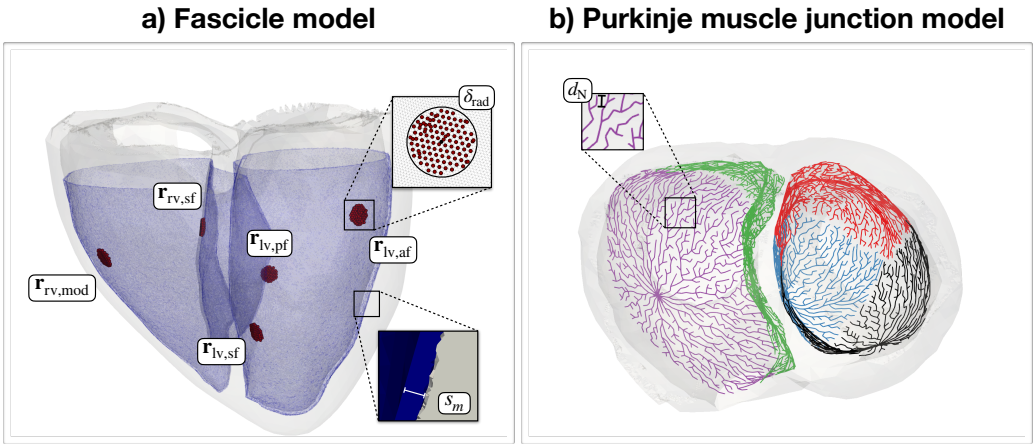

Figure 5.2: Two models to reproduce the effect of the HPS: a) fascicle model including a fast conducting SE-layer of thickness s_m (blue color) with three sites of earliest activation in the LV (anterior fascicle $\mathbf{r}_{\mathrm{lv,af}}$, posterior fascicle $\mathbf{r}_{\mathrm{lv,pf}}$, septal fascicle $\mathbf{r}_{\mathrm{lv,sf}}$) and two in the RV (septal fascicle $\mathbf{r}_{\mathrm{rv,sf}}$ and moderator band fascicle $\mathbf{r}_{\mathrm{rv,mod}}$). Nodes in a radius δ_{rad} around the roots $\mathbf{r}$ are stimulated. b) Model of the Purkinje muscle junctions as stimulation sites determined by an explicit representation of the HPS with minimal node distance d_{N}.

Table 5.3: Constitutive law parameters for the whole heart model.

Domain	Parameters								
	μ (Pa)	b_{ff}	b_{ss}	b_{nn}	b_{fs}	b_{fn}	b_{ns}	κ (Pa)	ρ_0 (kg m^{-2})
$\Omega_{\mathrm{RV,LV,RA,LA}}$	300	22	8.8	8.8	15.4	15.4	15.4	10^5	1082
$\Omega_{\mathrm{MV,TV,AV,PV}}$	10^6	-	-	-	-	-	-	10^5	1082
Ω_{OR}	7450	-	-	-	-	-	-	10^5	1082
Ω_{BP}	2000	-	-	-	-	-	-	10^4	1082
Ω_{AP}	2000	-	-	-	-	-	-	10^5	1082

same formulation is used except with negative sign for the contact forces $\mathbf{f}^{\mathrm{S}} = -\mathbf{f}^{\mathrm{M}}$. The gap function $g(\mathbf{x})$ is determined by projecting a point $\mathbf{x}^{\mathrm{m}} \in \Gamma^{\mathrm{M}}$ onto the surface Γ^{S} into the direction of the current normal direction $\mathbf{n}$. Depending on the distance between $\mathbf{x}^{\mathrm{m}}$ and the projected point $\mathbf{x}^{\mathrm{s}} \in \Gamma^{\mathrm{S}}$, the gap function reads

$$g(\mathbf{x}) = \begin{cases} \|\mathbf{x}^{\mathrm{m}} - \mathbf{x}^{\mathrm{s}}\|^2 / 2d & \text{for} \quad \|\mathbf{x}^{\mathrm{m}} - \mathbf{x}^{\mathrm{s}}\| < d\,, \\ \|\mathbf{x}^{\mathrm{m}} - \mathbf{x}^{\mathrm{s}}\| - \frac{d}{2} & \text{for} \quad \|\mathbf{x}^{\mathrm{m}} - \mathbf{x}^{\mathrm{s}}\| \geq d\,, \\ 0 & \text{for} \quad \|\mathbf{x}^{\mathrm{m}} - \mathbf{x}^{\mathrm{s}}\| > d_{\max}\,, \end{cases} \tag{5.13}$$

with the transition distance $d = 0.1$ mm and the maximal distance $d_{\max} = 8$ mm below which contact is maintained. This adaptation to the original formulation was made to yield a smooth transition in case the surfaces Γ^{M} and Γ^{S} start to overlap, which results in a change of direction of $\mathbf{n}$. The resulting difference in contact stress $k_{\mathrm{epi}} g(\mathbf{x})$ is shown in Figure 5.3. Based on image derived data, Strocchi et al. [116, 117] showed that epicardial displacement is larger close to the atrioventricular plane. Therefore, they introduced a spatially varying

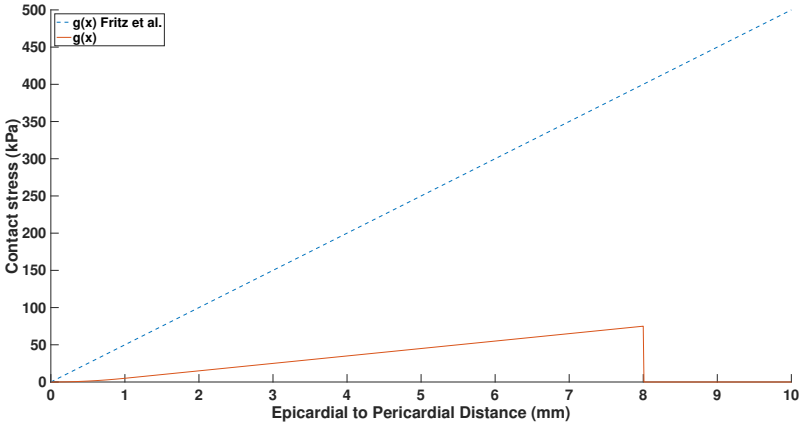

Figure 5.3: Contact stress resulting from the original formulation in Fritz et al. [20] and the adapted formulation used in this thesis.

penalty map to the general robin boundary condition which is applied to the epicardium with the full penalty being applied at the apex and the roof of the atria. For the contact problem of Fritz et al. [20] used in this thesis, a similar effect can be achieved by separating the pericardial material into apical and basal parts (Fig. 4.1). The separation makes it possible to choose a different penalization in these areas by defining different material parameters in the constitutive law. To take into account the larger penalty on the atrial roof, zero displacement Dirichlet boundary conditions $\mathbf{d} = \mathbf{0}$ are applied to the terminal ends of the SVC, inferior vena cava (IVC), left pulmonary veins (LPV), right pulmonary veins (RPV). The elasticity of the truncated veins would allow movement of the atrial wall while anchoring them to their respective approximate area. Together with the outer surface of the pericardial sac, the Dirichlet boundary is comprised in the surface Γ_0^{D}.

To model the influence of the circulatory system on the heart, the zero-dimensional (0D) model presented in Chapter 3.4 is used. Specifically, the equations (3.16)-(3.21) of the 0D model are coupled to the three-dimensional (3D) model of cardiac mechanics via the volume consistency constraint (3.24). Parameters of the circulatory system are given in Table 5.4.

5.3.1 Initial Displacement of the Reference Configuration

MRI data are typically acquired during the early diastolic state of the heart cycle when movement and chamber pressure are minimal. However, residual stress in the tissue cannot be measured with standard imaging techniques and the pressure inside the heart's cavities can only be measured by invasive procedures. Therefore, a pressure and stress-free reference configuration of the heart has to be estimated to accurately model the biomechanical diastolic function. Methods applied in the context of cardiac mechanics try to find a stress-free reference configuration iteratively by using fixed-point iterations, as originally proposed by Sellier et al. [174] and Bols et al. [175]. To increase the convergence rate and accelerate the fixed-point method by Sellier et al., the following augmentation approach proposed by

Table 5.4: Circulatory system parameters for the whole heart model. Refer to Chapter 3.4 for the system of equations.

Parameter	Value	Unit	Description
Pulmonary and systemic circulation			
R_{SysArt}	0.03	$mmHg \cdot s \cdot ml^{-1}$	systemic arterial resistance
C_{SysArt}	3.0	$ml \cdot mmHg^{-1}$	systemic arterial compliance
$V_{SysArtUnstr}$	800.0	ml	unstressed systemic arterial volume
R_{SysPer}	0.6	$mmHg \cdot s \cdot ml^{-1}$	systemic peripheral resistance
R_{SysVen}	0.03	$mmHg \cdot s \cdot ml^{-1}$	systemic venous resistance
C_{SysVen}	150.0	$ml \cdot mmHg^{-1}$	systemic venous compliance
$V_{SysVenUnstr}$	2850.0	ml	unstressed systemic venous resistance
R_{PulArt}	0.02	$mmHg \cdot s \cdot ml^{-1}$	pulmonary arterial resistance
C_{PulArt}	10.0	$ml \cdot mmHg^{-1}$	pulmonary arterial compliance
$V_{PulArtUnstr}$	150.0	ml	unstressed pulmonary arterial volume
R_{PulPer}	0.07	$mmHg \cdot s \cdot ml^{-1}$	pulmonary peripheral resistance
R_{PulVen}	0.03	$mmHg \cdot s \cdot ml^{-1}$	pulmonary venous resistance
C_{PulVen}	15.0	$ml \cdot mmHg^{-1}$	pulmonary venous compliance
$V_{PulVenUnstr}$	200.0	ml	unstressed pulmonary venous volume
ρ_{Blood}	1060	kg/m^3	blood density
Mitral valve			
A_{Ref}	15.0	cm^2	reference area
M_{max}	0.7	-	maximum area ratio
M_{min}	0.001	-	minimum area ratio
K_o	20.0	$mmHg^{-1} \cdot s^{-1}$	opening rate coefficient
K_c	6.0	$mmHg^{-1} \cdot s^{-1}$	closing rate coefficient
Tricuspid valve			
A_{Ref}	15.0	cm^2	reference area
M_{max}	0.7	-	maximum area ratio
M_{min}	0.001	-	minimum area ratio
K_o	20.0	$mmHg^{-1} \cdot s^{-1}$	opening rate coefficient
K_c	6.0	$mmHg^{-1} \cdot s^{-1}$	closing rate coefficient
Aortic valve			
A_{Ref}	7.0	cm^2	reference area
M_{max}	0.95	-	maximum area ratio
M_{min}	0.001	-	minimum area ratio
K_o	10.0	$mmHg^{-1} \cdot s^{-1}$	opening rate coefficient
K_c	6.0	$mmHg^{-1} \cdot s^{-1}$	closing rate coefficient
Pulmonary valve			
A_{Ref}	7.0	cm^2	reference area
M_{max}	0.98	-	maximum area ratio
M_{min}	0.001	-	minimum area ratio
K_o	20.0	$mmHg^{-1} \cdot s^{-1}$	opening rate coefficient
K_c	10.0	$mmHg^{-1} \cdot s^{-1}$	closing rate coefficient

Rausch et al. [176] is used: For each iteration k, solve the forward problem

$$\phi(\mathbf{X}^k) \begin{cases} \nabla \cdot (\mathbf{F}\mathbf{S}(\mathbf{d}, T_a = 0)) = \mathbf{0} & \text{in} \quad \Omega_k \,, \\ \mathbf{F}\mathbf{S}(\mathbf{d}, T_a = 0)\mathbf{N} = -p_{LV}^{ED} J \mathbf{F}^{-T} \mathbf{N} & \text{on} \quad \Gamma_k^{LV} \,, \\ \mathbf{F}\mathbf{S}(\mathbf{d}, T_a = 0)\mathbf{N} = -p_{RV}^{ED} J \mathbf{F}^{-T} \mathbf{N} & \text{on} \quad \Gamma_k^{RV} \,, \\ \mathbf{F}\mathbf{S}(\mathbf{d}, T_a = 0)\mathbf{N} = -p_{LA}^{ED} J \mathbf{F}^{-T} \mathbf{N} & \text{on} \quad \Gamma_k^{LA} \,, \\ \mathbf{F}\mathbf{S}(\mathbf{d}, T_a = 0)\mathbf{N} = -p_{RA}^{ED} J \mathbf{F}^{-T} \mathbf{N} & \text{on} \quad \Gamma_k^{RA} \,, \\ \mathbf{d} = \mathbf{0} & \text{on} \quad \Gamma_k^{D} \,, \end{cases} \tag{5.14}$$

by applying an end-diastolic pressure $p_{\mathrm{C}}^{\mathrm{ED}}$ for $\mathrm{C} \in \{\mathrm{LV}, \mathrm{RV}, \mathrm{LA}, \mathrm{RA}\}$ to an intermediate configuration of the heart with coordinates $\mathbf{X}^k$ with no active stress. The resulting node coordinates $\mathbf{x}^k$ can be used to calculate the nodal error $\mathbf{R}^k = \mathbf{x}^k - \mathbf{x}^{\mathrm{dat}}$ w. r. t. the target coordinates $\mathbf{x}^{\mathrm{dat}}$. Finally, the reference coordinates are updated $\mathbf{X}^{k+1} = \mathbf{X}^k - \beta \mathbf{R}^k$ with the augmentation parameter β as shown in Algorithm 5.1. After solving the forward problem

Algorithm 5.1 Augmented unloading strategy adopted from [28]

procedure Unloading($\Omega_0, p_{\mathrm{LV}}^{\mathrm{ED}}, p_{\mathrm{RV}}^{\mathrm{ED}}, p_{\mathrm{LA}}^{\mathrm{ED}}, p_{\mathrm{RA}}^{\mathrm{ED}}$)
  initialize $\mathbf{X}^1 = \mathbf{x}^{\mathrm{dat}}$; $k = 0$; $\beta = 1$
  while $\left\|\mathbf{R}^k\right\| \geq \varepsilon$ **do**
    update counter, $k = k + 1$
    solve forward problem, $\mathbf{x}^k = \phi(\mathbf{X}^k)$
    calculate residual vector, $\mathbf{R}^k = \mathbf{x}^k - \mathbf{x}^{\mathrm{dat}}$
    if $k > 1$ **then**
      update augmentation parameter, $\beta = -\beta \frac{\mathbf{R}^{k-1} : [\mathbf{R}^k - \mathbf{R}^{k-1}]}{[\mathbf{R}^k - \mathbf{R}^{k-1}] : [\mathbf{R}^k - \mathbf{R}^{k-1}]}$
    end if
    update reference vector, $\mathbf{X}^{k+1} = \mathbf{X}^k - \beta \mathbf{R}^k$
  end while
  return stress-free reference configuration, $\mathbf{X} = \mathbf{X}^k$
end procedure

$\phi(\mathbf{X})$ once again with the end-diastolic pressure values $p_{\mathrm{C}}^{\mathrm{ED}}$, the target configuration is recovered and the solution $\mathbf{d}$ together with the pressure can be used as initial conditions for the coupled problem:

$$\mathbf{d}^0 = \mathbf{d}, \quad p_{\mathrm{C}}^0 = p_{\mathrm{C}}^{\mathrm{ED}}.$$

5.3.2 Numerical Approximation of the Coupled Problem

In this section, the numerical approximation scheme of the coupled problem is described in more detail. At first, the spatial discretization in terms of the continuous finite element method (FEM) is introduced before moving on to the time discretization schemes. Finally, the segregated and staggered solution strategy is outlined. For the sake of simplicity, only the case of linear elements will be considered, for which the degrees of freedom are located at the vertices of the tetrahedra. Nevertheless, space discretization is possible with quadratic tetrahedra as well.

Space discretization

For the spatial discretization, two nested tetrahedral meshes Ω_{h_1} and Ω_{h_2} of the reference domain Ω_0 are introduced, where h stands for the maximum diameter of each finite element $K \in \Omega_h$, with $h_1 < h_2$. Ω_{h_1} is generated from Ω_{h_2} by splitting each element of Ω_{h_2} into 8 new elements until the desired resolution is reached. Due to the steep depolarization wave

front present in the electrophysiology model ($\mathcal{IAE}$), mesh Ω_{h_1} is used for electrophysiology and consequently Ω_{h_2} for the mechanics model ($\mathcal{M}$). The notation $\dot{u} = \frac{\partial u}{\partial t}$ and $\ddot{u} = \frac{\partial^2 u}{\partial t^2}$ is adopted for time derivatives. To reduce the number of indices, the transmembrane voltage is redefined as $v = V_\mathrm{m}$.

Due to the two nested meshes used for the different physics models, it is necessary to interpolate certain quantities in between the two domains. For this purpose, a linear mapping operator $\mathbf{X}_{h_1} = \psi(\mathbf{X}_{h_2})$ is determined once to define the connectivity between the vertexes $\mathbf{X}_{h_1}$ and $\mathbf{X}_{h_2}$ of the meshes. With this mapping, any function u with the values u_i at the nodes $i = 1, \ldots, k$ can be interpolated inside the element using its node-shape functions with

$$\hat{u} = \sum_{i=1}^{k} \phi_i u_i \,. \tag{5.15}$$

Monodomain equation. Let there be a finite-dimensional function space $\mathcal{P}_{h_1}$ on each finite element K with the dimensions $N_{h_1} = \dim \mathcal{P}_{h_1}$ and its set of basis functions $\{\phi_i\}_{i=1}^{N_{h_1}}$. Then the space-discretized formulation of the monodomain equation is given by

$$\begin{aligned} &\beta C_\mathrm{m} \int_{\Omega_{h_1}} \dot{v}_{h_1}(t)\phi_i \,\mathrm{d}\Omega_{h_1} + \beta \int_{\Omega_{h_1}} I_\mathrm{ion}(v_{h_1}(t), \mathbf{w}_{h_1}(t), \mathbf{q}_{h_1}(t))\phi_i \,\mathrm{d}\Omega_{h_1} \\ &+ \beta \int_{\Omega_{h_1}} I_\mathrm{app}(t)\phi_i \,\mathrm{d}\Omega_{h_1} = \int_{\Omega_{h_1}} (J_{h_1}\mathbf{F}_{h_1}^{-1}\mathbf{D}\mathbf{F}_{h_1}^{-\mathsf{T}}\nabla v_{h_1}(t)) \cdot \nabla\phi_i \,\mathrm{d}\Omega_{h_1} \,, \quad \forall i = 1, \ldots, N_{h_1} \,, \end{aligned} \tag{5.16}$$

with $v_{h_1}(t) = \sum_{j=1}^{N_{h_1}} v_{j,h_1}(t)\phi_j$ being the approximated solutions of the transmembrane voltage. The deformation tensor $\mathbf{F}_{h_1} = \mathbf{F}(\mathbf{d}_{h_1})$ is calculated by interpolating the approximated mechanical solution $\mathbf{d}_{h_2}$ between the two nested meshes Ω_{h_2} and Ω_{h_1}. After gathering all degrees of freedom (DoF) in $\underline{\mathbf{v}}_{h_1}(t) = \{v_{j,h_1}(t)\}_{j=1}^{N_{h_1}}$, equation (5.16) can be transformed into matrix-vector notation

$$\mathbf{K}\underline{\mathbf{v}}_{h_1}(t) = \beta C_\mathrm{m}\mathbf{M}\dot{\underline{\mathbf{v}}}_{h_1}(t) + \beta\mathbf{I}_\mathrm{ion}(\underline{\mathbf{v}}_{h_1}(t), \underline{\mathbf{w}}_{h_1}(t), \underline{\mathbf{q}}_{h_1}(t)) + \beta\mathbf{I}_\mathrm{app}(t) \,, \tag{5.17}$$

with

$$\begin{aligned} (\mathbf{K})_{ij} &= \int_{\Omega_{h_1}} (J_{h_1}\mathbf{F}_{h_1}^{-1}\mathbf{D}\mathbf{F}_{h_1}^{-\mathsf{T}}\nabla\phi_j) \cdot \nabla\phi_i \,\mathrm{d}\Omega_{h_1} \,, \\ (\mathbf{M})_{ij} &= \int_{\Omega_{h_1}} \phi_j\phi_i \,\mathrm{d}\Omega_{h_1} \,, \\ (\mathbf{I}_\mathrm{ion}(\underline{\mathbf{v}}_{h_1}(t), \underline{\mathbf{w}}_{h_1}(t), \underline{\mathbf{q}}_{h_1}(t)))_i &= \int_{\Omega_{h_1}} I_\mathrm{ion}(v_{h_1}(t), \mathbf{w}_{h_1}(t), \mathbf{q}_{h_1}(t))\phi_i \,\mathrm{d}\Omega_{h_1} \,, \\ (\mathbf{I}_\mathrm{app}(t))_i &= \int_{\Omega_{h_1}} I_\mathrm{app}(t)\phi_i \,\mathrm{d}\Omega_{h_1} \,. \end{aligned}$$

In the proposed framework, operator splitting is used to decouple the parabolic diffusion problem from the ordinary differential equations (ODEs) of the reaction system. Therefore, Equation (5.17) reduces to

$$\mathbf{M}\dot{\underline{\mathbf{v}}}_{h_1}(t) = \frac{1}{\beta C_\mathrm{m}}\mathbf{K}\underline{\mathbf{v}}_{h_1}(t) \,, \tag{5.18}$$

and the ODEs are solved separately on the vertexes $\mathbf{X}_{h_1} \in \Omega_{h_1}$.

Mechanics. Similar to before, a set of vector-valued basis functions $\{\phi_i\}_{i=1}^{N_{h_2}}$ is defined in a finite-dimensional function space $\mathcal{P}^3_{h_2}$ on each finite element K with the dimensions $N_{h_2} = \dim \mathcal{P}^3_{h_2}$. The space-discretized version of the mechanics model is then given by

$$\begin{aligned}
&\int_{\Omega_{h_2}} \rho_0 \ddot{\mathbf{d}}_{h_2}(t) \cdot \phi_i \,\mathrm{d}\Omega_{h_2} + \int_{\Omega_{h_2}} \mathbf{F}_{h_2}\mathbf{S}(\mathbf{d}_{h_2}(t), T_{\mathrm{a},h_2}(t)) \colon \nabla\phi_i \,\mathrm{d}\Omega_{h_2} \\
&\quad - \sum_{\mathrm{C}\in\{\mathrm{LV,RV,LA,RA}\}} p_{\mathrm{C}}(t) \int_{\Gamma^{\mathrm{C}}_{h_2}} J_{h_2}\mathbf{F}_{h_2}^{-\mathsf{T}}\mathbf{N}_{h_2} \cdot \phi_i \,\mathrm{d}\Gamma^{\mathrm{C}}_{h_2} - \int_{\Gamma^{\mathrm{M}}_{h_2}} [k_{\mathrm{epi}} g(\mathbf{x}_{h_2})\mathbf{n}_{h_2}] \cdot \phi_i \,\mathrm{d}\Gamma^{\mathrm{M}}_{h_2} \\
&\quad + \int_{\Gamma^{\mathrm{S}}_{h_2}} [k_{\mathrm{epi}} g(\mathbf{x}_{h_2})\mathbf{n}_{h_2}] \cdot \phi_i \,\mathrm{d}\Gamma^{\mathrm{S}}_{h_2} = 0, \quad \forall i = 1,\dots,N_{h_2}\,,
\end{aligned} \tag{5.19}$$

with $\mathbf{d}_{h_2}(t) = \sum_{j=1}^{N_{h_2}} \mathbf{d}_{j,h_2}(t) \cdot \phi_j$ being the approximated solutions of the displacement. Furthermore, the microscopic active tension $T_{\mathrm{a},h_2}(t)$ is interpolated from Ω_{h_1} using (5.15). In matrix-vector notation, Eq. (5.19) simplifies to

$$\mathbf{M}^{(2)}\underline{\ddot{\mathbf{d}}}_{h_2}(t) + \mathbf{f}_{\mathrm{int}}(\underline{\mathbf{d}}_{h_2}(t), T_{\mathrm{a},h_2}(t)) + \mathbf{f}_{\mathrm{ext}}(\underline{\mathbf{d}}_{h_2}(t)) = 0\,, \tag{5.20}$$

with

$$\begin{aligned}
(\mathbf{M}^{(2)})_{ij} &= \rho_0 \int_{\Omega_{h_2}} \phi_j \cdot \phi_i \,\mathrm{d}\Omega_{h_2}\,, \\
(\mathbf{f}_{\mathrm{int}}(\underline{\mathbf{d}}_{h_2}(t), T_{\mathrm{a},h_2}(t)))_i &= \int_{\Omega_{h_2}} \mathbf{F}_{h_2}\mathbf{S}(\mathbf{d}_{h_2}(t), T_{\mathrm{a},h_2}(t)) \colon \nabla\phi_i \,\mathrm{d}\Omega_{h_2}\,, \\
(\mathbf{f}_{\mathrm{ext}}(\underline{\mathbf{d}}_{h_2}(t)))_i &= - \sum_{\mathrm{C}\in\{\mathrm{LV,RV,LA,RA}\}} p_{\mathrm{C}}(t) \int_{\Gamma^{\mathrm{C}}_{h_2}} J_{h_2}\mathbf{F}_{h_2}^{-\mathsf{T}}\mathbf{N}_{h_2} \cdot \phi_i \,\mathrm{d}\Gamma^{\mathrm{C}}_{h_2} \\
&\quad - \int_{\Gamma^{\mathrm{M}}_{h_2}} [k_{\mathrm{epi}} g(\mathbf{x}_{h_2})\mathbf{n}_{h_2}] \cdot \phi_i \,\mathrm{d}\Gamma^{\mathrm{M}}_{h_2} + \int_{\Gamma^{\mathrm{S}}_{h_2}} [k_{\mathrm{epi}} g(\mathbf{x}_{h_2})\mathbf{n}_{h_2}] \cdot \phi_i \,\mathrm{d}\Gamma^{\mathrm{S}}_{h_2}\,.
\end{aligned}$$

To damp nonphysical oscillations in the solutions to this equation, it is extended by a term for damping:

$$\mathbf{M}^{(2)}\underline{\ddot{\mathbf{d}}}_{h_2}(t) + \mathbf{f}_{\mathrm{int}}(\underline{\mathbf{d}}_{h_2}(t), T_{\mathrm{a},h_2}(t)) + \mathbf{f}_{\mathrm{ext}}(\underline{\mathbf{d}}_{h_2}(t)) + \mathbf{C}\underline{\dot{\mathbf{d}}}_{h_2}(t) = 0\,, \tag{5.21}$$

where $\mathbf{C} = \alpha_1\mathbf{M}^{(2)} + \alpha_2\nabla\mathbf{f}_{\mathrm{int}}(\underline{\mathbf{d}}_{h_2}(t), T_{\mathrm{a},h_2}(t))$ is the so-called Rayleigh damping matrix with the damping parameters α_1 and α_2. More detail on the choice of these parameters can be found in Appendix A. The integrals in the semi-discretized equations (5.21) and (5.18) are solved numerically using appropriate quadrature rules for triangles and tetrahedrons as shown in Appendix D.

Time discretization

For the time discretization of Equations (5.18) and (5.21), a segregated and staggered approach is employed, meaning that the problems ($\mathcal{IAE}$) and ($\mathcal{MC}$) are solved sequentially and at different time-step sizes. A sketch of this sequential and staggered numerical scheme is shown in Figure 5.4. First, let the time interval $[0,T]$ be partitioned in N_T time steps

$t^n = n\Delta t_{\mathcal{M}}$ for $n = 0,\dots,N_T$ with a time step size of $\Delta t_{\mathcal{M}} = T/N_T$. This is the largest time step and it is attributed to the mechanics problem ($\mathcal{M}$). For the circulatory system ($\mathcal{C}$) and the electrophysiology ($\mathcal{IAE}$), intermediate time steps are chosen such that a step from t^n to t^{n+1} is given by $t^{n+\frac{m}{N_{\text{sub,X}}}}$ sub-steps with $m = 1,\dots,N_{\text{sub,X}}$ for $N_{\text{sub,C}} = \frac{\Delta t_{\mathcal{M}}}{\Delta t_{\mathcal{C}}}$ and $N_{\text{sub,E}} = \frac{\Delta t_{\mathcal{M}}}{\Delta t_{\mathcal{E}}}$. The approximation of the time-dependent variables at time step t^n at the example of the transmembrane voltage, is given by $\underline{\mathbf{v}}_{h_1}^n = \underline{\mathbf{v}}_{h_1}(t^n)$. Problem ($\mathcal{IAE}$) is solved as followed:

- Solutions for $\underline{\mathbf{v}}_{h_1}^n$, $\underline{\mathbf{w}}_{h_1}^n$, $\underline{\mathbf{q}}_{h_1}^n$, and $\underline{\mathbf{s}}_{h_1}^n$ are obtained using first order Godunov splitting:
  1. First, the ODE system of the reaction part is solved at each vertex using explicit time integration methods. This requires the local fiber stretch $\underline{\lambda}_{h_1}^n$ and its derivative $\frac{\underline{\lambda}_{h_1}^n - \underline{\lambda}_{h_1}^{n-1}}{\Delta t_{\mathcal{E}}}$, which are interpolated from the coarse mesh Ω_{h_2} once at time t^n.

$$\underline{\mathbf{w}}_{h_1}^{n+\frac{m}{N_{\text{sub,E}}}} = \underline{\mathbf{w}}_{h_1}^n + \Delta t_{\mathcal{E}} \underline{\mathbf{G}}_{\mathbf{w}}(\underline{\mathbf{v}}_{h_1}^n, \underline{\mathbf{w}}_{h_1}^n, \underline{\mathbf{q}}_{h_1}^n), \tag{5.22}$$

$$\underline{\mathbf{q}}_{h_1}^{n+\frac{m}{N_{\text{sub,E}}}} = \underline{\mathbf{q}}_{h_1}^n + \Delta t_{\mathcal{E}} \underline{\mathbf{G}}_{\mathbf{q}}(\underline{\mathbf{v}}_{h_1}^n, \underline{\mathbf{w}}_{h_1}^n, \underline{\mathbf{q}}_{h_1}^n, \underline{\lambda}_{h_1}^n), \tag{5.23}$$

$$\underline{\mathbf{s}}_{h_1}^{n+\frac{m}{N_{\text{sub,E}}}} = \underline{\mathbf{s}}_{h_1}^n + \Delta t_{\mathcal{E}} \underline{\mathbf{G}}_{\mathbf{s}}(\underline{\mathbf{s}}_{h_1}^n, \underline{\mathbf{q}}_{h_1}^n, \underline{\lambda}_{h_1}^n, \frac{\underline{\lambda}_{h_1}^n - \underline{\lambda}_{h_1}^{n-1}}{\Delta t_{\mathcal{E}}}), \tag{5.24}$$

$$\tilde{\underline{\mathbf{v}}}_{h_1}^{n+\frac{m}{N_{\text{sub,E}}}} = \underline{\mathbf{v}}_{h_1}^n + \frac{\Delta t_{\mathcal{E}}}{C_{\text{m}}}[\mathbf{I}_{\text{ion}}(\underline{\mathbf{v}}_{h_1}^n, \underline{\mathbf{w}}_{h_1}^n, \underline{\mathbf{q}}_{h_1}^n) + \mathbf{I}_{\text{app}}(t)]. \tag{5.25}$$

  2. Next, use the intermediate solution $\tilde{\underline{\mathbf{v}}}_{h_1}^{n+\frac{m}{N_{\text{sub,E}}}}$ to integrate the diffusion part (5.18) in time by means of the Crank-Nicolson method:

$$\left(\frac{\beta C_{\text{m}}}{\Delta t_{\mathcal{E}}}\mathbf{M} + \theta\mathbf{K}\right) \underline{\mathbf{v}}_{h_1}^{n+\frac{m}{N_{\text{sub,E}}}} = \left(\frac{\beta C_{\text{m}}}{\Delta t_{\mathcal{E}}}\mathbf{M} - (1-\theta)\mathbf{K}\right) \tilde{\underline{\mathbf{v}}}_{h_1}^{n+\frac{m}{N_{\text{sub,E}}}}, \tag{5.26}$$

     using $\theta = 0.5$. The linear system (5.26) is then solved using the generalized minimum residual method (GMRES) with a Jacobi preconditioning to obtain $\underline{\mathbf{v}}_{h_1}^{n+\frac{m}{N_{\text{sub,E}}}}$.

- Interpolate the active tension T_{a,h_2}^n on the fine mesh Ω_{h_1} once per time step at t^n.

The strategy to solve problem ($\mathcal{MC}$) for time step t^{n+1} is as follows:

- Obtain solutions for $\underline{\mathbf{d}}_{h_2}^{n+1}$, $\mathbf{c}^{n+1}$, $\mathbf{p}_{\text{C}}^{n+1}$ through an iterative procedure.
  1. Begin by updating $\mathbf{p}_{\text{C}}^{n+1}$ as described in Chapter 3.4 before solving the equations of the circulatory system with a fourth order accurate explicit Runga-Kutta

method:

$$\mathbf{c}^{n+1} = \mathbf{c}^n + \frac{\Delta t_{\mathcal{C}}}{6}(\mathbf{K}_1 + 2\mathbf{K}_2 + 2\mathbf{K}_3 + K_4)\,, \tag{5.27}$$

$$\mathbf{K}_1 = \mathbf{G}_{\mathbf{c}}(t^n, \mathbf{c}^n, \mathbf{p}^n)\,, \tag{5.28}$$

$$\mathbf{K}_2 = \mathbf{G}_{\mathbf{c}}(t^{n+\frac{\Delta t_{\mathcal{C}}}{2}}, \mathbf{c}^n + \frac{\Delta t_{\mathcal{C}}}{2}\mathbf{K}_1, \mathbf{p}^n)\,, \tag{5.29}$$

$$\mathbf{K}_3 = \mathbf{G}_{\mathbf{c}}(t^{n+\frac{\Delta t_{\mathcal{C}}}{2}}, \mathbf{c}^n + \frac{\Delta t_{\mathcal{C}}}{2}\mathbf{K}_2, \mathbf{p}^n)\,, \tag{5.30}$$

$$\mathbf{K}_4 = \mathbf{G}_{\mathbf{c}}(t^{n+1}, \mathbf{c}^n + \Delta t_{\mathcal{C}}\mathbf{K}_3, \mathbf{p}^n)\,. \tag{5.31}$$

2. Solve (5.21) in time using the Generalized-α method [177]:

$$\mathbf{M}^{(2)}\ddot{\underline{\mathbf{d}}}_{h_2}^{n+1-\alpha_m} + \mathbf{f}_{\text{int}}^{n+1-\alpha_f} + \mathbf{f}_{\text{ext}}^{n+1-\alpha_f} + \mathbf{C}\dot{\underline{\mathbf{d}}}_{h_2}^{n+1-\alpha_f} = \mathbf{r}(\underline{\mathbf{d}}_{h_2}^{n+1}, t^{n+1}) = 0\,, \tag{5.32}$$

using the finite difference approximations

$$\underline{\mathbf{d}}_{h_2}^{n+1} = \underline{\mathbf{d}}_{h_2}^{n} + \Delta t_{\mathcal{M}}\dot{\underline{\mathbf{d}}}_{h_2}^{n} + \left(\frac{1}{2} - \beta\right)\Delta t_{\mathcal{M}}^2\ddot{\underline{\mathbf{d}}}_{h_2}^{n} + \beta\Delta t_{\mathcal{M}}^2\ddot{\underline{\mathbf{d}}}_{h_2}^{n+1} \tag{5.33}$$

$$\dot{\underline{\mathbf{d}}}_{h_2}^{n+1} = \dot{\underline{\mathbf{d}}}_{h_2}^{n} + (1-\gamma)\Delta t_{\mathcal{M}}\ddot{\underline{\mathbf{d}}}_{h_2}^{n} + \Delta t_{\mathcal{M}}\gamma\ddot{\underline{\mathbf{d}}}_{h_2}^{n+1}\,, \tag{5.34}$$

and the time discrete combinations of displacements, velocities, accelerations and times

$$\underline{\mathbf{d}}_{h_2}^{n+1-\alpha_f} = (1-\alpha_f)\underline{\mathbf{d}}_{h_2}^{n+1} + \alpha_f\underline{\mathbf{d}}_{h_2}^{n}\,, \tag{5.35}$$

$$\dot{\underline{\mathbf{d}}}_{h_2}^{n+1-\alpha_f} = (1-\alpha_f)\dot{\underline{\mathbf{d}}}_{h_2}^{n+1} + \alpha_f\dot{\underline{\mathbf{d}}}_{h_2}^{n}\,, \tag{5.36}$$

$$\ddot{\underline{\mathbf{d}}}_{h_2}^{n+1-\alpha_m} = (1-\alpha_m)\ddot{\underline{\mathbf{d}}}_{h_2}^{n+1} + \alpha_m\ddot{\underline{\mathbf{d}}}_{h_2}^{n}\,, \tag{5.37}$$

$$t^{n+1-\alpha_f} = (1-\alpha_f)t^{n+1} + \alpha_f t^n\,, \tag{5.38}$$

to formulate (5.32) in terms of the unknown displacement at time t^{n+1}:

$$\begin{aligned}\mathbf{r}(\underline{\mathbf{d}}_{h_2}^{n+1}, t^{n+1}) = &-\mathbf{M}^{(2)}[-m_1(\underline{\mathbf{d}}_{h_2}^{n+1} - \underline{\mathbf{d}}_{h_2}^{n}) + m_2\dot{\underline{\mathbf{d}}}_{h_2}^{n} + m_3\ddot{\underline{\mathbf{d}}}_{h_2}^{n}] \\ &-\mathbf{C}[-c_1(\underline{\mathbf{d}}_{h_2}^{n+1} - \underline{\mathbf{d}}_{h_2}^{n}) + c_2\dot{\underline{\mathbf{d}}}_{h_2}^{n} + c_2\ddot{\underline{\mathbf{d}}}_{h_2}^{n}] \\ &+\mathbf{f}_{\text{int}}^{n+1} - \mathbf{f}_{\text{ext}}^{n+1}\,,\end{aligned} \tag{5.39}$$

with

$$m_1 = \frac{1-\alpha_m}{\beta\Delta t_{\mathcal{M}}^2}, \qquad m_2 = \frac{1-\alpha_m}{\beta\Delta t_{\mathcal{M}}}, \qquad m_3 = \frac{1-\alpha_m-2\beta}{2\beta}\,,$$
$$c_1 = \frac{(1-\alpha_f)\gamma}{\beta\Delta t_{\mathcal{M}}}, \quad c_2 = \frac{(1-\alpha_f)\gamma-\beta}{\beta}, \quad c_3 = \frac{(\gamma-2\beta)(1-\alpha_f)}{2\beta}\Delta t_{\mathcal{M}}\,.$$

The most robust method to solve non-linear algebraic equations such as (5.39) is Newton's method. Linearizing (5.39) using a Taylor expansion around the current value of the displacement $\underline{\mathbf{d}}_{h_2}^{n+1}$ and dropping terms of higher order results in the linear model

$$\mathbf{r}(\underline{\mathbf{d}}_{h_2}^{n+1}, t^{n+1}) + \mathbf{A}\Delta\underline{\mathbf{d}}_{h_2}^{n+1} = 0\,, \tag{5.40}$$

with the system Jacobian matrix

$$\mathbf{A} = m_1 \mathbf{M}^{(2)} + c_1 \mathbf{C} + (1-\alpha_f)(\nabla \mathbf{f}_{\text{int}}^{n+1} - \nabla \mathbf{f}_{\text{ext}}^{n+1}) \,. \tag{5.41}$$

The most popular choice for the algorithmic parameters is

$$\alpha_m \,, \alpha_f \leq \frac{1}{2} \,, \quad \gamma = \frac{1}{2} + \alpha_m - \alpha_f \quad \text{and} \quad \beta = \frac{1}{4}\left(\gamma + \frac{1}{2}\right)^2 \,,$$

which ensures unconditional stability, optimal dissipation and second-order accuracy. Values for the Newmark-β method and other α-methods are given in Table 5.5.

3. With $\underline{\mathbf{d}}_{h_2}^{n+1}$, check the volume constraint (3.24). If satisfied, stop the iteration procedure. Otherwise, go back to point 1.

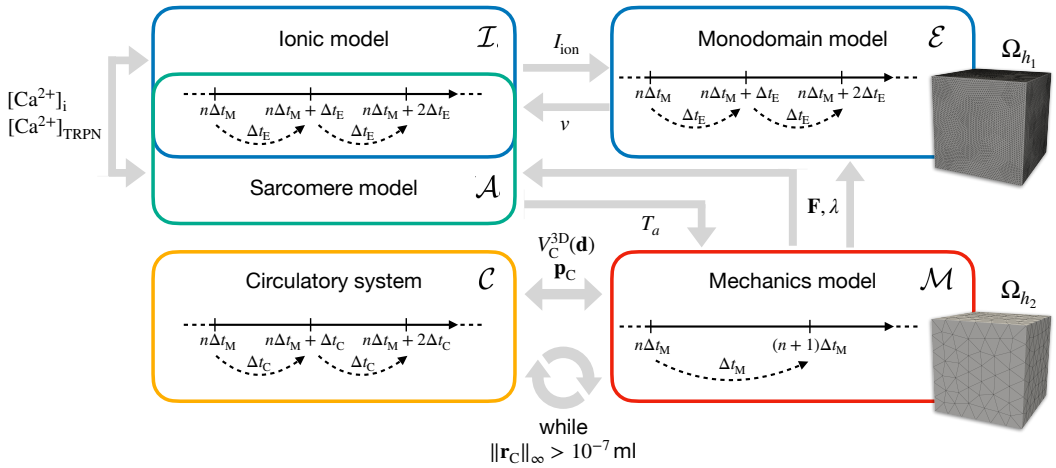

Figure 5.4: Sketch of the segregated and staggered numerical scheme.

Table 5.5: Selected parameter values in order to achieve first order accuracy for the N-β method, second order accuracy for the α methods and corresponding unconditional stability conditions.

Method	α_m	α_f	β	γ
N-β	0	0	$\frac{1}{4}(\gamma+\frac{1}{2})^2$	$\geq \frac{1}{2}$
HHT-α	0	$0 \leq -\alpha_{HHT} \leq \frac{1}{2}$	$\frac{1}{4}(1-\alpha_{HHT})^2$	$\frac{1}{2} - \alpha_{HHT}$
WBZ-α	$\alpha_{WBZ} \leq 0$	0	$\frac{1}{4}(1-\alpha_{WBZ})^2$	$\frac{1}{2} - \alpha_{WBZ}$
CH-α	$3\alpha_f - 1$	$\leq \frac{1}{2}$	$(1-\alpha_f)^2$	$\frac{3}{2} - 2\alpha_f$

5.4 Numerical Results for the Coupled 3D-0D Whole Heart Problem

In this section, the numerical results of the fully coupled 3D-0D whole heart model are presented. First, changes on the cellular level are shown after successfully coupling the ionic models of CRN and ORd to the L17 sarcomere model. Next, the result of electrophysiological simulations using the $\mathcal{IAE}$ model are shown for the different HIS-Purkinje models proposed in Chapter 5.3. Finally, simulations using the 3D-0D whole heart model with varying degrees of electromechanical coupling are compared. Whole heart simulations were performed on the anatomical model presented in Chapter 4 using two nested meshes: Ω_0 was discretized using 186,114 linear tetrahedral elements with $h_2 = 3.12 \pm 0.73$ mm with a total of 94,953 DoF resulting in the domain Ω_{h_2} for mechanical simulations. For electrophysiology simulations, elements of Ω_{h_2} were split uniformly twice to result in the domain Ω_{h_1} with $h_1 = 0.81 \pm 0.18$ mm, 6,453,906 linear tetrahedral elements and a total of 1,250,647 DoF. All simulations were run on a 2019 Apple iMac$^{\text{TM}}$ using 8 MPI processes and 40 GB of memory. Time integration was done using the increments $\Delta t_{\mathcal{M}} = 0.001$ s, $\Delta t_{\mathcal{C}} = 0.0001$ s, $\Delta t_{\mathcal{E}} = 0.000\,05$ s.

5.4.1 Cellular Electromechanical Model

The transmembrane voltage V_{m}, intracellular calcium concentration $[\text{Ca}^{2+}]_{\text{i}}$, calcium bound to troponin C $[\text{Ca}^{2+}]_{\text{TRPN}}$, and active tension T_{a} under isometric conditions ($\lambda \in [0.8, 1.2]$) are shown in Figure 5.5 for the ORd+L17 model. Compared to the original implementation of the ORd and L17 models (depicted by the dashed lines), the coupled ORd+L17 shows variations in the calcium transient (CaT) and the action potential. With the exception of the endocardial variant, the repolarization phase is prolonged by up to 8 ms depending on the applied stretch. In the endocardial variant of the model, the repolarization phase is slightly shorter for $\lambda \leq 1$ and longer for $\lambda > 1$. The intracellular calcium concentration $[\text{Ca}^{2+}]_{\text{i}}$ decreases when the cell is in a stretched condition ($\lambda > 1$), since more calcium ions are bound to troponin C (vice versa for compressed cells). However, this relationship changes as soon as V_{m} reaches $\approx 95\,\%$ repolarization and $[\text{Ca}^{2+}]_{\text{i}}$ requires more time to return to its diastolic concentration in stretched cells. Introducing the coupling between troponin and the intracellular calcium concentration changes the amount of calcium bound to troponin C $[\text{Ca}^{2+}]_{\text{TRPN}}$ in different isometric conditions due to the altered availability of intracellular calcium. This results in a slight change in tension development. Qualitatively the same observations were made for the coupled CRN+L17 model, which is why the results are omitted here and the interested reader is referred to the Bachelor thesis of Stephanie Appel [36].

The CaT of the cell models differ from the experimental traces used by Land et al. to calibrate their model regarding key biomarkers such as time to peak of the calcium transient (TPCaT) and relaxation times to 50 % and 90 % decay from the peak calcium concentration

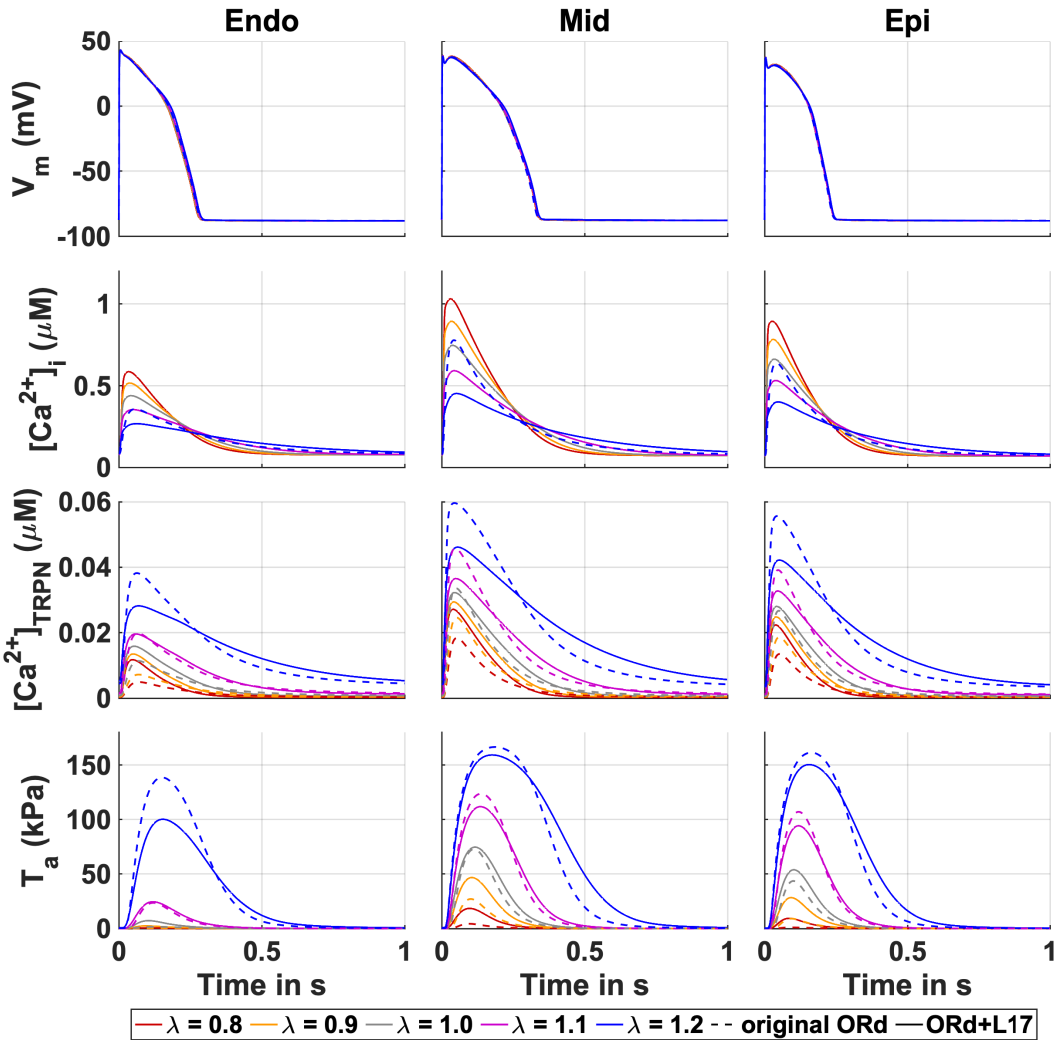

Figure 5.5: Transmembrane voltage V_m, intracellular calcium concentration $[\mathrm{Ca}^{2+}]_\mathrm{i}$, calcium bound to troponin C $[\mathrm{Ca}^{2+}]_\mathrm{TRPN}$, and active tension T_a under isometric conditions. Dashed lines show original ORd and L17 models and solid lines show the coupled ORd+L17 model.

(RT_{50}, RT_{90}). Therefore, a re-parameterization of the tension model by Land et al. was necessary after introducing the bidirectional coupling into the models of Courtemanche et al. and O'Hara et al.

For the atrial model, the parameters from Land et al. [14] were used. In tissue simulations this choice of parameters caused unphysiological behavior due to the introduction of length-dependent effects. An unphysiological rise in tension in the atria was observed during the contraction of the ventricles. The passive increase in volume and the atrioventricular plane displacement (AVPD) resulted in the atria being stretched by the ventricles, thus prolonging the time of contraction of the atria. Land et al. [14] encountered the same problem and suggested faster atrial contraction and crossbridge cycling rates as a solution. The CaT of the Courtemanche et al. electrophysiological model already promoted a faster contraction

with faster TPCaT compared to physiological values. Therefore, calcium cycling rates were left unchanged. Instead, the change in calcium sensitivity with respect to λ_f was reduced to $\beta_1 = -0.5$ and the half-activation point was increased to $[Ca^{2+}]^{ref}_{T50} = 1.05\,\mu M$. The re-parameterized atrial electromechanical model (Courtemanche-Land opt.) showed a time to peak tension TPT$= 73.5$ ms and $RT_{50} = 78.1$ ms after a total of 1000 cycles at a basic cycle length (BCL) of 1 s (Figure 5.6), which is in close agreement with atrial human tissue preparation data (Table 5.6).

Table 5.6: Literature values for time to peak of calcium transient (TPCaT) and active tension development (TPT) as well as relaxation time to 50 %, 90 % and 95 % respectively (RT_{50}, RT_{90}, RT_{95}) from human tissue preparations. The list of ventricular values were originally compiled in [160].

	Calcium transient			Active tension			
Tissue	**TPCaT (ms)**	**RT_{50} (ms)**	**RT_{90} (ms)**	**TPT (ms)**	**RT_{50} (ms)**	**RT_{95} (ms)**	**Ref.**
Ventricle	47.8 ± 10.0	151.1 ± 89.2	315.6 ± 161.2	-	-	-	[178]
Ventricle	-	-	-	165 ± 7	116 ± 6	334 ± 43	[179]
Ventricle	-	-	-	157 ± 10	117 ± 8	477 ± 31	[180]
Ventricle	-	-	-	235.0 ± 13.4	153 ± 71	309 ± 13.7	[181]
Ventricle	-	-	-	151.0 ± 6.1	98.0 ± 7.7	173.0 ± 10.7	[181]
Atria	52.5 ± 3.1	177.5 ± 9.0	-	109.6 ± 3.6	110.2 ± 84.0	-	[182]
Atria	-	-	-	85.0 ± 5.5	66.1 ± 5.9	-	[183]
Atria	-	-	-	88.3 ± 2.5	73.3 ± 1.7	-	[183]

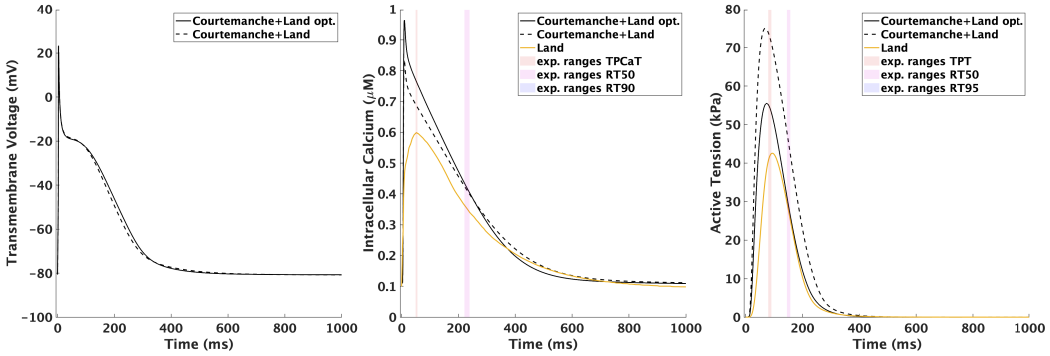

Figure 5.6: Action potential (left), CaT (center), and active tension (right) of the optimized (solid line) and the original (dashed line) atrial model with reference experimental values from literature [183]. **TPCaT:** time to peak of calcium transient; **TPT:** time to peak tension; **RT50/90/95:** relaxation times to 50/90/95 % decay from peak calcium/tension. Only the last cycle is visualized. From [35], licence CC-BY 4.0.

As a baseline for the ventricular model, the parameterization of [94] is used. First, the modifications suggested by Margara et al. [160] to the Hill coefficient of cooperative activation and the tropomyosin rate constant were adopted. Additionally, the same value for the half-activation point $[Ca^{2+}]^{ref}_{T50} = 1.05\,\mu M$ was used as for the atrial model. This reduced diastolic resting tension, which otherwise exceeded 2 kPa in tissue simulations

in pre-stressed ($\lambda_f > 1$) conditions. The CaT and active tension development of the final ventricular model is shown in Figure 5.7. Compared to the original model by Land et al. [94], the optimized model (OHaraRudy+Land opt.) showed more physiological behavior compared to experimental data after stimulating the model for 1000 cycles at a BCL of 1 s (TPT = 154.8 ms, RT50= 121.7 ms, RT95= 275.0 ms). To achieve deformations comparable with MRI data, the parameter T_{ref} in the OHaraRudy+Land opt. model was set to 480 kPa in multi-scale simulations. All adjusted parameters are given in Table 5.7.

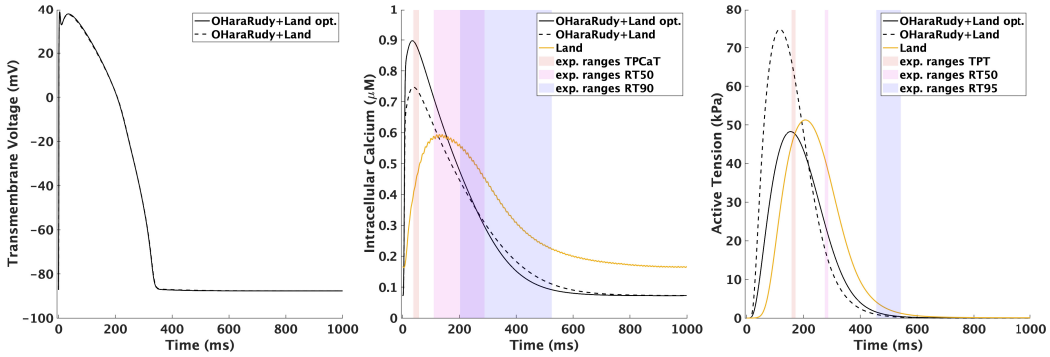

Figure 5.7: Action potential (left), CaT (center), and active tension (right) of the optimized (solid line) and the original (dashed line) ventricular model with reference experimental values from literature [179]. **TPCaT:** time to peak of calcium transient; **TPT:** time to peak tension; **RT50/90/95:** relaxation times to 50/90/95 % decay from peak calcium/tension. Only the last cycle is visualized. From [35], licence CC-BY 4.0.

Table 5.7: Optimized parameters for the atrial and ventricular tension development model. The original values are taken from [14, 94]. Values not listed in this table are unchanged from the original publications.

	Atria		Ventricle	
Parameter	**Original value**	**Optimized**	**Original value**	**Optimized**
k_u	1/ms	1/ms	1/ms	0.04/ms
n_{Tm}	5	5	5	2.4
$[Ca^{2+}]^{ref}_{T50}$	0.86 µM	1.05 µM	0.805 µM	1.05 µM
β_1	-2.4	-0.5	-2.4	-2.4

5.4.2 Electrophysiology

Electrophysiology on the tissue level was simulated using the monodomain equation with the cellular models CRN+L17 in the atria and ORd+L17 in the ventricles. Initial conditions for the cellular models were found by pacing a single cell for 1000 cycles with a basic cycle

length (BCL) of 1.2 s. The state of each model was then used as an initial condition on each vertex $\mathbf{X}_{h_1} \in \Omega_{h_1}$. Two simulations were conducted: one with the Fascicle model to initiate ventricular depolarization and one with the Purkinje muscle junction model (Figure 5.2). The local activation times (LATs) in the atria are shown in Figure 5.8. Depolarization starts at the SAN close to the SVC and spreads throughout the RA via the crista terminalis (CT) and pectinate muscles (PMs). After ≈ 30 ms, the depolarization wave propagates through the BB to the LA. The atria take approximately 100 ms to fully depolarize.

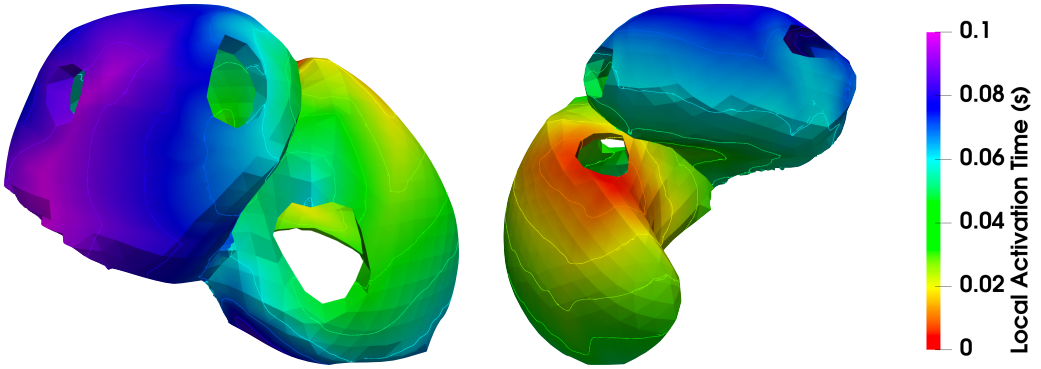

Figure 5.8: Local activation times in the atria in the posterior (left) and anterior (right) view. Contours show isochrones in 10 ms steps.

Depolarization in the ventricles starts after approximately 170 ms for both models of the His-Purkinje system (HPS). In the case of the Fascicular model shown in Figure 5.9a), total activation of the ventricles takes about 100 ms with the right ventricular outflow tract being activated last. The depolarization propagates away from the five distinct early activation sites (EAS) in a circular pattern and spreads throughout the myocardium. In agreement with Durrer et al. [59], the majority of the ventricular myocardium is activated within 50 ms to 60 ms.

Figure 5.9b) shows the activation pattern in the ventricles when using the Purkinje muscle junction model. Similar to the Fascicle model, depolarization starts at the EAS and the majority of the myocardium is activated within 60 ms. In contrast to the Fascicle model, depolarization is more fractionated due to the dedicated activation at the Purkinje muscle junctions and the myocardium in the apical segments take longer to activate. Nevertheless, the global activation pattern in both HPS models is qualitatively the same, which is why the Fascicle model is used for the remaining simulations and preferred over the Purkinje muscle junction model due to the more simple setup.

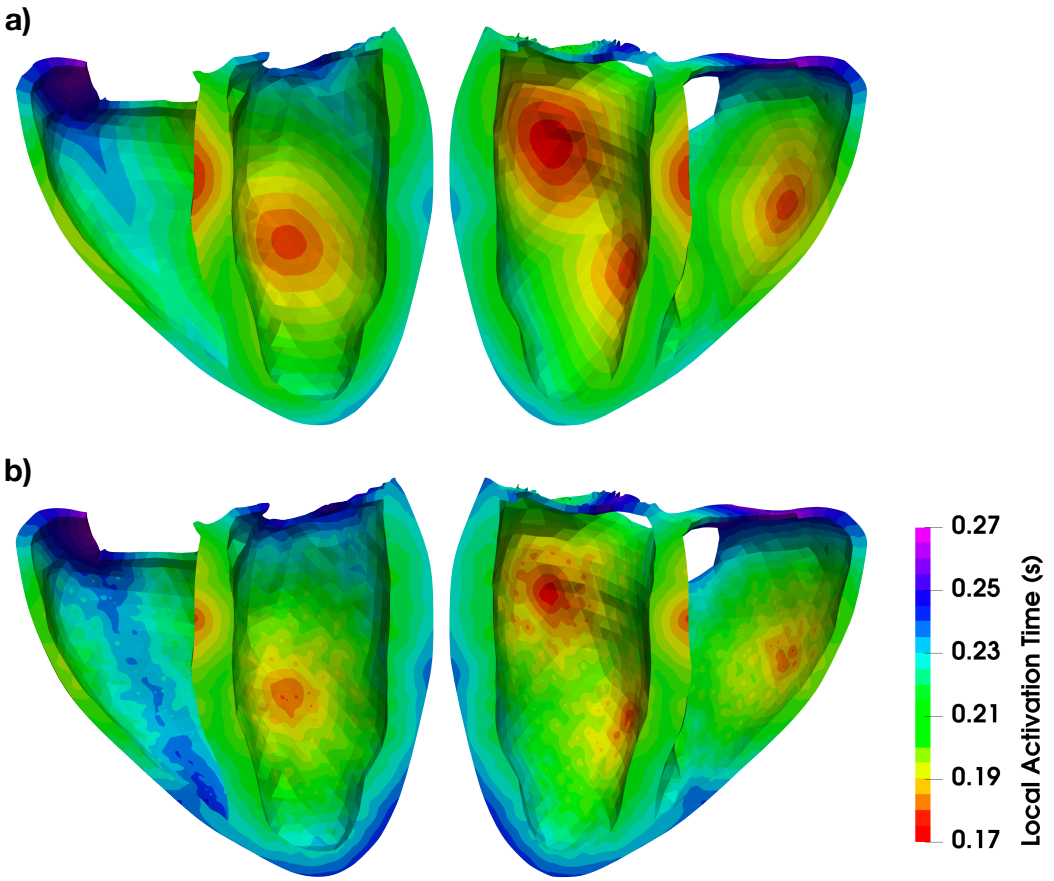

Figure 5.9: Local activation times in the ventricles for a) the fascicular activation model and b) the Purkinje muscle junction model. The ventricles are split in anterior and posterior views.

5.4.3 3D-0D Whole Heart

Unloading

The first step before starting the fully coupled simulations is to find a stress free state for the mechanical model. This was accomplished by using the unloading procedure described in Algorithm 5.1 with the end-diastole (ED) pressure $p_{\mathrm{LV}}^{\mathrm{ED}} = p_{\mathrm{LA}}^{\mathrm{ED}} = 8\,\mathrm{mmHg}$ and $p_{\mathrm{RV}}^{\mathrm{ED}} = p_{\mathrm{RA}}^{\mathrm{ED}} = 4\,\mathrm{mmHg}$. It took a total of five iterations of the unloading algorithm to converge with an L2 norm of the residual $\|\mathbf{R}\|_2 = 7.38 \times 10^{-4}\,\mathrm{mm}$. The largest errors were located in the free wall of the RV with a maximum value of 0.92 mm while the rest of the heart was generally below 50 µm.

End-Diastolic Pressure-Volume Relationship (EDPVR)

Parameters for the constitutive law were determined using the optimization scheme proposed by Kovacheva et al. [27]. However, these parameters were optimized on a much coarser mesh of the current heart model using quadratic tetrahedral elements. To evaluate if these parameters (Table 5.3) still result in a good fit to the EDPVR of Klotz et al. [173] in the improved mesh (refer to Chapter 4), the forward problem $\phi(\mathbf{X})$ (5.14) was solved with the pressure $p_{\mathrm{LV}}^{\mathrm{ED}} = 30\,\mathrm{mmHg}$ in the LV and $p_{\mathrm{LA}}^{\mathrm{ED}} = p_{\mathrm{RV}}^{\mathrm{ED}} = p_{\mathrm{RA}}^{\mathrm{ED}} = 0\,\mathrm{mmHg}$ in the other chambers. The resulting EDPVR is shown in Figure 5.10. Even though a set of parameters is used that was optimized for a differently discretized mesh, the simulated EDPVR still matches the Klotz EDPVR well, especially considering the variance of the measured data points by Klotz et al.

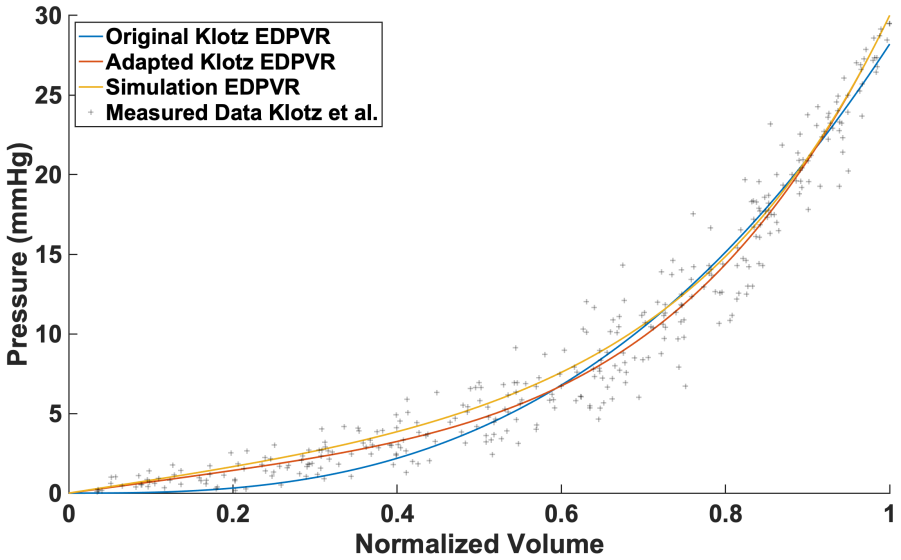

Figure 5.10: Original EDPVR and data points of Klotz et al. [173], adapted Klotz EDPVR from Kovacheva et al. [27], and simulated EDPVR using the refined model.

In vivo, the heart is surrounded by the pericardium, which acts as a protective layer and prevents excessive dilation in cases of acute volume overload. In the case of the simulated EDPVR shown in Figure 5.10, the pericardial boundary condition was not taken into account and there was no pressure in the other chambers. As a result, the LV was able to expand without any limitations except for the build up internal stress of the tissue that balances the build up in pressure. In whole heart simulations, the pericardium and the pressure from the other chambers will generally restrict the motion of the LV. To investigate how this will affect the EDPVR of all chambers, the forward problem $\phi(\mathbf{X})$ was adapted to accommodate three different scenarios: i) inflating every chamber of the heart separately ("Klotz" EDPVR); ii) EDPVR without the influence of the pericardium but all chambers are inflated simultaneously

(EDPVR without Contact); iii) all chambers are inflated simultaneously and the pericardium restricts only the outward motion (EDPVR with Contact). The resulting EDPVRs for all chambers are shown in Figure 5.11. Inflating all chambers simultaneously already has a measurable impact on the respective EDPVR. The slope of the EDPVRs becomes more steep and the RA and RV are affected more than the LV and LA. Including the pericardium further increases this behavior. Especially in the RV and RA the change in volume becomes severely restricted as soon as the pressure is larger than 2 mmHg and 3 mmHg for the RV and RA, respectively. Since case iii) reflects the simulation settings for the whole heart simulations

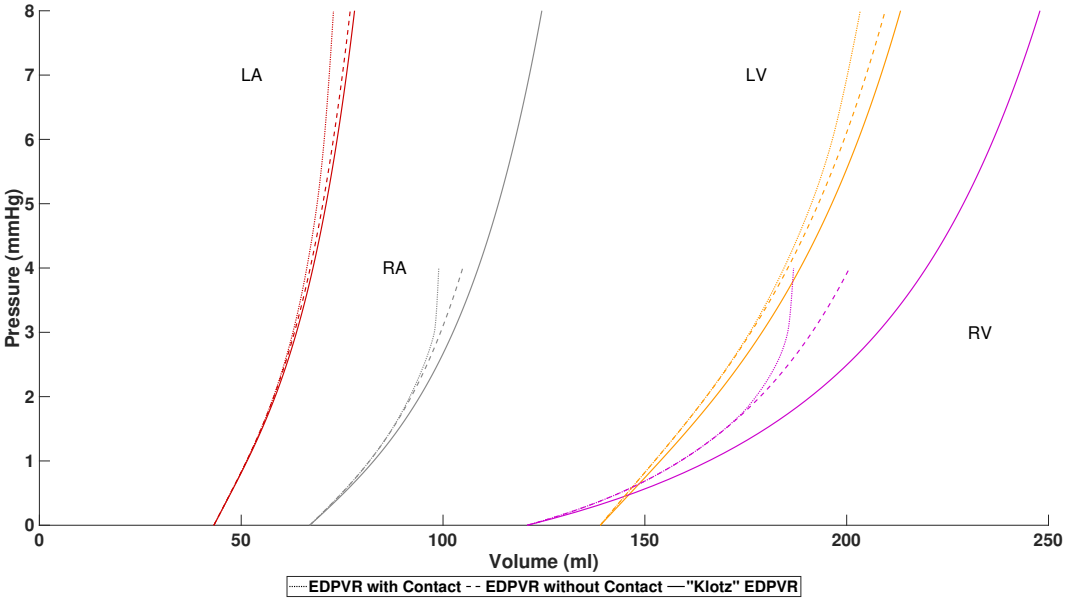

Figure 5.11: EDPVR of the LV, RV, LA, and RA for the scenarios i) "Klotz" EDPVR (solid line), ii) EDPVR without Contact (dashed line), iii) EDPVR with Contact (dotted line).

best, initial values for the displacement $\mathbf{d}$ are determined using the adapted forward problem $\phi(\mathbf{X})$ with the ED pressure from the unloading procedure and the stress free coordinates $\mathbf{X}$. The stress free and prestressed heart are shown in Figure 5.12.

Whole Heart Electromechanical Simulations

Three simulations were conducted on the whole heart with different levels of electromechanical coupling. The first simulation is done with the minimally coupled electromechanics model with precomputed LAT ($\mathcal{E}_{\text{LAT}}$-$\mathcal{MC}$). LATs were taken from the previously discussed simulation using the electrophysiology model ($\mathcal{IAE}$). Since LATs are used to activate mechanical contraction, the L17 model needs to be supplied with a calcium transient. Therefore, a fixed calcium transient of the CRN+L17 and ORd+L17 models in isometric conditions with $\lambda = 1.1$ is used to account for the initial displacement in the prestressed condition. The circulatory system was initialized with the parameters given in Table 5.8. It took a total

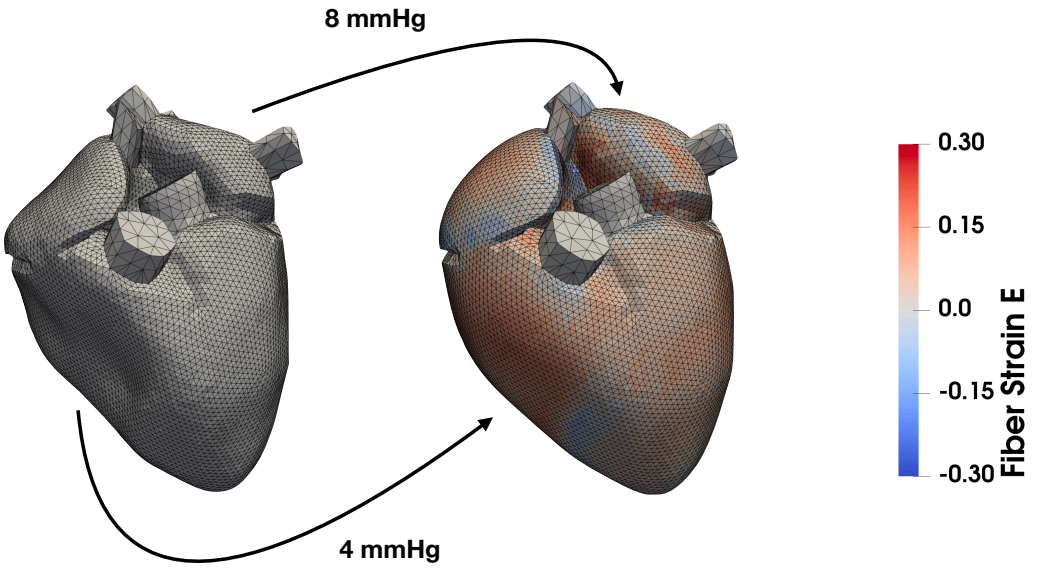

Figure 5.12: The fiber strain of the stress free (left) and prestressed (right) heart is shown. An ED pressure of $8\,\mathrm{mmHg}$ and $4\,\mathrm{mmHg}$ was used in the left and right heart chambers, respectively.

Table 5.8: Initial conditions for the circulatory system.

Parameter	Value		Unit	Description
	Initial	Limit Cycle		
V_{Tot}	5680.0	5680.0	ml	total blood volume
V_{SysArt}	1000.0	965.4	ml	systemic arterial volume
V_{PulArt}	300.0	255.4	ml	pulmonary arterial volume
V_{PulVen}	300.0	297.1	ml	pulmonary venous volume
p_{LV}	8.0	6.2	mmHg	left ventricular pressure
p_{LA}	8.0	5.7	mmHg	left atrial pressure
p_{RV}	4.0	5.6	mmHg	right ventricular pressure
p_{RA}	4.0	4.8	mmHg	right atrial pressure
Q_{AV}	0.0	-2.5	$\mathrm{ml}\cdot\mathrm{s}^{-1}$	aortic valve flow
Q_{PV}	0.0	-0.8	$\mathrm{ml}\cdot\mathrm{s}^{-1}$	pulmonary valve flow
Q_{MV}	0.0	17.1	$\mathrm{ml}\cdot\mathrm{s}^{-1}$	mitral valve flow
Q_{TV}	0.0	3.0	$\mathrm{ml}\cdot\mathrm{s}^{-1}$	tricuspid valve flow
η_{AV}	0.0	0.0	-	aortic valve state
η_{PV}	0.0	0.0	-	pulmonary valve state
η_{MV}	0.0	0.07	-	mitral valve state
η_{TV}	0.0	0.03	-	tricuspid valve state

of eight heart beats for the model to reach a stable limit cycle with a difference in stroke volume (SV) of less than 1 ml. Simulations using the $\mathcal{IAE}$-$\mathcal{MC}$ and $\mathcal{IAE}_{\mathrm{MEF}}$-$\mathcal{MC}$ models are computationally much more expensive, since electrophysiology and mechanics have to be solved. Therefore, these models were initialized using the displacement and circulatory system parameters of the limit cycle using the $\mathcal{E}_{\mathrm{LAT}}$-$\mathcal{MC}$ model. As a result, it took only two

heart beats to stabilize the system. Average simulation times for a single heart beat of 1.2 s are given in Table 5.9.

Table 5.9: Average simulation times using different levels of electromechanical coupling on a 2019 Apple iMac^{TM} using 8 MPI processes and 40 GB of memory.

Model	Task	Computational time
$\mathcal{E}_{\text{LAT}}$-$\mathcal{MC}$	simulation of a 1.2 s heart beat	80 min
$\mathcal{IAE}$-$\mathcal{MC}$	simulation of a 1.2 s heart beat	256 min
$\mathcal{IAE}_{\text{MEF}}$-$\mathcal{MC}$	simulation of a 1.2 s heart beat	2247 min

Hemodynamic parameters of the three simulations are shown in Figure 5.13. Due to the similarities in the results, only the results of the $\mathcal{E}_{\text{LAT}}$-$\mathcal{MC}$ model are discussed. Atrial PV-loops exhibit the typical figure-of-eight shape, with the A-wave and the V-wave both present. However, the V-wave is significantly smaller compared to the A-wave, indicating a larger emphasis on active emptying compared to passive emptying of the atria. Additionally, a short spike in pressure with little change in volume (C-wave) can be observed in both atria immediately after the onset of ventricular contraction. Ventricular PV-loops follow the four major phases of the cardiac cycle: isovolumetric contraction, ejection, isovolumetric relaxation, and filling. Systolic blood pressure is elevated in both, the LV and RV, compared to a healthy individual ($p_{\text{LV}} = 140$ mmHg and $p_{\text{RV}} = 48$ mmHg). The E/A ratio is a marker of the function of the left ventricle of the heart. It represents the ratio of peak blood flow during LV relaxation in early diastole (the E wave) to peak blood flow in late diastole caused by atrial contraction (the A wave) (see Figure 5.13, bottom left panel). With an E/A ratio of 1.13, the LV is considered to function in the physiological range (0.75 < E/A ratio < 1.5). For the different levels of coupling considered in the three models, only a small difference can be observed in the hemodynamic parameters. A small reduction in stroke volume ($\Delta\text{SV} = 3$ ml) and systolic pressure ($\Delta p = 3$ mmHg) can be observed in the ventricles when moving from the minimally coupled $\mathcal{E}_{\text{LAT}}$-$\mathcal{MC}$ model to the $\mathcal{IAE}$-$\mathcal{MC}$ model. Similar changes are seen in the atria, where active emptying is enhanced. Between the $\mathcal{IAE}$-$\mathcal{MC}$ and $\mathcal{IAE}_{\text{MEF}}$-$\mathcal{MC}$ model, there is no noticeable difference.

Since MEF mainly affects the electrophysiological model, a comparison of the transmembrane voltage V_{m} between the $\mathcal{IAE}$ model and the two electromechanical $\mathcal{IAE}$-$\mathcal{MC}$ and $\mathcal{IAE}_{\text{MEF}}$-$\mathcal{MC}$ models is shown in Figure 5.14. Looking at the scale of the whole heart, almost no difference is visible between the three models. In fact, only a lower voltage during the plateau phase of the action potential can be observed in the RA at 80 ms. To see differences on a smaller scale, the transmembrane voltage V_{m} and the intracellular calcium concentration $[\text{Ca}^{2+}]_{\text{i}}$ at two distinct vertexes are shown in Figure 5.15. One point was located in the posterior roof of the LA and the other point was located in the free wall of the LV close to the base. On the cellular level, a difference between the model with and without MEF can be observed. Using the $\mathcal{IAE}_{\text{MEF}}$-$\mathcal{MC}$ model, depolarization begins 0.4 ms earlier in the vertex of the ventricle compared to the models without MEF and repolarization is

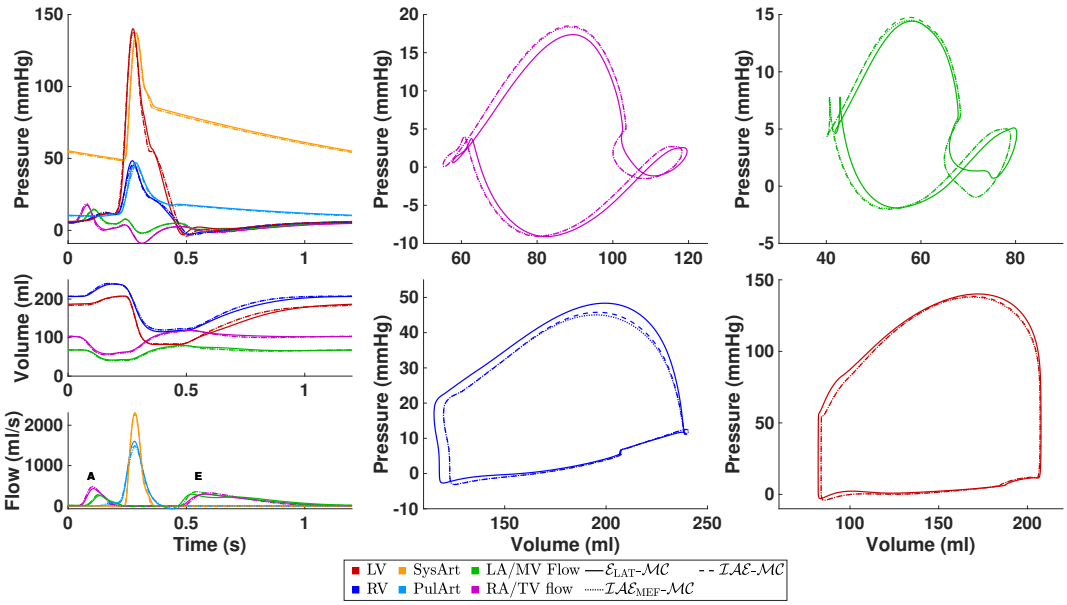

Figure 5.13: Results of the circulatory system for the simulations using the $\mathcal{E}_{\mathrm{LAT}}$-$\mathcal{MC}$ (solid lines), $\mathcal{IAE}$-$\mathcal{MC}$ (dashed lines), and $\mathcal{IAE}_{\mathrm{MEF}}$-$\mathcal{MC}$ (dotted lines) models after reaching a stable limit cycle. First column from top to bottom: (1) Wiggers diagram showing pressure with respect to time; (2) cavity volume with respect to time; (3) flow through mitral valve (MV), tricuspid valve (TV), systemic arterial flow (SysArt), and pulmonary arterial flow (PulArt). The second and third column show the phase diagrams of the pressure-volume relationship for the left atrium (LA), left ventricle (LV), right atrium (RA), and right ventricle (RV).

prolonged by 8 ms. In the atrial vertex, using the $\mathcal{IAE}_{\mathrm{MEF}}$-$\mathcal{MC}$ model introduced a delay of 1 ms in the depolarization. However, no difference during repolarization could be observed. The difference between the $\mathcal{IAE}$ model and the two coupled variants is more clear. Due to the coupling on the cellular level, V_{m} was reduced during the plateau phase and repolarization was prolonged. This can be traced back to the changes in the calcium transient, which are more significant in the atrial model than in the ventricular one.

Validation

To validate the numerical results of the personalized heart model, time resolved cine magnetic resonance imaging (MRI) in 2-, 3-, and 4-chamber long axis view was analyzed (Chapter C). Specifically, important mechanical biomarkers of the LV such as volume, wall thickness, atrioventricular plane displacement (AVPD), and rotation were evaluated and compared to the numerical results as shown in Figure 5.16. Notice that the comparison of the initial LV volume and wall thickness illuminated significant deviations between the MRI data and the created anatomical model which are most likely related to the initial segmentation of the endo- and epicardial surfaces of the heart. The mean wall thickness of the LV in the cine MRI data was 2.86 mm lower than in the model. As a consequence, the initial volume of the LV was 32.52 ml less than in the actual data. This makes a direct comparison with absolute

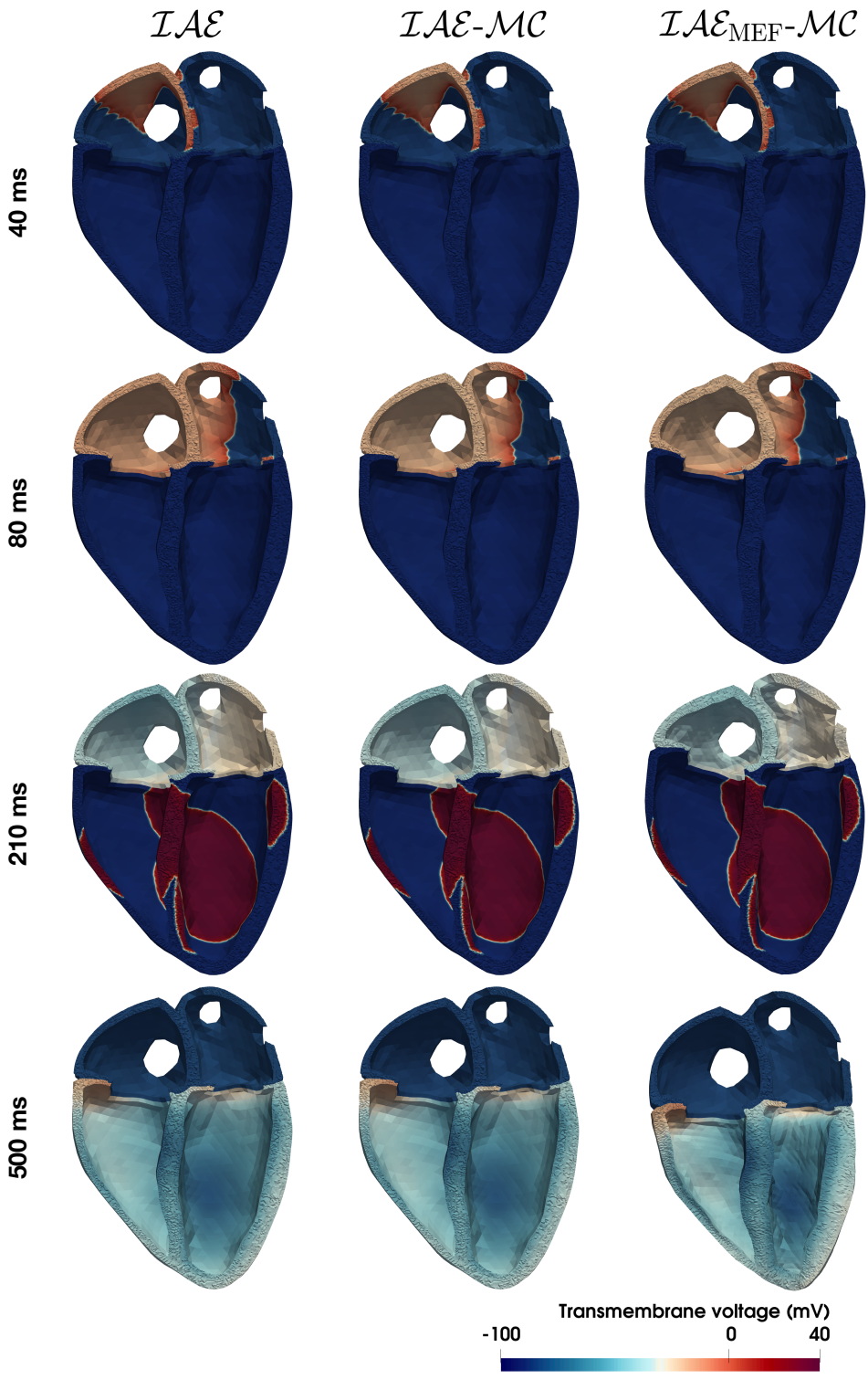

Figure 5.14: Comparison of the transmembrane voltage V_{m} using the $\mathcal{IAE}$, $\mathcal{IAE}$-$\mathcal{MC}$, and $\mathcal{IAE}_{\mathrm{MEF}}$-$\mathcal{MC}$ models in four chamber long axis view.

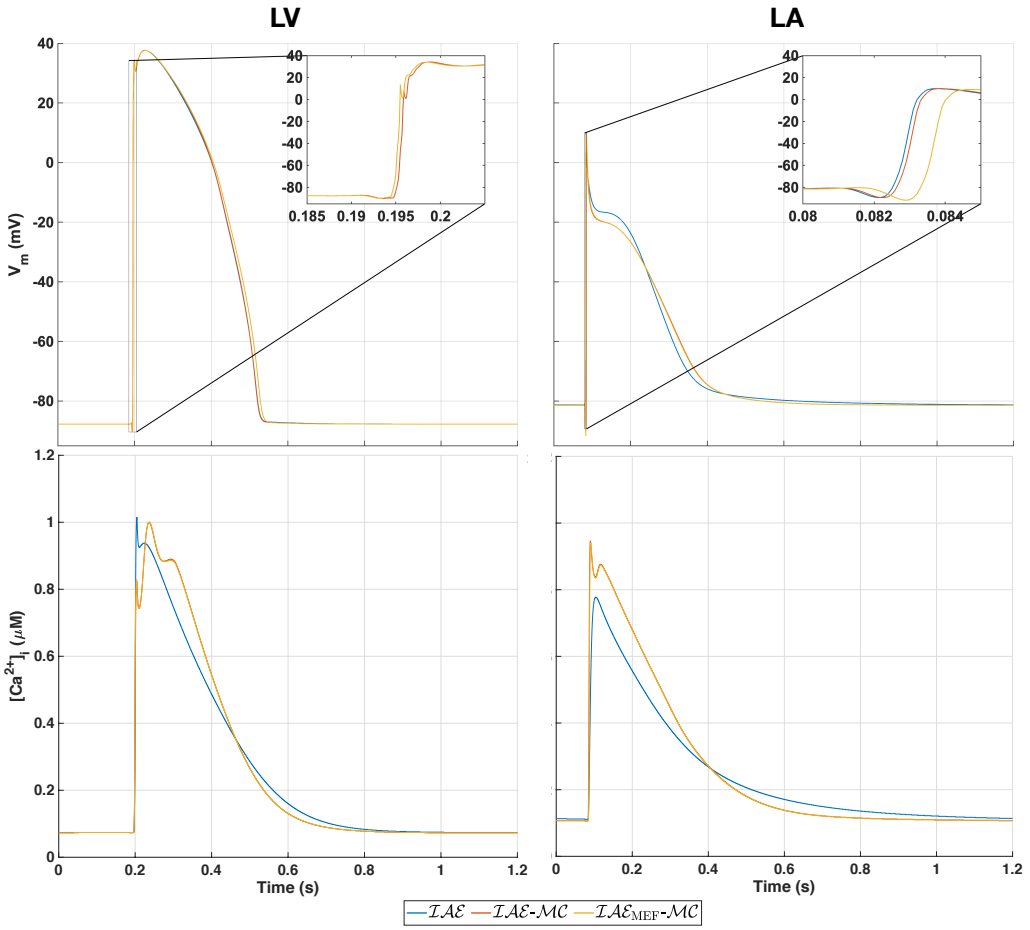

Figure 5.15: Transmembrane voltage V_m and intracellular calcium concentration $[\mathrm{Ca}^{2+}]_\mathrm{i}$ of a single cell for the $\mathcal{IAE}$, $\mathcal{IAE}$-$\mathcal{MC}$, and $\mathcal{IAE}_\mathrm{MEF}$-$\mathcal{MC}$ models. A representative atrial cell was picked from the posterior roof of the left atrium and a ventricular cell was picked from the left ventricular free wall closer to the base. The inset figures show a close up of the upstroke in V_m.

values impractical. Therefore, LV volume and mean wall thickness are normalized to their initial values.

Looking at the LV volume reveals a significant difference in the timings of the phases of the cardiac cycle. ED is reached at 240 ms in the model, which is 23 ms after ED is reached in the MRI data. For end-systole (ES) the opposite is observed, with a timing of 430 ms in the model and 577 ms in the MRI data. This discrepancy is present in all of the evaluated biomarkers. Nevertheless, the relative increase in volume due to the atrial kick and the ejection fraction (EF) of the LV are identical. With $\mathrm{SV}_\mathrm{LV} = 125\,\mathrm{ml}$ and $\mathrm{SV}_\mathrm{RV} = 123\,\mathrm{ml}$, ventricular stroke volumes are close to the values derived from imaging data ($\mathrm{SV}_\mathrm{LV}^\mathrm{MRI} = 141\,\mathrm{ml}$, $\mathrm{SV}_\mathrm{RV}^\mathrm{MRI} = 129\,\mathrm{ml}$) while keeping the difference in the initial volumes in mind. With a peak ejection rate (PER) of 2300 ml/s, the LV in the model ejects blood during systole almost three times as fast as the MRI data suggests (816 ml/s). The exact opposite is the case for LV peak filling rate (PFR), which is about three times lower in the

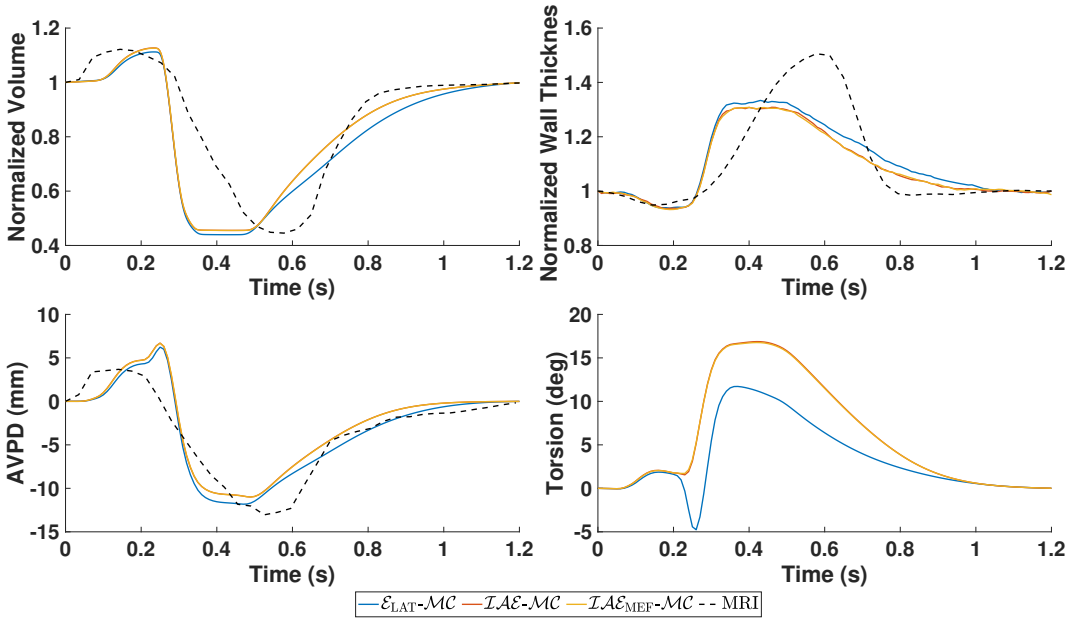

Figure 5.16: Calculated biomarkers of the LV for the simulations using the $\mathcal{E}_{\mathrm{LAT}}$-$\mathcal{MC}$, $\mathcal{IAE}$-$\mathcal{MC}$, and $\mathcal{IAE}_{\mathrm{MEF}}$-$\mathcal{MC}$ models after reaching a stable limit cycle compared to MRI data of the volunteer.

model (290 ml/s vs 968 ml/s). Notice that PFR is higher in the simulations using the coupled $\mathcal{IAE}$-$\mathcal{MC}$ and $\mathcal{IAE}_{\mathrm{MEF}}$-$\mathcal{MC}$ models (352 ml/s) but still considerably lower than in the MRI data.

Wall thickness of the LV decreases by approximately 6% during atrial contraction in both, the in silico models and the MRI data. From ED to ES, the LV wall thickness increased by about 40% in the $\mathcal{E}_{\mathrm{LAT}}$-$\mathcal{MC}$ model and by 38% in the $\mathcal{IAE}$-$\mathcal{MC}$ and $\mathcal{IAE}_{\mathrm{MEF}}$-$\mathcal{MC}$ models. Compared to the observed fractional wall thickening in the MRI data (56%), wall thickening in the three models is too low.

AVPD was measured relative to the position of the valves during diastasis. Negative values are associated with the movement of the valves towards the apex. During the contraction of the atria, the mitral valve was pulled up by 4.3 mm. Peak AVPD was reached at ES with a displacement of -11.8 mm for the mitral valve. However, before moving towards the apex, the valve moved up to 1.5 mm in the opposite direction, which is associated with the bulging of the Mitral valve into the left atrium. This behavior could not be observed in the MRI data, since the temporal resolution was too low to capture it. In total, with an AVPD from ED to ES of -16.1 mm the numerical results match the MRI data (-16.53 mm) very well. The two coupled models show a slightly reduced AVPD of -15.8 mm.

Lastly, the rotational behavior of the LV was analyzed by calculating the net angle of rotation between basal and apical segments. Since it was not possible to analyze rotation from the available MRI data, numerical results are compared to literature values. During atrial contraction, the LV untwists itself for a short period of time due to the expansion of the chamber. In the case of the $\mathcal{E}_{\mathrm{LAT}}$-$\mathcal{MC}$ model, the LV briefly rotates in the opposite direction during the onset of ventricular contraction. In the coupled models, this cannot be observed.

The peak of rotation is reached during ES with net angles of rotation of 11.7° and 16.8° for the $\mathcal{E}_{\mathrm{LAT}}$-$\mathcal{MC}$ and $\mathcal{IAE}$-$\mathcal{MC}$/$\mathcal{IAE}_{\mathrm{MEF}}$-$\mathcal{MC}$ models, respectively. However, if the absolute angle of rotation during ventricular contraction is considered, the LV in the $\mathcal{E}_{\mathrm{LAT}}$-$\mathcal{MC}$ model rotates 16.4° as well. All three simulations agree with values that are reported in literature (13° to 27° [184]).

5.5 Discussion

5.5.1 Electromechanical Coupling

The contraction of the heart muscle is the result of a bidirectional coupling between electrophysiology and mechanics. On the one hand, cardiac excitation-contraction coupling describes the series of events that lead from an electrical impulse to the contraction of the heart. On the other hand, the propagation of electrical signals is influenced by mechano-electric feedback (MEF) mechanisms. Currently, three major mechanisms are known to contribute to MEF: 1) the deformation of cardiac tissue during contraction and relaxation changes the electrical gradient; 2) the transmembrane voltage V_{m} is directly modified through stretch activated currents (SACs); 3) the stretch in the cells changes the binding affinity of calcium to troponin C, thus altering the intracellular levels of calcium. With the exception of SACs, the influence of the remaining MEF mechanisms on the numerical results have been assessed in this study using three variations of the electromechanical model presented in Chapter 5.3: the minimally coupled electromechanics model with precomputed LAT ($\mathcal{E}_{\mathrm{LAT}}$-$\mathcal{MC}$); the fully coupled electromechanics model without MEF ($\mathcal{IAE}$-$\mathcal{MC}$); the fully coupled electromechanics model with MEF ($\mathcal{IAE}_{\mathrm{MEF}}$-$\mathcal{MC}$). While a change in stretch is neglected in the $\mathcal{E}_{\mathrm{LAT}}$-$\mathcal{MC}$ model, the $\mathcal{IAE}$-$\mathcal{MC}$ model includes MEF on the cellular level by changing the binding affinity of calcium to troponin C. In a single cell, this promotes a change in the intracellular calcium concentration $[\mathrm{Ca}^{2+}]_{\mathrm{i}}$, the action potential duration, and force production of the sarcomere. As shown in Figures 5.6 and 5.7, the cellular electromechanical models proposed in this study yield physiologically accurate active tension in line with data from human tissue preparations after a reparameterization in the L17 tension model to adjust for the difference calcium transients in the CRN and ORd ionic models. Considering these effects in the whole heart changes hemodynamic parameters such as SV and peak filling rate, $[\mathrm{Ca}^{2+}]_{\mathrm{i}}$, wall thickening, and AVPD. All of these adaptations are the result of the changing force production introduced on the cellular level due to the change in stretch. Adding the influence of deformation on the diffusion tensor in the $\mathcal{IAE}_{\mathrm{MEF}}$-$\mathcal{MC}$ only has minor influences on the output of the whole heart in the evaluated scenario. As shown in two exemplary locations of the left atrium and the left ventricle (Fig. 5.15), a small shift in the arrival times of the depolarization wave was observed. This suggests a change of the conduction velocity due to the deformation which confirms the theoretical considerations in Chapter 5.2. Nevertheless, it is still heavily debated how the deformation of the heart affects conduction velocity. Experimental measurements by Dominguez et al. [185] indicate

an increase in conduction velocity in Purkinje cells. Others report a decrease in conduction velocity in epicardial cells, atrial, and ventricular myocardium [186–188]. Considering the minimal influence on the model output and the considerable increase in computational cost of the $\mathcal{IAE}_{\text{MEF}}$-$\mathcal{MC}$ model (Table 5.9), it is sufficient to use the $\mathcal{IAE}$-$\mathcal{MC}$ model in most applications.

The validation of the numerical results with MRI data showed a considerable deviation in mechanical biomarkers of the LV. Especially the dynamics of the contraction do not represent the MRI data well. During relaxation, the reduction in stress and increase in ventricular volume is too slow. As a result, no clear diastasis phase can be observed in the model. Furthermore, the rate of contraction during systole is higher and the model reaches end-systole more than twice as fast as the MRI data suggests. This behavior can be observed in other simulation studies using the Land et al. tension model [17, 94] or other tension models based on sliding filament theory [20, 90], suggesting that not all mechanisms of cardiac contraction are fully represented in the most recent models. A simulation study by Campbell suggests that an acceleration of the relaxation can be achieved by introducing interfilamentory movement resulting from compliance in the sarcomere [189]. Possibly, a similar effect could result from an increase in myocardial stiffness and should be investigated further. The use of phenomenological tension models seems to circumvent these problems, as results in Kovacheva, E. [190] or the Control simulation in Chapter 11 suggest.

A limitation of our electromechanical model is that the dependence on stretch rate $\frac{\partial \lambda}{\partial t}$ in Eq. (5.10c) had to be neglected by setting $\frac{\partial \lambda}{\partial t} = 0$ for all numerical experiments. Adding stretch rate dependence introduced strong nonphysical oscillations in the multi-scale model resulting in an unstable numerical scheme. Regazzoni et al. [191] identified the source of these instabilities to be an inconsistent treatment of macroscopic and microscopic strains in staggered solution strategies of deformation in conjunction with an active stress model with a stretch rate dependence. This condition applies to the staggered approach described in Chapter 5.3.2 and should be solved in the future by implementing the proposed stabilization term in [191].

5.5.2 Circulatory System

As demonstrated in the numerical experiments, the closed-loop circulatory system model is strongly coupled to the deformation problem and can reproduce major features of the human circulatory system. In the atria, the typical figure-of-eight shape is observed in the PV-loops consisting of an A- and a V-loop corresponding to the atrial and ventricular contraction respectively. Additionally, a short increase in pressure in early systole known as the C-wave can be observed. Physiologically, this is the result of the atrioventricular valve's cusps bulging into the atria during ventricular isovolumetric contraction. In the model, this observation was made possible by including physical representations of the valves in the mechanical mesh and was visible in the AVPD as well (Fig. 5.16). In the ventricular PV-loops, the four major phases are present: 1) isovolumetric contraction; 2) ejection of blood from the ventricles; 3) isovolumetric relaxation; 4) passive filing with blood. Except for LV

volume, no data related to the circulatory system were available from the healthy volunteer. Therefore, the parameterization of the circulatory system model is motivated entirely by values obtained from literature and might not be fully representative to our specific case. The systolic pressures of the LV and the RV are too high for a healthy heart and are likely the result of the steep increase in stress due to the tension model. An optimized tension model could potentially address this issue and properly reflect systolic and diastolic behavior of the ventricles.

5.5.3 Numerical Considerations

The simulation framework proposed in this study was previously verified in N-version benchmarks that investigated the spatio-temporal convergence of the electrophysiological system [192] and the mechanical system [39], respectively.

For the solution of the monodomain equation, a small spatial resolution is required to avoid spatial undersampling artifacts leading to a reduction in conduction velocity or even conduction block. With an average spatial discretization of 0.8 mm of the electrophysiological domain, a coarser mesh was used than all of the values tested in [192]. Recently, Woodworth et al. published in [193] a convergence study for the monodomain problem coupled to the ten-Tusscher-Panfilov (TTP) cell model [194]. The spatial discretization, which is needed to be in the convergence region, is out of scope of the technical requirements for the simulations of this work. However, to match prescribed velocities [17] for the electrical activation pattern, the conductivity values are increased for the whole heart simulations. As shown in Figures 5.9 and 5.8, the resulting activation sequence matches normal patterns observed in humans [59, 195].

The benchmark of the mechanical deformation problem only considered a simplified approach, which cannot be directly translated to a whole heart simulation scenario. However, it includes important aspects of cardiac function such as the active contraction of the heart muscle, pressure boundary conditions, and a complex distribution of fiber orientations. Even though the participating groups used a variety of finite elements (tetrahedral and hexahedral) of different order and the DoF ranged between 10^2 and 10^6, the results were astonishingly similar. A major problem is that it was not reported specifically how incompressibility was enforced and what kind of parameters were used. This has a significant impact on the outcome of the simulations. Especially in the case of tetrahedral elements, penalty formulations were used to enforce quasi-incompressibility, which promotes volumetric locking effects. However, Marx et al. [28] used stabilized locking free P1P1 elements to show that the passive behavior of the LV can be modeled equally well with linear P1 elements. They showed that volumetric locking in linear elements can be compensated to a certain degree by assuming material parameters that correspond to a softer material. In the case of this study, volumetric locking was compensated for by reducing the penalty parameter κ in the incompressiblilty constraint from 10^6 to 10^5, which was enough to preserve the EDPVR of the LV compared to a previous study of Kovacheva et al. [27] that used quadratic elements.

There is currently no extensive existence result nor convergence study available for the fully coupled electromechanical problem. Some results were first presented by Andreianov et al. [196] and an extensive proof is given in [197], where an active strain decomposition was assumed in contrast to the active stress formulation used in this work. Moreover, the equations of finite elasticity were linearized and assumed to be isotropic. The authors mention that the proof is extensible to anisotropic and polyconvex material formulations, for which there are some existence results [198, Chapter 7]. Unfortunately, the material formulation and boundary conditions used in this work do not satisfy the necessary assumptions.

PART III

REPRODUCIBLE VERIFICATION OF MODEL COMPONENTS

Chapter 6

Electrophysiology

For the verification of the electrophysiological core model, a simulation setup of an N-version benchmark [38] is used. Additionally, solutions for different spatial and temporal resolutions are presented.

6.1 Problem Definition

The geometry of the tissue model is defined by a cuboid $\Omega_{\text{cuboid}} \to \mathbb{R}^3$ with dimensions $20.0 \times 7.0 \times 3.0\,\text{mm}^3$ and is shown in Figure 6.1. For each time $t \in (0, T]$, find the transmembrane

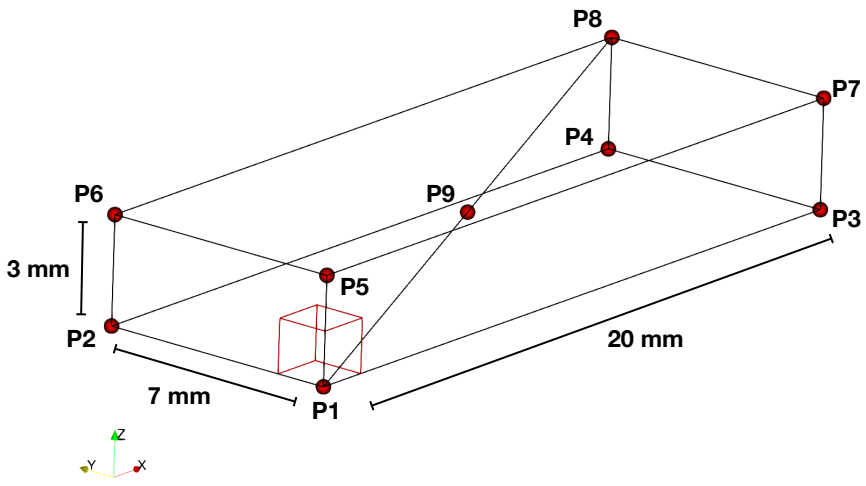

Figure 6.1: Simulation domain for the electrophysiology problem. Shown are the dimensions and the evaluation points as well as the stimulus area (red box).

potential $V_{\text{m}}\colon (0, T] \times \Omega_{\text{Cuboid}} \to \mathbb{R}$, the set of state variables $\mathbf{w}\colon (0, T] \times \Omega_{\text{Cuboid}} \to \mathbb{R}^{n_{\mathbf{w}}}$ and

$\mathbf{q}\colon (0,T]\times\Omega_{\text{Cuboid}}\to\mathbb{R}^{n_\mathbf{q}}$ such that

$$\begin{cases} \beta\left[C_\text{m}\frac{\partial V_\text{m}}{\partial t}+I_\text{ion}(V_\text{m},\mathbf{w},\mathbf{q})+I_\text{app}(t)\right]=\nabla\cdot(\mathbf{D}\nabla V_\text{m}) & \text{in} \quad \Omega_\text{Cuboid} \\ \frac{\partial\mathbf{w}}{\partial t}-\mathbf{G}_\mathbf{w}(V_\text{m},\mathbf{w},\mathbf{q})=\mathbf{0} & \text{in} \quad \Omega_\text{Cuboid} \\ \frac{\partial\mathbf{q}}{\partial t}-\mathbf{G}_\mathbf{q}(V_\text{m},\mathbf{w},\mathbf{q})=\mathbf{0} & \text{in} \quad \Omega_\text{Cuboid} \\ \mathbf{D}\nabla V_\text{m}\cdot\mathbf{N}=0 & \text{on} \quad \partial\Omega_\text{Cuboid} \\ V_\text{m}=V_\text{m}^0,\quad \mathbf{w}=\mathbf{w}^0,\quad \mathbf{q}=\mathbf{q}^0 & \text{in} \quad \Omega_\text{Cuboid}\times 0\,. \end{cases} \tag{6.1}$$

The ionic current I_ion, the gating variables $\mathbf{w}$, and the ionic concentrations $\mathbf{q}$ are defined by the model of ten-Tusscher-Panfilov (TTP) [194] with $n_\mathbf{w}=12$ and $n_\mathbf{q}=6$. The conductivity tensor for the cuboid is defined as

$$\mathbf{D}=\sigma_f\mathbf{f}\otimes\mathbf{f}+\sigma_s\mathbf{s}\otimes\mathbf{s}+\sigma_n\mathbf{n}\otimes\mathbf{n}\,, \tag{6.2}$$

where the fiber direction $\mathbf{f}$ is aligned with the x-axis. Suitable values for β, C_m, σ_f, σ_s, and σ_n are given in Table 6.1. The externally applied stimulation current I_app is defined by the

Table 6.1: Model Parameters for the verification problem given by Eq. (6.1).

Parameter	Value	Unit	Description
$(\sigma_\text{f},\sigma_\text{s},\sigma_\text{n})$	$(0.13337, 0.01761, 0.01761)$	S/m	conductivities in Ω_Cuboid
β	140000	1/m	membrane surface-to-volume ratio
C_m	0.01	F/m^2	membrane capacitance
A	50000	A/m^3	stimulus amplitude
τ	0.002	s	stimulus duration

following protocol:

$$I_\text{app}(t)=\begin{cases} A & \text{in} \quad \Omega_\text{stim}\times(0,\tau] \\ 0 & \text{otherwise} \end{cases} \tag{6.3}$$

where A is the stimulus amplitude, τ is the stimulus duration, and $\Omega_\text{stim}\to\mathbb{R}^3$ is a subspace of Ω_Cuboid with dimensions $1.5\times1.5\times1.5\,\text{mm}^3$ originating from the coordinates $x=y=z=0$. Initial values for the transmembrane voltage V_m^0, the gating variables $\mathbf{w}^0$, and the ionic concentrations $\mathbf{q}^0$ are given in Table 6.2.

6.2 Results

The problem described in Chapter 6.1 was solved using linear tetrahedrons with five different element sizes $h=\{0.1,0.2,0.3,0.4,0.5\}$ mm and four different time step sizes $\Delta t=\{0.05,0.01,0.005,0.001\}$ ms. Activation times were determined at each vertex of the domain Ω_Cuboid as soon as the transmembrane voltage V_m surpassed a threshold of 0 mV. The activation times along the diagonal line from P1 to P8 for all combinations of spatial

Table 6.2: Initial values for the ionic model by TTP.

Value	Unit	Description
-85.23	mV	transmembrane potential
0.00621	-	rapid time-dependent potassium current Xr1 gate
0.4712	-	rapid time-dependent potassium current Xr2 gate
0.0095	-	slow time-dependent potassium current Xs gate
0.00172	-	fast sodium current m gate
0.7444	-	fast sodium current h gate
0.7045	-	fast sodium current j gate
3.373×10^{-5}	-	L-type Ca current d gate
0.7888	-	L-type Ca current f gate
0.9755	-	L-type Ca current f2 gate
0.9953	-	L-type Ca current fCass gate
0.999998	-	transient outward current s gate
2.42×10^{-8}	-	transient outward current r gate
0.000126	mM	intracellular calcium
3.64	mM	sarcoplasmic reticulum calcium
0.00036	mM	subspace calcium
0.9073	-	ryanodine receptor
8.604	mM	intracellular sodium
136.89	mM	intracellular potassium

and temporal discretizations are shown in Figure 6.2 and 6.3. Activation times in point P8 represent an accumulation of any errors as the wave propagates across the cuboid. Time discretization did not have a significant impact on the solution of the problem. Only at a time increment of $\Delta t = 0.05$ ms the accumulated error at point P8 starts to increase with smaller spatial resolutions.

The impact of spatial resolution on the activation times is much more significant. The morphology of the solutions suggests that the perceived conduction velocity increases as the mesh is more and more refined. At point P8, the activation time converges to a solution of 37.74 ms with only a 0.22 ms difference between the solutions using $h = 0.1$ mm and $h = 0.2$ mm. Compared to the converged solution of 42.75 ms reported in Niederer et al. [38], the largest error in the presented simulations lies within 13% at a discretization of $h = 0.5$ mm. It is unclear, why the converged solution in this study deviates from the one in [38] by 5 ms. However, the solutions from all spatial resolutions presented here lie within the range of 37.8 ms to 48.7 ms that was reported from all groups in the benchmark at the highest spatial and temporal resolutions.

Activation times at points P1 to P9 for a spatial discretization of $h = 0.1$ mm are shown in Table 6.3.

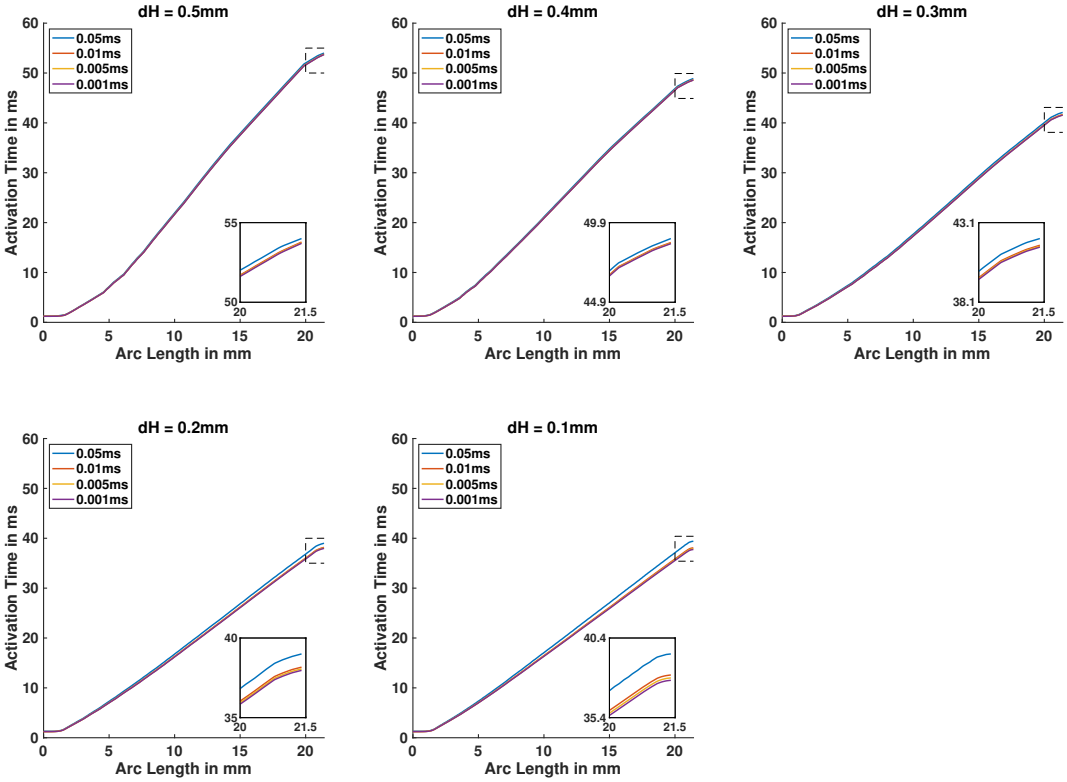

Figure 6.2: Activation times for the different spatial (panels) and temporal (denoted by color) discretizations on the diagonal line from P1 to P8.

Table 6.3: Activation times in ms at points P1 to P9 for a spatial discretization of $h = 0.1\,\mathrm{mm}$.

point	$\Delta t = 0.05\,\mathrm{ms}$	$\Delta t = 0.01\,\mathrm{ms}$	$\Delta t = 0.005\,\mathrm{ms}$	$\Delta t = 0.001\,\mathrm{ms}$
P1	1.3	1.23	1.225	1.221
P2	25.95	25.32	25.23	25.156
P3	32.35	31.23	31.08	30.953
P4	39.2	37.87	37.69	37.54
P5	8.0	7.78	7.755	7.731
P6	26.55	25.88	25.785	25.711
P7	32.95	31.8	31.64	31.512
P8	39.4	38.08	37.895	37.745
P9	18.45	17.81	17.725	17.655

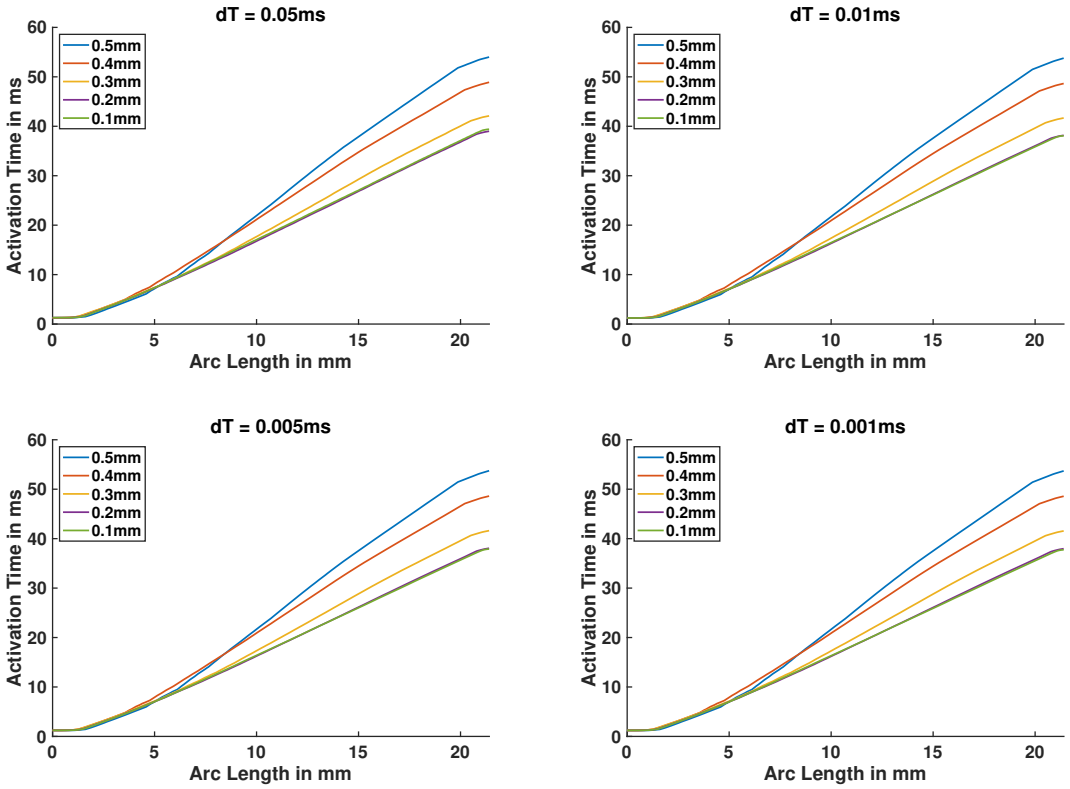

Figure 6.3: Activation times for the different spatial (denoted by color) and temporal (panels) discretizations on the diagonal line from P1 to P8.

Chapter 7

Mechanics

To investigate the influence of spatial discretization, the order of the used finite elements, and to verify the mechanics core module, simulations based on problem 3 as proposed by Land et al. [39] were run. Problem 3 was chosen, since it captures several aspects important to cardiac mechanics that apply to the whole heart as well. It includes a pressure boundary condition that depends on the deformed surface orientation and area as well as the inclusion of active stress. Furthermore, it utilizes the same transverse isotropic constitutive law as other simulations in this thesis and a complex fiber distribution throughout the myocardial wall.

7.1 Problem Definition

The domain Ω_0 of the undeformed geometry of an idealized left ventricle (LV) is defined using a parameterization for a truncated ellipsoid:

$$\mathbf{X} = \begin{pmatrix} x \\ y \\ z \end{pmatrix} = \begin{pmatrix} r_s \sin u \cos v \\ r_s \sin u \sin v \\ r_l \cos u \end{pmatrix}. \tag{7.1}$$

The endocardial surface Γ_0^{endo} is defined by $r_s = 7\,\text{mm}$, $r_l = 17\,\text{mm}$, $u \in [-\pi, -\arccos\frac{5}{17}]$, and $v \in [-\pi, \pi]$. The epicardial surface is defined by $r_s = 10\,\text{mm}$, $r_l = 20\,\text{mm}$, $u \in [-\pi, -\arccos\frac{5}{20}]$, and $v \in [-\pi, \pi]$. The base plane is used for the Dirichlet boundary condition Γ_0^{D} and is implicitly defined by the range of u at $z = 5\,\text{mm}$.

Fiber angles α are defined as -90° at the epicardial surface and $+90^\circ$ at the endocardial surface.

Using the governing equation for the deformation of a nearly-incompressible solid in steady-state equilibrium, find the displacement $\mathbf{d}\colon \Omega_0 \to \mathbb{R}^3$ such that

$$\begin{cases} \nabla \cdot (\mathbf{FS}) = \mathbf{0} & \text{in} \quad \Omega_0\,, \\ \mathbf{FSN} = -p_{\text{endo}} J \mathbf{F}^{-\mathsf{T}} \mathbf{N} & \text{on} \quad \Gamma_0^{\text{endo}}\,, \\ \mathbf{d} = \mathbf{0} & \text{on} \quad \Gamma_0^{\text{D}}\,, \\ \mathbf{S} = \mathbf{S}_{\text{p}} + T_{\text{a}} \mathbf{f}\mathbf{f}^{\mathsf{T}}\,, \end{cases} \tag{7.2}$$

with a constant pressure $p_{\text{endo}} = 15\,\text{kPa}$, the unit column vector in the fiber direction $\mathbf{f}$, the surface normal $\mathbf{N}$, and a constant active stress $T_{\text{a}} = 60\,\text{kPa}$. Passive stress is given by $\mathbf{S}_{\text{p}} = \frac{\partial W}{\partial \mathbf{E}}$ using the strain energy density

$$\begin{aligned} W(\mathbf{E}) &= \frac{\kappa}{2}(J-1)^2 + \frac{\mu}{2}(\exp(Q)-1)\,, \\ Q &= b_{\text{f}} E_{\text{ff}}^2 + b_{\text{t}}(E_{\text{ss}}^2 + E_{\text{nn}}^2 + E_{\text{sn}}^2 + E_{\text{ns}}^2) + b_{\text{fs}}(E_{\text{fs}}^2 + E_{\text{sf}}^2 + E_{\text{fn}}^2 + E_{\text{nf}}^2)\,, \end{aligned} \tag{7.3}$$

with $\mu = 2\,\text{kPa}$, $b_{\text{f}} = 8$, $b_{\text{t}} = 2$, $b_{\text{fs}} = 4$, and $\kappa = 1\,\text{MPa}$.

7.2 Results

Five different spatial discretizations (Figure 7.1) for the idealized LV were used and each was simulated with linear and quadratic tetrahedral elements, respectively. For each simulation, three important aspects of left ventricular function were evaluated:

1) apico-basal shortening in terms of the deformed apex position;
2) twist in terms of the deformation of an endocardial line;
3) cavity volume.

The results are shown in Figure 7.2. It becomes clear that quadratic tetrahedral elements suffer less from volumetric locking effects especially with fewer degrees of freedom (DoF). With the exception of discretization N1, all simulations with quadratic elements show the same behavior. Linear tetrahedral elements show larger deviations in twist close to the base and are less accurate for the calculation of the cavity volume. Based on these results, one can assume that two transmural elements are sufficient when using quadratic elements. For linear tetrahedrons, four transmural elements are sufficient to decrease the error in apex displacement to around 1% and in volume to around 10%.

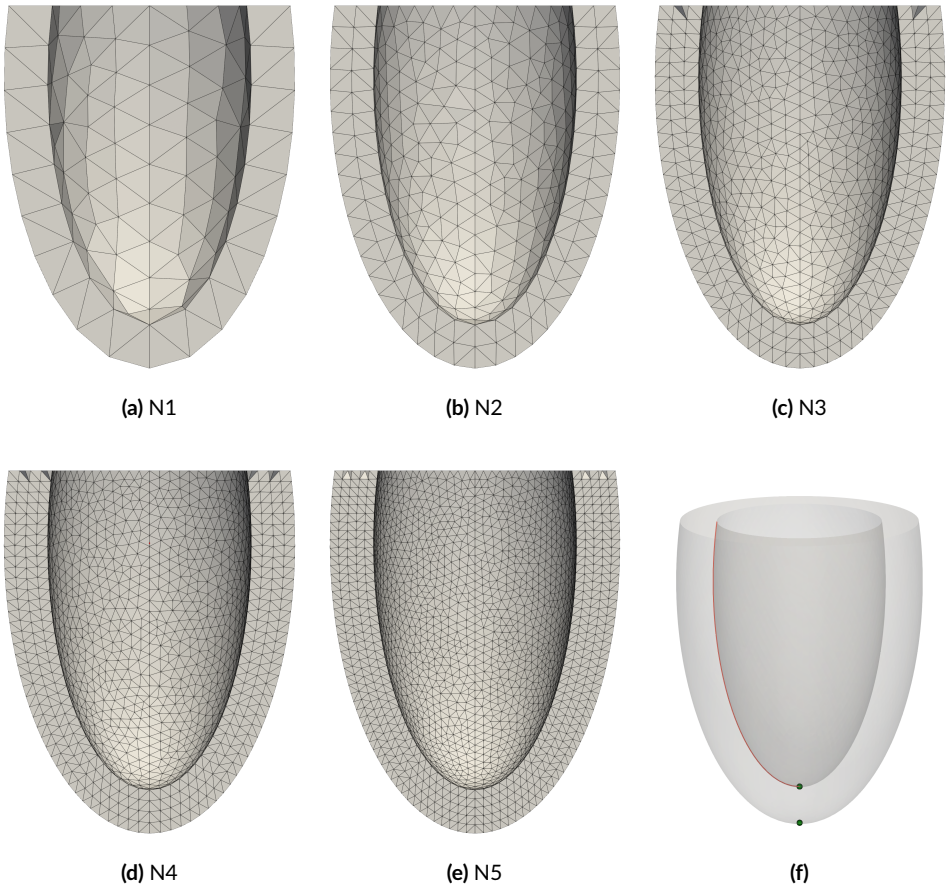

(a) N1 **(b)** N2 **(c)** N3

(d) N4 **(e)** N5 **(f)**

Figure 7.1: Discretizations used to solve problem three with degrees of freedom (DoF) for linear and quadratic elements: (a) N1, 1098/6450 DoF; (b) N2, 5343/35460 DoF; (c) N3, 15768/110643 DoF; (d) N4, 33819/245430 DoF; (e) N5, 63357/468834 DoF. (f) line and points that were used to evaluate the deformed configuration.

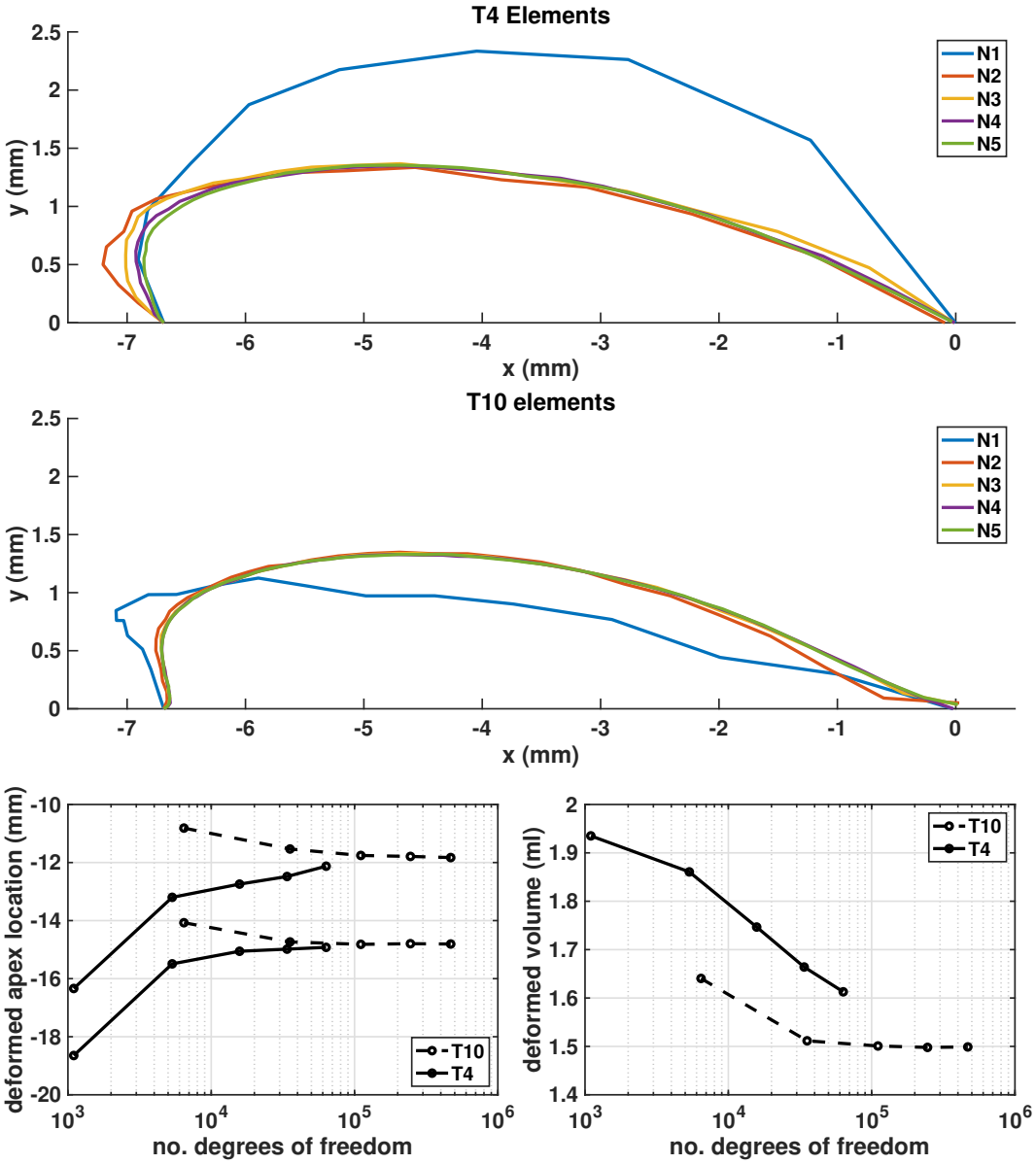

Figure 7.2: Top: deformation of a line that shows twist using linear elements. Middle: deformation of a line that shows twist using quadratic elements. Bottom left: endocardial and epicardial apex z-coordinate in the deformed configuration. Bottom right: cavity volume of the deformed configuration. T4: linear elements, T10: quadratic elements.

Chapter 8

Electromechanics

Similar to the electrophysiology and the mechanics problems described in the previous two chapters, a verification problem for the electromechanical problem is of interest. So far, there is no established benchmark problem that is suited for the verification of the electromechanically coupled system. Therefore, a new problem is provided that reuses implementations of familiar models for the ionic current and force generation.

8.1 Problem Definition

The geometry of the tissue model is defined by a cuboid $\Omega_0 \to \mathbb{R}^3$ with dimensions $20.0 \times 16.0 \times 12.0\,\mathrm{mm}^3$ and is shown in Figure 8.1. For a time $t \in (0,T]$ in the reference domain Ω_0, find the transmembrane voltage $V_\mathrm{m}\colon (0,T] \times \Omega_0 \to \mathbb{R}$, the vector of gating variables $\mathbf{w}\colon (0,T] \times \Omega_0 \to \mathbb{R}^{n_\mathbf{w}}$, the vector of ionic concentrations $\mathbf{q}\colon (0,T] \times \Omega_0 \to \mathbb{R}^{n_\mathbf{q}}$, the mechanical displacement $\mathbf{d}\colon (0,T] \times \Omega_0 \to \mathbb{R}^3$, and the state variables of the active stress model $\mathbf{s}\colon (0,T] \times \Omega_0 \to \mathbb{R}^{n_\mathbf{s}}$ such that

$$
\begin{cases}
\frac{\partial \mathbf{w}}{\partial t} - \mathbf{G}_\mathbf{w}(V_\mathrm{m}, \mathbf{w}, \mathbf{q}) = \mathbf{0} & \text{in} \quad \Omega_0\,, \\
\frac{\partial \mathbf{q}}{\partial t} - \mathbf{G}_\mathbf{q}(V_\mathrm{m}, \mathbf{w}, \mathbf{q}) = \mathbf{0} & \text{in} \quad \Omega_0\,, \\
\frac{\partial \mathbf{s}}{\partial t} - \mathbf{G}_\mathbf{s}(\mathbf{s}, [\mathrm{Ca}^{2+}]_\mathrm{i}, \lambda, \frac{\partial \lambda}{\partial t}) = \mathbf{0} & \text{in} \quad \Omega_0\,, \\
\beta \left[C_\mathrm{m} \frac{\partial V_\mathrm{m}}{\partial t} + I_\mathrm{ion}(V_\mathrm{m}, \mathbf{w}, \mathbf{q}) + I_\mathrm{app}(t) \right] = \nabla \cdot (J\mathbf{F}^{-1}\mathbf{D}\mathbf{F}^{-\mathsf{T}} \nabla V_\mathrm{m}) & \text{in} \quad \Omega_0\,, \\
(J\mathbf{F}^{-1}\mathbf{D}\mathbf{F}^{-\mathsf{T}} \nabla V_\mathrm{m}) \cdot \mathbf{N} = 0 & \text{on} \quad \partial\Omega_0\,, \\
\rho_0 \frac{\partial^2 \mathbf{d}}{\partial t^2} - \nabla \cdot (\mathbf{F}\mathbf{S})) = \mathbf{0} & \text{in} \quad \Omega_0\,, \\
\mathbf{S} = \mathbf{S}_\mathrm{p} + T_\mathrm{a}(\mathbf{s}, \mathbf{F}) \mathbf{f}\mathbf{f}^\mathsf{T}\,, & \\
V_\mathrm{m} = V_\mathrm{m}^0, \quad \mathbf{w} = \mathbf{w}^0, \quad \mathbf{q} = \mathbf{q}^0, \quad \mathbf{s} = \mathbf{s}^0, \quad \mathbf{d} = \mathbf{d}^0 & \text{in} \quad \Omega_0 \times 0\,.
\end{cases}
\tag{8.1}
$$

Electrophysiological properties are reused from Chapter 6, i.e. the ionic current I_ion, the gating variables $\mathbf{w}$, and the ionic concentrations $\mathbf{q}$ are defined by the ten-Tusscher-Panfilov (TTP) model with the initial conditions given in Table 6.2. The fibers $\mathbf{f}$, sheets $\mathbf{s}$, and

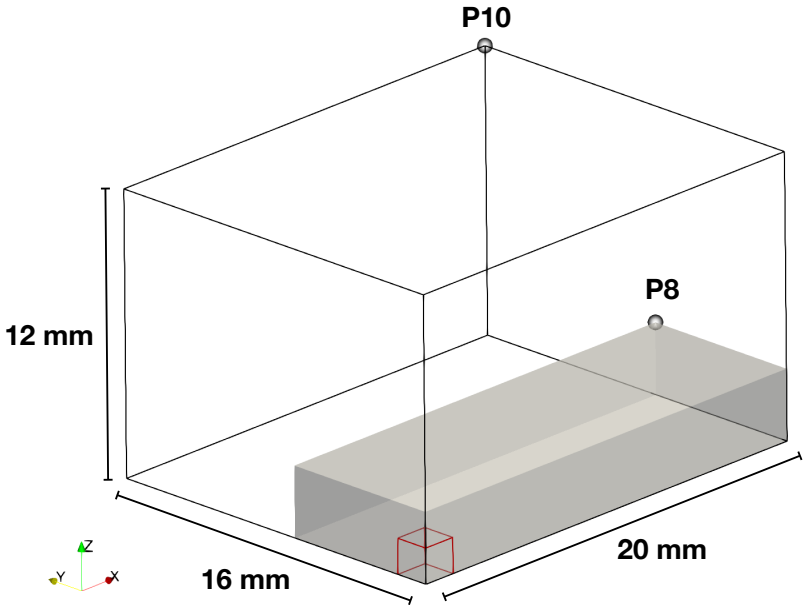

Figure 8.1: Simulation domain for the electromechanics problem. Shown are the dimensions and the evaluation points as well as the stimulus area (red box). The gray area shows the domain overlap with the electrophysiology benchmark presented in Chapter 6.

sheetnormals $\mathbf{n}$ coincide with the x-, y-, and z-axis of the reference frame, respectively. Values for β, C_m, σ_f, σ_s, σ_n, and the stimulus current I_app are given in Table 6.1.

Sarcomere dynamics are described by the model of human cardiac contraction (L17) by Land et al. [94]. Initial values for $\mathbf{s}^0$ are given in Table 8.1.

Table 8.1: Initial values $\mathbf{s}^0$ for the sarcomere model by L17.

Value	Unit	Description
0	-	force generating state S
0	-	pre-powerstroke state W
0	-	calcium bound to troponin CaTRPN
1	-	blocked state B
0	-	mean distortion of crossbridges in S state ζ_S
0	-	mean distortion of crossbridges in W state ζ_W
0	-	viscoelastic strain $\mathrm{C_d}$

At the time $t = 0\,\mathrm{s}$, the domain Ω_0 is assumed to be at rest, i.e. $\mathbf{d}^0 = \mathbf{0}$, $\mathbf{F} = \mathbb{1}$, $\lambda = (\mathbf{Ff})^\mathsf{T}(\mathbf{Ff}) = 1$, and $\frac{\partial \lambda}{\partial t} = 0\,\mathrm{s}^{-1}$. Passive stress is given by $\mathbf{S}_\mathrm{p} = 2\frac{\partial W}{\partial \mathbf{C}}$ using the strain energy density by Holzapfel-Ogden [107] as defined in Eq. (B.15) with $a = 330\,\mathrm{Pa}$, $a_{ff} = 18\,535\,\mathrm{Pa}$, $a_{ss} = 2564\,\mathrm{Pa}$, $a_{fs} = 417\,\mathrm{Pa}$, $b = 9.242$, $b_{ff} = 15.972$, $b_{ss} = 10.446$, $b_{fs} = 11.602$, and

$\kappa = 1\,\text{MPa}$. Furthermore, Eq. (8.1) is extended by zero normal displacement conditions $\mathbf{dN} = 0$ at the boundaries Ω_{stim} where the stimulus is applied.

8.2 Results

Solutions of the previously defined problem with different spatial resolutions are provided here. The domain Ω_0 by two meshes. One with a spatial resolution of h_1 for the electrophysiology model ($\mathcal{IAE}$), and one with a spatial resolution of h_2 for the mechanics model ($\mathcal{M}$). Three distinct setups were simulated with the fully coupled electromechanics model with MEF ($\mathcal{IAE}_{\text{MEF}}$-$\mathcal{M}$): A:$\{h_1, h_2\} = \{0.5, 0.5\}$ mm, B:$\{h_1, h_2\} = \{0.5, 1.0\}$ mm, C:$\{h_1, h_2\} = \{0.25, 1.0\}$ mm. Time increments for $\mathcal{M}$ was set to $\Delta t_{\mathcal{M}} = 0.001\,\text{s}$ and for $\mathcal{IAE}$ it was set to $\Delta t_{\mathcal{E}} = 0.000\,01\,\text{s}$. Additionally, simulation setup B is used to solve the fully coupled electromechanics model without MEF ($\mathcal{IAE}$-$\mathcal{M}$) and the $\mathcal{IAE}$ model to have a reference for the transmembrane voltage V_{m} with the already verified implementation of the monodomain equation. Since the geometry was chosen in such a way that the domain has an overlapping region with the electrophysiology benchmark in Chapter 6, point P8 is used to compare the action potential and evaluate the activation time. The transmembrane voltage V_{m} is shown in Figure 8.2. First, it can be seen that the solution with the $\mathcal{IAE}$-$\mathcal{M}$ model is identical with the monodomain reference solution. This is important, since it proofs that there is no implementation error in the numerical scheme of the coupling. The activation time at point P8 was 58.1 ms for the monodomain reference solution. Remember that the activation time of point P8 in the smaller domain of the electrophysiology benchmark at the same 0.5 mm resolution was 53.698 ms. This difference can only be explained by the increased domain, since all other settings were the same. Furthermore, there is only a minimal change in activation time ($\Delta\text{AT} = 0.1\,\text{ms}$) when MEF is considered and a reduction in the spatial resolution of the mechanics problem yielded almost identical results. Only when the spatial resolution of the electrophysiological domain was reduced, it was possible to observe a notable difference in the activation time at P8 ($\Delta\text{AT} = 15.8\,\text{ms}$). This result was expected, since it reflects the same behavior which was present in Chapter 6.

The displacement at point P10 is shown in Figure 8.3. Recall, that these results are affected by both, the convergence of the mechanics and the electrophysiology models. Due to the change in conduction velocity at lower spatial resolutions of the electrophysiology problem, active contraction is triggered earlier and peak displacement is reached earlier as well. Besides from this temporal shift due to the spatial error in the electrophysiology, the maximum values and the contraction pattern remain similar for all other simulations.

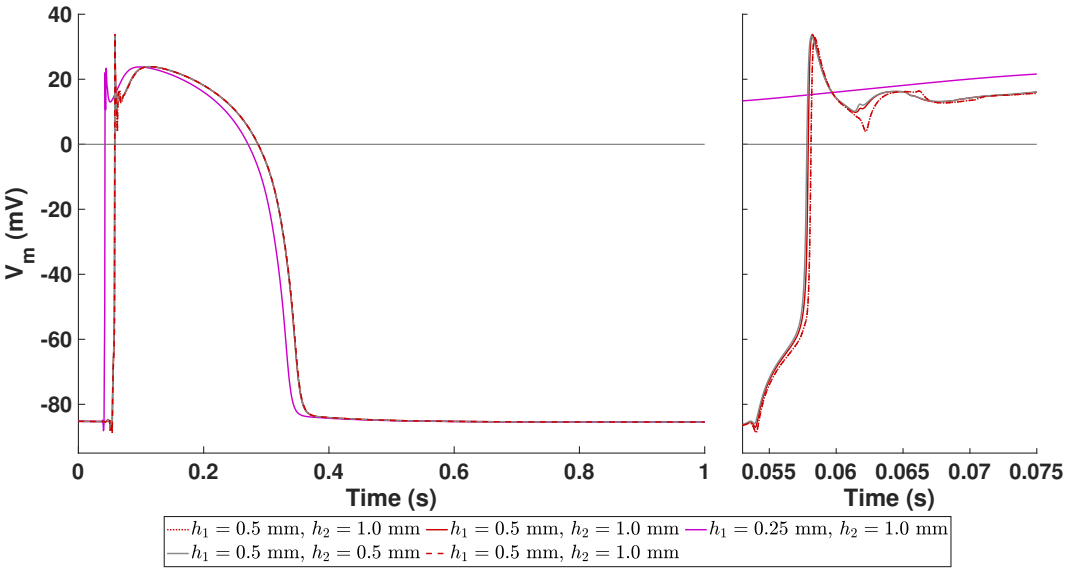

Figure 8.2: Transmembrane voltage V_m at point P8 as shown in Figure 8.1. Line color denotes the resolution that was used. Dotted lines depict simulations with the fully coupled electromechanics model without MEF ($\mathcal{IAE}$-$\mathcal{M}$). Dashed lines indicate a simulation with the $\mathcal{IAE}$. Solid lines used the fully coupled electromechanics model with MEF ($\mathcal{IAE}_\mathrm{MEF}$-$\mathcal{M}$). The panel on the right zooms into the upstroke of the action potential.

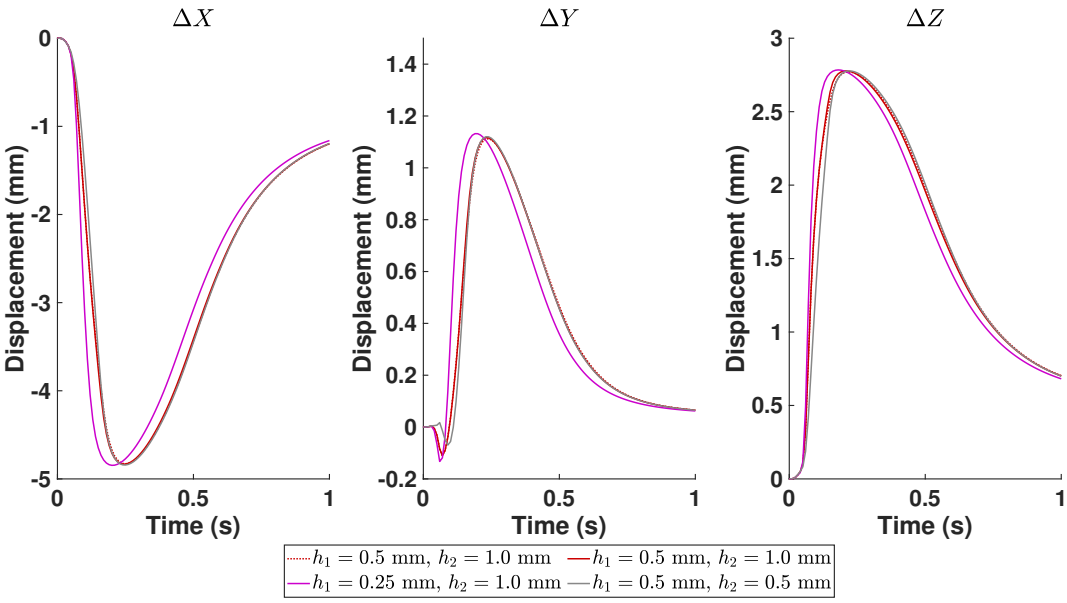

Figure 8.3: Displacement of point P10 in x-, y-, and z-coordinates. Line color denotes simulations with different spatial resolutions. Dotted lines depict simulations with the fully coupled electromechanics model without MEF ($\mathcal{IAE}$-$\mathcal{M}$). Solid lines used the fully coupled electromechanics model with MEF ($\mathcal{IAE}_\mathrm{MEF}$-$\mathcal{M}$).

PART IV

ANALYSIS OF LEFT VENTRICULAR MECHANICS

Chapter 9

Orthotropic Active Contraction in the Ventricles

Some passages (including the motivation, results, and discussion) of this chapter have been quoted verbatim from the publication [40].

Modern magnetic resonance imaging (MRI) methods have become a widespread clinical tool to diagnose function as well as malfunction of cardiac mechanics especially in the left ventricle (LV). It makes the non-invasive assessment of in-vivo ventricular wall motion possible and opens a window for an interpretation of the data with regards to the development of local wall stress. Additionally, MRI simultaneously serves as the main data foundation and validation tool for in-silico studies.

To simulate the aforementioned local wall stresses with finite element (FE) techniques, there exists a wide variety of cellular tension development models based on measured human or animal tissue preparations that can be divided into two main groups: biophysical models based on physiological first principles or phenomenological models. The latter have shown to be able to reproduce the deformation patterns observed in MRI data. However, most of the time this is only possible whilst neglecting physiological properties such as the dependence of active stress on fiber stretch or the range of fiber stretch the model produces during ventricular systole. Biophysical models on the other hand, do not produce the amount of stress necessary to accomplish deformation patterns similar to those observed in MRI data due to the lower force generation during contraction.

As a potential approach to overcome these problems, we implemented an active stress tensor including components in the sheet and normal direction with added shear stress similar to [159, 199] in our existing FE framework. This is based on experimental data that show a simultaneous development of fiber, cross-fiber and shear stresses in a barium contracted rabbit myocardium by Lin & Yin [200]. They showed that the stress in cross-fiber or normal direction $\mathbf{S}(\mathbf{n}_0, \mathbf{n}_0)$ lies between 20 and 62% of the stress in fiber direction $\mathbf{S}(\mathbf{f}_0, \mathbf{f}_0)$. To assess how this new form of an active stress tensor changes the deformation patterns of the LV, we ran a sensitivity study including four parameters and observed how they changed major biomarkers during contraction: wall thickness, longitudinal shortening, torsion, and

ejection fraction. Finally, we compared our results to clinically reported values of healthy subjects.

9.1 Materials and Methods

9.1.1 Idealized Left Ventricular Geometry

A truncated ellipsoid obtained from a cardiac mechanics benchmark [39] was used to represent an idealized LV. The mesh was scaled by a factor of 3.75 to obtain a more realistic end-diastolic volume (EDV) of 133.55 ml (Fig. 9.1). Furthermore, the ellipsoid was closed at the base to represent the mitral valve and a mesh that represents the surrounding tissue was added around the epicardium. For the spatial discretization, a total number of ≈8k quadratic tetrahedra with ≈13.5k nodes was used. Fiber $\mathbf{f}_0$, sheet $\mathbf{s}_0$, and (sheet-)normal $\mathbf{n}_0$ directions were calculated on a high-resolution LV geometry using the Laplace-Dirichlet-Rule-Based-Method (LDRBM) presented in [141] ($\alpha_{epi} = -70°$, $\alpha_{endo} = 80°$, $\beta_{epi} = \beta_{endo} = 0°$) and interpolated onto the 5 Gaussian quadrature points of each element of the tetrahedral mesh used in this study.

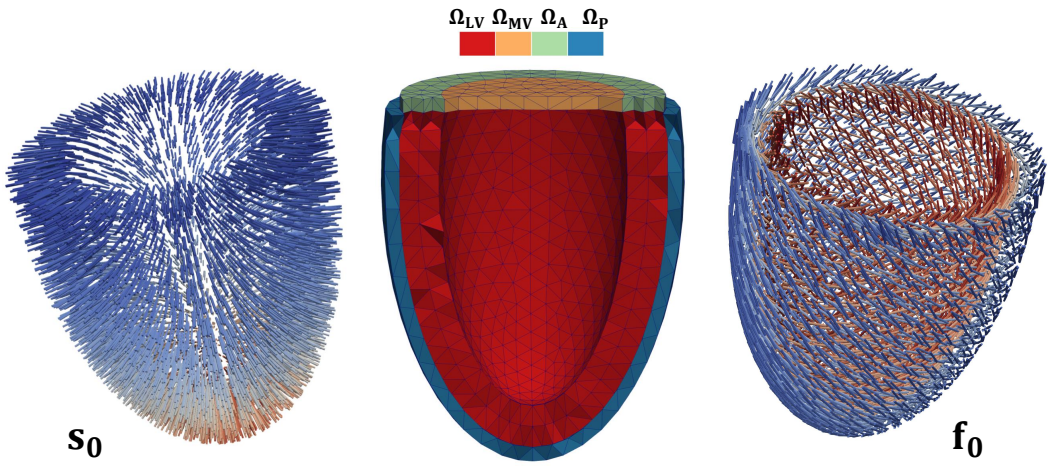

Figure 9.1: Idealized left ventricular geometry with fiber ($\mathbf{f}_0$) and sheet ($\mathbf{s}_0$) directions. The LV is discretized with ten-node tetrahedrons and the computational domain $\Omega_0 = \Omega_{\text{LV}} \subset \Omega_{\text{MV}} \subset \Omega_{\text{A}} \subset \Omega_{\text{P}}$ is separated into LV, mitral valve (MV), mitral valve annulus (A), and surrounding tissue (P).

9.1.2 Modeling Ventricular Biomechanics

The mechanics of the LV were modeled by means of the linear momentum equation as described in Chapter 3 by solving the system of equations given by problem $\mathcal{MC}$. Ventricular myocardium was assumed to be hyperelastic, transversely isotropic and nearly incompressible as described by the constitutive model of Guccione et al. [201] with $\mu = 528\,\text{Pa}$, $b_f = 8.5$, $b_t = 3.4$ and $b_{fs} = 5.95$. Quasi incompressibility was enforced by adding a penalty term:

$$\Psi_{\text{Vol}} = \frac{\kappa}{2}(\det \mathbf{F} - 1)^2\,, \tag{9.1}$$

with κ = 1 MPa to the constitutive equation. This value keeps the volumetric changes of the tissue below 10%. Time integration was performed using the Generalized-α scheme outlined in Chapter 5.3.2 with $\beta = 0.3$, $\gamma = 0.6$, and $\alpha_f = \alpha_m = 0$. An active stress formulation was used ($\mathbf{S} = \mathbf{S}_\text{p} + \mathbf{S}_\text{a}$) with the following orthotropic active stress tensor:

$$\mathbf{S}_\text{a} = T_\text{a}(K_\text{ff}\frac{\mathbf{f}_0 \otimes \mathbf{f}_0}{\lambda_\text{f}^2} + K_\text{ss}\frac{\mathbf{s}_0 \otimes \mathbf{s}_0}{\lambda_\text{s}^2} + K_\text{nn}\frac{\mathbf{n}_0 \otimes \mathbf{n}_0}{\lambda_\text{n}^2} + K_\text{ns}\frac{\mathbf{n}_0 \otimes \mathbf{s}_0}{\lambda_\text{ns}^2} + K_\text{sn}\frac{\mathbf{s}_0 \otimes \mathbf{n}_0}{\lambda_\text{sn}^2})\,, \tag{9.2}$$

where T_a is the cellular active tension, and $K_\text{ff}, K_\text{ss}, K_\text{sn}, K_\text{ns}$ as well as K_nn are orthotropic activation parameters. The stretches are given by $\lambda_{ij} = \sqrt{\mathbf{i}_0 \cdot \mathbf{C}\mathbf{j}_0}$ for $i, j \in \{f, s, n\}$. Active tension development on a cellular level was determined using the model described by Land et al. [94]. This model incorporates a dependence on fiber stretch ratio λ_f and is driven by an experimentally measured calcium transient [178].

As boundary conditions, the frictionless and permanent contact handling problem from Fritz et al. [20] as described in Chapter 5.3 was solved between the epicardial surface of the LV and the inner surface of an additional ellipsoid mesh. On the outer surface of this surrounding ellipsoid, Dirichlet boundary conditions were applied.

The pressure within the LV was determined by a simplified closed-loop lumped parameter model of the circulatory system of the same form as Eq. (3.15), with the state variables $\mathbf{c}\colon (0,T] \to \mathbb{R}^3$ that are associated with the chamber and vessel volumes

$$\mathbf{c} = (V_\text{LV}, V_\text{Art}, V_\text{Ven})^\mathsf{T}\,, \tag{9.3}$$

and the vector $\mathbf{p}\colon (0,T] \to \mathbb{R}^3$ collects the pressure values in all compartments of the system

$$\mathbf{p} = (p_\text{LV}, p_\text{Art}, p_\text{Ven})^\mathsf{T}\,. \tag{9.4}$$

The system of ordinary differential equations (ODEs) is given by

$$\frac{\mathrm{d}V_\text{LV}}{\mathrm{d}t} = Q_\text{Ven} - Q_\text{Art}, \quad \frac{\mathrm{d}V_\text{Art}}{\mathrm{d}t} = Q_\text{Art} - Q_\text{Per}, \quad \frac{\mathrm{d}V_\text{Ven}}{\mathrm{d}t} = Q_\text{Per} - Q_\text{Ven}\,, \tag{9.5}$$

with the blood flow

$$\begin{cases} Q_\text{Art} = \max\left\{\frac{p_\text{LV} - p_\text{CArt}}{R_\text{AV} + R_\text{Art}}, 0\right\} \\ Q_\text{Ven} = \max\left\{\frac{p_\text{Ven} - p_\text{LV}}{R_\text{Ven}}, 0\right\}, \end{cases} \quad Q_\text{Per} = \frac{p_\text{CArt} - p_\text{Ven}}{R_\text{Per}}\,, \tag{9.6}$$

and the pressure

$$p_{\mathrm{CArt}} = \frac{V_{\mathrm{Art}}}{C_{\mathrm{Art}}}, \quad p_{\mathrm{Art}} = p_{\mathrm{LV}} - Q_{\mathrm{Art}} R_{\mathrm{AV}}, \quad p_{\mathrm{Ven}} = \frac{V_{\mathrm{Ven}}}{C_{\mathrm{Ven}}}, \tag{9.7}$$

in the system. Coupling between the circulatory system and the finite element mechanics model is still realized via the volume consistency constraint for the LV (Eq. (3.24)) as described in Chapter 3.4.

A pre-stressed end-diastolic state was achieved by first finding the pressure free state using the method described by Algorithm 5.1 and inflating the LV by applying a pressure of 7.5 mmHg to the endocardial surface.

9.1.3 Mechanical Biomarkers

There are typically four distinct features that can be observed during ventricular contraction: wall thickening (WT), longitudinal shortening (LS), torsion (Θ) and ejection fraction (EF). WT is the relative displacement between points on the endocardium and epicardium at the same position relative to the heart's long axis

$$\mathrm{WT} = 100 \frac{T - T_0}{T_0}, \tag{9.8}$$

where T and T_0 are the mean wall thicknesses during end-systole (ES) and end-diastole (ED) calculated using the Eulerian PDE approach introduced in [202]. Longitudinal shortening (LS) is calculated as the fractional change in distance between the endocardial base and apex from ED (L_0) to ES (L)

$$\mathrm{LS} = 100 \frac{L_0 - L}{L_0}. \tag{9.9}$$

Torsion Θ is approximated as the net difference between apical and basal rotation from two short axis slices during ES using

$$\cos(\Theta) = \frac{\mathbf{r}_{\mathrm{Base}} \cdot \mathbf{r}_{\mathrm{Apex}}}{\|\mathbf{r}_{\mathrm{Base}}\| \cdot \|\mathbf{r}_{\mathrm{Apex}}\|}, \tag{9.10}$$

where $\mathbf{r}_{\mathrm{Base}}$ and $\mathbf{r}_{\mathrm{Apex}}$ are points on the basal and apical epicardium respectively. Lastly, ejection fraction (EF) was evaluated in this study using the EDV and the end-systolic volume (ESV) from the lumped parameter model of the circulatory system:

$$\mathrm{EF} = 100 \frac{\mathrm{EDV} - \mathrm{ESV}}{\mathrm{EDV}}. \tag{9.11}$$

Physiological ranges of these four mechanical biomarkers are shown in Table 9.1.

9.1.4 Sensitivity Analysis

To investigate how sensitive the mechanical biomarkers are to changes in the parameters of an orthotropic stress tensor in the form of Eq. (9.2), the parameters T_{ref}, K_{ss}, K_{sn}, K_{ns} and K_{nn}

Table 9.1: Reference values observed in healthy subjects.

Mechanical biomarker	Values	Unit	Ref
WT	18 – 100	%	[203]
LS	13 – 21	%	[204]
Θ	13 – 27	deg	[184]
EF	48 – 69	%	[205]

were varied using a one-at-a-time (OAAT) approach. Here, T_{ref} refers to the maximal active tension at resting length in the Land et al. tension model with a default value of 120 kPa. The baseline values for the other parameters were set to $K_{\text{ss}} = K_{\text{sn}} = K_{\text{nn}} = 0$ and $K_{\text{ff}} = 1$ with $K_{\text{sn}} = K_{\text{ns}}$ at all times. For the OAAT, ten values per parameter were determined by the lower and upper bounds A and B of the parameter ranges summarized in Table 9.2 through

$$x_{i,j} = A_i + (j-1)\frac{B_i - A_i}{n_{\text{val}} - 1}, \quad i = 1,2,3,4 \tag{9.12}$$

where $j = 1,2,3,\ldots,n_{\text{val}}$ will be referred to as case number with $n_{\text{val}} = 10$.

Table 9.2: Parameter ranges for the sensitivity study.

Parameter	Range of values	Unit	Ref.
T_{ref}	80 – 440	kPa	[94]
K_{ss}	0.0 – 0.6	-	[199, 200]
K_{sn}	0.0 – 0.07	-	[199]
K_{nn}	0.0 – 0.6	-	[199, 200]

9.2 Results

The biomarker sensitivity study using the OAAT approach is shown in Fig. 9.2. The PV-loop and deformation pattern during ED and ES for a reference simulation with $T_{\text{ref}} = 120$ kPa and $K_{\text{ss}} = K_{\text{sn}} = K_{\text{nn}} = 0$ is shown in Fig. 9.3. Almost all cases show either monotonically increasing or decreasing, non-linear behavior. Increasing stress in the sheet direction (K_{ss}) reduces all the mechanical biomarker values by up to 50% of the initial values. The results show that physiological ranges of EF can only be reached with either high values of active tension (T_{ref}) or additional tension in the normal direction (K_{nn}). However, the resulting EF is still at the low end of clinical reference values and increased active stress in the normal direction leads to values of LS outside the healthy range. Using higher active tension keeps LS constant above a certain threshold (case number > 3) and starts to decrease again for values of T_{ref} above 400 kPa. Although shear stress (K_{sn}) in the tissue does not affect EF, LS, and WT at all, the torsion Θ decreases by up to 3°. An even stronger reduction of torsion can be observed through additional stress in the sheet and normal directions.

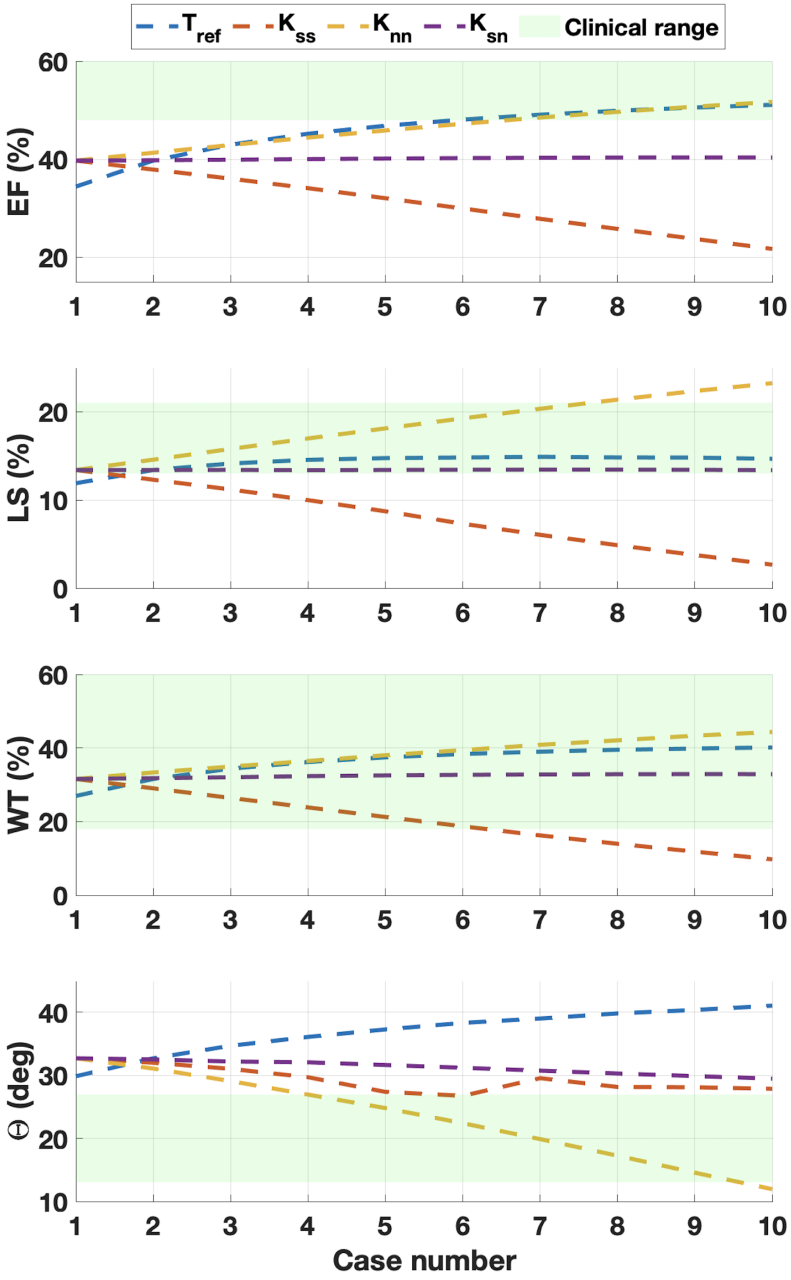

Figure 9.2: Change of EF, LS, WT, and Θ depending on the parameters T_{ref}, K_{ss}, K_{sn} and K_{nn}. From [40], licence CC-BY 4.0.

9.2.1 Whole Heart Simulation

So far, the effect of an orthotropic stress tensor was only evaluated on an idealized LV. To identify how it will affect the biomarkers of a LV in a whole heart scenario, a setup in the ideal range identified in the previous study, i.e. $0.25 \leq K_{\text{nn}} \leq 0.45$, was tested. For the

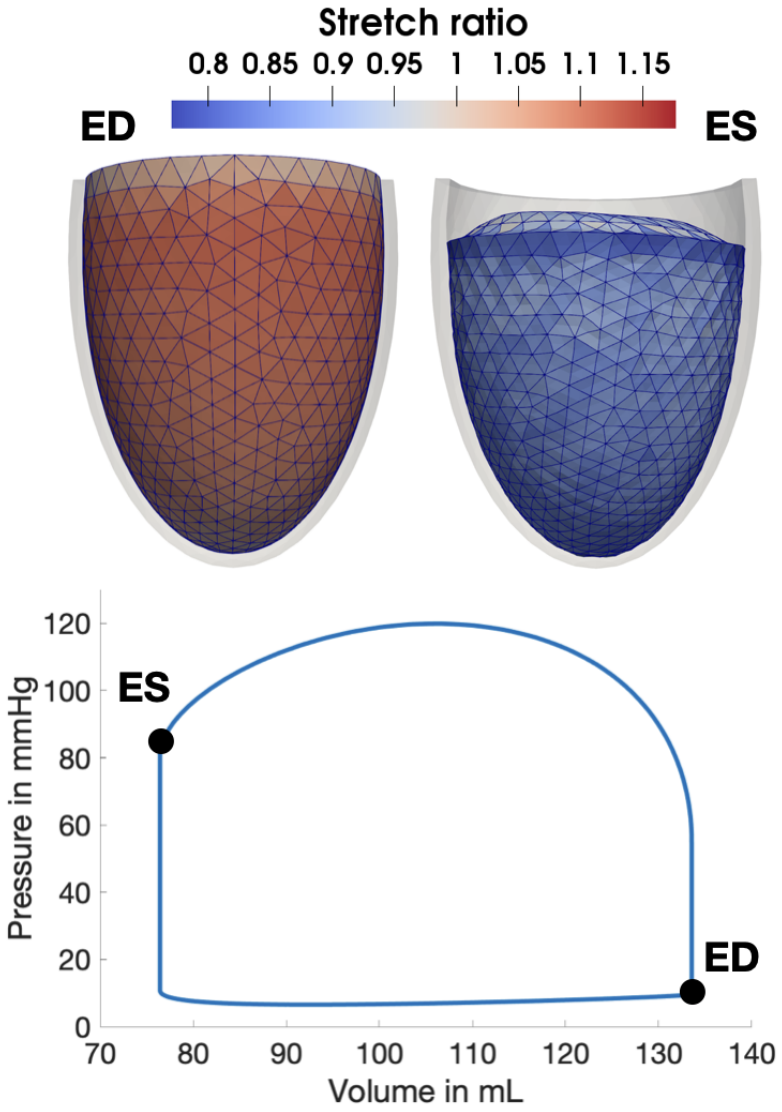

Figure 9.3: Reference Case. At the top, the deformation of the LV during ED and ES with stretch distribution is shown. The PV-loop is shown at the bottom. From [40], licence CC-BY 4.0.

simulations, the Control setup described in Chapter 11.1 was used. The scenarios in Table 9.3 were tested and the biomarkers were evaluated as previously described.

The PV-loop, mean WT, LS, and torsion of the LV for the different whole heart simulation setups are shown in Fig. 9.4. Independent of the simulation setup, it can be observed that during atrial contraction (< 200 ms) the wall thickness decreases due to blood being actively pumped into the LV and the LV gets elongated due to the movement of the atrioventricular plane towards the base of the heart. Additionally, this results in a brief untwisting of the LV. During ventricular contraction, blood gets ejected due to an increasing wall thickness, shortening, and twisting of the ventricle. In the f/n and f-/n setup (Table 9.3), the added wall

Table 9.3: Parameter setup and calculated biomarkers for the whole heart simulations.

				Biomarker			
Setup	K_{ff}	K_{ss}	K_{nn}	EF	WT	LS	Θ
Control	1.0	0.0	0.0	59%	49%	15%	17%
f/n	1.0	0.0	0.3	58%	48%	16%	9%
f-/n	0.7	0.0	0.3	54%	44%	16%	5%
f+	1.3	0.0	0.0	61%	52%	15%	17%

stress in the normal direction to the sheets increases EDV and reduces EF, WT, and torsion of the LV.

In all of the simulations, EF, WT, and LS lie within the reference values observed in healthy individuals (Table 9.1). However, from the evaluated biomarkers in Table 9.3, it becomes clear that EF and WT reduces in the f/n and f-/n cases while LS is basically unchanged compared to the Control case. Furthermore, a significant reduction in the torsion of the LV was observed in cases with added stress in the normal direction.

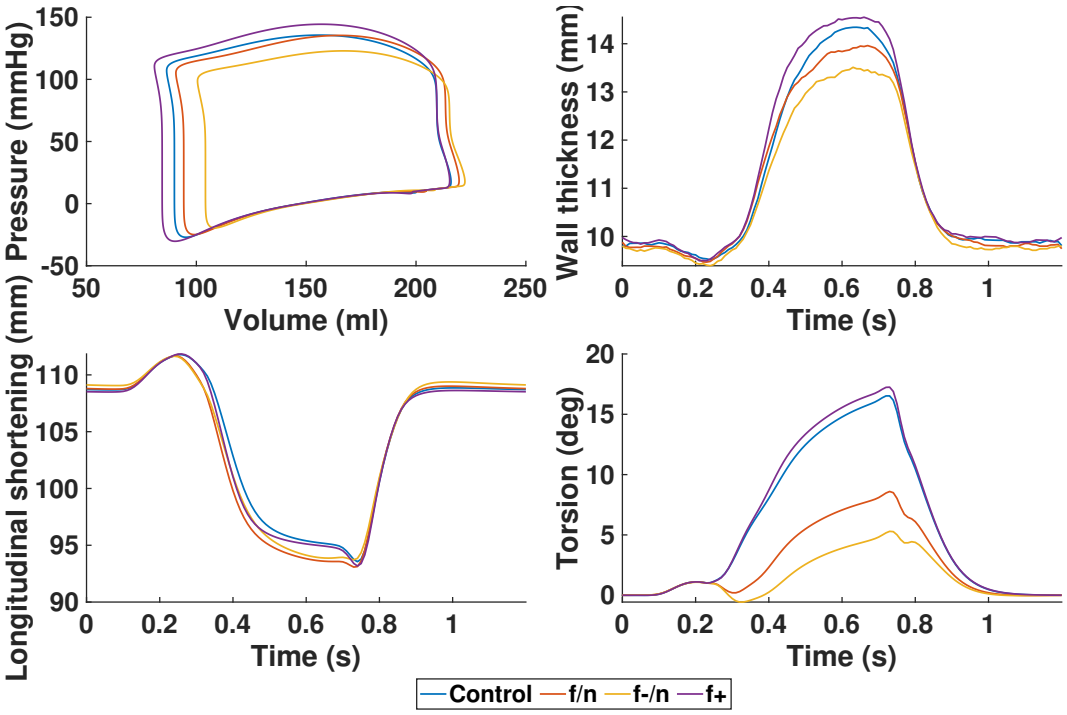

Figure 9.4: Pressure-volume loop, mean wall thickness, longitudinal shortening, and torsion of the LV for the different whole heart simulation setups given in Table 9.3.

9.3 Discussion

In this study, we presented a sensitivity analysis on the effect of using an orthotropic stress tensor on four major mechanical biomarkers characterizing LV systole. Using an idealized LV, we found that varying the considered parameters either led to a monotonic increase or decrease of the evaluated mechanical biomarkers EF, LS, WT, and Θ. The change in Θ due to an increase in K_{ss} is an exception to this. However, we observed a $\pm 5^{\circ}$ increase in standard deviation due to measurement errors and asymmetries in contraction in cases 7 to 10 which can explain this behavior.

The scaling parameter of the active tension model T_{ref} was positively correlated with EF, WT, LS, and Θ. However, reaching healthy values of EF above 50% was only possible by choosing T_{ref} larger than 320 kPa. These are unusually high values compared to typical values used in other modeling studies ($T_{\mathrm{ref}} < 180$ kPa). The other option which led to a healthy EF, was to add stress in the normal direction with up to 60% of T_{a}. Additionally, this increased LS above clinically reported values and constrained the twisting motion of the LV. Adding stress in the sheet direction using the parameter K_{ss} reduced all four mechanical biomarkers by up to 50% of their initial values. The additional contraction in the sheet direction constrains the displacement of the LV by counteracting WT. The imposed nearly incompressible material behavior forces the tissue to expand in the fiber and normal direction, hence the lower LS. Shear stress is found to be negligible with no effect on EF, LS and WT. However, we observed a 3° reduction in torsion of the LV. This is not necessarily an undesirable outcome, since torsion in general is above the clinically observed range in our reference configuration. Based on these results, we found that a stress tensor with a component in the normal direction can help in achieving a more physiological deformation pattern in the idealized LV. In particular, choosing $0.25 \leq K_{\mathrm{nn}} \leq 0.45$ helped to keep the observed biomarkers in the range of clinical observations.

Additionally, we performed four simulations to investigate the influence of an orthotropic stress tensor in a whole heart model. The results confirm that additional stress in the sheetnormal direction reduces torsion by 8%, resulting in pathological behavior, since the torsion of the whole heart model in the Control case is already at the lower end of literature values [184]. Furthermore, setup f/n effectively increases the total amount of tension in the LV. Therefore, setup f-/n was used to evaluate what happens in the case of added sheetnormal stress but with equal net tension in the LV. Unsurprisingly, it results in an even less effective systolic phase of the LV with a 5% reduction in EF and in WT, and a reduction of torsion by 12%. The decreased WT is compensated slightly by a larger LS. Overall, this indicates that reduced torsion and WT are the main drivers of the reduction in EF. Although, a reduction in torsion was already indicated by the simulations with the idealized ventricle, a reduction in WT was not. In fact, in the simulations using the idealized ventricle, WT increased notably. The reason for this is most likely to be found in the fiber orientation, since the whole heart model was set up with sheet angles $\beta \neq 0$. Hence, the sheetnormal direction is oriented slightly into the wall and not parallel to it, distributing the force vector proportionally into

the radial and longitudinal directions, which in turn promotes a decrease in WT. For $\beta = 0$, the force vector only points into longitudinal direction, promoting longitudinal shortening and an increase in WT.

To be able to make a fair comparison between the f/n case and the Control case, a fourth scenario was added denoted as f+. In the f+ setup, K_{ff} was increased to 1.3 to balance the total amount of tension in the heart. Interestingly, this setup results in a 2% increase in EF and a 3% increase in WT without the loss of physiological function w. r. t. LS and torsion.

In conclusion, a dispersion of fiber stress into the sheetnormal plane can help to promote a physiological contraction of the LV, while a dispersion of fiber stress into the sheet plane will result in unphysiological contraction patterns for EF, WT, LS, and torsion. However, orthotropic stress should be used with caution when simulating with whole heart models due to contradicting results compared to an idealized LV and the dependence on fiber orientation should be further investigated.

Chapter 10

Analysis of Left Ventricular Rotation in Heart Failure Patients

This chapter outlines a study that has been published in the journal Frontiers in Physiology [41]. Most passages (including the motivation, results, and discussion) of this chapter have been quoted verbatim from the publication.

In the healthy human heart, left ventricular (LV) ejection and filling is supported by the twisting and untwisting of the ventricle during systole and diastole, respectively. This twisting or wringing motion is determined by several anatomical and physiological features such as age, contractility, structure of the myocardium, and muscle fiber orientation [206]. Furthermore, the electrical activation pattern of the LV is heterogeneous due to the His-Purkinje system and the anisotropic conduction of the electrical potential [207]. Consequently, the activation pattern of the LV follows an endocardial to epicardial direction. Combined with the counter-directional helical arrangement of the endo- and epicardial muscle fibers, this results in a clockwise and counterclockwise rotation of the basal and apical segments, respectively.

In pathological cases, this wringing motion of the LV can be disrupted by dyssynchronous mechancial activation resulting in a reduced LV ejection fraction (EF) [208]. Dyssynchrony may originate from different sources such as an abnormal electrical activation in patients with left bundle branch block (LBBB) or post-ischemic remodeling and geometric alterations in heart failure patients [209, 210]. Multiple studies confirmed changes in LV rotational behavior in heart failure patients using MRI tagging and speckle tracking echocardiography [211–214]. Setser et al.[215] specifically observed rigid-body type (RBT) rotation in patients with end-stage heart failure, meaning apical and basal segments were rotating in the same direction. Cardiac resynchronization therapy (CRT) with an implanted device is often used in patients showing ventricular dyssynchrony in an attempt to restore LV EF. However, around 40% of patients do not respond to this kind of intervention. One reason might be a bad choice for the pacing site [216]. Therefore, it is important to optimize CRT parameters for each patient and LV rotation has become increasingly important for this purpose [217].

Jadczyk et al. [218] investigated electromechanical coupling and scar tissue burden with respect to rotational patterns observed in patients showing heart failure with reduced

ejection fraction (HFrEF) and LBBB. In their cohort of 30 patients, they found six cases showing normal wringing rotation and 24 cases showing RBT rotation. They concluded that remodeling changes the physiological gradient in electromechanical activation, which causes regional delays in mechanical activation and thus dyssynchronous contraction of the LV. In contrast, following a physiological propagation of electrical and mechanical activation, an intact electromechanical coupling (with constant electromechanical delay) will result in a wringing motion. However, due to the small number of study participants the results by Jadczyk et al. [218] should be considered with caution. To elucidate the role of the different contributing mechanisms suggested in [218], we performed an in silico study under controlled conditions informed by their in vivo electromechanical mapping data. Specifically, we hypothesized that the altered electrical activation pattern is sufficient to change wringing rotation to RBT. Spatiotemporal electromechanical parameters including local activation time (LAT), local rotational electromechanical delay (LEMD), and total rotational electromechanical delay (TEMD) were combined with local scar burden derived from late gadolinium enhanced magnetic resonance imaging (LGE-MRI) and incorporated into the left ventricle (LV) model. LV rotational patterns are analyzed and classified into two groups defined as normal wringing rotation and RBT. Finally, the classification based on the simulation results is compared to the clinical classification.

10.1 Materials and methods

10.1.1 Anatomical Finite Element Model

As a representation of the LV, a truncated ellipsoid with varying wall thickness was used. The wall thickness changes from 7 mm at the base to 3.5 mm at the apex. With a sphericity index of 1.58, the ellipsoid has a similar shape as the left ventricles of the patient cohort in [218]. The meshes were created in Gmsh [139] using a fully parameterized workflow and quadratic tetrahedral elements. A rule-based method based on [141] was used to generate the local fiber and sheet architecture $\mathbf{Q} = \{\mathbf{f}_0, \mathbf{s}_0, \mathbf{n}_0\}$ of the myocardium with fiber angles of 60° at the endocardium and -60° at the epicardium (Fig. 10.1). Furthermore, ventricular coordinates were computed according to Schuler et al. [153] and used to separate the ventricle into the 17 segments classified by the American Heart Association (AHA; [154]). The 9 segments used by the NOGA XP system (Biosense Webster, Irvine, CA, USA) were defined equally. The NOGA XP segmentation consists of four basal segments (basoseptal, basolateral, posterobasal, anterobasal), four mid-ventricular segments (midseptal, midlateral, midposterior, midanterior), and one apical segment.

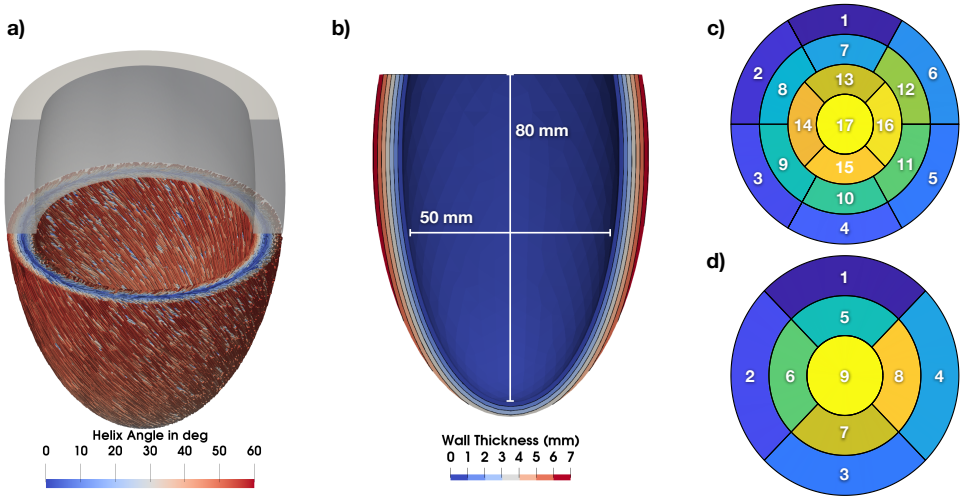

Figure 10.1: a) Myocyte orientation in the LV colorized with the corresponding helix angle. b) Long axis cut through the LV with contours showing the wall thickness. Additionally, lengths for the calculation of the sphericity index are shown. c) 17 AHA segments. d) 9 NOGA XP segments. From [41], licence CC-BY 4.0.

10.1.2 Electromechanical Computational Model

The kinematics of the LV are determined by solving the governing equation for the balance of linear momentum as described in Chapter 3. The second Piola-Kirchhoff stress tensor $\mathbf{S} = \mathbf{S}(\mathbf{d}, T_\mathrm{a})$ incorporates both, the passive and active mechanics of the myocardium using the relationship in Equation (3.12). Passive stress in cardiac tissue is modeled using the hyperelastic strain-energy function proposed by Usyk et al. [106]. Active stress due to the contraction of the cardiac muscle acts along the myocyte orientation $\mathbf{f}_0$ with the scalar value of the contractile force $T_\mathrm{a} = T_\mathrm{a}(t, \lambda_\mathrm{f})$. The phenomenological model by Niederer et al. [84] is used to describe the temporal development of force generation:

$$\begin{cases} T_\mathrm{a}(t,\lambda_\mathrm{f}) = T_\mathrm{peak}\,\phi(\lambda)\tanh^2(\frac{t_\mathrm{s}}{\tau_c})\tanh^2(\frac{t_\mathrm{dur}-t_\mathrm{s}}{\tau_r}) & \text{for} \quad 0 < t_\mathrm{s} < t_\mathrm{dur}\,, \\ \phi(\lambda_\mathrm{f}) = \max\{\tanh(\mathrm{ld}(\lambda_\mathrm{f}-\lambda_0)), 0\}\,, \\ \tau_c = \tau_{c0} + \mathrm{ld}_\mathrm{up}(1-\phi(\lambda_\mathrm{f}))\,, \\ t_\mathrm{s} = t - t_\mathrm{a} - t_\mathrm{emd}\,, \end{cases} \tag{10.1}$$

where λ_f is the fiber stretch, and t_a is the time of mechanical activation determined from electroanatomical mapping as detailed in Section 10.1.3. All parameters for the passive and active mechanics are given in Table 10.1.

The boundary condition $\mathbf{F}\mathbf{S}(\mathbf{d}, T_\mathrm{a}(\mathbf{s}, \mathbf{F}))\mathbf{N} = -p_\mathrm{LV}(t) J \mathbf{F}^{-\mathrm{T}}\mathbf{N}$ is imposed on the endocardium Γ_0^endo to account for the pressure $p_\mathrm{LV}(t)$ applied by the blood inside the LV. $p_\mathrm{LV}(t)$

Table 10.1: Input parameters for the electromechanical computational model.

Parameter	Value	Unit	Description
Passive biomechanics			
ρ_0	1082	kg/m^3	tissue density
κ	1	MPa	bulk modulus
μ	651.12	Pa	shear modulus
b_{ff}	11	-	fiber strain scaling
b_{ss}	4.4	-	radial strain scaling
b_{nn}	2.2	-	cross-fiber in-plain strain scaling
b_{fs}	7.7	-	shear strain in fiber-sheet plane scaling
b_{fn}	6.6	-	shear strain in fiber-normal plane scaling
b_{ns}	3.3	-	shear strain in sheet-normal plane scaling
Active biomechanics			
λ_0	0.7	-	minimum fiber stretch
t_{emd}	0.0	s	electromechanical delay
T_{peak}	50	kPa	peak isometric tension
t_{dur}	0.42	s	duration of active contraction
τ_{c0}	0.14	s	base time constant of contraction
ld	5.0	-	degree of length dependence
ld_{up}	0.5	s	length dependence of upstroke time
τ_r	0.05	s	time constant of relaxation
t_{cycle}	0.8	s	length of heart cycle

is determined by a 0D circulation model $\mathcal{C}$ and the coupling condition $V_{\mathrm{LV}}^{\mathrm{3D}} = V_{\mathrm{LV}}^{\mathrm{0D}}$ ensures volume consistency, which has to be satisfied at each time step $t \in (0, T]$. Since the model in this study only includes the LV, the simplified circulatory model defined by Eqs. (9.3)-(9.7) is utilized.

Additionally, the interaction between the LV epicardium Γ_0^{epi} and the surrounding tissue [20, 115, 116] is considered by the boundary condition $\mathbf{F}\mathbf{S}(\mathbf{d}, T_{\mathrm{a}}(\mathbf{s}, \mathbf{F}))\mathbf{N} = \mathbf{f}^{\mathrm{epi}}$. The contact handling algorithm proposed by [20] as described in Chapter 5.3 is used in this study. This ensures a more realistic movement of the ventricle along the long axis of the heart with improved mitral valve displacement during systole.

Since the LV is under constant stress due to the flow of blood, we have to find a suitable initial stress distribution. Therefore, we first find a stress-free state of the LV by solving an inverse elasto-static problem with Algorithm 5.1. Then, the stress-free configuration is inflated with a pressure $p_{\mathrm{LV}} = 8\,\mathrm{mmHg}$ to find the displacement $\mathbf{d}$.

10.1.3 Clinical Data Integration

Jadczyk et al. [218] performed an intra-cardiac mapping study on 30 heart failure patients showing reduced ejection fraction. They acquired LV end-diastolic and end-systolic volume using transthoracic echocardiography, local scar burden using LGE-MRI, and electromechanical mapping using the NOGA XP system, which allows simultaneous measurement of local electrical activity and mechanical motion. Using the catheter, local activation time (LAT) was measured as the time that passed since the first electrical activation in the LV.

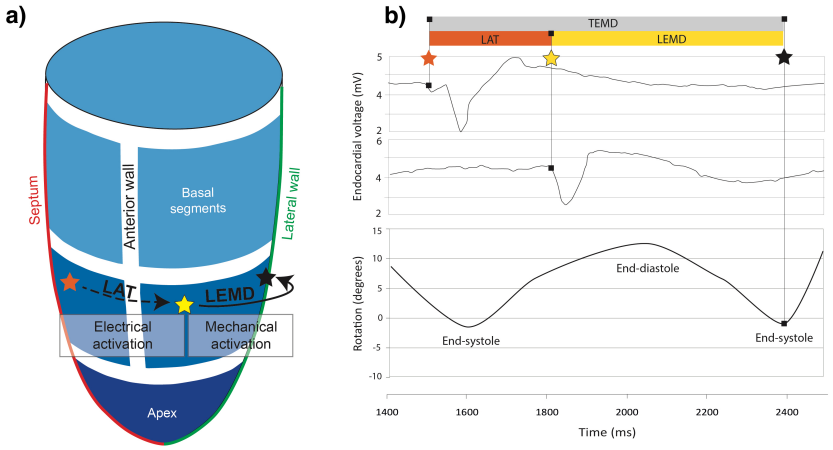

Figure 10.2: a) 3D model of the left ventricle showing the relation between local activation time (LAT) and local electromechanical delay. b) Electromechanical parameters of the left ventricle and how they relate to endocardial voltage and rotation. The orange star indicates the first electrical activation in the LV. The yellow star indicates measured electrical activity at another location in the LV. As the tissue at this position starts to contract, the LV begins to rotate. The time when peak rotation is reached, is symbolized by a black star. From [41], licence CC-BY 4.0.

The time between the LAT and the measured peak systolic rotation of the point is defined as the local electromechanical delay (LEMD). Together, both of these values give the total electromechanical delay (TEMD) as shown in Figure 10.2. The measurements from each patient were incorporated into the LV geometry presented in Section 10.1.1 by assigning the LGE-MRI data via the 17 American Heart Association (AHA) segments and LAT, LEMD, and TEMD via the 9 segments of the NOGA XP system. To better differentiate between the potential influence of both, altered mechanical activation and scar burden, we first simulate all cases with only the measurements from the NOGA XP system and add local scar burden from LGE-MRI in a second run.

Jadczyk et al. [218] defined the LEMD parameter as the time interval between the local electrical activation of the segment and its peak of systolic rotation, not the onset of mechanical activation. This is an accepted approach in clinical studies of human LV mechanics [210]. Since LEMD is the only available parameter that relates to the mechanical activation including electromechanical delay, the onset of mechanical activation is set as $t_\mathrm{a} = \mathrm{LAT} + \mathrm{LEMD}$ in each segment and assigned to the center of the endocardial surface that belongs to the corresponding segment. To avoid sharp transitions between the segments due to the low resolution of the available LEMD data, all values are interpolated over the whole endocardium using Laplacian minimization [219]. The resulting endocardial activation is then mapped to the volumetric myocardium using nearest neighbor interpolation and propagated transmurally with a transverse conduction velocity of $\mathrm{CV}_{\mathbf{s}_0} = 0.4\,\mathrm{m/s}$ [220]. This adds an activation delay to all points $\mathbf{X}$ based on the distance from the endocardium $D(\mathbf{X})$:

$$t_\mathrm{a}(\mathbf{X}) = t_\mathrm{a}(\mathbf{X} \in \Gamma_0^\mathrm{endo}) + \frac{D(\mathbf{X})}{\mathrm{CV}_{\mathbf{s}_0}}, \tag{10.2}$$

resulting in a maximal transmural delay of epicardial activation of 17.5 ms at the base where the wall thickness is 7 mm.

Local scar burden was incorporated by the percentage of enhanced area determined from LGE-MRI measurements on a segment-by-segment basis. It is assumed that the myocardium in enhanced areas was subject to remodeling processes and thus shows a decreased contractility. To reflect this in our model, the maximal contractility T_{peak} was reduced by the same amount as the percentage of the measured LGE intensity in the respective segment.

10.1.4 Evaluation Metrics

The main focus of this study is to determine different rotation patterns in the LV emerging from locally altered electromechanical delay. Therefore, we need to calculate the rotation angle as well as rotation direction of points located on the endocardial wall with respect to the heart's long axis. In our idealized LV model, the long axis corresponds to the z-axis of the global coordinate system in basal-apical direction. Hence, we extract all endocardial points $\mathbf{r} = \mathbf{X} \in \Gamma_0^{\text{endo}}$ in each segment, project them onto the (x,y) plane, and use the relationship

$$\cos\alpha = \frac{\mathbf{r}_{\text{ED}} \cdot \mathbf{r}_{\text{ES}}}{|\mathbf{r}_{\text{ED}}| \cdot |\mathbf{r}_{\text{ES}}|} \tag{10.3}$$

to calculate the angular displacement α from end-diastole (ED) to end-systole (ES). The direction of rotation was determined through

$$\det(\mathbf{r}_{\text{ED}}, \mathbf{r}_{\text{ES}}) \tag{10.4}$$

with values > 0 indicating counterclockwise rotation and values < 0 indicating clockwise rotation. ED and ES states are determined from the pressure-volume relationship $p_{\text{LV}}(V_{\text{LV}})$ resulting from the 0D circulation model $\mathcal{C}$. Additionally, we use Lagrangian particle tracking to visualize three dimensional trajectories of points located on the endocardium. Finally, the simulations are classified into one of two categories based on their rotational behavior: 1) wringing rotation denoted as Group A when basal segments show clockwise rotation and apical segments show counterclockwise rotation; 2) rigid-body-type (RBT) rotation denoted as Group B when the segments show either predominantly clockwise or predominantly counterclockwise rotation. The latter is realized by using a threshold of $\pm 3^\circ$ to decide whether a segment is rotating clockwise or counterclockwise, respectively. If 9 or more segments show the same rotation pattern, the case is assigned to Group B.

10.2 Results

We studied how locally altered electromechanical activation determines the diverse LV rotation patterns observed in HFrEF patients diagnosed with LBBB using in-silico models of the LV in a total of 31 cases. 30 of them were informed by patient specific measurements of

LAT and LEMD using the measured data reported in [218] with the NOGA XP system as well as scar burden using the percentage of enhanced area from LGE-MRI. Additionally, we simulated a Control case without variations in LEMD and without scar tissue. For 3 of the clinical cases, simulations failed with the parameter set given in Table 10.1. Thus, simulation results are reported for 27 clinical cases. Since the rotational analysis of the simulations with and without local scar burden showed only minor differences and the classification was the same, results are reported for the cases including local scar burden unless otherwise stated.

Based on Eqs. (10.3) and (10.4), we calculated the angle of rotation for all endocardial points and evaluated sectorial (basal, medial, apical) as well as segmental (17 AHA segments) mean values in each time step. Figure 10.3 shows the dynamic rotational behavior of the LV in the basal and apical segments (left panel) as well as the sectorial mean angle of rotation during end-systole (right panel). The results for the Control case are shown at the top. In

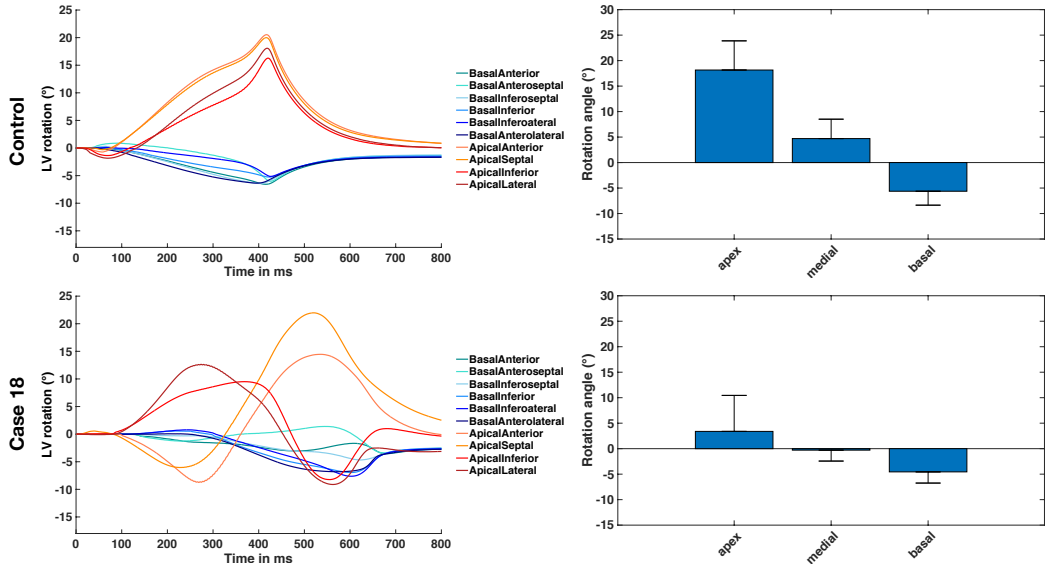

Figure 10.3: Rotational dynamics of the basal and apical segments during one whole heart beat (left panel) and sectorial mean end-systolic rotation angle (right panel). The Control case is shown on the top and represents wringing rotation. Case 18 is shown on the bottom and was classified as RBT rotation. From [41], licence CC-BY 4.0.

the first 100 ms, the LV experienced a short untwist meaning that apical segments rotated clockwise with up to $-3°$ and basal segments rotated counterclockwise with up to $1°$. Right after this first phase, apical and basal segments start to rotate in the opposite direction until end-systole is reached (at about 410 ms). The mean angle of rotation was $18°$, $5°$, and $-6°$ for the apical, medial, and basal sectors, respectively. At the bottom of Figure 10.3, the results for Case 18 are shown. Here, we could not observe a clear phase of untwisting. However, apical segments show opposite directions of rotation throughout the simulated heartbeat.

First, anterior and septal segments showed up to -10° of clockwise rotation while lateral and inferior segments rotated counterclockwise with up to 12°. Towards end-systole however, the direction of rotation switches to the exact opposite behavior, leading to a predominantly clockwise rotation of basal and apical segments. This is reflected in the sectorial mean angle of end-systolic rotation as well. The apical sector showed significantly lower rotation compared to the Control case, whereas the medial sector switched from counterclockwise to clockwise rotation. Basal segments showed slightly lower angles of rotation compared to Control.

In the Lagrangian particle tracking of the Control case (Figure 10.4), the wringing rotation could be clearly observed. Apical segments distinctly showed counterclockwise rotation up until end-systole. Additionally, we observed a translational movement towards the lateral side of the LV. In the medial and basal segments, the contraction was much more symmetrical and the myocardium in these segments rotated predominantly in a clockwise manner. However, the rotation is not as dominant as the shortening in the long axis in these segments.

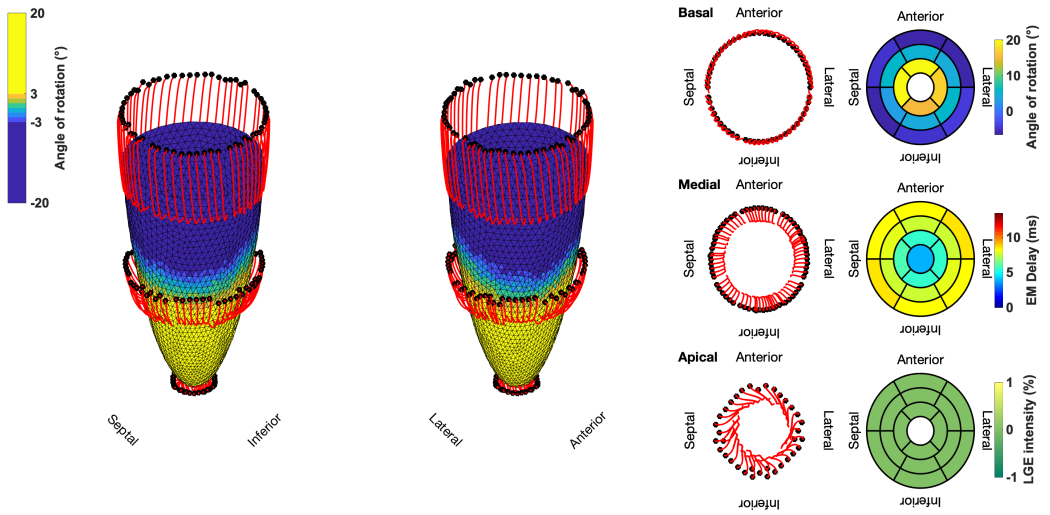

Figure 10.4: Three-dimensional trajectories (red lines) of selected points on the endocardium in the basal, medial, and apical sectors for the Control case. The endocardial surface during end-systole is shown with rotational values depicted on the faces of the mesh. Solid black dots represent the initial positions. Bullseye plots show the segmental mean values of the angle of rotation, electromechanical (EM) delay, and LGE intensity. From [41], licence CC-BY 4.0.

Compared to the Control case, Case 18 showed a markedly different contraction pattern (Figure 10.5). Most notably, the symmetry of the homogeneous contraction pattern is lost. Inferior-lateral segments in the basal and medial sectors displayed less wall thickening, yet more shortening in the long axis compared to the Control case. Apical segments underwent

a significant translation towards the anterior-lateral side of the LV with a more pronounced clockwise rotation. Due to the higher LGE intensities in basal septal and basal inferior segments, the LV shows less wall thickening and less longitudinal shortening compared to the Control case.

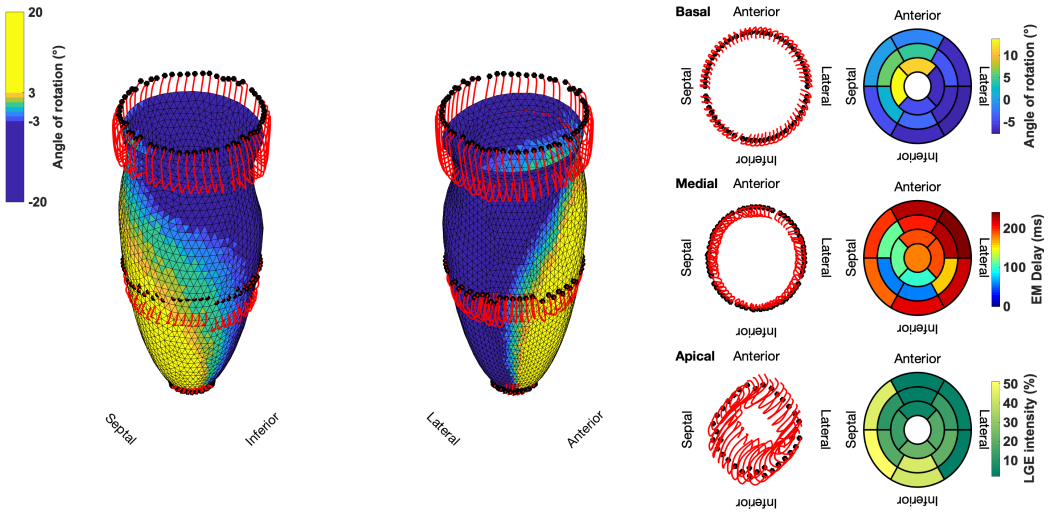

Figure 10.5: Three-dimensional trajectories (red lines) of selected points on the endocardium in the basal, medial, and apical sectors for Case 18. The endocardial surface during end-systole is shown with rotational values depicted on the faces of the mesh. Solid black dots represent the initial positions. Bullseye plots show the segmential mean values of the angle of rotation, electromechanical (EM) delay, and LGE intensity. From [41], licence CC-BY 4.0.

Two examples of the difference in the evaluated angle of rotation are given in Figure 10.6 in case we include or exclude local scar burden in the simulations. Case 15 (patient with the overall highest intensity values in the LGE-MRI data) showed slightly smaller rotation angles in some segments when local scar burden is incorporated into the model. With up to 5°, the change in the angle of rotation is largest in apical and medial segments. However, no change in the direction of rotation was observed. For Case 18, we observed similar changes in the magnitude of peak rotation. Angular differences occured mostly in segments with increased LGE intensity.

Lastly, the results of the binary classification for each of the 17 AHA segments in the Control case and the 27 clinically informed simulations are shown in Figure 10.7. Each segment was classified by its mean angle of rotation during end-systole. The color red depicts clockwise rotation and blue counterclockwise rotation. Cases with the majority of segments (≥ 9) rotating clockwise were classified as RBT rotation (Group B), which was the case for three cases (6, 10, 18). No case was classified in Group B with a predominantly counterclockwise rotation, since the basal segments rotated clockwise in the majority of

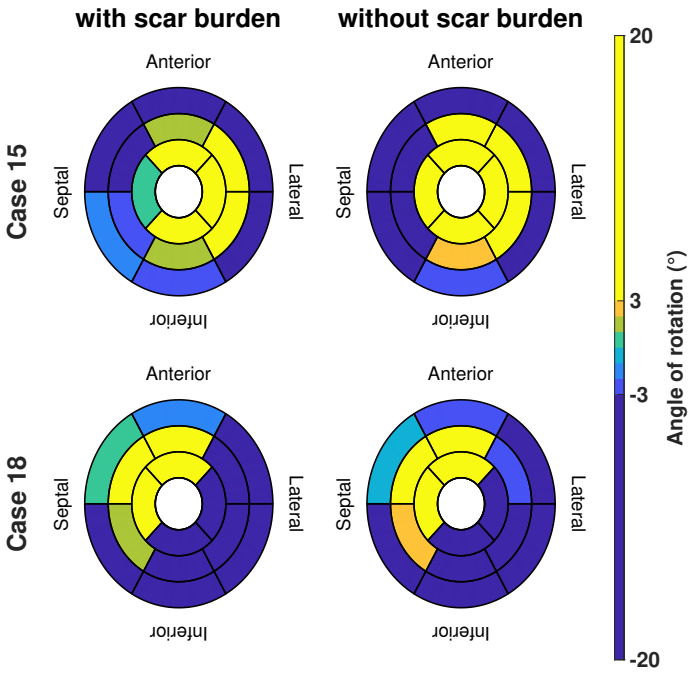

Figure 10.6: Angle of rotation for Cases 15 and 18 shown in bullseye perspective for simulations with and without local scar burden. From [41], licence CC-BY 4.0.

cases. One repeating pattern in those three cases is that the lateral-inferior side of the LV was predominantly rotating in clockwise direction, while the anterior-septal side was dominated by counterclockwise rotation. All other cases were classified as wringing rotation (Group A). Based on the clinical recordings directly, [218] classified 20% of the patients in Group A ($n = 6$) and 80% in Group B ($n = 24$). Furthermore, 73% ($n = 22$) of patients in Group B showed clockwise RBT rotation and predominantly counterlockwise RBT rotation was observed in 7% ($n = 2$). Compared to the clinical classification, the in silico model results yielded matching classifications for Group A in 50% ($n = 3$) of the cases and in 0% of the cases for Group B.

10.3 Discussion

We presented results of a total of 27 mechanical simulations of an idealized LV that were informed by electroanatomical maps recorded with the NOGA XP system and additional LGE-MRI data. Results of one additional simulation without a patient specific input served as a control case. We evaluated the angle of rotation of each point on the endocardium and accumulated mean values on a segmental (17 AHA segments) and sectorial (basal, medial, apical) basis. Based on the segmental mean values, we determined the direction of rotation to be either clockwise (negative rotation values) or counterclockwise (positive rotation values).

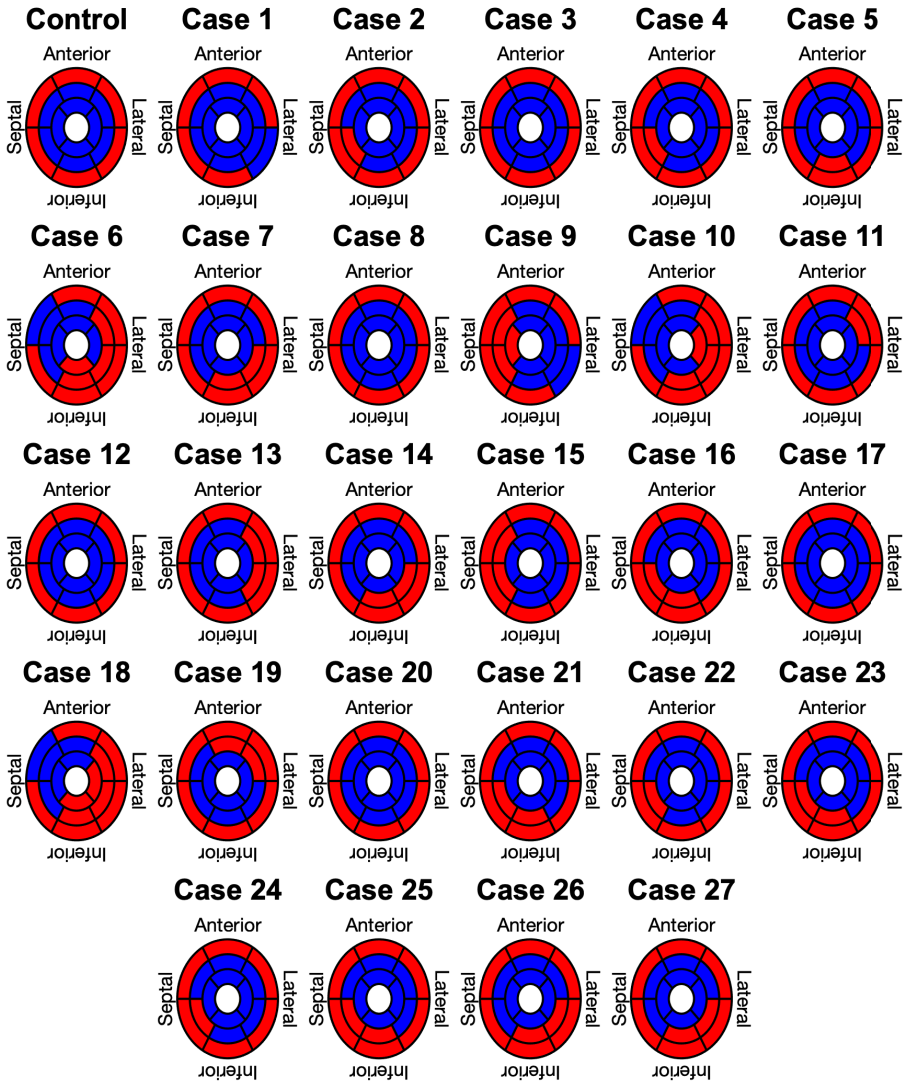

Figure 10.7: Segment based analysis of end-systolic rotation around the long axis of the LV. A binary classification was used in each segment to determine clockwise (red) or counterclockwise (blue) rotation. From [41], licence CC-BY 4.0.

Finally, each simulation was classified as wringing type rotation (Group A) or RBT rotation (Group B) and compared to the clinically assessed classification.

The Control case was parameterized to yield a physiological contraction pattern that could be used as a comparison since all other cases involve data from patients suffering from HFrEF and LBBB. Hence, we presumed the electrical activation to be synchronized such that the subendocardial mechanical contraction is homogeneous throughout the LV and spreading transmurally towards the epicardium. The evaluated rotation pattern concurs with observations made in healthy individuals quantitatively and qualitatively [221, 222]. First, we observed a brief untwisting (clockwise rotation of the apex and counterclockwise

rotation of the base) of the LV during isovolumetric contraction. This has been observed in clinical measurements as well [206, 223] and is linked to the initial contraction of the subendocardial layer followed by the contraction of the subepicardial layer. During ejection, the LV starts to twist normally (counterclockwise rotation of the apex and clockwise rotation of the base). [184] reported mean rotational values of -6.9° for the base and 13° for the apex in 247 healthy volunteers using two-dimensional speckle-tracking echocardiography. With up to -6°, the Control case in this study matches these data well at the base. However, the up to 20° of rotation at the apex is larger. This can be explained by numerous factors, e.g. it is known that preload, afterload, contractility and age have an influence on the twist angle [206, 223]. Another significant factor is the choice of the apical imaging plane, since rotation values can vary widely depending on where the rotation is measured [222, 224]. Based on these facts, we think that the Control case successfully represents physiological contraction in humans.

Electrical activation and consequently mechanical contraction of the LV in the pathological cases was determined by patient specific measurements of electroanatomical maps. LAT and LEMD were directly integrated into the LV model using the segments defined by the NOGA XP catheter system. LGE-MRI intensity was used as a surrogate for scar tissue in the LV. Typically, scar tissue undergoes a remodeling process that involves build-up of collagen in the myocardium [225], which can result in a reorganization of the underlying fiber structure. Thus, an acknowledged way of modeling scar tissue is to impose an isotropic fiber structure with increased stiffness in the constitutive model [84]. Since we only had access to the LGE intensity as a percentage in each of the 17 AHA segments and we used the same geometrical model for all cases, it was not possible to easily implement it this way. Instead, we decided to reduce the active tension in the respective segment by the same percentage as the LGE intensity was increased with respect to the mean blood pool value (image intensity ratio, IIR). Thus, for IIR=1.2 (20% above the mean blood pool intensity), the active tension was reduced by 20% to 0.8 $\times$ the reference value. This approach is motivated by the fact that in case of unchanged contractility, a stiffer myocardium would result in less deformation.However, this is a simplification due to the nonlinear nature of the constitutive law given in Eq. (B.12). Furthermore, we effectively smooth the effect of local scar tissue over the entire segment. Other than the altered electromechanical delay captured by the LEMD values from electroanatomical mapping and the aforementioned LGE intensity to capture the effect of scar tissue, no further patho-mechanisms were considered in the simulations. Hence, the emerging rotation patterns in the pathological cases originate from these changes only.

The classification into Group A (wringing rotation) and Group B (RBT rotation) was based on the evaluation of the mean angle of rotation in the 17 AHA segments. It clearly showed that most cases were classified into Group A. With the exception of 3 cases, all cases were classified different than in the classification based directly on the clinical rotation data, which means we cannot confirm the hypothesis postulated in [218] with the in silico model presented in this study. However, we identified 3 cases with predominantly clockwise rotation. Additionally to the basal segments, the medial and apical inferior-lateral side of the

LV started to rotate clockwise instead of counterclockwise. Noticeably, this was accompanied by a significant translational movement of the apical region towards the anterior-lateral side of the LV. This can potentially skew the results when Eqs. (10.3) and (10.4) are used to determine the angle and direction of rotation around a fixed axis [226], since a translation can be mistaken as a rotation. Nonetheless, the rotational dynamics shown in Figure 10.3 of Case 18 show a similar pattern compared to a HFrEF case in [206]. There, apical rotation is reduced and undergoes both, a counterclockwise and then clockwise rotation.

Furthermore, the following limitations apply to our study:

1. LEMD was defined as the time interval between the local electrical activation of the segment and its peak systolic rotation, not the onset of mechanical activation. If we assume a similar length of active contraction in each segment, this should not pose a problem and LEMD can be interpreted as a local delay. However, different contractility can be expected especially in segments that show enhanced regions in LGE-MRI due to scar tissue and the associated tissue remodeling. This is especially important, since we observe a significantly longer time interval between electrical activation and peak systolic rotation in our simulations (489 ± 45 ms compared to the 369 ± 59 ms in the clinical measurements).
2. The presented in-silico model neglects the influence of the atria and the right ventricle on rotation of the LV. Atrial data was not available for these patients at all and for the right ventricle no electroanatomical mapping data was available. We decided to use the same LV geometrical model for all patients to isolate the effect of electromechanical activation on rotation.
3. A reason for the small differences in simulations in which scar burden was considered could be the simple way of transferring LGE intensity directly into a decrease in contractility. Although it is a straightforward approach and easy to implement, scar tissue is more complex and typically accompanied by other pathomechanisms in addition to a reduction in contractility. For example, fiber orientation in the LV of patients with dilated cardiomyopathy is typically reorganized [227]. Furthermore, the stiffness of the myocardium increases and electrical conductivity decreases due to extracellular matrix remodeling [228]. A detailed investigation of the effect of these additional mechanisms requires personalized LV anatomical models including information on pathological changes and was beyond the scope of this study, which focuses on the effect of dyssynchronous activation.

In conclusion, we combined a state-of-the-art model of heart mechanics and in vivo data of 30 patients to analyze rotational dynamics in the LV. Our preliminary classification of LV rotation showed normal wringing rotation as well as RBT rotation. However, a comparison with the clinical classification based on in vivo NOGA XP maps yielded no correlation, suggesting that isolated changes of electromechanical activation are not sufficient to explain abnormal rotation patterns in patients with HFrEF and LBBB. More research is necessary to expand the knowledge about electromechanical coupling and rotational behavior especially in terms of CRT response. The results presented in the current study aimed to address a

potential methodological approach and stimulate further scientific investigations in the field of cardiac simulation.

PART V

MODELING PATHOLOGICAL SCENARIOS IN THE WHOLE HEART

Chapter 11

Standard Ablation Strategies for the Treatment of Atrial Fibrillation

Although atrial fibrillation (AF) can often be managed pharmacologically, catheter ablation is now considered as a first line treatment for paroxysmal AF patients [229]. Unfortunately, the long-term success rates of catheter ablation of AF are not satisfactory yet. One reason could be long term adaptations of the atria to compensate for ablation-induced impairment of atrial function. Thomas et al. [230] analyzed the effect of atrial radio frequency ablation (RFA) on the atrial mechanical function. They concluded that multiple linear RFA lesions may impair atrial contractility and that the reduced atrial function is partly due to loss of viable myocardial tissue but may also be caused by the altered atrial activation. Different ablation strategies with the aim to prevent AF and its recurrence exist but their respective impacts on the ventricular mechanics and hemodynamics have not been studied systematically. In this context, cardiac modeling opens up the possibility to get a better understanding of how RFA affects the mechanical behavior and the pumping function of the heart by applying different treatment strategies to the same virtual patient under controlled conditions, which is not feasible in a clinical context.

While in the past most attention in the field of cardiac modeling had been paid to the simulation of the ventricles, and still is an active field of research [115, 123, 127, 231, 232], modeling of the atria has moved into focus in the last years. However, most publications deal with atrial electrophysiology and there are only a few addressing atrial mechanics [233]. Jernigan et al. [234] published a study on the mechanical properties of porcine left atrium, which were assessed with uniaxial tests. In 2011, Di Martino et al. [235] presented a computational model of the porcine left atrium, which allowed to analyze the wall stress due to the mitral valve movement, obtained from raw multi-detector computed tomography data. The mechanical properties were modeled based on biaxial experiments with porcine atrial tissue. In the same year, Di Martino et al. [236] analyzed how ventricular tachypacing affects the spatial and temporal stress distribution of the left atrial wall. Bellini et al. [237] provided a comprehensive characterization of the passive biomechanics of the left human atria based on a Fung-type elastic strain energy potential. These publications all deal with the passive

mechanical behavior of the atria. Models for the active contraction of the atria have only been published recently [14, 15] and the simulation of whole heart models is becoming more feasible [35]. A recent study by Hormann et al. [16] modeled atrial systole using standard ablation strategies in a non-pathological and a dilated atrium to study the impact of ablation lesions on the mechanical performance of the atria. Their model was able to detect differences in left atrial contractility and ejection fraction for multiple activation sequences resulting from RFA and atrial fibrillation-induced atrial remodelling represented by a reduction in global conduction velocity. Since they were only interested in atrial systole, the ventricles were only represented by a passive stiffness and they only included a Windkessel to model the hemodynamics of the atria, thus neglecting a change in pre- and afterload over multiple heart beats. Another study that dealt with atrial mechanics was published by Phung et al. [238]. Unlike Hormann et al. [16], they connected the left atrium to a circulation model to produce more realistic hemodynamics and validated their baseline model to pre-treatment data by means of left atrial wall motion. Phung et al. found that ablating the posterior wall had a smaller impact on atrial function compared to other ablation patterns such as pulmonary vein isolation or wide area circumferential ablation. They explained this with the little movement of this region in the pre-treatment model and thus small contribution to atrial function. A significant limitation of the study by Phung et al. was the missing representation of electrical propagation in the model.

We hypothesize that ablation scars in the atria also have an effect on the ventricles. During ventricular contraction, the atrioventricular plane is pulled towards the apex, the atria are stretched and their volume is increased. This mechanism supports the filling of the atria with blood from the venae cavae and the pulmonary veins. Eventually, this blood volume is available for ventricular filling during ventricular relaxation. An increased stiffness of the atria due to ablation scars may impede atrioventricular plane displacement (AVPD) and consequently also atrial filling. Accordingly, two effects may affect the ventricular filling negatively: On the one hand, a reduced filling capacity of the atria during the ventricular systole and therefore less blood volume available for the ventricular filling. On the other hand, a reduced active contribution of the atrium due to an altered atrial activation induced by the ablation scars. Here, the effect certainly depends on the respective ablation pattern and the amount of ablated tissue. Alhogbani et al. [239] assessed the contribution of the left atrium to the filling of the left ventricle using cardiac magnetic resonance imaging (MRI) for 120 normal subjects. They reported that the contribution of the atria to ventricular filling increases with age and is in the range of $10\% - 40\%$. Considering that about 70% of the patients with AF are between 65 and 85 years old [240], the implications of RFA on the atrial contraction should not be disregarded. To overcome the limitations of the studies by Hormann et al. and Phung et al. [16, 238], we utilize our previously published four-chamber heart model including a closed-loop circulatory system, electrophysiological wave propagation and myocardial contraction [35] to extend a previous study from our group [241] by analyzing the impact of five commonly used ablation lesions on cardiovascular performance. Furthermore, we analyze how the stiffening of scar tissue due to an accumulation of collagen in the myocardium affects the deformation of the heart and in particular AVPD. The sensitivity of

the model towards changes in the stiffness of the scars is evaluated on one particular scar pattern. Finally, we introduce the effects of AF related fibrosis globally by reducing the diffusion coefficient.

11.1 Materials and Methods

11.1.1 Whole Heart Finite Element Model

For this study, the heart model which was introduced in Chapter 4 was used. As described in Chapter 5.3.2, two nested meshes with linear tetrahedrons were defined: $\Omega_{\mathrm{h}_1} = \Omega_{\mathrm{EP}}$ for the electrophysiology and $\Omega_{\mathrm{h}_2} = \Omega_{\mathrm{M}}$ for the mechanics problem. Ω_{M} contains 128,976 elements with an average edge length of $h_2 = 3.17 \pm 0.84$ mm (take note that this value includes the coarse mesh of the pericardium) and Ω_{EP} contains 50,058,295 elements with an average edge length of $h_1 = 0.4 \pm 0.09$ mm.

11.1.2 Electromechanical PDE Model

The electromechanical model used in this study to simulate a four-chamber model of a human heart is the one introduced in Chapter 5.3 with some adaptations to reduce the amount of computational effort required to simulate all the different setups and to make the personalization of the model more simple.

Since the focus of this study is on mechanical features and not on the subtleties of mechanoelectric feedback, we only implement excitation-contraction coupling mechanisms and forego the effects of deformation on electrical propagation. This means, the monodomain equation is solved on the fixed reference domain Ω_{EP} with $\mathbf{F} = \mathbb{1}$ and $J = 1$ resulting in the standard formulation (3.6). Furthermore, no mechanical feedback on the calcium transient is used in the ionic models of Courtemanche-Ramirez-Nattel (CRN) [155] and O'Hara-Rudy-dynamic (ORd) [156]. The conductivities in the diffusion tensor $\mathbf{D}$ were set to the values given in Table 11.1 to achieve a complete depolarization of the atria in 100 ms [242] and conduction velocities (CVs) of 0.6 m/s, 0.4 m/s, 0.2 m/s in fiber, sheet, and sheet-normal directions in the ventricles [220]. The external stimulus I_{app} is applied at the junction of the right atrial appendage and the superior vena cava [58] to initiate the depolarization wave in the atria. In the ventricles, the fascicular model shown in Figure 5.2 is used with the sites of earliest activation given in Table 11.2.

Passive mechanics of the myocardium is modeled using the strain energy function by Usyk et al. [106] with a small adaption to its formulation

$$\Psi^{(\mathrm{U})}(\mathbf{C}) = \frac{\kappa}{2}(\ln J)^2 + \frac{\mu}{2}(\exp(\alpha Q) - 1)\,,$$
$$Q = b_{\mathrm{ff}}E_{\mathrm{ff}}^2 + b_{\mathrm{ss}}E_{\mathrm{ss}}^2 + b_{\mathrm{nn}}E_{\mathrm{nn}}^2 + b_{\mathrm{fs}}(E_{\mathrm{fs}}^2 + E_{\mathrm{sf}}^2) + b_{\mathrm{fn}}(E_{\mathrm{fn}}^2 + E_{\mathrm{nf}}^2) + b_{\mathrm{ns}}(E_{\mathrm{ns}}^2 + E_{\mathrm{sn}}^2)\,,$$

Table 11.1: Electrophysiological parameters for the whole heart model.

Parameter	Value	Unit	Description
$(\sigma_f, \sigma_s, \sigma_n)$	$(0.1979, 0.1046, 0.0363)$	S/m	conductivities in ventricular bulk tissue
$(\sigma_f, \sigma_s, \sigma_n)$	$(0.5756, 0.3042, 0.1046)$	S/m	conductivities in ventricular subendocardial layer
$(\sigma_f, \sigma_s, \sigma_n)$	$(1.0812, 0.1821, 0.1821)$	S/m	conductivities in atrial bulk tissue
$(\sigma_f, \sigma_s, \sigma_n)$	$(10^{-12}, 10^{-12}, 10^{-12})$	S/m	conductivities in scar tissue
β	140000	1/m	membrane surface-to-volume ratio
C_m	0.01	F/m^2	membrane capacitance
t_{AVN}	0.160	s	atrio-ventricular conduction delay
Heart rate	50	1/60 s	–

Table 11.2: Sites of earliest activation in terms of the coordinate system Cobiveco [26]: a apicobasal; m transmural; r rotational; v transventricular. δ_m and δ_{rad} are the transmural and radial extent of the activation site, respectively.

Root point	Extent		
$\mathbf{x}_{root} = \{a, m, r, v\}$	δ_m	δ_{rad}	Fascicle description
$\{0.62, 1, 0.075, 0\}$	0.05	3 mm	LV mid-posterior superior
$\{0.55, 1, 0.175, 0\}$	0.05	3 mm	LV mid-posterior inferior
$\{0.85, 1, 0.57, 0\}$	0.05	3 mm	LV basal anterior paraseptal
$\{0.40, 1, 0.825, 0\}$	0.05	3 mm	LV mid septal
$\{0.45, 1, 0.825, 1\}$	0.05	3 mm	RV mid septal
$\{0.80, 1, 0.44, 1\}$	0.05	3 mm	RV free wall anterior
$\{0.85, 1, 0.25, 1\}$	0.05	3 mm	RV free wall posterior

where a scaling factor α is introduced into the exponential part. The anisotropic scaling factors b_{ij} were fixed using the values $b_{ff} = 1$, $b_{ss} = 0.4$, $b_{nn} = 0.3$, $b_{fs} = 0.7$, $b_{fn} = 0.6$, $b_{ns} = 0.2$ and only the parameters μ and α had to be adjusted in the process. Purely passive tissue with no predefined fiber orientation was modeled as a Neo-Hookean solid (B.10). All constitutive law parameters are given in Table 11.3. Active tension development is modeled

Table 11.3: Choice of parameters for the constitutive law models given by equations (B.12) and (B.10)

Domain	μ (Pa)	α	κ (Pa)	ρ_0 (kg/m^3)
Ω_V	325.56	22	10^6	1082
Ω_A	325.56	22	10^6	1082
Ω_{Valves}	10^6	-	10^6	1082
$\Omega_{Vessels}$	$14.9 \cdot 10^3$	-	10^6	1082
$\Omega_{Peri,apical}$	$2 \cdot 10^3$	-	10^6	1082
$\Omega_{Peri,basal}$	$2 \cdot 10^3$	-	$5 \cdot 10^4$	1082
Ω_{Scars}	651.12	110	10^6	1082

using the phenomenological model by Niederer et al. given in Equation (10.1) and triggered by the local activation time $t_a(\mathbf{x})$, which is defined as the time when the transmembrane voltage V_m reaches a threshold of $V_m^{thresh} = -20\,\text{mV}$. For a description and values of the remaining

parameters, we refer to Table 11.4. Normally, the process of excitation-contraction-coupling

Table 11.4: Active tension parameters for the whole heart model.

Parameter	Value		Unit	Description
	Atria	Ventricle		
λ_0	0.7	0.7	-	minimum fiber stretch
t_{emd}	0.01	0.03	s	electro-mechanical delay
S_{peak}	50 (RA), 80 (LA)	900 (RV), 450 (LV)	kPa	peak isometric tension
t_{dur}	0.22	0.54	s	duration of active contraction
τ_{c0}	0.06	0.25	s	base time constant of contraction
ld	5.0	5.0	-	degree of length dependence
ld_{up}	0.5	0.5	s	length dependence of upstroke time
τ_r	0.06	0.08	s	time constant of relaxation
t_{cycle}	1.2	1.2	s	length of heart cycle

is mediated by an increase of intracellular calcium [47] immediately after depolarization. Atrial myocytes typically have shorter action potentials and consequently shorter calcium transients compared to ventricular myocytes due to different gene expressions and ionic channel composition [243]. To account for these differences, we adapted the atrial tension to have a shorter contraction duration such that tension development in the atria and ventricles don't overlap temporarily.

11.1.3 Modeling of Ablation Scars

We performed a semi-automatic ablation procedure in the left atrium of our four chamber heart model using the rule-based approach described by [150, 244]. Five commonly used ablation lesions were placed in the domain Ω_{EP}: pulmonary vein isolation (PVI), a mitral isthmus line (MIL), an anterior line (AL), a roof line (RL), and a posterior box lesion (BL) which includes the RL. All lesions were applied transmurally with an average width of 5 mm and mapped to the mechanical domain Ω_M (Figure 11.1). For the simulations, we consider the isolated effect of each single ablation lesion as well as all medically feasible combinations. The electrophysiological tissue conductivity in the affected regions was effectively set to zero to reflect perfect ablations. Therefore, the threshold voltage V_m^{thresh} is never reached and no active tension is developed. Additionally, we model ablated tissue mechanically as isotropic regions with increased tissue stiffness. Consequently, we adapt the constitutive model in Equation (B.12) by setting the anisotropic scaling parameters to $b_{ff} = b_{ss} = b_{nn} = 1$ and $b_{fs} = b_{fn} = b_{ns} = 0.5$. The increased stiffness of the scar tissue is achieved by choosing α five times higher and μ two times higher than in the bulk tissue [84]. This approximates the expected increase in tissue stiffness due to a build-up of collagen in the myocardium as observed in animal studies [225].

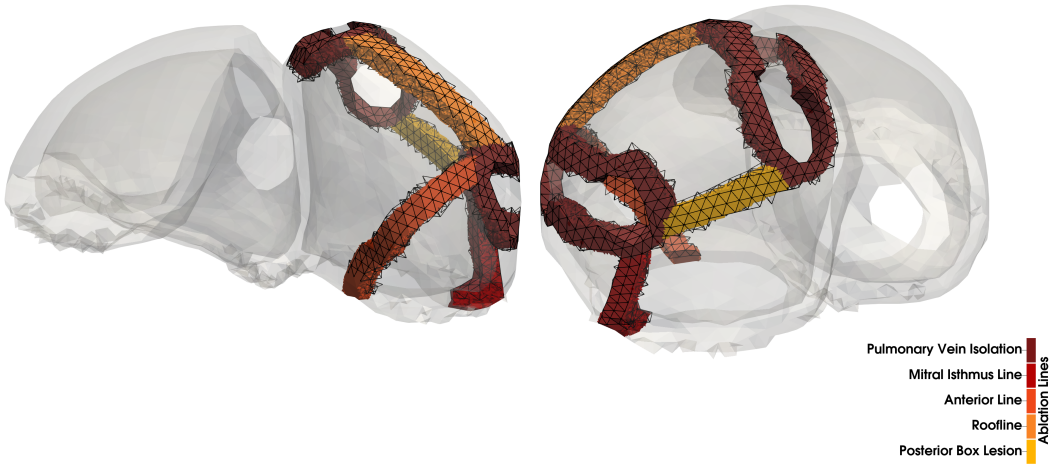

Figure 11.1: Superior (left) and posterior (right) view of the atria with the considered ablation lesions in the electrophysiological domain Ω_{EP}: PVI, MIL, AL, RL, BL. The superimposed wiremesh shows the ablation lesions after mapping to the mechanical domain Ω_{M}.

11.1.4 Simulation Setup and Initialization

In total, ten simulations were conducted including nine combinations of the five ablation lines shown in Figure 11.1 and a control case without ablation.

First, the cellular models are paced at a cycle length of 1.2 s for a total of 1000 cycles. The final values of the state variables $\{V_{\text{m}}, \mathbf{w}, \mathbf{q}\}$ are used as initial values on the vertices of Ω_{EP}. Second, the reference configuration Ω_{M} was unloaded using Algorithm 5.1. We used typical diastatic pressure values in the four chambers: $p_{\text{RV}} = p_{\text{RA}} = 4\,\text{mmHg}$; $p_{\text{LV}} = p_{\text{LA}} = 8\,\text{mmHg}$. Subsequently, the unloaded configuration was inflated with the same pressure values to pre-stress the tissue. Even though the ablation lines have different material parameters than healthy tissue, we used the same unloaded configuration for all ten simulation setups. As long as the global stiffness of the material is similar, this assumption should not affect the overall results in this study [27]. For all simulations, time integration was done using the increments $\Delta t_{\mathcal{M}} = 0.001\,\text{s}$, $\Delta t_{\mathcal{C}} = 0.0001\,\text{s}$, $\Delta t_{\mathcal{E}} = 0.00001\,\text{s}$.

11.2 Results

We investigated the influence of standard clinical ablation patterns on the pumping efficiency of the human heart by simulating a total of ten cases: First, we calibrated the model parameters to match the cine MRI data of the volunteer to simulate a healthy control case. Next, we introduced different combinations of the basic ablation patterns shown in Figure 11.1 into the left atrium in nine additional simulations. All ten simulations were analyzed with regards to the activation sequence, blood volume, and correlation between the amount of

inactive and ablated tissue with ejection fraction (EF) of the left atrium. Furthermore, we investigated the influence of the ablation lesions on the ventricular function with a focus on AVPD and ventricular stroke volume (SV).

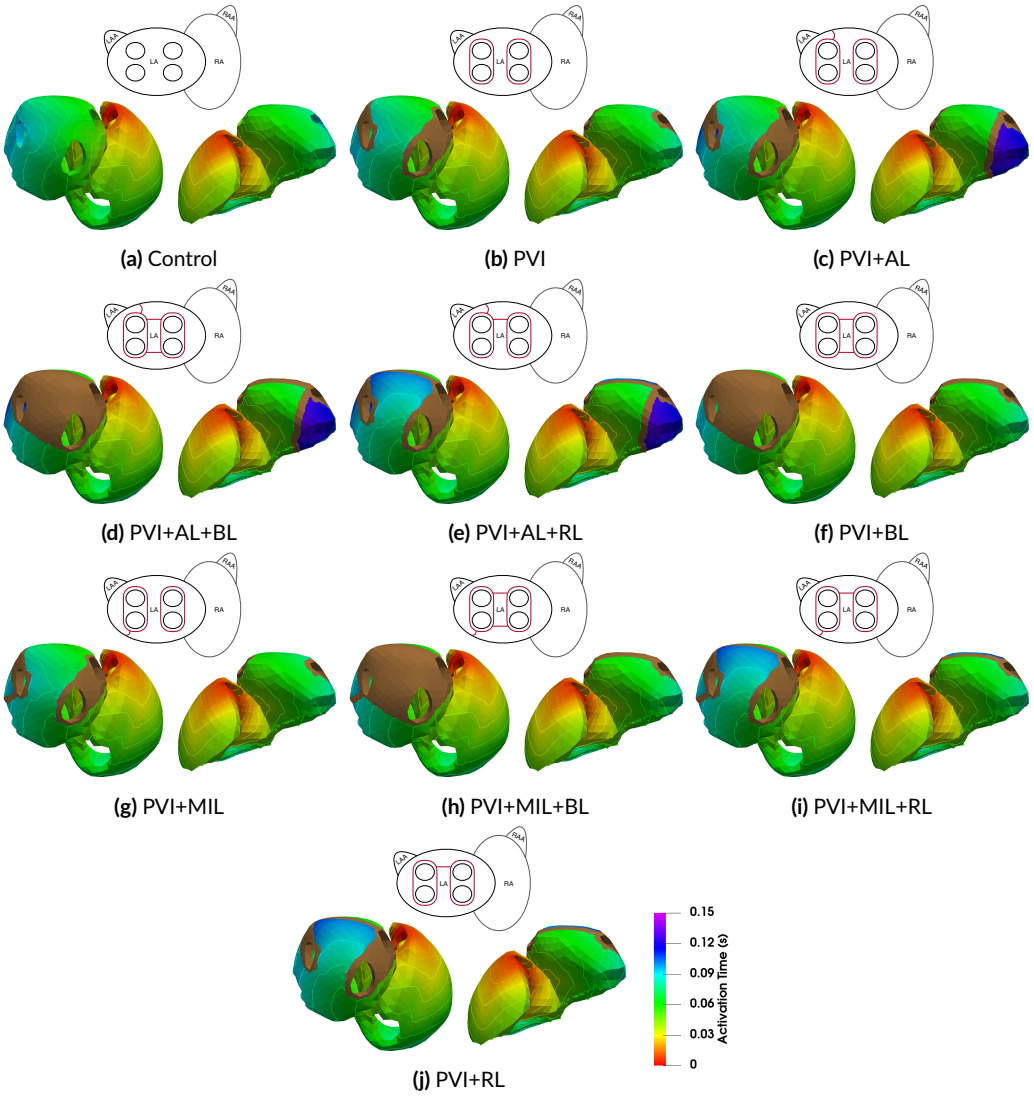

Figure 11.2: Activation maps and isochrones of the depolarization wave in sinus rhythm. A brown color denotes inactive tissue. The pictogram of the atria at the top of each model indicates the applied ablation lesions (red lines).

Figure 11.2 shows the atrial activation time maps for all ten simulations during sinus rhythm. In the healthy control case (Figure 11.2a), the activation starts at the sinus node and propagates from the right atrium (RA) to the left atrium (LA) via four pathways: the Bachmann bundle on the anterior side, a middle and upper posterior interatrial connection, and via the coronary sinus. The depolarization in the left atrium starts after 29 ms at the

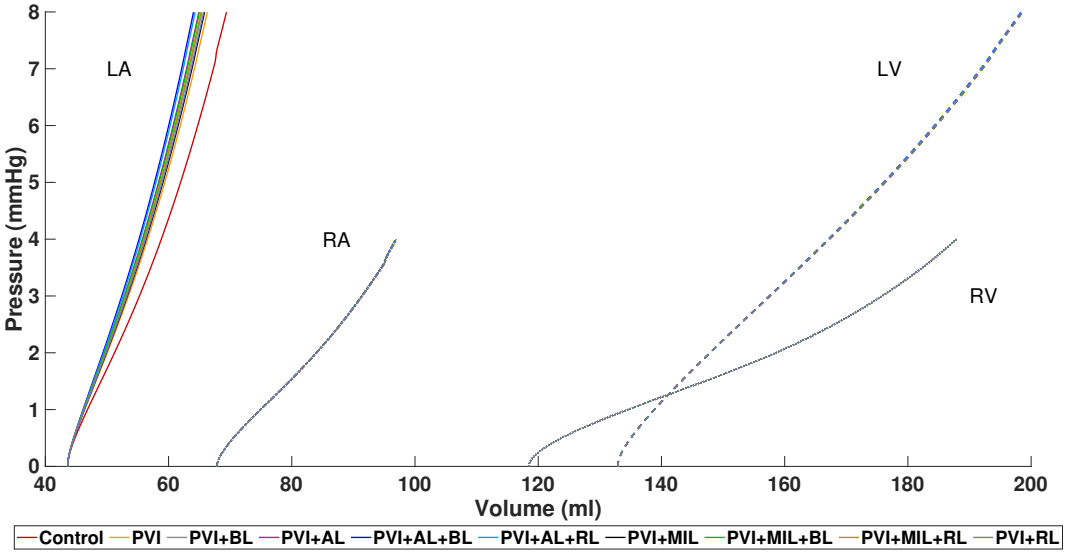

Figure 11.3: End-diastolic pressure-volume relationship (EDPVR) for the left atrium (LA), right atrium (RA), left ventricle (LV) and right ventricle (RV) for all simulations.

entry site of the Bachmann bundle. The last activation of the atria occurs after 97 ms at the posterior side of the mitral valve annulus. The ablation lesions that have the biggest influence on atrial activation time are PVI+RL and PVI+AL. As a consequence of the RL lesion, the activation of the left atrial roof can only occur from the posterior side resulting in an activation delay of around 30 ms in this area ($\approx$ 100 ms in PVI+AL+RL compared to $\approx$ 70 ms in Control). The AL lesion blocks an activation of the left atrial appendage (LAA) through the Bachmann bundle on the anterior side, thus delaying the depolarization of the LAA significantly. Therefore, total atrial activation takes 147 ms in cases with an AL lesion. Compared to PVI+AL, PVI+MIL does not alter the activation sequence significantly, the MIL lesion coincides with the area of latest activation in the LA in our setup. Circumferential PVI alone does not notably alter the activation sequence of the LA. Although the activation sequence is not drastically changed by PVI+BL, a large amount of tissue stays inactive due to the isolation of the LA posterior wall by this specific scar.

Figure 11.3 shows the end-diastolic pressure-volume relationship (EDPVR) of all four chambers resulting from the inflation of the pressure-free state during the initialization process described in Section 11.1.4. Starting from an identical pressure-free state, we observe that the volume of the LA in the pre-stressed state is reduced by up to 5.4 mL (-7.8%) if stiffer scar tissue is present compared to the healthy case. However, the reduction in volume does not correlate with the amount of ablated tissue in the LA (e.g., PVI+AL has a lower volume and less ablated tissue than PVI+BL). The volume of the other chambers remains almost identical with differences of less than $\pm 0.1\%$.

Figure 11.4 shows the amount of blood in the LA until peak LA systole. Peak systole was determined as the time when the maximal output of blood volume is reached. We can observe for all cases that it takes a slightly different amount of time to reach this point.

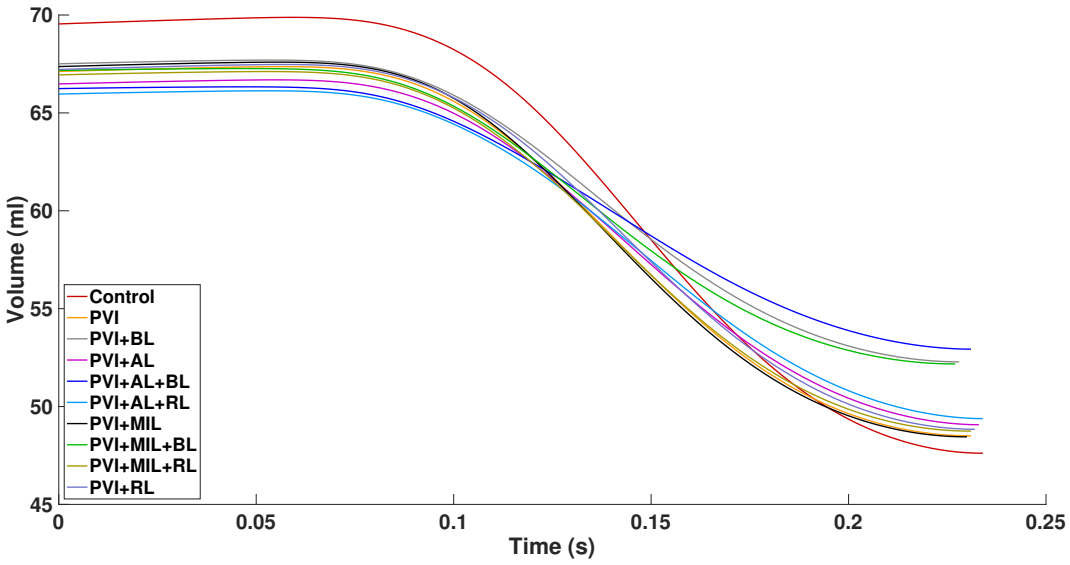

Figure 11.4: Blood volume traces during left atrial systole. Atrial systole lasts from the externally applied stimulation of the sinus node to the time of maximal contraction of the left atrium.

The change in atrial EF due to the different ablation patterns is summarized in Table 11.5 alongside the amount of ablated and subsequently inactive tissue. A linear regression model shows that the amount of inactive tissue is highly correlated ($R^2 = 0.95$) with the change in ejection fraction (ΔEF) compared to the healthy case (Figure 11.6). Ablated tissue and ΔEF show a much weaker correlation ($R^2 = 0.70$).

Table 11.5: Indicators of left atrial function for the control case and different ablation lesions.

Case	Stroke Volume (mL)	EF (%)	ΔEF (pp)	Ablated Tissue (%)	Inactive Tissue (%)
Control	21.93	31.53	0	0	0
PVI	18.61	27.73	3.80	8.67	14.30
PVI+BL	15.22	22.55	8.97	12.18	28.96
PVI+AL	17.41	26.18	5.34	11.22	17.69
PVI+AL+BL	13.31	20.09	11.43	14.72	32.35
PVI+AL+RL	16.58	25.13	6.39	13.31	20.28
PVI+MIL	18.91	28.07	3.45	10.03	16.10
PVI+MIL+BL	14.99	22.31	9.21	13.53	30.76
PVI+MIL+RL	18.19	27.18	4.35	12.12	18.68
PVI+RL	18.38	27.34	4.18	10.76	16.88

pp percentage points

The strain maps of the Control and PVI+AL+BL cases are shown in Figure 11.5. During atrial systole, two differences can be observed in the PVI+AL+BL case compared to the Control case. First, strain values at the position of the ablation lesions suggest that the fibers remain elongated during atrial contraction. However, they shorten a bit compared to the diastolic state. Second, the isolated posterior roof of the left atrium gets stretched past the strain values during diastole since there is no contraction of the fibers in that area. During

ventricular systole, the differences in the strain maps between the Control and PVI+AL+BL are very small. Only in the scars themselves a 50% reduced fiber strain can be observed. The increased stiffness of the scars has a more pronounced effect on the mean stress $\mathbf{S}_{\mathrm{ff}} = \mathbf{f}_0 \cdot \mathbf{S}\mathbf{f}_0$ of the tissue. In general, mean diastolic stress is increased two to three times in the posterior roof and scar surroundings (3.7 kPa vs. 1.2 kPa). Due to the missing contraction of the posterior wall in the PVI+AL+BL case, mean stress is generally lower during atrial systole. During ventricular systole however, mean stress is increased two-fold in scar tissue (42 kPa vs. 18 kPa) while stress in the posterior wall is nearly equal between the two cases.

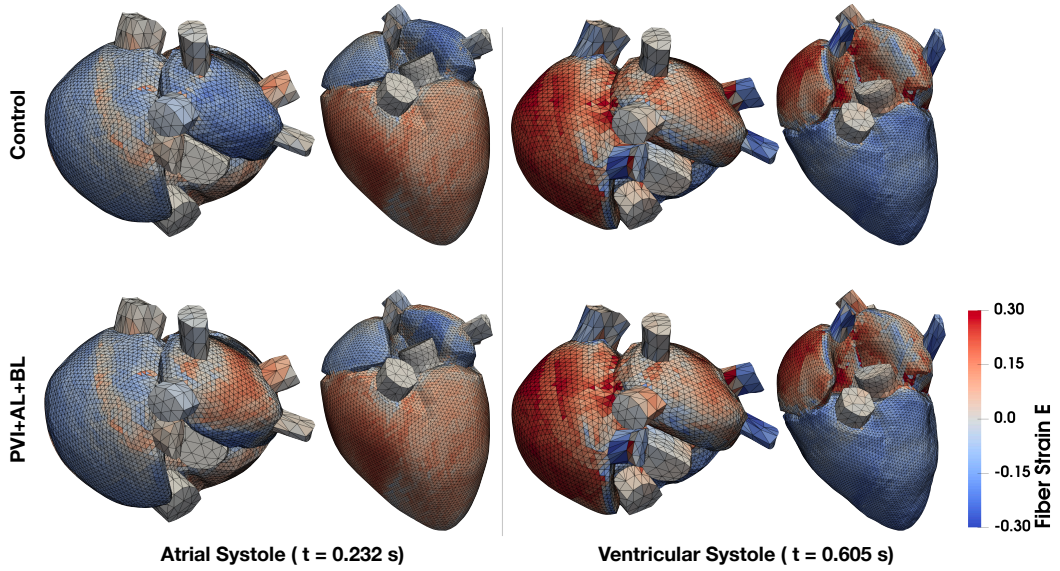

Figure 11.5: Green Lagrange strain E_{ff} in fiber direction of the Control and PVI+AL+BL case is shown during atrial and ventricular systole, respectively.

Figure 11.7 shows the time course of pressure and volume in all four chambers of the heart. Besides the decrease in systolic function of the LA, we observe that passive filling of the LA during ventricular contraction is restricted (7% to 10% lower compared to control) in the presence of ablation lesions. At the same time, we observe an increase in LA pressure of up to 12% compared to the control case. Furthermore, there is an additional peak in LA pressure at the beginning of ventricular systole (0.28 s) which is more pronounced in simulations that include the ablation lesions AL and BL, suggesting the changed activation sequence or the increase in inactive tissue as a source. In the case of PVI+AL+BL, the pressure is 20% higher compared to the control case. Except for small deviations in volume (within 1 mL of each other) at the beginning of the heart beat, the RA is unaffected by the ablation lesions in the LA.

The contribution of the atrial contraction to ventricular filling reduces in the presence of scars in the LA. This can be observed in the reduced end-diastolic volume (EDV) of the LV. However, this effect is not very pronounced and only reduces the volume contribution by

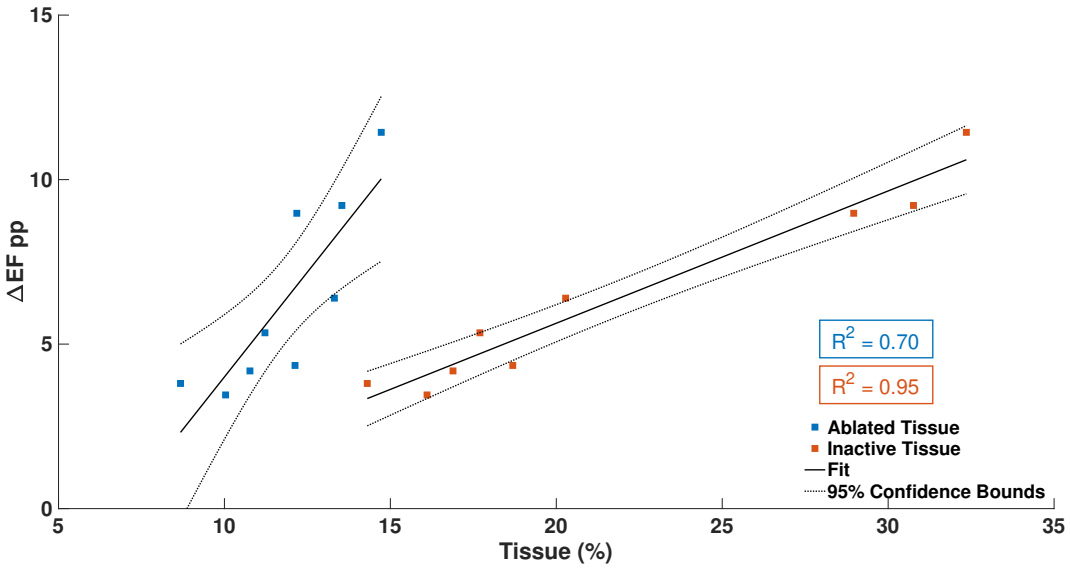

Figure 11.6: Relationship between the ablated tissue (blue squares)/inactive tissue (orange squares) and the percentage point difference in ejection fraction (ΔEP pp) with a fitted linear regression model.

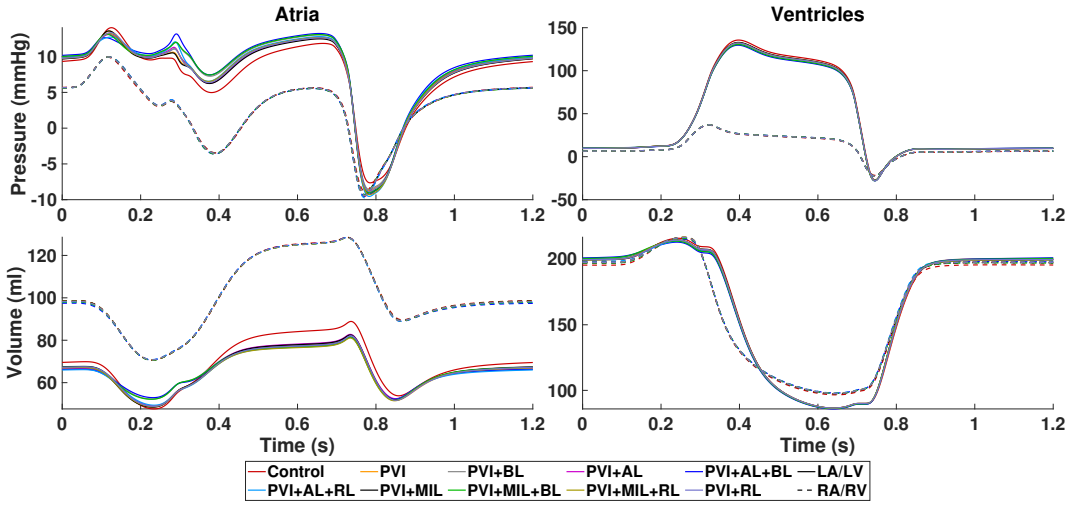

Figure 11.7: Atrial (left column) and ventricular (right column) pressure (top row) and volume (bottom row) courses during one heart cycle. Different colors denote the simulation results of the healthy control case and all simulations including scars. Left atrium and ventricle are shown with solid lines while right atrium and ventricle are shown with dashed lines.

the atria by up to 1.4% as shown in Figure 11.8 (right graph). End-systolic volumes (ESV) of the LV lie within 1% of each other while peak systolic pressure is reduced by 6 mmHg. Furthermore, the increased stiffness of the scars in the LA caused a reduction of the AVPD of the mitral valve (Figure 11.8, middle graph) from +3.90 mm in the control case to +2.76 mm in PVI+AL+BL during atrial contraction. During ventricular contraction, AVPD is reduced from −12.33 mm in the control case to −11.87 mm in PVI+MIL+RL and PVI+RL. Similar

behavior for AVPD and blood volume can be observed in the RV (Figure 11.7 and 11.8, left graph).

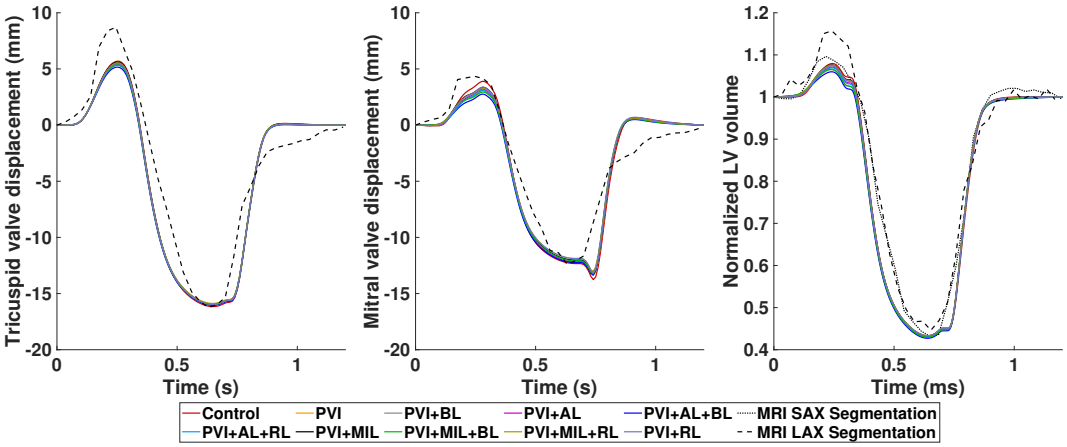

Figure 11.8: Left: Atrioventricular valve plane displacement (AVPD) of the tricuspid valve. Center: AVPD of the mitral valve. Right: Normalized blood volume in the left ventricle during one heart cycle. Different colors denote the simulation results of the healthy control case and all simulations including scars. Simulation results are compared to data from cine MRI short axis (SAX, dotted line) and long axis (LAX, dashed line) segmentations.

11.2.1 Model Sensitivity Towards Scar Stiffness

Since there is not a lot of definitive data on how the stiffness of atrial scar tissue changes compared to healthy myocardium, a sensitivity analysis was conducted to investigate how scar stiffness relates to pressure and volume changes in the heart. Stiffness is mainly controlled by the parameters μ and α in the constitutive model (B.12). Therefore, different combinations of these parameters were chosen for the scars in the PVI+AL+BL case and the outcome on pressure and volume was evaluated based on the relative difference x_{diff} to a PVI+AL+BL simulation with $2 \cdot \mu$ and $5 \cdot \alpha$:

$$x_{\text{diff}} = \frac{x - x^{\text{ref}}}{x^{\text{ref}}_{\text{max}} - x^{\text{ref}}_{\text{min}}} .$$

The results for the left atrium are shown in Figure 11.9. The biggest difference was observed when scar tissue is modeled using the same parameters as for healthy myocardium ($1 \cdot \mu$ and $1 \cdot \alpha$, anisotropic). Both, pressure and volume differences, are largest during ventricular contraction and relaxation. Pressure changed by up to 9% and volume by up to 25%. In general, an increase in stiffness is related to a decrease in volume and an increase in pressure (vice versa with decreased stiffness). Changes in the other chambers of the heart are in the range of 1% to 3%.

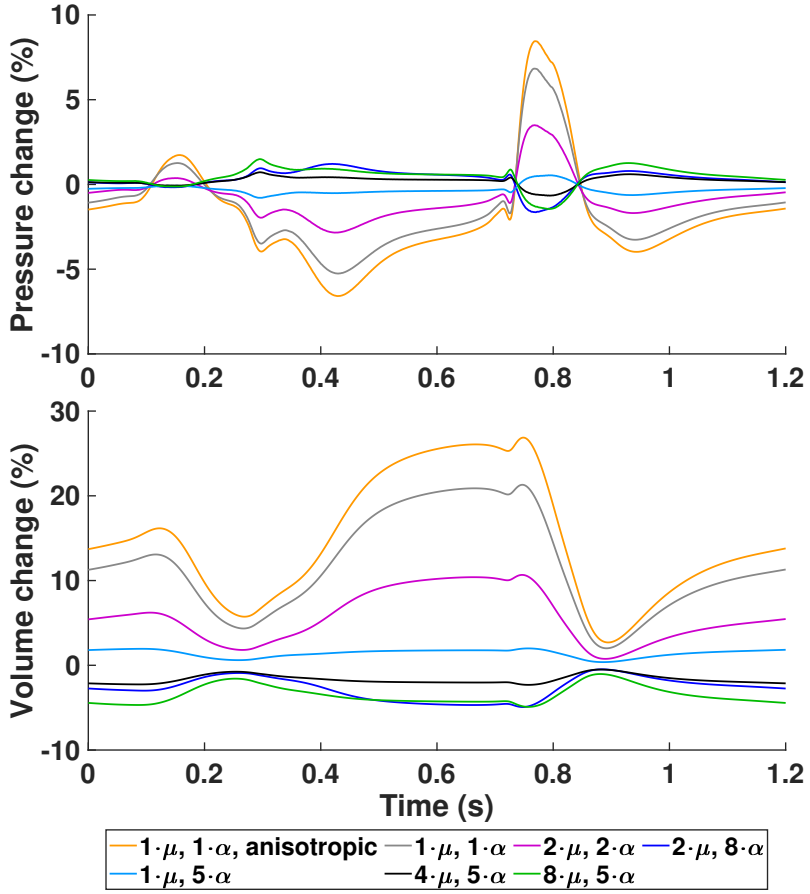

Figure 11.9: Simulation results of the case PVI+AL+BL for varying scar stiffness. The change in pressure and volume of the left atrium is relative to a PVI+AL+BL reference simulation with $2 \cdot \mu$ and $5 \cdot \alpha$ and normalized by their peak-to-peak values.

11.2.2 Reduction of Conduction Velocity

Atrial myocardium that was exposed to long lasting AF can appear to have a reduced conduction velocity due to the presence of fibrosis as a result of electrical and structural remodeling. Therefore, six additional simulations were performed to investigate how a reduced conduction velocity in the atria affects the rest of the heart. For the Control, PVI+AL, and PVI+RL cases the conductivity in both atria was reduced by 25% and 50%, respectively, to cover the diverse spectrum of atrial remodeling. Figure 11.10 shows the activation time maps for the three cases in both scenarios. As expected, reduced conductivities result in a reduced conduction velocity and subsequently in a prolongation of atrial activation. In the case of 50% reduction in conductivity, this results in a 19 ms delay of left atrial emptying in the three scenarios. The change in ejected volume due to this delay is insignificant. The delay in contraction does, however, affect blood pressure in the left atrium. Especially in the case of an AL lesion, since the left atrial appendage takes up to 200 ms to activate which in turn results in a temporal overlap of atrial and ventricular contraction.

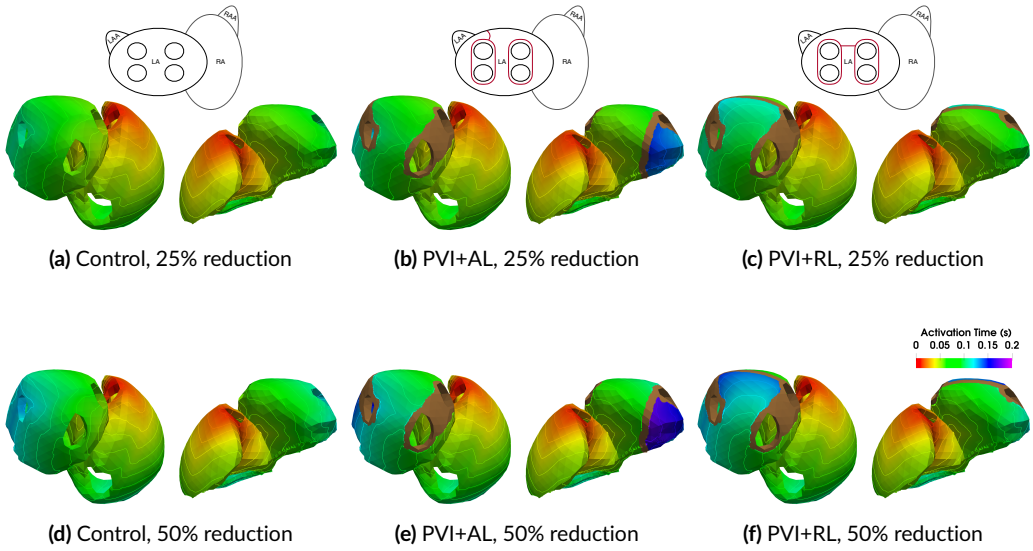

(a) Control, 25% reduction **(b)** PVI+AL, 25% reduction **(c)** PVI+RL, 25% reduction

(d) Control, 50% reduction **(e)** PVI+AL, 50% reduction **(f)** PVI+RL, 50% reduction

Figure 11.10: Activation time map and isochrones for the Control (a+d), the PVI+AL (b+e), and the PVI+RL (c+f) cases with a 25% and 50% reduction in conductivity.

11.3 Discussion

We presented an electromechanically coupled four-chamber heart model including a closed-loop circulatory system that can be used to predict the acute hemodynamic effects of atrial ablation therapy. We used patient specific measurements of AVPD and LV volume from MRI data to parameterize a healthy control case and performed a total of nine virtual ablations in the LA based on combinations of five standardized ablation lesions. The impact of these scars on deformation and cardiovascular performance was evaluated using common biomarkers such as local activation time (LAT), EF, and AVPD.

For the control case, we parameterized the active tension model for the atria and the ventricles such that the simulation results qualitatively matched the LV volume and AVPD evaluated from the volunteer's cine MRI data (see Fig. 11.8). Due to missing data from our healthy volunteer, the majority of parameters for the electrophysiological model and the circulatory system have been adapted from literature values of healthy subjects. Hence, most clinical biomarkers can be reproduced faithfully. With a root-mean-square error of $\mathrm{RMSE}^{\mathrm{LV}}_{\mathrm{Vol}} = 0.02$, $\mathrm{RMSE}^{\mathrm{LV}}_{\mathrm{AVPD}} = 0.38\,\mathrm{mm}$, $\mathrm{RMSE}^{\mathrm{RV}}_{\mathrm{AVPD}} = 0.99\,\mathrm{mm}$ for the normalized LV volume, mitral valve displacement, and tricuspid valve displacement, respectively, the simulated data match the experimental data well. Therefore, we are confident that our model can reproduce physiological deformation patterns.

The ablation lesions in this work were modeled as perfectly isolating tissue. Since there is a scarcity of data on elastomechanical properties of ablation scars in the atria, we increased the mechanical stiffness induced by an accumulation of collagen in the myocardium as it was observed in animal studies [225]. Although these data are based on ventricular remodeling after myocardial infarction, we assume that it is a valid assumption, which is supported by

the findings of [245]. They suggest that RFA scars behave elastomechanically like tissue in zones of chronic myocardial infarction. Additionally, ablated tissue was modeled as isotropic with no preferred direction, since [108] showed that non-reinforced infarcts formed scars with no significant alignment of collagen fibers. This should also be valid for ablations using electroporation or pulse field ablation, since the electrically isolating effect is the same as in RFA. Mechanical changes of the tissue as a result of electroporation are less clear. However, it most likely results in a stiffening of the tissue as well. The increased stiffness resulted in a change of the left atrial EDPVR that did not only correlate with the amount of ablated tissue as one might expect (compare Fig. 11.3 and Tab. 11.5) but rather with a combination of the extent and position of the scars which is in agreement with Phung et al. [238].

With the model presented in this manuscript being more comprehensive than the one published by [16] and [238], our simulations confirm their results for the behavior during atrial systole. In particular, our findings confirm a linear correlation between the change in left atrial EF and the amount of inactive tissue (see Fig. 11.6). This concurs with in vivo observations by [245] in 40 patients who showed a reduced left atrial EF after RFA procedures ($18 \pm 11\%$). Furthermore, a significant change in the activation sequence of the LA due to the ablation lesions AL and RL was observed. Especially the delay in activation of the LAA through the AL lesion can be problematic since a large delay in LAA activation might lead to an overlap with LV contraction. This was observed in our simulations in the form of a sudden increase in LA pressure at the beginning of LV contraction. Such asynchronous contraction patterns are known to cause electrical and mechanical remodeling of the LA [246, 247]. The reduction in stroke volume of the LA results in a lower EDV of the LV. However, this only accounts for maximally 1.8% of LV stroke volume, which would likely not make a significant difference in well being for the patient. The volunteer in this study was a young and healthy male and thus the atrial kick only contributed 11% - 15% to the EDV of the LV. This contribution can be up to 40% especially in older people [239]. Hence, a reduced atrial contraction would likely have a much higher impact on LV performance in these patients.

The increased stiffness of the scar tissue did have a measurable effect during ventricular systole. We observed a reduced AVPD during both atrial and ventricular contraction. The restricted movement of the valve plane resulted in reduced maximal volumes and increased maximal pressures of the LA during LV systole. In the LV, the reduced stroke volume and valve plane movement result in a lower peak pressure during systole. Overall, the right side of the heart is seemingly unaffected by the ablation scars in the LA. Nevertheless, there are slight changes in volume during mid-diastole in the RV due to the adaptations of the closed-loop circulatory system to the changes in pre- and afterload.

11.3.1 Limitations and Perspectives

The focus of this study was to investigate the impact of ablation on the cardiovascular performance of the heart using a computational framework that accounts for the majority of

known physiological mechanisms. In order to do so, we had to make assumptions on some aspects of the model, which may affect the results:

1. Long-lasting AF can lead to electrical, contractile, and structural remodeling of atrial myocytes [248]. In this study, we assumed that all remodeling processes are reversed after a sufficient amount of time has passed. Therefore, the results presented here are more relevant for long-term performance changes due to ablation.
2. We did not account for AF-related atrial fibrosis, which can lead to more complex propagation patterns. For this purpose, a biomechanical model of fibrosis needs to be developed first.
3. Even though it is a valid approach to use linear tetrahedral elements to solve the monodomain equation (3.6), it is known that this element type is prone to volumetric locking in solid mechanics problems. Nevertheless, a recent study has shown that errors in simulated hemodynamic outcomes are small enough when compared to observational uncertainties in clinical measurements [123]. In terms of motion, strains and stresses, [123] observed minor quantitative differences but essentially the same qualitative behavior. Hence, we decided to accept small errors due to volumetric locking in exchange for faster computation to make the amount of simulations required for this study feasible.

Chapter 12

Electromechanical Remodeling During Heart Failure in DCM

This Chapter is based on a Master thesis written by Albert Dasí [42], which was conceptualized and supervised by myself.

Dilated cardiomyopathy (DCM) is one of the most common cardiac disorders [249] and is clinically indicated with an increasing loss of heart function, which ultimately can result in the death of the patient if left untreated. DCM is mainly characterized by an enlargement of the ventricles as well as the atria [250] resulting in progressive eccentric hypertrophy accompanied by remodeling of the cardiac muscle fibers. This remodeling of the muscle fibers combined with the more spherical shape typically results in a severely reduced stroke volume with an ejection fraction (EF) of less than 40 % [251] and elevated levels of wall stress [252]. Excessive dilation of the ventricles can further lead to an enlargement of the atrioventricular valve area. As a consequence, the valves cannot close properly during ventricular systole which further decreases pumping efficiency. Furthermore, microscopic examinations reveal additional extracellular matrix remodeling, characterized by an increase in perivascular and interstitial fibrotic areas [228]. Besides stiffening the heart and increasing the cavity pressure, fibrosis deteriorates the electrical conduction. Considering that DCM patients are at high risk of developing heart failure (HF), electrophysiological changes caused by the extracellular matrix modification, cellular uncoupling, altered Ca^{2+} homeostasis and ion channel remodeling, are equally likely to occur. These electrophysiological abnormalities have shown to be consistent in every HF case [253], DCM included. Although the majority of HF cases (70 % [252]) developed from DCM are due to the chamber dilation and its mechanical implications, there is a high incidence (the remaining 30%) of ventricular arrhythmia which can cause sudden cardiac death. In this sense, the risk of arrhythmogenesis becomes higher with deteriorating left ventricle (LV) function.

The numerous aspects that have to be considered make DCM extremely difficult to deal with and computational models can aid in understanding the complex disease mechanisms. In the past, several studies have tackled the assessment of DCM using computational models [254–262]. However, none of them have considered every aspect of the disease but focused

on specific ones, such as the importance of treating people with poor heart contraction or the hazard of altered electrical activity. Therefore, this project aims at developing a highly detailed model of a failing heart, which provides a complete picture of the disease. Furthermore, this study will assert which remodeling hampers the contractile activity of the heart the most and if a correlation exists between the structural and physiological changes.

12.1 Adaptations to the Electromechanical Heart Model

In order to properly model a case of DCM, several aspects of the electromechanical heart model presented in Part II of this thesis have to be changed. One aspect is the change of the heart's structure itself, which has to represent the dilation of the chambers, the thinning of the walls, and the rearrangement of cardiac muscle cells. Another one is the remodeling that takes place on the cellular level. Since no heart geometry of a DCM case was readily available, the already existing heart model (Fig. 4.1) is adapted. Additionally, stretch activated currents (SACs) are added to the description of the monodomain equation.

12.1.1 Anatomical Remodeling

At first, the remodeling of the anatomy itself due to DCM was introduced by manipulating the mesh mechanically, using a strategic application of different pressure values and boundary conditions with the goal to increase left and right ventricular cavity volume, compression and elongation of the myocardium. The changes of LV and right ventricle (RV) geometrical characteristics given in Table 12.1 are achieved in a two-step process and reproduced previous attempts of describing ventricular remodeling [254–258, 262] best:

1. Apply a pressure of 7000 Pa and 900 Pa to the endocardium of the LV and RV, respectively. Simultaneously, apply a pressure of 50 Pa to the endocardium of both atria and the epicardium to avoid an overall shift in position of the heart itself. To stop the atrioventricular valves from bulging excessively into the atria during this process, zero displacement Dirichlet boundary conditions were applied to the vertexes of the tricuspid valve (TV) and on the atrial side of the mitral valve (MV) a pressure of 7000 Pa was applied to achieve the desired compression and enlargement of the mitral valve annulus [250].
2. After this procedure, the RV volume had increased a bit too much ($\approx 50\%$) compared to the control model. Therefore, a negative pressure of -100 Pa was applied to the endocardium of the RV while simultaneously fixing the vertexes of the rest of the mesh.

This procedure deformed the mesh in such a way that it was necessary to remesh the heart model based on the new surface boundaries to maintain a good element quality throughout the mesh. The result of the anatomical remodeling process is shown in Figure 12.1.

For electrophysiological simulations, the same mesh was refined several times as described in Chapter 5.3.2. Additionally, the myocardium in the ventricles was subdivided into endocardial, myocardial, and epicardial layers of unequal thickness. The proportions of the layers was set to [18-64-18]% in the LV and [23.5-53-23.5]% in the RV based on findings by Dusturia et al. [263].

Table 12.1: Geometrical characteristics of the two heart models used in this project. Percentage indicates change w. r. t. the control model.

Heart Model	Diam. RV (cm)	Diam. LV (cm)	WT RV (cm)	WT LV (cm)	Vol. RV (ml)	Vol. LV (ml)
Control	5.24	4.81	0.361	1.41	188.51	200.56
DCM	5.4 (+3.05%)	6.42 (+33.47%)	0.336 (-6.93%)	0.927 (-34.26%)	248.04 (+31.58%)	425.45 (+112.13%)

WT: Wall thickness; **Diam.:** Diameter; **Vol.:** Volume.

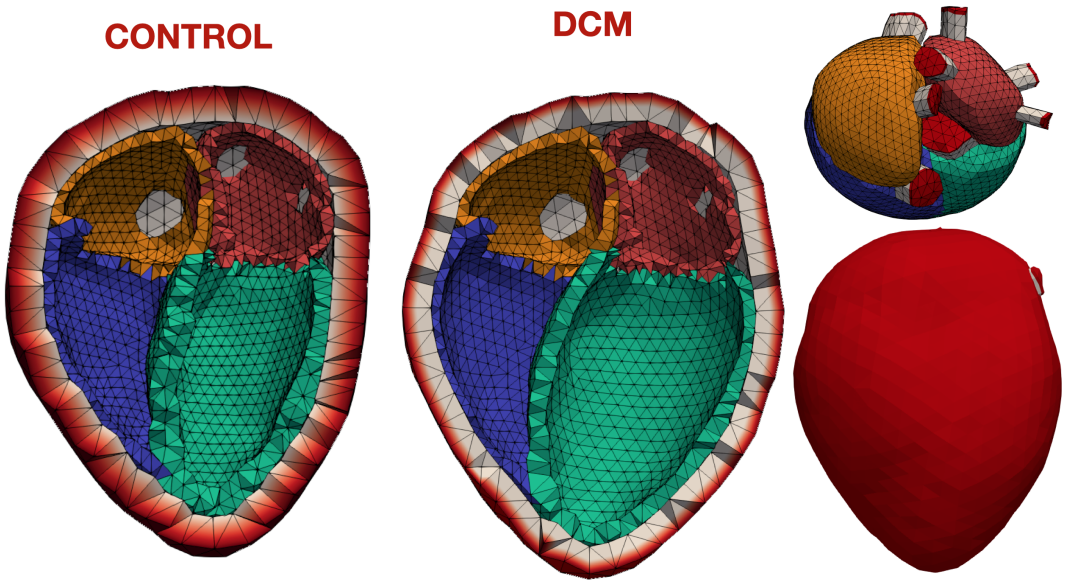

Figure 12.1: Tetrahedral meshes of the control and DCM model clipped in the long axis to showcase the difference in cavitiy size and wall thickness. Red vertexes indicate surfaces with zero displacement Dirichlet boundary conditions. Reprinted with permission from [42].

As a result of the dilation of the LV, the sphericity increases and the LV becomes more round shaped. In the process, remodeling takes place in the myocardium and the

orientation of the myofibers changes throughout the wall. To reflect this in our model, the Laplace-Dirichlet-Rule-Based-Method (LDRBM) by Bayer et al. [141] is used to create three different fiber setups. The first is the same as in the control model, i.e. $\alpha_{\text{endo}} = 60°$ and $\alpha_{\text{epi}} = -60°$. The second case was inspired by literature [254, 259], which reported helical angles of $\alpha_{\text{endo}} = 30°$ and $\alpha_{\text{epi}} = -30°$ in DCM cases. Since the dilation in our model is much more prominent in the LV, a third case was added that differentiates helical angles between the left and right ventricle: $\alpha_{\text{endo}} = 30°$ and $\alpha_{\text{epi}} = -30°$ in the LV and $\alpha_{\text{endo}} = 60°$ and $\alpha_{\text{epi}} = -60°$ in the RV. The resulting fiber configurations are shown in Figure 12.2.

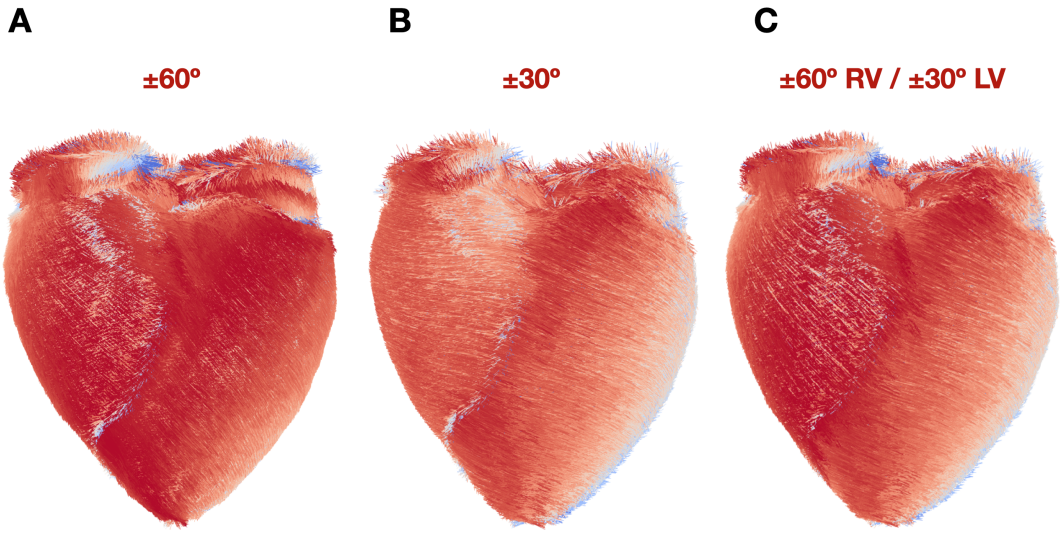

Figure 12.2: Three fiber configurations which are tested on the DCM model. Reprinted with permission from [42].

12.1.2 Stretch Activated Currents

The electromechanical model of cellular activity O'Hara-Rudy-dynamic (ORd)-Land (L17) for the ventricle which was proposed in Chapter 5.1 is modified for the case of DCM and HF in general.

First, the modifications of Mora et al. [264] to the fast sodium current I_{Na} were adopted by shifting the steady state activation (m_{ss}) and inactivation gates (h_{ss} and j_{ss}) as suggested by Passini et al. [157] to match the curves in the ten-Tusscher-Panfilov (TTP) model [194]. Additionally, the conductance G_{Na} was reduced by 60% to maintain $(\frac{\mathrm{d}V_{\text{m}}}{\mathrm{d}t})_{\text{max}}$ in the range of $260\,\mathrm{V\,s^{-1}}$. Furthermore, the conductance G_{NaL} of the late sodium current I_{NaL} was doubled to match values of voltage clamp experiments [265].

Second, the formulation of the ionic current I_{ion} was extended by SACs such that

$$C_{\text{m}}\frac{\mathrm{d}V_{\text{m}}}{\mathrm{d}t} + I_{\text{ion}}(V_{\text{m}}, \mathbf{w}, \mathbf{q}) + I_{\text{sac}}(V_{\text{m}}, \lambda) = I_{\text{app}}(t)\,. \tag{12.1}$$

The SAC proposed by Pueyo et al. [266] was used, which includes potassium selective and non-selective SACs in the form of

$$I_{\mathrm{sac}}^{\mathrm{NS}}(V_{\mathrm{m}},\lambda)=\begin{cases} G_{\mathrm{SAC}}^{\mathrm{NS}}\left(\frac{\lambda-1}{\lambda_{\max}-1}\right)\left(V_{\mathrm{m}}-E_{\mathrm{SAC}}^{\mathrm{NS}}\right) & \text{for} \quad \lambda\geq 1\,, \\ 0 & \text{otherwise} \quad , \end{cases} \tag{12.2}$$

$$I_{\mathrm{sac}}^{\mathrm{K}}(V_{\mathrm{m}},\lambda)=\begin{cases} G_{\mathrm{SAC}}^{\mathrm{K}}\left(\frac{\lambda-1}{\lambda_{\max}-1}\right)\left(\frac{1}{1+\exp\left(\frac{V_{\mathrm{m}}-19.05}{29.98}\right)}\right) & \text{for} \quad \lambda\geq 1\,, \\ 0 & \text{otherwise} \quad , \end{cases} \tag{12.3}$$

with $\lambda_{\max}=1.1$, $G_{\mathrm{SAC}}^{\mathrm{NS}}=0.006\,\mathrm{nS\,pF^{-1}}$, $G_{\mathrm{SAC}}^{\mathrm{K}}=0.2882\,\mathrm{nS\,pF^{-1}}$, and the reversal potential $E_{\mathrm{SAC}}^{\mathrm{NS}}=-10\,\mathrm{mV}$. Notice that the SACs are included in the equations for the intracellular concentrations $[\mathrm{Ca}^{2+}]_{\mathrm{i}}$, $[\mathrm{Na}^{+}]_{\mathrm{i}}$, and $[\mathrm{K}^{+}]_{\mathrm{i}}$ of the ORd model such that they change to

$$\begin{aligned}\frac{\partial[\mathrm{Ca}^{2+}]_{\mathrm{i}}}{\partial t}=&\frac{1}{1+\frac{[\mathrm{CMDN}]_{\max}K_{\mathrm{CMDN}}}{([\mathrm{Ca}^{2+}]_{\mathrm{i}}+K_{\mathrm{CMDN}})^2}}\left[-(I_{\mathrm{pCa}}+I_{\mathrm{Cab}}+\frac{I_{\mathrm{sac}}^{\mathrm{NS}}}{3}-2I_{\mathrm{NaCa}})\frac{A_{\mathrm{cap}}}{2Fv_{\mathrm{myo}}}\right.\\ &\left.-J\frac{v_{\mathrm{nsr}}}{v_{\mathrm{myo}}}+J_{\mathrm{Ca}}\frac{v_{\mathrm{ss}}}{v_{\mathrm{myo}}}-\frac{\partial[\mathrm{Ca}^{2+}]_{\mathrm{TRPN}}}{\partial t}\right]\,,\end{aligned} \tag{12.4}$$

$$\frac{\partial[\mathrm{Na}^{+}]_{\mathrm{i}}}{\partial t}=-\left(I_{\mathrm{Na}}+I_{\mathrm{NaL}}+3I_{\mathrm{NaCa}}+3I_{\mathrm{NaK}}+I_{\mathrm{Nab}}+\frac{I_{\mathrm{sac}}^{\mathrm{NS}}}{3}\right)\frac{A_{\mathrm{cap}}}{Fv_{\mathrm{myo}}}+J_{\mathrm{diff,Na}}\frac{v_{\mathrm{ss}}}{v_{\mathrm{myo}}}\,, \tag{12.5}$$

$$\begin{aligned}\frac{\partial[\mathrm{K}^{+}]_{\mathrm{i}}}{\partial t}=&-\left(I_{\mathrm{to}}+I_{\mathrm{Kr}}+I_{\mathrm{Ks}}+I_{\mathrm{K1}}+I_{\mathrm{Kb}}+I_{\mathrm{sac}}^{\mathrm{K}}+\frac{I_{\mathrm{sac}}^{\mathrm{NS}}}{3}+I_{\mathrm{app}}-2I_{\mathrm{NaK}}\right)\frac{A_{\mathrm{cap}}}{Fv_{\mathrm{myo}}}\\ &+J_{\mathrm{diff,K}}\frac{v_{\mathrm{ss}}}{v_{\mathrm{myo}}}\,.\end{aligned} \tag{12.6}$$

For an explanation of all the different currents and parameters, the reader is referred to the original publication [156].

12.1.3 Cellular Remodeling in DCM and HF

To model the cellular uncoupling, ion channel alterations and abnormal Ca^{2+} handling associated with remodeling in HF patients, the adaptations to the ORd model proposed by Gomez et al. [253] were adopted. A short overview of the changes to the ionic model parameters is given in Table 12.2. Furthermore, experimental studies [228] have shown that the filaments of the sarcomere present an increased Ca^{2+} sensitivity in HF patients with a reduced amount of $[\mathrm{Ca}^{2+}]_{\mathrm{i}}$ to achieve half activation. In our model, this is reflected by modifying Equation (5.6) with a factor of 0.6.

12.1.4 Organ Remodeling in DCM and HF

In DCM, the myocardium is subject to not only cellular remodelling, but also remodelling of the organ itself. Due to the increased blood pressure [267–269] and stress on the myocardium, myocytes are progressively damaged and replaced with connective tissue to strengthen the

Table 12.2: Changes in the ORd model to simulate HF according to Gomez et al. [253].

Ionic parameter modified	% change in the HF model compared to normal
I_{NaL}	180%
τ_{hL}	180%
I_{to}	40%
I_{K1}	68%
I_{NaK}	70%
I_{NCX}	175%
J_{SERCA}	50%
I_{leak}	130%
CaMKa	150%
$J_{rel,NP,\infty,Ca^{2+}sensitivity}$	80%

heart wall. This leads to an increased stiffness of the myocardium which has been reported to be five times higher [260, 261]. Furthermore, the presence of connective tissue in the myocardium reduces the amount of cell-to-cell connections resulting in decreased conduction velocities (CVs) [260]. These tissue specific adaptations are considered in our model by increasing the shear stress modulus μ five-fold in the strain energy function (B.12) and by decreasing the conductivity σ in the diffusion tensor $\mathbf{D}$ of the monodomain equation by 20%. Additionally, an increased end-diastole (ED) blood pressure of $p^{\mathrm{ED}}_{\mathrm{LV,LA}} = 21\,\mathrm{mmHg}$ and $p^{\mathrm{ED}}_{\mathrm{RV,RA}} = 6.5\,\mathrm{mmHg}$ was used in the unloading algorithm proposed in Chapter 5.3.1. Finally, the resistances and the compliance of the systemic blood circulation were modified according to experimental data collected from DCM patients as shown in Table 12.3.

Table 12.3: Literature values for parameters of the systemic blood circulation model in DCM patients. **R** in $\mathrm{mmHg \cdot s \cdot ml^{-1}}$, **C** in $\mathrm{ml \cdot mmHg^{-1}}$.

	Carroll et al. [270]	**Malcolm et al.** [271]	**Pepine et al.** [272]	Baseline values **Schuler et al.** [131]	Chosen values **DCM model**
	DCM	Control (DCM)	Control (DCM)	Control	DCM
R_{SysArt}	– –	– –	0.07 ± 0.02 (0.10 ± 0.02)	0.07 –	– 0.10
C_{SysArt}	– 0.85 ± 0.84	2.00 ± 0.18 (1.29 ± 0.12)	– –	2.00 –	– 1.00
R_{SysPer}	– 1.62 ± 0.56	– –	1.03 ± 0.28 (1.81 ± 0.57)	0.90 –	– 1.70

12.1.5 Simulation Setup

After introducing the changes to our model described in the previous sections, the respective influence of the different HF and DCM specific disease mechanisms on the contraction of the heart can be evaluated. Therefore, the simulation study is designed to cover the influence of the fiber orientation, electrophysological and mechanical HF remodeling, a decrease in conductivity, and an increased stiffness of the myocardium. A short overview of the specifications are given in Table 12.4. The full list is given in Table 12.8. Besides from

Table 12.4: Specifications for the different simulation setups considered in DCM. Electrophysiology ($\mathcal{E}$); Mechanics ($\mathcal{M}$).

Feature	Case	Description
Fiber architecture	0	Fiber gradient of $\pm 60°$ at endocardium and epicardium
	1	Fiber gradient of $\pm 30°$ and $\pm 60°$ in the RV and LV, respectively
HF - E	0	Original ORd model: O'Hara et al. [273]
	1	Modifications proposed by Gomez et al. [253]
HF - M	0	Original L17 model: Land et al. [274]
	1	Modifications based on Bollen et al. [228]
Conductivity	0	Normal ventricular conductivity
	1	20% decrease in conductivity
Stiffness	0	Normal ventricular stiffness
	1	Five-folds increase in ventricular stiffness

testing the influence of individual mechanisms, the combinations and interactions of the mechanisms were evaluated as well. However, this is an immense computational effort especially when using the fully coupled electromechanics model with MEF ($\mathcal{IAE}_{\text{MEF}}$-$\mathcal{MC}$). Therefore, the different simulation setups are broken down into more manageable pieces according to the model they would presumeably influence the most. First, the $\mathcal{E}_{\text{LAT}}$-$\mathcal{MC}$ model is used to evaluate the changes in the circulatory system and the stiffening of the myocardium. The latter is done in three separate runs, where first only the ventricles are subject to the increased stiffness and subsequently the stiffness in the annular rings of the valves and the atria is increased as well. The component $\mathcal{E}_{\text{LAT}}$ indicates that the electrical propagation was precomputed once with the electrophysiology model ($\mathcal{IAE}$) and local activation times (LATs) are used in conjunction with a static calcium transient ([275] in the atria and [178] in the ventricles) to initiate sarcomere contraction in the L17 model.

The remaining simulations are done using the fully coupled electromechanical model. Nevertheless, the modular structure of our simulation framework enables a reduction in computational cost even in those cases. Since all pathological mechanisms considered in this thesis only affect the ventricles, it is acceptable to use precomputed LATs in the atria and only use the ventricles in the coupled model.

Parameters used in the electrophysiological model are given in Table 12.5. Since the ventricles were partitioned into endo-, mid-, and epicardial layers, the ORd model was

used with its respective heterogeneous variants. For the stimulation protocol, the Purkinje muscle junction model as described in Chapter 5.3 was used to reproduce LATs reported in Durrer et al. [59]. The passive properties of the myocardium were described by the strain energy function of Guccione et al. [201] with the parameters set to the ones in Table 12.6 for the control case. Besides the HF remodeling in the L17 model, parameters were adjusted according to Appel et al. [36, 37] when used in conjunction with the endocardial ORd model to achieve a more homogeneous contraction pattern. Due to the lower resolution of the mechanical mesh in this study, spatial discretization was done using ten-node tetrahedral elements with quadratic shape functions to reduce locking effects. The mean edge length of the mechanical mesh was $h_2 = 7.51 \pm 2.9\,\text{mm}$ with 89718 quadratic tetrahedral elements and 139593 DoF. For the electrophysiology mesh, 640256 linear tetrahedrons with a mean edge length of $h_1 = 1.7 \pm 0.4\,\text{mm}$ and a total of 134117 DoF was used. Take note that the electrophysiology mesh for the coupled simulations only contains the ventricles. Time integration was done using the increments $\Delta t_{\mathcal{M}} = 0.001\,\text{s}$, $\Delta t_{\mathcal{C}} = 0.0001\,\text{s}$, $\Delta t_{\mathcal{E}} = 0.00001\,\text{s}$.

Table 12.5: Parameters for the electrophysiological model.

Parameter	Value	Unit	Description
$(\sigma_\text{f}, \sigma_\text{s}, \sigma_\text{n})$	$(1.6250, 0.3250, 0.3250)$	S/m	conductivities in ventricular myocardium
$(\sigma_\text{f}, \sigma_\text{s}, \sigma_\text{n})$	$(1.3000, 0.2600, 0.2600)$	S/m	conductivities in ventricular myocardium in DCM
$(\sigma_\text{f}, \sigma_\text{s}, \sigma_\text{n})$	$(0.7458, 0.2295, 0.2295)$	S/m	conductivities in atrial myocardium
$(\sigma_\text{f}, \sigma_\text{s}, \sigma_\text{n})$	$(2.1245, 0.7458, 0.7458)$	S/m	conductivities in Bachmann's bundle (BB)
$(\sigma_\text{f}, \sigma_\text{s}, \sigma_\text{n})$	$(2.1245, 0.7458, 0.7458)$	S/m	conductivities in pectinate muscle (PM)
$(\sigma_\text{f}, \sigma_\text{s}, \sigma_\text{n})$	$(2.1245, 0.7458, 0.7458)$	S/m	conductivities in crista terminalis (CT)
$(\sigma_\text{f}, \sigma_\text{s}, \sigma_\text{n})$	$(0.2332, 0.2332, 0.2332)$	S/m	conductivities in isthmus
β	140000	1/m	membrane surface-to-volume ratio
C_m	0.01	F/m^2	membrane capacitance
t_AVN	0.150	s	atrio-ventricular conduction delay
BCL	1.0	s	basic cycle length ($= 1/\text{heartrate}$)

Table 12.6: Constitutive law parameters for the whole heart model in the control case. For DCM, μ was increased by a factor of 5.

Domain	Parameters								
	$\mu\,(\text{Pa})$	b_ff	b_ss	b_nn	b_fs	b_fn	b_ns	$\kappa\,(\text{Pa})$	$\rho_0\,(\text{kg m}^{-2})$
$\Omega_\text{RV,LV,RA,LA}$	308.9	17.72	7.9	7.9	12.4	12.4	12.4	10^6	1082
Ω_P	308.9	17.72	7.9	7.9	12.4	12.4	12.4	10^6	1082
$\Omega_\text{MV,TV,AV,PV}$	50000	-	-	-	-	-	-	$2 \cdot 10^5$	1082
Ω_OR	14900	-	-	-	-	-	-	$2 \cdot 10^5$	1082
Ω_FAT	3725	-	-	-	-	-	-	$2 \cdot 10^5$	1082

12.2 Results

12.2.1 Circulatory System Adaptations

The effect of adjusting the circulatory system with respect to literature values of DCM cases is evaluated using the $\mathcal{E}_{\text{LAT}}$-$\mathcal{MC}$ model. Although increasing the systemic resistance and reducing the systemic compliance result in a reduction of the EF (17% to 12%) and stroke volume (SV) (67 ml to 49 ml), the end-systolic (ED) and ED pressure is more in line with experimental observations [276–280]. Therefore, the modified settings are used for the rest of the simulations.

Biomarkers	Org.	Mod.
EF (%)	17	12
SV (ml)	67	49
LVEDV (ml)	378	396
LVEDP (mmHg)	10	16
LVESP (mmHg)	64	95

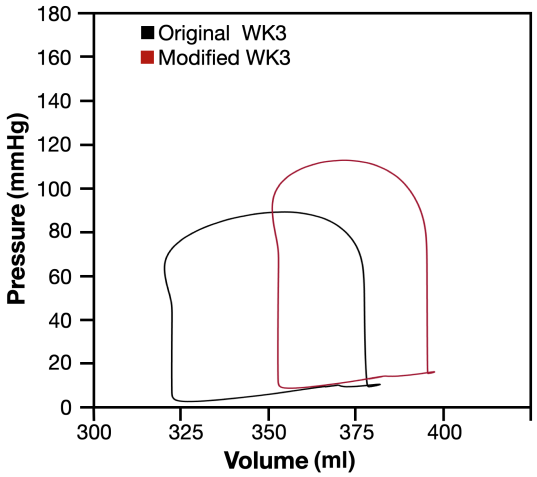

Figure 12.3: Left ventricle pressure-volume loops and characteristic biomarkers of the original and modified three-element Windkessel (WK3) model. Reprinted with permission from [42].

12.2.2 Increased Stiffness of the Myocardium

In order to specify which part of the myocardium should be stiffened, three different settings are evaluated and compared to the control case using the $\mathcal{E}_{\text{LAT}}$-$\mathcal{MC}$ model. Figure 12.4 illustrates that stiffening the ventricles and rings (S_{VR}) is the situation that better preserves the values from the Control case. S_{VR} shows an enhanced mechanical response compared to stiffening only the ventricles (S_{V}), in terms of EF (12% in S_{VR} vs. 11% in S_{V}) and SV (41 ml in S_{VR} vs. 37 ml in S_{V}), and a proper ED pressure compared to control (22 mmHg in S_{VR} vs. 16 mmHg in Control) [267–269]. Accordingly, S_{VR} will be the case to compare against control stiffness in the coupled approach.

Biomarkers	Control	S_V	S_{VR}	S_{VRA}
EF (%)	12	11	12	11
SV (ml)	49	37	41	40
LVEDV (ml)	396	346	349	331
LVEDP (mmHg)	16	20	22	13
LVESP (mmHg)	95	76	82	63

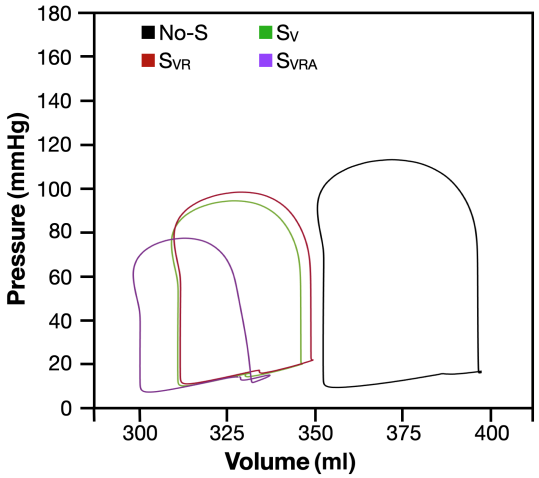

Figure 12.4: Left ventricle pressure-volume loops and characteristic biomarkers of four scenarios in which different structures of the myocardium are stiffened. **S:** Stiffness; **V:** Ventricles; **R:** Rings; **A:** Atria. Reprinted with permission from [42].

12.2.3 Fiber Reorganization

The orientation of cardiac muscle cells changes in the process of eccentric hypertrophy of the ventricles. The dilation of the chamber leads to a more spherical arrangement of the muscle fibers and thus a reduction of the helix angle throughout the myocardium. To evaluate the effect of different fiber orientations, three different setups were tested using the fully coupled model. Figure 12.5 shows the contraction of the heart for helix angles of $\pm 30^\circ$ in LV / $\pm 60^\circ$ in RV, and $\pm 30^\circ$ or $\pm 60^\circ$ in both ventricles, respectively.

The more concentric arrangement of fibers in the LV leads to a loss in wringing motion and a contraction that elongates the LV instead of shortening it. Furthermore, it is accompanied by a reduction of atrioventricular plane displacement (AVPD). This behavior cannot be compensated for by larger helix angles in the RV. MRI of DCM patients does not support these contraction patterns (e.g. [280]). Therefore, for further simulations of DCM, the helix angle $\pm 60^\circ$ is used in both ventricles.

12.2.4 Reduced Conductivity

LATs of the simulations with and without reduced conductivity in the ventricles is shown in Figure 12.6. The depolarization starts in the sinoatrial node (SAN) next to the superior vena cava (SVC) and propagates to the left atrium (LA) via the interatrial connections and the Bachmann's bundle (BB). In accordance with Guyton and Hall [281], the atria are fully depolarized within 90 ms.

After a fixed delay of 150 ms, the ventricles start to depolarize at the Purkinje muscle junctions. In the Control case, the ventricles are fully depolarized within 70 ms, matching

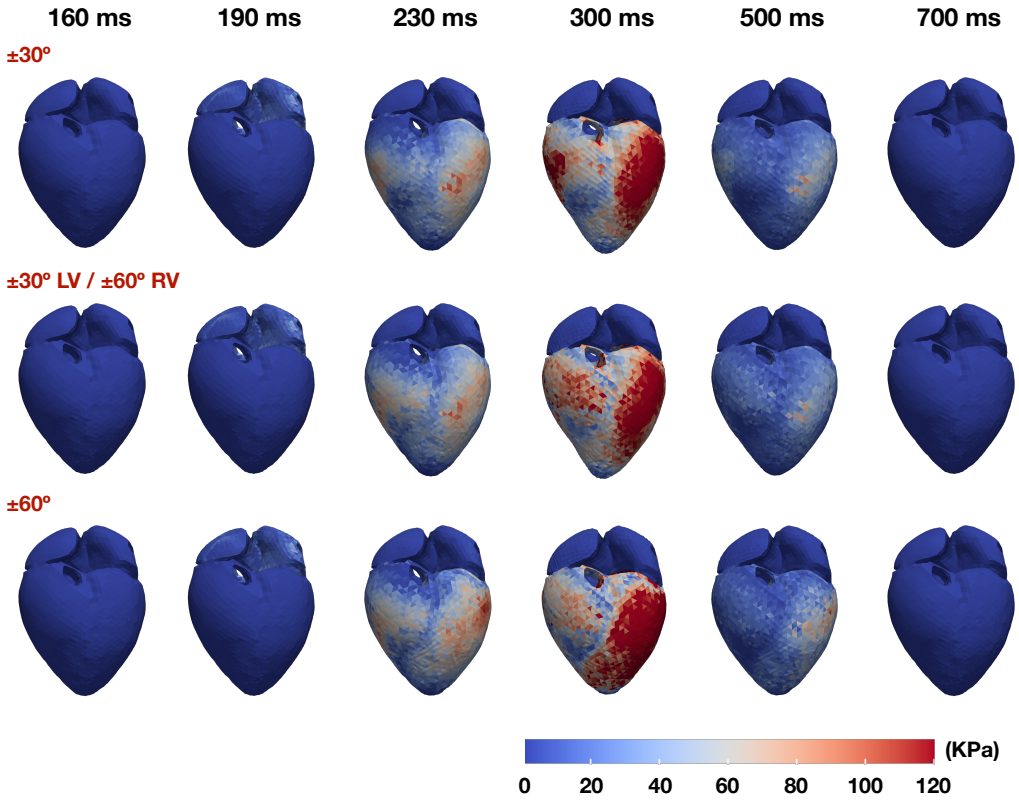

Figure 12.5: Active tension during the entire heart beat is shown for varying helix angles in the LV and RV. Reprinted with permission from [42].

observations by Durrer et al. [59]. The reduction in conductivity in the DCM case prolongs total ventricular activation by 20 ms.

Despite the measurable differences in LATs, decreasing ventricular conductivity does not affect mechanical contraction. This holds true even when combined with an increased stiffness of the ventricles as shown in Figure 12.7. Therefore, the reduction of conductivity is not further discussed to avoid duplicated results.

12.2.5 Cellular Remodeling

Influence of Stretch Activated Currents

The influence of SACs on the transmembrane voltage V_{m}, intracellular calcium concentration $[\mathrm{Ca}^{2+}]_{\mathrm{i}}$, and active tension T_a in the coupled ORd+L17 model under isometric conditions ($\lambda \in [0.8, 1.2]$) is shown in Figure 12.8. As expected from the formulation of SACs by Pueyo et al. [266], $I_{\mathrm{sac}} = 0$ in contracted cardiomyocytes ($\lambda \leq 1$). For $\lambda > 1$, the SAC is depolarizing the cell resulting in a raised resting membrane voltage when the cell itself is not excited. Furthermore, calcium uptake into the cell is increased by the SAC enhancing

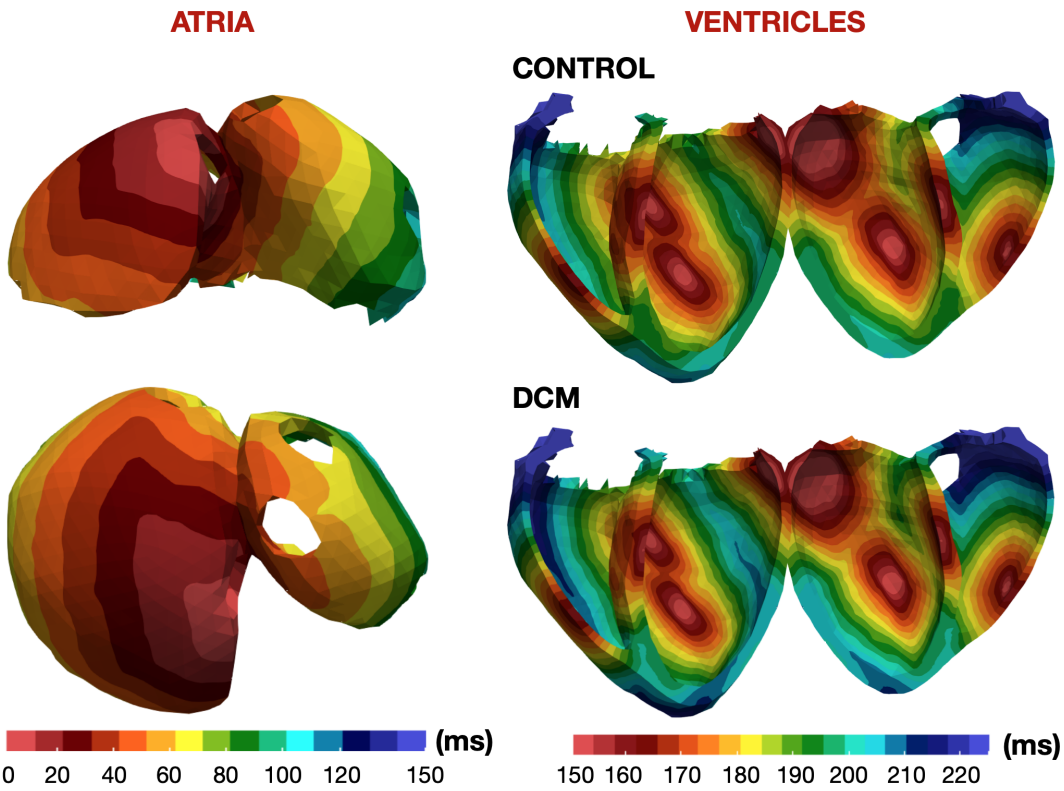

Figure 12.6: LATs in the atria and ventricles in the Control and DCM case. Conductivity of the ventricles in DCM was reduced by 20%. Reprinted with permission from [42].

the possibility for calcium ions to bind to troponin C. Consequently, more crossbridges are formed, leading to an increase in tension development. This result is in agreement with the behavior previously reported in atrial myocytes [282]. Even though peak $[Ca^{2+}]_i$ at a stretch of 1.2 is highest in the epicardial variant of the cell model, the developed tension is the same in all three variants, suggesting that all troponin C binding sites are occupied already. SACs equally promote the shortening of the action potential duration and a reduction in peak membrane voltage, which is the result of a shift in the intracellular concentration of not only calcium, but also sodium and potassium.

Remodeling Derived From Heart Failure

Remodeling due to HF is introduced at the cellular level and the effect on the transmembrane voltage V_m, intracellular calcium concentration $[Ca^{2+}]_i$, calcium bound to troponin C $[Ca^{2+}]_{TRPN}$, and active tension T_a is shown in Figure 12.9. To better identify the changes resulting from electrophysiological (HF-E) and mechanical (HF-M) remodeling, the suggested changes by Gomez et al. [253] and Bollen et al. [228] were introduced separately into the model. The control model refers to the ORd+L17 model with SACs using $\lambda = 1$ such

Biomarkers	Test 00	Test 01	Test 02	Test 03
EF (%)	14	13	14	13
SV (ml)	56	46	56	46
SW (Nm)	0.85	0.59	0.85	0.59
LVEDV (ml)	405	353	405	353
LVEDP (mmHg)	20	24	20	24
LVESP (mmHg)	124	105	124	105

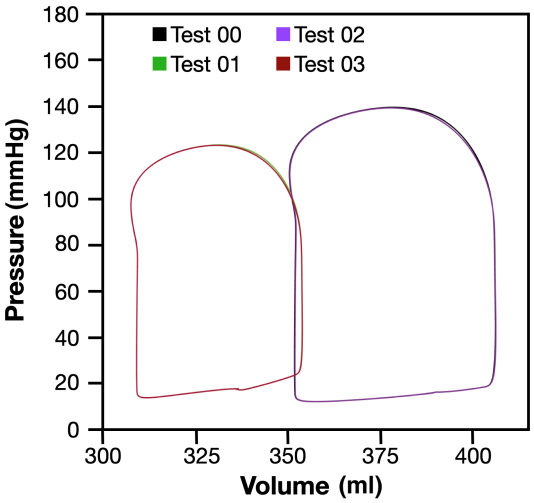

Figure 12.7: Left ventricle pressure-volume loops and characteristic biomarkers of the Control (Test 00), increased stiffness (Test 01), reduced conductivity (Test 02), and reduced conductivity with increased stiffness (Test 03). Test 00 and 02 as well as Test 01 and 03 are overlapping. Reprinted with permission from [42].

that effects from electromechanical coupling and SACs have no effect and changes from remodeling can be clearly separated.

When mechanical remodeling is considered, cardiomyocytes are modified to present an increased sensitivity to calcium and a reduced half activation point. As a result, more calcium can bind to troponin C leading to an increased formation of crossbridges and higher active tension. This is illustrated well by comparing the HF-M and Control cases. Electrophysiological remodeling has an overall detrimental effect on the cell. Due to the reduced intracellular calcium concentration, the affinity of calcium to bind to troponin C is reduced as well, resulting in a decrease of active tension. Both of these effects are in agreement with experimental observations [253]. Combining both types of remodeling means that the respective effects negate themselves to some degree. However, overall tension development is still altered. Most noticeable is a shift in the time to peak tension compared to the non-remodeled case.

Remodeling in Tissue Simulations

After looking at the effects of HF derived remodeling on the cellular level, it was evaluated on the tissue level as well. The transmembrane voltage V_{m} and active tension T_a using the original ORd-L17 model (Test 03), electrophysiological remodeling (Test 11), and electromechanical remodeling (Test 15) is shown in Figure 12.10. Purely electrophysiological remodeling results in a longer repolarization period of the ventricles. Additionally, the developed active tension is reduced. The same result is achieved by implementing electromechanical remodeling, except that the active tension is increased compared to pure electrophysiological

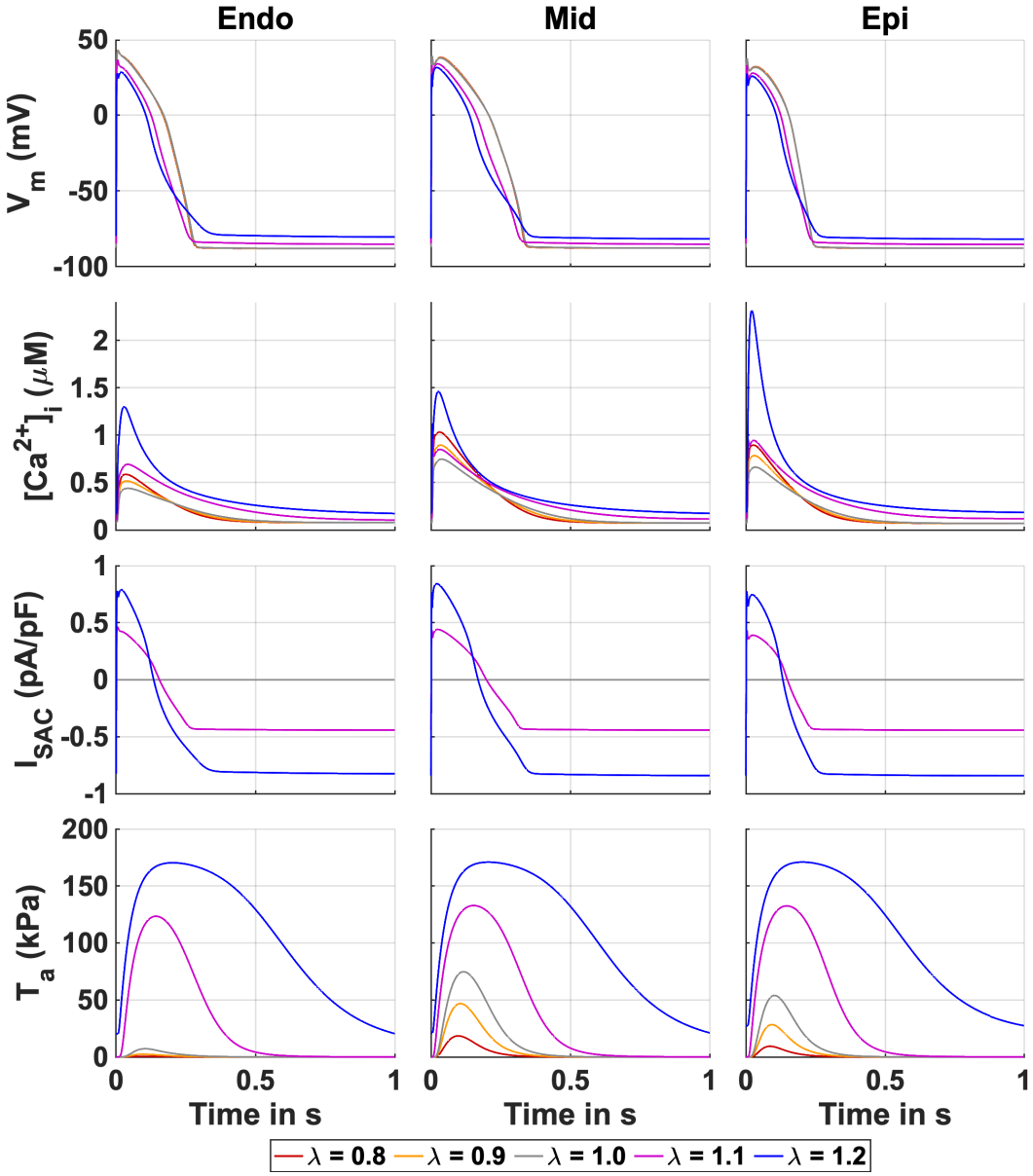

Figure 12.8: Transmembrane voltage V_{m}, intracellular calcium concentration $[\mathrm{Ca}^{2+}]_{\mathrm{i}}$, stretch activated current $I_{\mathrm{sac}} = I_{\mathrm{sac}}^{\mathrm{NS}} + I_{\mathrm{sac}}^{\mathrm{K}}$, and active tension T_a under isometric conditions.

remodeling. These observations are consistent with the results of the previously discussed cellular simulations.

12.3 Discussion

The goal of this project was to develop and evaluate a detailed computational model of DCM. For this purpose, different pathomechanisms related to DCM were implemented and

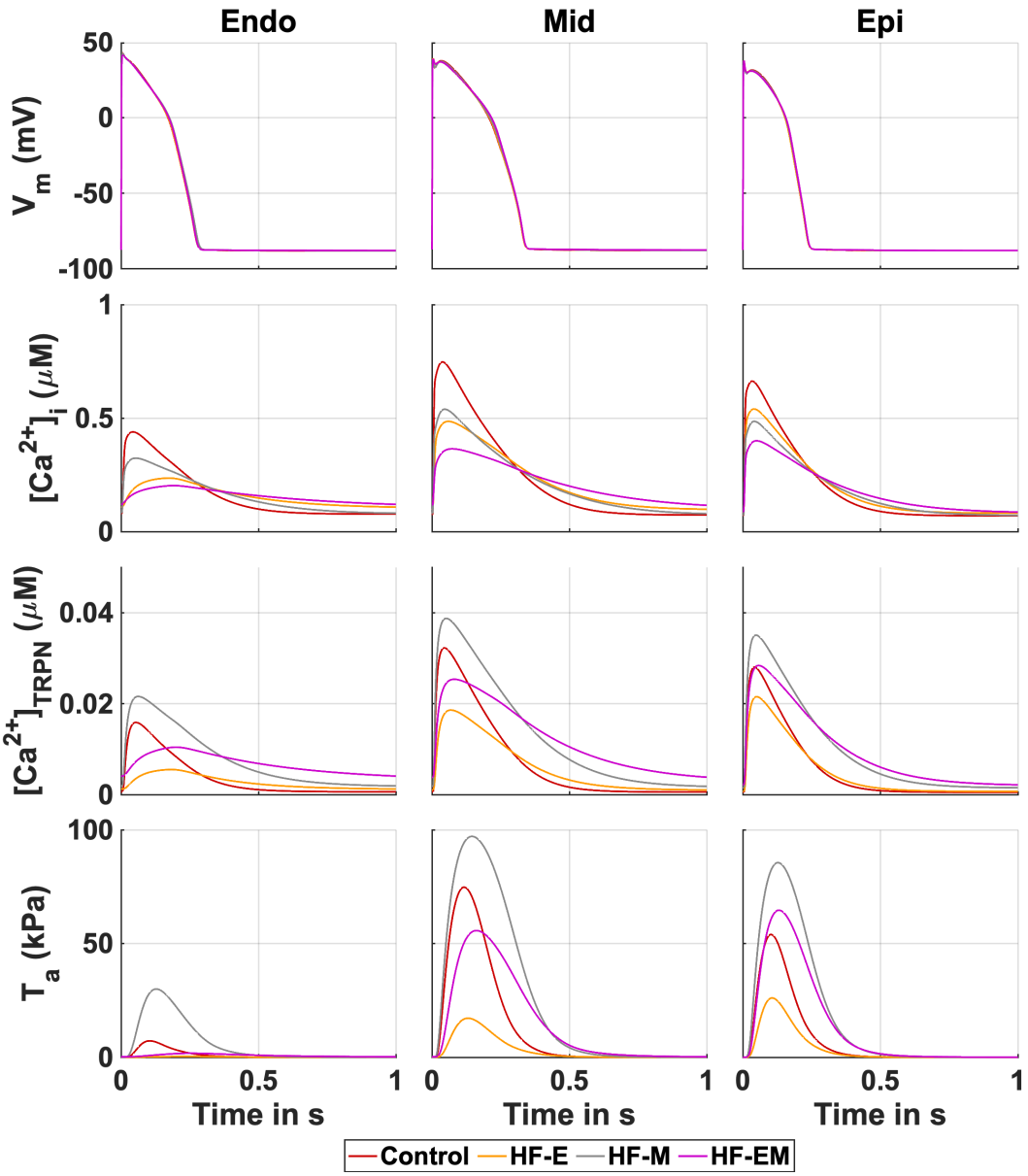

Figure 12.9: Transmembrane voltage V_{m}, intracellular calcium concentration $[\mathrm{Ca}^{2+}]_{\mathrm{i}}$, calcium bound to troponin C $[\mathrm{Ca}^{2+}]_{\mathrm{TRPN}}$, and active tension T_a in the control model and remodeling derived from heart failure. Heart failure scenarios are separated into electrophysiological remodeling (HF-E), mechanical remodeling (HF-M) and both (HF-EM).

tested on the cellular level and in whole heart simulations to gain insight into the individual relevance of each mechanism towards the disease and how they correlate with each other. Accordingly, the main findings resulting from this work are:

1. Cellular alterations, especially those affecting electrophysiology, are mainly responsible for the poor mechanical activity of the heart in patients with DCM.

2. Multi-scale alterations of the myocardium, such as fiber reorganization and cellular uncoupling, have little effect on the mechanical behavior.
3. Structural remodeling and increased stiffness of the myocardium as well as adaptations of the circulatory system are necessary to replicate in vivo observations.

12.3.1 Anatomical Remodeling

An anatomical model of the heart of a healthy volunteer was adapted to reproduce typical features of DCM, namely the dilation of the LV and thinning of the walls. In the process, the diameter of the LV was increased by approximately 33% [254, 256, 262] from an initial value of 48.1 mm to 64.2 mm. Both of these match values reported in literature for healthy hearts $50(8)$ mm [283] and dilated hearts in computational ($64(8)$ mm [284]) and experimental studies ($70(10)$ mm [285]; $69(9)$ mm [286]). The myocardium of the LV and the septum was thinned by 33% in order to impair contraction, which, among other things, is determined by the size and shape of the heart [284]. The ED volume of the ventricles in our model (425.45 ml and 248.04 ml for the LV and RV, respectively) was higher than values reported for DCM patients (269 ± 93 ml [286]; 317 ± 98 ml [287] for the LV; 219 ± 39 ml for the RV). This is most likely due to the already above average ventricular volumes of the volunteers anatomy (LV: 200.56 ml vs. 136 ± 24 ml [288]).

12.3.2 Fiber Arrangement

The influence of the myofiber architecture was analysed through the development of three fiber configurations using a rule-based algorithm [289]. Apart from the linear variation of $\pm 60^\circ$ across the myocardium, reported in numerous works [254, 290], a transmural gradient of $\pm 30^\circ$ was also studied. Two fiber configurations were set to $\pm 30^\circ$, in accordance with other computational studies [259], since some authors [227] have proven that healthy hearts present steeper fiber angles at endocardium and epicardium than DCM, which are characterized by oblique orientations.

Whether or not DCM patients are subject to fiber reorganization is a matter of controversy. Nonetheless, modeling the exact alteration is far from straightforward. One publication [260] has even claimed that the myofiber transmural gradient is increased in DCM patients, based on studies conducted with failing canine hearts [291]. Nevertheless, Helm et al. [291] observed little change in the myofiber angle regardless of the global dilation, in accordance with other experimental works with canine models [292]. Eggen et al. [227], who compared healthy and DCM human hearts, stated that the fibers were more obliquely arranged in DCM, highlighting a major predisposition around $\pm 40^\circ$. Statistical differences between both groups could not be confirmed.

Although it can be hypothesized that the fiber reorganization results from the DCM heart assuming a more spherical shape [249, 252], this work has shown that a low fiber

gradient does not reproduce a realistic contractile activity. Neither a helical angle of $\pm 30^{\circ}$ at endocardium and epicardium, nor the model which only considers an impaired LV did yield a proper contraction of the ventricles. Similar results have been reported by Finsberg et al. [293], who analyzed the effect of different fiber architectures on healthy hearts. The authors showed that, although models developed with lower angles fitted experimental pressure-volume loops, they behaved poorly in terms of the circumferential strain. Indeed, they argued that only steep fiber gradients, pointing out $\pm 70^{\circ}$ and $\pm 80^{\circ}$, showed a proper mechanical response.

The elongation of the ventricles observed when the fiber angle varied linearly around $\pm 30^{\circ}$ has been previously reported by Tokuda et al. [294]. The authors detected that fiber architectures of $\pm 20^{\circ}$ and $\pm 40^{\circ}$ presented elevated twist angles compared to $\pm 60^{\circ}$ and $\pm 80^{\circ}$, which in turn increased the torsion of the ventricles. As a result, when analyzing the end-systole (ES) geometry between lower and normal fiber gradients, similar outcomes were obtained. This proves that only steeper fiber angles at or above $\pm 60^{\circ}$ enable a realistic contraction of the heart.

12.3.3 Conductivity

Cellular uncoupling and subsequent slowed conduction derived from HF were modeled by decreasing ventricular conductivity by 20% [260, 295]. Although it had a clear impact in the electrophysiological model, causing a delay of around 20 ms in the ventricular LATs, no further alterations were found in the mechanics. Not only did it not have a detrimental effect on the contractile activity, evaluated through the assessment of the pressure-volume loops and characteristic circulatory curves, but it also led to similar biomarkers to those obtained in the Control case. These results are consistent with previous in silico studies [295]. Constantino et al. [295] evaluated the influence of four remodeling features on the mechanical behavior of the heart: stiffness, slowed conduction, altered structure of the heart (both fibers and heart geometry) and abnormal calcium handling. The assessment of the multiple combinations proved that changes in the ventricular conductivity hardly modified the electromechanical delay, which is the time period between the depolarization of cardiomyocytes and cellular contraction.

Although it may seem that Constantino et al. [295] provided enough evidence that a reduction in conductivity is not necessary, they modeled the abnormal calcium handling through little variations in the relaxation rate and peak amplitude of the calcium transient. By contrast, the electrophysiological remodeling proposed by Gomez et al. [253], adopted in the present work, considered a transmurally dependent modification of twelve variables in the ORd model. The severe effect of this remodeling on the action potential, intracellular calcium transient and active tension, which has been perfectly illustrated in Figure 12.9, made it crucial to evaluate again the integrated effect of the alterations included at cellular and organ level.

Gomez et al. [253] evaluated the effect of cellular uncoupling in a one dimensional transmural ventricular strand. Four cases of decreased conductivity were assessed: no-

uncoupling (0% reduction), mild (25% reduction), normal (50% reduction) and severe uncoupling (75% reduction). Although the mechanical implications of hampering the ventricular conductivity were not investigated, the unicellular uncoupling, together with the insertion of fibrosis, resulted in the dispersion of the action potential duration and transmural repolarization.

Moreover, it should be taken notice that the heart has been paced with a basic cycle length of 1000 ms, which accounts for a resting state. In a stress situation, the heart rate can reach values up to 180 to 200 beats per minute [281], which translates into a basic cycle length of 300 ms. In DCM, the myocardium needed a period of time slightly longer than 240 ms to be entirely activated, which made it almost 600 ms if we consider the 200-300 ms that stand for the action potential duration. If the heart had been subject to increased pacing, slowing the ventricular conduction might have had a greater impact, since it could also lead to the generation of arrhythmias [253].

12.3.4 Stiffness

The increased stiffness observed in DCM patients [228, 296] was modeled by upscaling the shear modulus in the Guccione et al. [201] constitutive model [260, 261]. Apart from stiffening only the ventricles, the mechanical response of the myocardium when the rings and atria were likewise stiffened was evaluated. The latter was considered since the rings [297] and atria [250] might be subject to structural alterations in DCM patients as well. Indeed, the pressure-volume loops obtained when stiffening both, ventricles and rings (S_{VP}), were more accurate than those in which only the ventricles (S_V) were considered.

12.3.5 Cellular remodeling

Electrophysiology

The electrophysiological remodeling proposed by Gomez et al. [253] proved to impact mechanical activity to the greatest degree. The results at the cellular level suggest that this is due to an abnormal calcium homeostasis, characterized by reduced systolic and elevated diastolic calcium concentrations. Besides decreasing the overall tension developed by the model, the electrophysiological remodeling delays the diastolic relaxation of the myocardium. The prolongation of the ventricular repolarization can lead to several problems, especially considering that the dispersion of the action potential duration is highly proarrhythmic [253]. Adeniran et al. [298] adopted the same cellular remodeling and observed that this outcome was more pronounced when the heart was paced with a basic cycle length of 500 ms. The risks subject to increasing the pacing in HF has already been mentioned and both, ion channel remodeling and cellular uncoupling, potentially worsen the situation.

Mechanics

To the best of our knowledge, no previous work has tried to modify parameters in the Land et al. [274] model to reproduce the effects of HF. Adeniran et al. [298] introduced modifications in the Tran et al. [299] model to mimic the myofilament behaviour in failing hearts. However, their changes were based on experimental studies looking at patients with HF with preserved EF. Therefore, a potential formulation is presented for the first time in this work. It is based on experimental results [228], but it is only when the electrophysiological remodeling is considered as well, that the model properly imitates the mechanical performance of DCM patients.

12.3.6 Validation

In this last section, experimental results from literature are used to validate the computational model of a DCM heart in this study. Table 12.7 gathers the biomarkers obtained through the LV pressure-volume loops for simulations with the fully coupled model. Cases in which the fiber gradient was $\pm 30^{\circ}$ and the conductivity was decreased have been omitted due to their limited impact on mechanic function.

Ejection fraction The range of EF measured in the DCM model was between 9% and 15%. Although the results are below the experimental values, it must be taken into account that the EF obtained with the baseline heart was around 30%. Therefore, if relative values are examined instead, the reduction in the EF achieved after implementing anatomical and HF remodeling ranges from 50% to 70%. This is consistent with the experimental results collected in Table 12.7. Radau et al. [280] observed an average reduction in EF of 48% (from 63% in healthy subjects to 33% in DCM patients). A greater decrease of 65% for Group I (from 61% to 22% in controls and patients, respectively) and 67% for Group II (20% for DCM patients), was shown by Wittstein et al. [279]. Similarly, Warriner et al. [278] detected reductions of 51% for Group I (from 65% to 32%) and 62% for Group II (from 65% to 25%). To summarize, an EF in the computational model ranging from 12% (60% reduction) to 15% (50% reduction) is in agreement with experimental values. Furthermore, even the absolute values are in the range of previous in silico models [295], in which an EF of 11% was obtained for the failing model.

Volume The results obtained for the SV and left ventricular ED volume are in accordance with the experiments. SV in DCM patients ranges from 33 ml to 95 ml, which covers every value obtained through the different combinations of features. Yet, the SV produced by the model is below the experimental average. For left ventricular end-diastolic volume (EDV), several Tests are within the reported intervals, with Test 15 being the best approximation.

Table 12.7: Patients characteristics and computational biomarkers. Reprinted with permission from [42].

	Study n° Patients	**EF** **%**	**SV** **ml**	**SW** **Nm**	**LVEDV** **ml**	**LVEDP** **mmHg**	**LVESP** **mmHg**
In-Vivo	Alter et al. [276] 8	25 ± 8	75 ± 20	0.367 ± 0.157	315 ± 54	28 ± 11	114 ± 20
	Kim et al. [277] 18	33 ± 9	–	–	–	22 ± 8	113 ± 14
	Warriner et al. [278]						
	Group I – 62*	32 ± 10	71 ± 21	–	237 ± 62	–	–
	Group II – 129*	25 ± 10	63 ± 30	–	273 ± 98	–	–
	Wittstein et al. [279]						
	Group I – 8	22 ± 3	54 ± 5	–	270 ± 25	19 ± 1	117 ± 8
	Group II – 5	20 ± 3	45 ± 5	–	233 ± 39	21 ± 3	106 ± 4
	Radau et al. [280]						
	12**	33 ± 13	–	–	234 ± 63	–	–
	Test						
In-silico	00	14	56	0.853	405	20	124
	01	13	46	0.597	353	24	105
	04	15	57	0.807	379	20	110
	05	14	50	0.629	340	24	106
	08	–	–	–	–	–	–
	09	9	33	0.250	353	25	68
	12	–	–	–	–	–	
	15	12	40	0.366	333	25	80

EF: Ejection fraction; **SV:** Stroke volume; **SW:** Stroke work; **LVEDV:** Left ventricle end-diastolic volume; **LVEDP:** Left ventricle end-diastolic pressure; **LVESP:** Left ventricle end-sistolic pressure;.
* High portion of patients (50%) with ischemic DCM. No differentiation between idiopathic and ischemic DCM
** Sunnybrook Cardiac Data. Cardiac Atlas Project
– Simulations that finished unsuccessfully

Stroke work Similar to the left ventricular EDV, Test 15 did yield almost identical results to those reported in literature (0.366 Nm in the model vs. 0.367 ± 0.157 Nm in Alter et al. [276]). Apart from Test 15, only Test 09 is in the range of experimental values, although its EF and SV are considerably low.

Pressure All simulations present a left ventricular ES pressure in agreement with the studies collected in Table 12.7, mostly due to the modifications implemented in the circu-

latory system. Regarding the left ventricular ES pressure, only Test 15 and Test 09 seem considerably low compared to the experimental results. However, when the pressure-volume loops are considered, Test 15 matches the shape and values of those gathered in experimental studies Figure 12.11.

Test 15, which considers increased stiffness, modifications in the circulatory system and cellular remodeling, is the combination that best reproduces the characteristics reported for DCM patients.

Table 12.8: All considered Tests are listed here. **EP:** Electrophysiology; **M:** Mechanics.

Test	Fiber angle	HF – EP	HF – M	Conductivity	Stiffness
0	0	0	0	0	0
1	0	0	0	0	1
2	0	0	0	1	0
3	0	0	0	1	1
4	0	0	1	0	0
5	0	0	1	0	1
6	0	0	1	1	0
7	0	0	1	1	1
8	0	1	0	0	0
9	0	1	0	0	1
10	0	1	0	1	0
11	0	1	0	1	1
12	0	1	1	0	0
13	0	1	1	0	1
14	0	1	1	1	0
15	0	1	1	1	1
16	1	0	0	0	0
17	1	0	0	0	1
18	1	0	0	1	0
19	1	0	0	1	1
20	1	0	1	0	0
21	1	0	1	0	1
22	1	0	1	1	0
23	1	0	1	1	1
24	1	1	0	0	0
25	1	1	0	0	1
26	1	1	0	1	0
27	1	1	0	1	1
28	1	1	1	0	0
29	1	1	1	0	1
30	1	1	1	1	0
31	1	1	1	1	1

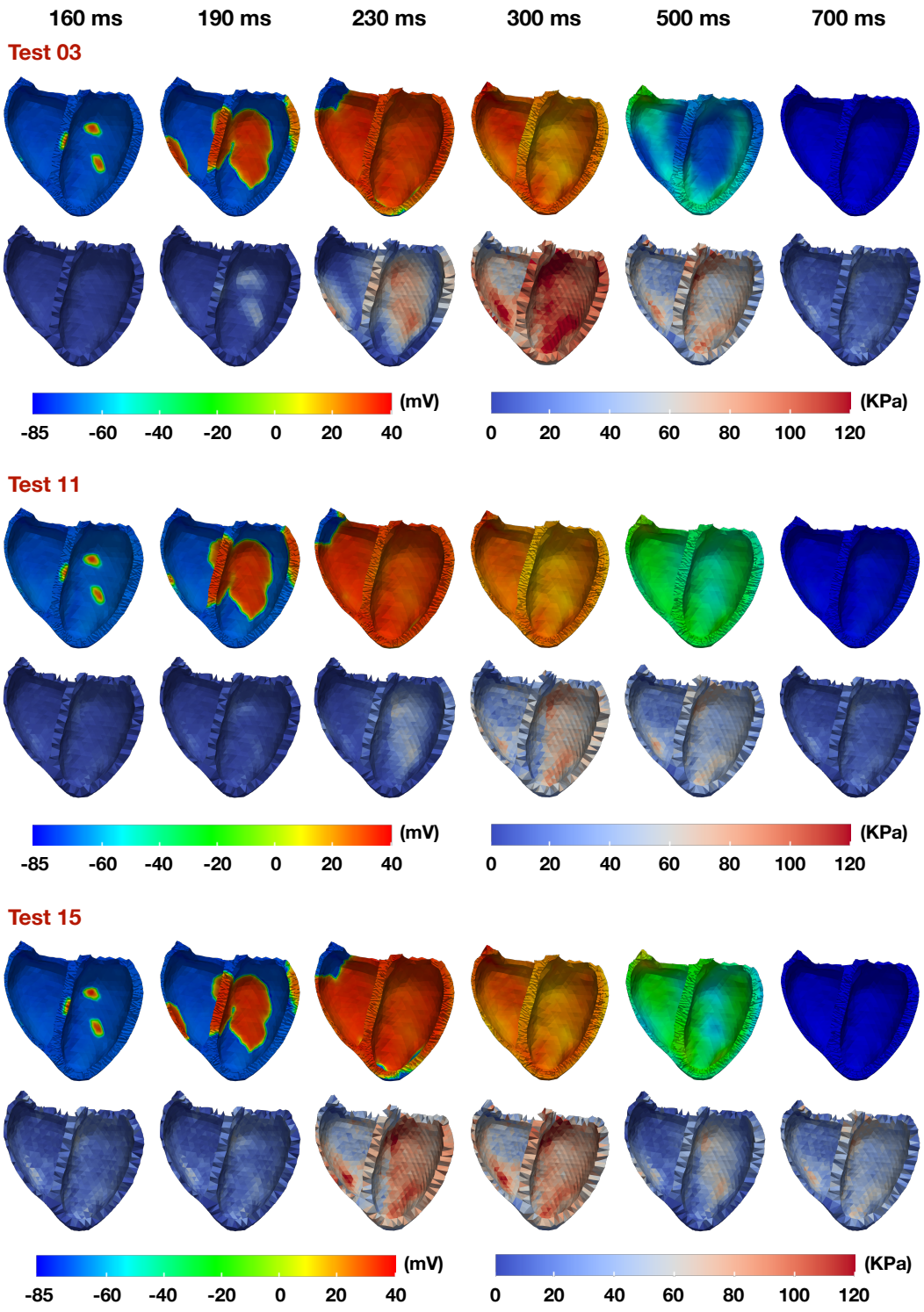

Figure 12.10: Changes in membrane potential and active tension in simulations with the original ORd+L17 model (Test 03), HF remodeling of electrophysiology (Test 11), and electromechanical HF remodeling (Test 15). Reprinted with permission from [42].

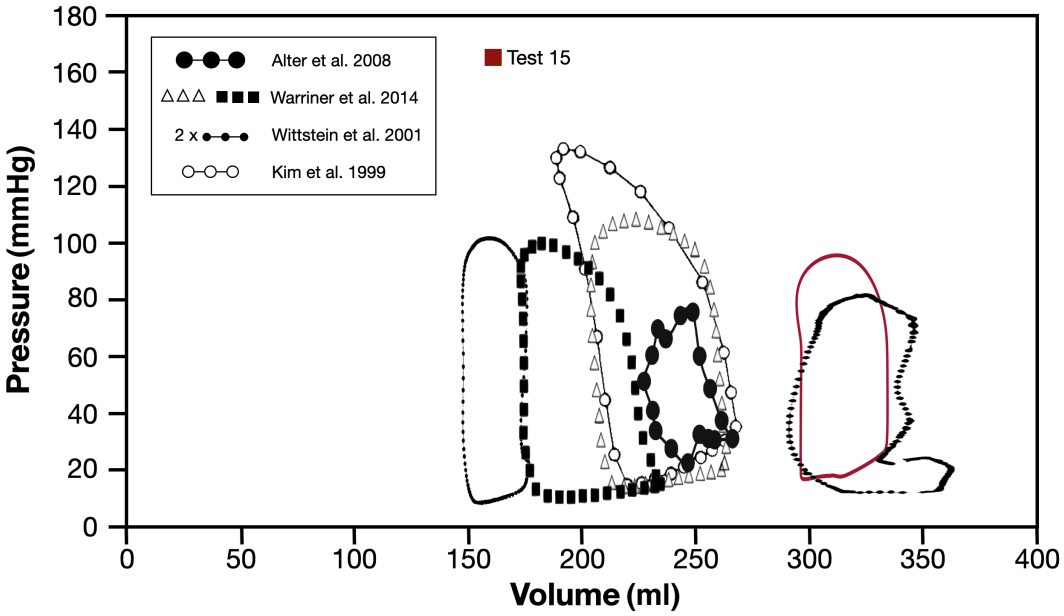

Figure 12.11: Comparison of the left ventricle pressure-volume loops between experimental and computational results. Reprinted with permission from [42].

PART VI

FINAL REMARKS

Chapter 13

Conclusion & Outlook

In this thesis, a framework for the numerical approximation of the electromechanical function of the human heart including the circulatory system was developed.

To model the chain of events that are required to describe the process of excitation contraction coupling, it was first necessary to establish a model of a cardiac muscle cell, which accurately represents ion dynamics across the cell membrane and the mechanical activation of the sarcomere. The purpose of the model is to simulate the human physiology, which is why the established models of Courtemanche-Ramirez-Nattel (CRN) [155] and O'Hara-Rudy-dynamic (ORd) [156] were used for the representation of ion dynamics in the atria and ventricles, respectively. Sarcomere dynamics were described by the most recent model of human cardiac contraction by Land et al. [14, 94]. A link between these models was established by replacing the algebraic formulation of the troponin buffer in the CRN and ORd models by the evolution of calcium bound to troponin from the L17 model. As a result, the binding affinity of calcium to troponin C is now dependent on the length of the sarcomere, which leads to a change in the intracellular calcium concentration when the muscle cell is stretched or shortened. Consequently, the repolarization and the force development of the cell was altered. After a reparameterization of the model, the intracellular calcium concentration and generated active tension were able to reproduce measurements from human tissue preparations. So far, only a model of ventricular excitation-contraction coupling has been proposed in literature [160]. As far as atrial models are concerned, the model proposed in this work is one of the most sophisticated models with regard to electromechanical function that can be used in whole heart modeling scenarios.

In the next step, a numerical framework had to be set up to couple the electrophysiology model ($\mathcal{IAE}$) to the 3D-0D mechanics model ($\mathcal{MC}$). Since software solutions for the individual problems already existed in the research group, the best way to couple the models was in a segregated approach, meaning the $\mathcal{IAE}$ and $\mathcal{MC}$ models are solved sequentially. To accommodate for the different requirements of space and time discretization, the core models for electrophysiology, mechanics, and the circulatory system are solved with different time steps. Furthermore, the $\mathcal{IAE}$ and $\mathcal{MC}$ models are solved on two nested meshes of the heart domain with different mesh sizes. However, the developed scheme to solve the coupled problem is not suitable for sarcomere models ($\mathcal{A}$) that include a dependence on the stretch

rate of the muscle cell. Therefore, the stabilization term for staggered solution strategies proposed by Regazzoni et al. [191] should be implemented in future studies. In general, the numerical foundation of the software that is used for the individual core modules is in need of improvements. Convergence properties of different time integration methods of the electrophysiology problem are currently investigated in cooperation with the Institute for Applied and Numerical Mathematics at KIT. Furthermore, solving the linear system of the mechanics problem should be done with suitable Krylov subspace methods and preconditioners such as algebraic multigrid methods. Currently, the linear system is solved using lower-upper (LU) decomposition. Therefore, computational resources become the limiting factor as soon as the size of the problem increases.

An advantage of the proposed segregated and staggered solution of the electromechanics problem is the easy way of implementing different levels of mechano-electric feedback (MEF). Simulations in sinus rhythm for example showed little to no change when the deformation was included in the monodomain equation compared to only coupling on the cellular level which changed the mechanical behavior of the heart.

The validation of the personalized whole heart model of a volunteer with magnetic resonance imaging (MRI) data revealed some discrepancies with respect to left ventricular activity. While absolute values such as peak atrioventricular plane displacement (AVPD), stroke volume (SV), and rotation match the MRI data, the dynamics are different. The electromechanical model using the Land (L17) model for active force generation promotes too fast of a contraction and a slower than typical relaxation even though the behavior on the cellular level agrees with measurements in human cells. The phenomenological model used in Chapter 11 did not have these problems due to an easier adaptation with fewer parameters. Both models have advantages and disadvantages with regards to their application. The phenomenological model is used more often throughout literature due to the easier adaptation to patient specific measurements. However, it lacks the ability to be coupled to the concentration of calcium, meaning it cannot adapt to different heart rates without reparameterization. Therefore, more effort should be put into the research and application of force generation models based on biophysical principles in whole heart simulations.

Finally, exemplary studies were presented that show the ability to adapt the model to pathological scenarios. The ability to investigate and answer clinically motivated questions is one of the main drivers of computational cardiac modeling. However, modeling pathological mechanisms is still an active field of research and a lot of assumptions have to be made due to the lack of data in clinical settings. In general, the lack of data and ways to constrain the parameterization of the fully coupled model is a major concern. Hundreds of the parameters in the model are based on literature only and there is no way of personalizing or validating them. Additionally, since everything is connected to each other, a change in parameters in one part of the model affects all other parts as well, which makes a calibration incredibly difficult. Therefore, depending on the goal of numerical studies, more simple models are better suited to properly reflect real life observations.

Appendix **A**

Determination of Rayleigh Damping Parameters

Rayleigh damping is an integral part of our simulation environment to avoid unphysical rigid-body oscillations when the mechanics are simulated using Equations (3.14). This requires the computation of the frequency dependent parameters α_1 and α_2 in the damping matrix $\mathbf{C} = \alpha_1\mathbf{M} + \alpha_2\nabla\mathbf{f}^{\text{int}}$ [102]. According to [18, 300], the best choice of these parameters is $\alpha_2 = 0$ (there is no physical justification to damp the higher modes of a solid body [301]) and $\alpha_1 = c\omega$, where $c \in \{2, 10\}$ is a constant and ω is the frequency. The following workflow is suggested to determine ω:

1. Identify a number of critical load cases with similar mechanical properties as the target numerical setup. For heart simulations, this can include the application of pressure or the active contraction of a piece of tissue.
2. Run these cases without Rayleigh damping.
3. Analyze the displacement $\mathbf{d}$ of a single point inside the geometry with respect to the minimum and maximum frequencies that are present in the system response.

After a spectral analysis of a large number of undamped simulations, Santiago et al. [18] chose the parameters as $c = 5$ and $\omega = 200\,\text{Hz}$. In our framework, $\alpha_1 = 500\,\text{s}^{-1}$ and $\alpha_2 = 0.005\,\text{s}$ results in good damping properties for the Guccione material as shown in Figure A.1. However, a wide range of values in α_1 delivers equally good results.

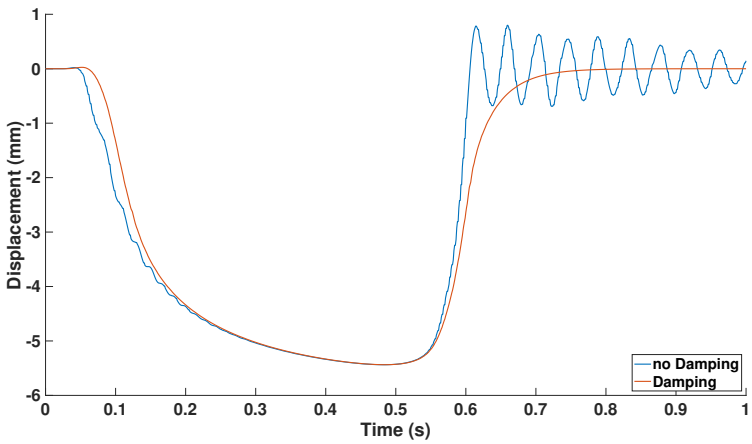

Figure A.1: Displacement of an exemplary simulation study with and without Rayleigh damping.

Appendix **B**

Derivation of the Passive Contribution to the 2nd Piola-Kirchhoff Stress

The material constitutive laws that are used in the balance of momentum equation relate the strain of the body with its stress. In the case of visco-elastic materials, the constitutive law may even depend on the rate of strain [109]. However, in cardiac mechanics, the focus is on elastic materials or in particular hyperelastic ones, i.e. the behaviour of the material is path-independent. As a consequence, we can define a stored strain energy density function Ψ to express the first Piola-Kirchhoff stress tensor as

$$\mathbf{P}(\mathbf{F}(\mathbf{X}),\mathbf{X}) = \frac{\partial \Psi(\mathbf{F}(\mathbf{X}),\mathbf{X})}{\partial \mathbf{F}}, \tag{B.1}$$

or in terms of the symmetric second Piola-Kirchhoff stress tensor

$$\mathbf{S}(\mathbf{C}(\mathbf{X}),\mathbf{X}) = 2\frac{\partial \Psi(\mathbf{C}(\mathbf{X}),\mathbf{X})}{\partial \mathbf{C}} = \frac{\partial \Psi(\mathbf{E}(\mathbf{X}),\mathbf{X})}{\partial \mathbf{E}}. \tag{B.2}$$

If the relationship between Ψ and $\mathbf{C}$ is independent of the material axes, Ψ can be expressed as a function of the invariants of $\mathbf{C}$ as

$$\Psi(\mathbf{C}(\mathbf{X}),\mathbf{X}) = \Psi(\mathrm{I}_\mathbf{C},\mathrm{II}_\mathbf{C},\mathrm{III}_\mathbf{C},\mathbf{X}), \tag{B.3}$$

where the invariants are defined as

$$\mathrm{I}_\mathbf{C} = \mathrm{tr}\,\mathbf{C} = \mathbf{C} : \mathbb{1} \tag{B.4}$$

$$\mathrm{II}_\mathbf{C} = \mathrm{tr}\,\mathbf{C}\mathbf{C} = \mathbf{C} : \mathbf{C} \tag{B.5}$$

$$\mathrm{III}_\mathbf{C} = \det \mathbf{C} = J^2. \tag{B.6}$$

It can also be convenient to consider isochoric invariants, replacing $\mathbf{C}$ with $\bar{\mathbf{C}} = J^{-2/3}\mathbf{C} = \mathrm{III}_\mathbf{C}^{-1/3}\mathbf{C}$. Furthermore, pseudo invariants can be introduced that describe the squared stretch along microstructural directions in anisotropic materials such as the myocardium:

$$\mathrm{I}_{ab} = \mathbf{C} : \mathrm{sym}(\mathbf{e}_a \otimes \mathbf{e}_b), \quad a,b \in \{f,s,n\}, \tag{B.7}$$

where $\mathrm{sym}(\mathbf{A}) = \frac{1}{2}(\mathbf{A} + \mathbf{A}^{\mathrm{T}})$ is the symmetric transformation. Near incompressibility can be achieved in hyperelastic materials by adding a volumetric energy component $U(J)$ to the distortional component $\Psi(\bar{\mathbf{C}})$:

$$\Psi(\mathbf{C}) = \Psi(\bar{\mathbf{C}}) + U(J)\,, \tag{B.8}$$

and

$$\mathbf{S} = 2\frac{\partial \Psi(\bar{\mathbf{C}})}{\partial \mathbf{C}} + 2\frac{\mathrm{d}U(J)}{\mathrm{d}J}\frac{\partial J}{\partial \mathbf{C}}\,. \tag{B.9}$$

In the following, the derivation of the 2nd Piola-Kirchhoff stress $\mathbf{S}$ of the constitutive models is given as they are implemented in *CardioMechanics*.

Neo-Hooke

A nearly incompressible Neo-Hookean material is defined by the hyperelastic energy potential

$$\Psi^{(\mathrm{NH})}(\mathbf{C}) = \frac{\mu}{2}(\mathrm{tr}\,\bar{\mathbf{C}} - 3) + \frac{\kappa}{2}(J-1)^2\,, \tag{B.10}$$

with the shear modulus μ, the bulk modulus κ, and the 2nd Piola-Kirchhoff stress

$$\begin{aligned}
\mathbf{S} &= \mu\frac{\partial\,\mathrm{tr}\,\bar{\mathbf{C}})}{\partial \mathbf{C}} + \kappa\frac{\mathrm{d}(J-1)^2}{\mathrm{d}J}\frac{\partial J}{\partial \mathbf{C}} \\
&= \mu\frac{\partial(\mathrm{III}_{\mathbf{C}}^{-1/3}\mathbf{C} : \mathbb{1})}{\partial \mathbf{C}} + \kappa 2(J-1)\cdot\frac{1}{2}J\mathbf{C}^{-1} \\
&= \mu\left[\mathrm{III}_{\mathbf{C}}^{-1/3}\mathbb{1} - \frac{1}{3}\mathrm{III}_{\mathbf{C}}^{-1/3-1}\mathrm{III}_{\mathbf{C}}\mathbf{C}^{-1}(\mathbf{C}:\mathbb{1})\right] + \kappa(J-1)J\mathbf{C}^{-1} \\
&= \mu\mathrm{III}_{\mathbf{C}}^{-1/3}(\mathbb{1} - \frac{1}{3}\mathrm{I}_{\mathbf{C}}\mathbf{C}^{-1}) + \kappa(J-1)J\mathbf{C}^{-1}\,,
\end{aligned} \tag{B.11}$$

where the relationship $\frac{\partial \mathrm{III}_{\mathbf{C}}}{\partial \mathbf{C}} = J^2\mathbf{C}^{-1}$ was used.

Usyk / Guccione

The incompressible strain energy density by Usyk et al. [106] is given by

$$\begin{aligned}
\Psi^{(\mathrm{U})}(\mathbf{C}) &= \frac{\kappa}{2}(\ln J)^2 + \frac{\mu}{2}(\exp(Q) - 1)\,, \\
Q &= b_{\mathrm{ff}}E_{\mathrm{ff}}^2 + b_{\mathrm{ss}}E_{\mathrm{ss}}^2 + b_{\mathrm{nn}}E_{\mathrm{nn}}^2 + b_{\mathrm{fs}}(E_{\mathrm{fs}}^2 + E_{\mathrm{sf}}^2) + b_{\mathrm{fn}}(E_{\mathrm{fn}}^2 + E_{\mathrm{nf}}^2) + b_{\mathrm{ns}}(E_{\mathrm{ns}}^2 + E_{\mathrm{sn}}^2)\,,
\end{aligned} \tag{B.12}$$

where $E_{\mathrm{ij}} = \mathbf{E}\mathbf{i}_0 \cdot \mathbf{j}_0$ for $i,j \in \{f,s,n\}$ are the entries of the Green-Lagrange strain tensor $\mathbf{E} = \frac{1}{2}(\mathbf{C} - \mathbb{1})$. The 2nd Piola-Kirchhoff stress is given by

$$\mathbf{S} = \mu\exp(Q)(b \odot E)_{ij} + \kappa\ln(J)\mathbf{C}^{-1} \quad \text{with} \quad \mathbf{b} = \begin{pmatrix} b_{\mathrm{ff}} & b_{\mathrm{fs}} & b_{\mathrm{fn}} \\ b_{\mathrm{sf}} & b_{\mathrm{ss}} & b_{\mathrm{sn}} \\ b_{\mathrm{nf}} & b_{\mathrm{ns}} & b_{\mathrm{nn}} \end{pmatrix}, \tag{B.13}$$

where $(A \odot B)_{ij} = (A)_{ij}(B)_{ij}$ is the Hadamard or Schur product of the matrices **A** and **B**. In general, the shear stress components are assumed to be of equal contribution

$$b_{ij} = b_{ji} \quad \text{for} \quad i \neq j\,. \tag{B.14}$$

Holzapfel-Odgen

The incompressible Holzapfel-Odgen strain energy density [107] can be written as a sum of isotropic and anisotropic components

$$\begin{aligned}\Psi^{(\mathrm{HO})}(\mathbf{C}) =& \frac{a}{2b}[\exp\big(b(\bar{\mathrm{I}}_{\mathbf{C}} - 3)\big) - 1] + \sum_{kl \in S} \frac{a_{kl}}{2b_{kl}}[\exp\big(b_{kl}(\mathrm{I}_{kl} - \delta_{kl})^2\big) - 1] \\ &+ \frac{\kappa}{4}(J^2 - 1 - 2\ln J)\,,\end{aligned} \tag{B.15}$$

where δ_{kl} denotes the Kronecker delta (zero unless $k = l$, in which case it is 1) and $S = \{ff, ss, fs\}$. The anisotropic invariants I_{ff} and I_{ss} do not support compression. Therefore, the associated strain energy density terms are zero if $\mathrm{I}_{ff}, \mathrm{I}_{ss} < 1$. The 2nd Piola-Kirchhoff stress tensor is given by

$$\begin{aligned}\mathbf{S} =& \frac{\kappa}{2}(J - \frac{1}{J})J\mathbf{C}^{-1} + \frac{a}{J^{2/3}}\exp\big(b(\bar{\mathrm{I}}_{\mathbf{C}} - 3)\big)[\mathbb{1} - \frac{1}{3}\mathrm{I}_{\mathbf{C}}\mathbf{C}^{-1}] \\ &+ \sum_{kl \in S} 2a_{kl}(\mathrm{I}_{kl} - 1)\exp\big(b_{kl}(\mathrm{I}_{kl} - \delta_{kl})^2\big)\mathrm{sym}(\mathbf{e}_k \otimes \mathbf{e}_l)\,.\end{aligned} \tag{B.16}$$

Appendix C

Analysis of MRI Data for the Purpose of Validation

An important aspect of in silico studies is the verification and validation of the simulation models. To validate the results of the simulations using the whole heart model, the MRI data of the volunteer was analyzed using the freely available software Segment (version 3.2 R8531, [302]). The free to use licence allows the user to segment the left ventricle (LV) and right ventricle (RV) endocardium and epicardium, respectively. Segmentation can be done automatically, semiautomatically or manually. Based on the segmentation, end-diastole (ED) and end-systole (ES) are determined and the volume is calculated. In the case of the available data of the volunteer that was used in this thesis, the exported data had to be processed in order to synchronize the cardiac phases, since the MRI data starts at ED and the simulations start with atrial contraction. The resulting LV volume with indicated ED and ES is shown in Figure C.1. RV volume is not available for this subject, since the automatic segmentation failed to produce good results and manual segmentation was only performed on ED and ES slices to obtain an estimate of the stroke volume (SV). Further statistics such as the end-diastolic volume (EDV), end-systolic volume (ESV), and SV are analyzed. An overview of the graphical user interface of Segment with the segmentation of the LV and RV for an exemplary slice is shown in Figure C.2.

Furthermore, it is possible to analyze atrioventricular plane displacement (AVPD) of the LV and RV. First, the atrioventricular plane has to be defined in the different long axis views by placing predefined points in the ED timeframe. Next, the AVPD is tracked automatically and the results are exported. An example of this process is shown in Figure C.3 and the time aligned displacement and velocity of the mitral valve (MV) and tricuspid valve (TV) are shown in Figure C.4.

Finally, the wall thickness of the LV was analyzed based on the segmentation of the short axis slices. Only slices that contain LV myocardium during the whole cycle were evaluated, hence the most apical and basal slices were disregarded. Slices 4, 5, and 6 were assigned as basal segments, slices 7, 8, and 9 as mid-ventricular segments, and slices 10, 11, and 12 as apical segments according to the American Heart Association (AHA). The

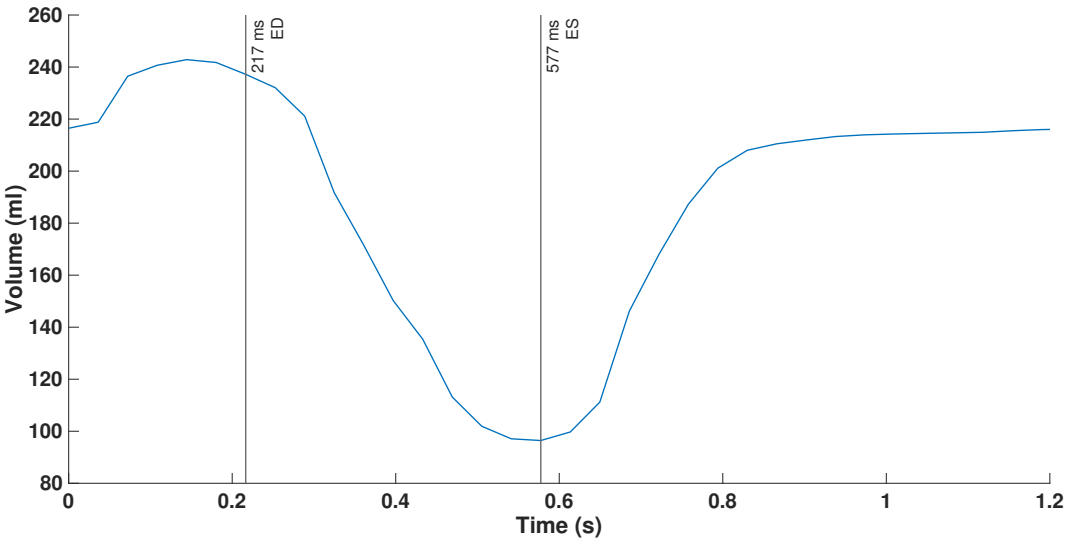

Figure C.1: LV volume determined from short axis cine MRI segmentations.

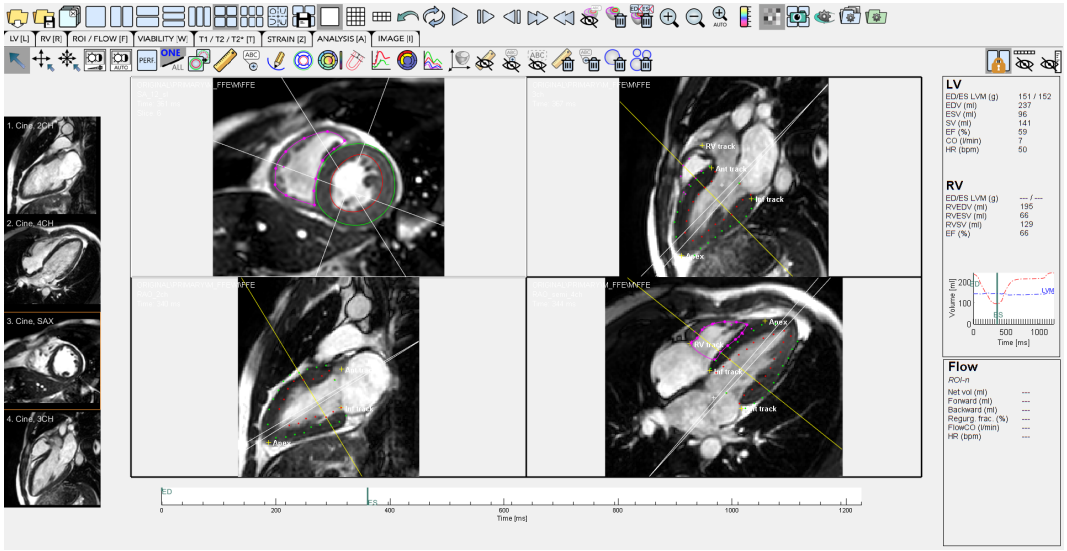

Figure C.2: Graphical user interface (GUI) of the software Segment. The GUI shows the cine MRI data in short axis (SAX), two chamber, three chamber, and four chamber view. Red lines and dots indicate LV endocardial segmentation, green lines and dots indicate LV epicardial segmentation, and magenta lines and dots indicate RV segmentation.

mean wall thickness was calculated for each segment from the available slices, for basal, mid-ventricular, and apical sectors, and the entire LV. The results for the full cardiac cycle are shown in Figure C.5 and as bullseye plots for ED and ES in Figure C.6. Table C.1 summarizes all important biomarkers analyzed using the software Segment.

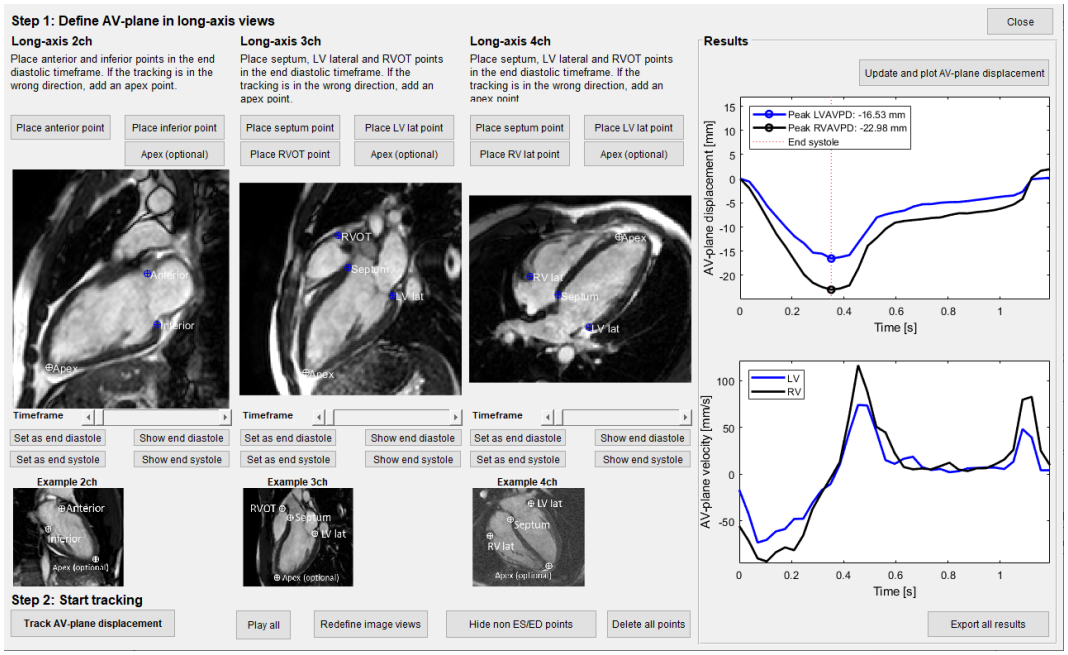

Figure C.3: GUI of the AVPD tracking tool in Segment.

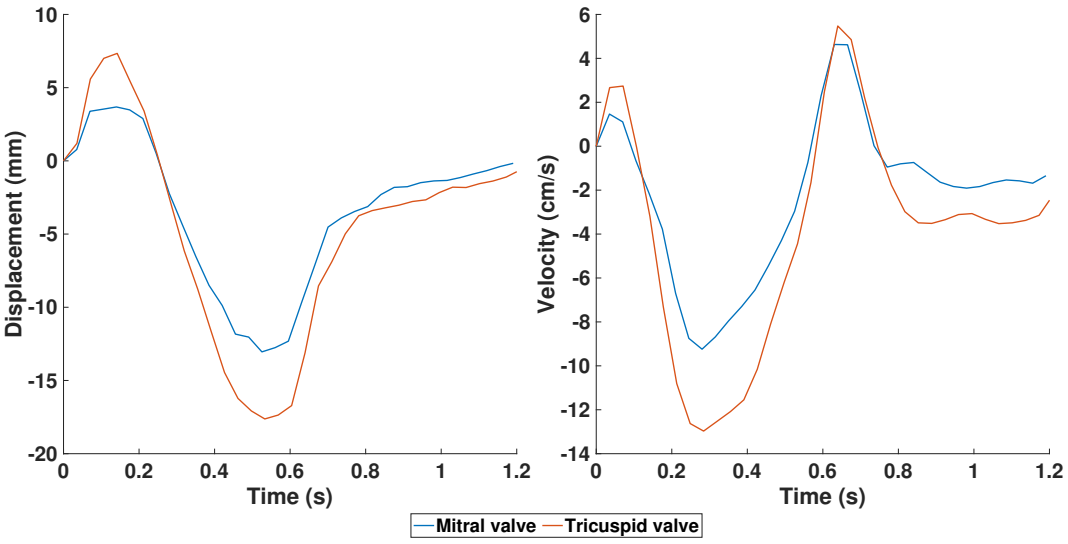

Figure C.4: Displacement and velocity of the MV and TV evaluated using the automated AV-plane tracking tool in Segment.

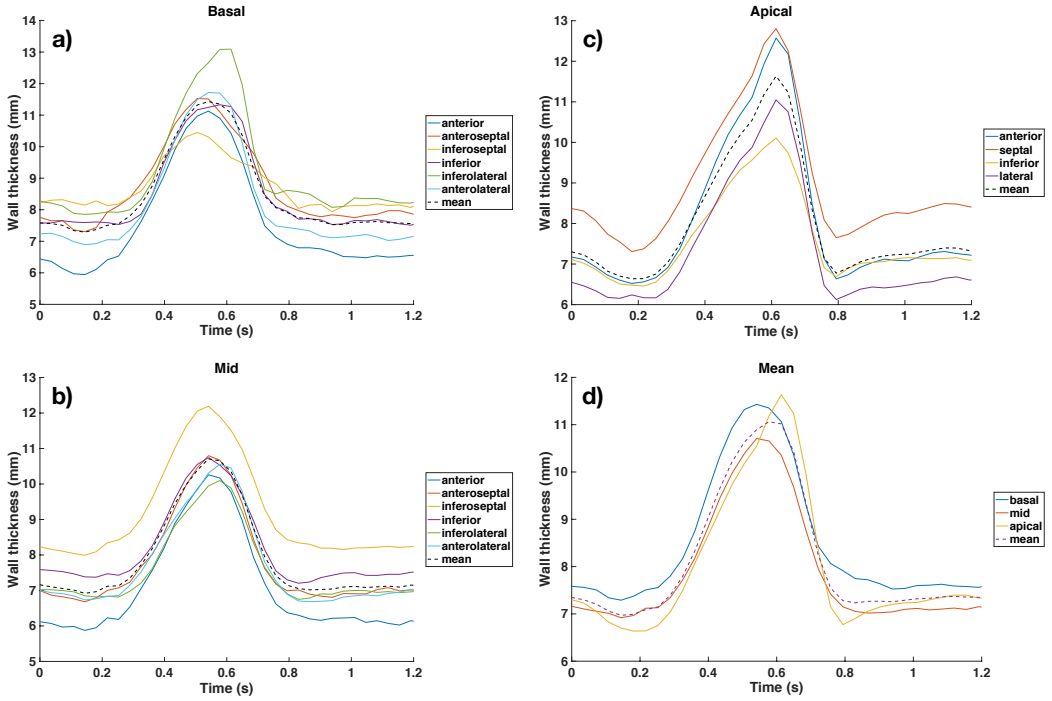

Figure C.5: Wall thickness evaluated from short axis cine MRI data for a) basal, b) mid-ventricular, c) apical segments. Panel d) shows the mean wall thickness of basal, mid-ventricular, and apical segments as well as the entire LV.

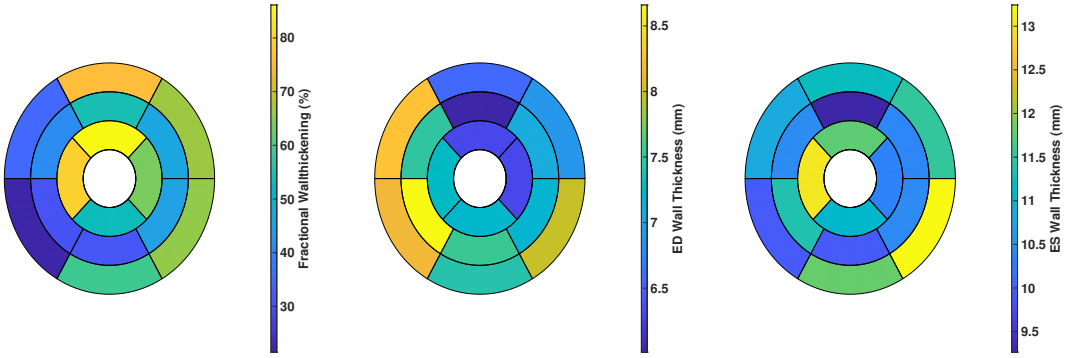

Figure C.6: Bullseye plots of ED and ES wall thickness and fractional wall thickening.

Table C.1: Summary of evaluated biomarkers from the subjects MRI data.

Biomarker	Value	Unit
Heart rate	50	bpm
LV		
End-diastolic volume (EDV)	237	ml
End-diastolic volume (EDV) index	114	ml/m^2
End-systolic volume (ESV)	96	ml
End-systolic volume (ESV) index	47	ml/m^2
Stroke volume (SV)	141	ml
Ejection fraction (EF)	59	%
Cardiac output (CO)	7.038	l/min
Peak filling rate (PFR)	968	ml/s
Peak ejection rate (PER)	816	ml/s
Body surface area (BSA)	2.073	m^2
End-diastolic diameter (EDD)	55	mm
End-diastolic length (EDL)	114.2	mm
Peak atrioventricular plane displacement (AVPD)	-16.53	mm
RV		
End-diastolic volume (EDV)	195	ml
End-systolic volume (ESV)	66	ml
Stroke volume (SV)	129	ml
Ejection fraction (EF)	66	%
Peak atrioventricular plane displacement (AVPD)	-22.98	mm

Appendix **D**

Numerical Integration – Gaussian Quadrature Rules

Two-dimensional integrals on triangles are conveniently expressed in terms of triangular coordinates as

$$\iint_{\Gamma_e} f(x,y)\mathrm{d}x\mathrm{d}y = A_e \sum_{i=1}^{n} W_i f(\zeta_1^i, \zeta_2^i, \zeta_3^i) + E \tag{D.1}$$

where $(\zeta_1^i, \zeta_2^i, \zeta_3^i) \in \Gamma_e$ are the triangular coordinates of evaluation point i, A_e is the area of the triangle e, and W_i is the weight of the evaluation point. The quadrature rules for triangles that were used in this work are listed in table D.1. Here, p denotes the order of the quadrature rule; thus, $E = \mathcal{O}\left(h^{p+1}\right)$ where h is the maximum edge length of the triangle. Similarly,

Table D.1: Weights and evaluation points for the integration on triangles.

n	W_i	ζ_1^i	ζ_2^i, ζ_3^i	p
1	1.0	0.33333333	0.33333333 0.33333333	1
3	0.33333333	0.66666667	0.16666667 0.16666667	2

integrals in three dimensions have the form

$$\iiint_{\Omega_e} f(x,y,z)\mathrm{d}x\mathrm{d}y\mathrm{d}z = V_e \sum_{i=1}^{n} W_i f(\zeta_1^i, \zeta_2^i, \zeta_3^i, \zeta_4^i) + E \tag{D.2}$$

where V_e is the volume of element e and $(\zeta_1^i, \zeta_2^i, \zeta_3^i, \zeta_4^i) \in \Omega_e$ are the tetrahedral coordinates of evaluation point i. Quadrature rules used on tetrahedra are given in table D.2.

Table D.2: Weights and evaluation points for the integration on tetrahedra.

n	W_i	ζ_1^i, ζ_2^i	ζ_3^i, ζ_4^i	p
1	1.0	0.25	0.25	1
		0.25	0.25	
4	0.25	0.585410196624969	0.138196601125011	2
		0.138196601125011	0.138196601125011	

References

[1] A. Timmis, N. Townsend, C. P. Gale, et al., "European Society of Cardiology: Cardiovascular Disease Statistics 2019," *European Heart Journal*, vol. 41, pp. 12–85, 2019. doi:10.1093/eurheartj/ehz859

[2] S. A. Niederer, J. Lumens, and N. A. Trayanova, "Computational models in cardiology." *Nature reviews. Cardiology*, 2018. doi:10.1038/s41569-018-0104-y

[3] R. Andlauer, G. Seemann, L. Baron, et al., "Influence of left atrial size on p-wave morphology: differential effects of dilation and hypertrophy," *Europace*, vol. 20, pp. iii36–iii44, 2018. doi:10.1093/europace/euy231

[4] H. J. Arevalo, F. Vadakkumpadan, E. Guallar, et al., "Arrhythmia risk stratification of patients after myocardial infarction using personalized heart models," *Nature Communications*, vol. 7, p. 11437, 2016. doi:10.1038/ncomms11437

[5] A. Prakosa, H. J. Arevalo, D. Deng, et al., "Personalized virtual-heart technology for guiding the ablation of infarct-related ventricular tachycardia," *Nature Biomedical Engineering*, 2018. doi:10.1038/s41551-018-0282-2

[6] A. Loewe, E. Poremba, T. Oesterlein, et al., "Patient-specific identification of atrial flutter vulnerability - a computational approach to reveal latent reentry paths," *Front. Phys.*, vol. 9, p. 1910, 2018. doi:10.3389/fphys.2018.01910

[7] H. Lehrmann, A. S. Jadidi, J. Minners, et al., "Novel electrocardiographic criteria for real-time assessment of anterior mitral line block," *JACC: Clinical Electrophysiology*, vol. 4, pp. 920–932, 2018. doi:10.1016/j.jacep.2018.03.007

[8] J. Corral-Acero, F. Margara, M. Marciniak, et al., "The 'digital twin' to enable the vision of precision cardiology." *European heart journal*, 2020. doi:10.1093/eurheartj/ehaa159

[9] L. Marx, M. A. F. Gsell, A. Rund, et al., "Personalization of electro-mechanical models of the pressure-overloaded left ventricle: fitting of windkessel-type afterload models." *Philosophical transactions. Series A, Mathematical, physical, and engineering sciences*, vol. 378, p. 20190342, 2020. doi:10.1098/rsta.2019.0342

[10] D. Chapelle, M. A. Fernández, J.-F. Gerbeau, P. Moireau, J. Sainte-Marie, and N. Zemzemi, "Numerical simulation of the electromechanical activity of the heart," vol. 5528, pp. 357–365, 2009. doi:10.1007/978-3-642-01932-6_39

[11] D. A. Nordsletten, S. A. Niederer, M. P. Nash, P. J. Hunter, and N. P. Smith, "Coupling multi-physics models to cardiac mechanics," *Progress in Biophysics and Molecular Biology*, vol. 104, pp. 77–88, 2011. doi:10.1016/j.pbiomolbio.2009.11.001

[12] R. Piersanti, F. Regazzoni, M. Salvador, et al., "3d–0d closed-loop model for the simulation of cardiac biventricular electromechanics," *Computer Methods in Applied Mechanics and Engineering*, vol. 391, p. 114607, 2022. doi:10.1016/j.cma.2022.114607

[13] A. Gerbi, L. Dede', and A. Quarteroni, "A monolithic algorithm for the simulation of cardiac electromechanics in the human left ventricle," *Mathematics in Engineering*, vol. 1, pp. 1–37, 2018. doi:10.3934/Mine.2018.1.1

[14] S. Land and S. A. Niederer, "Influence of atrial contraction dynamics on cardiac function." *International journal for numerical methods in biomedical engineering*, vol. 34, 2018. doi: 10.1002/cnm.2931

[15] C. M. Augustin, T. E. Fastl, A. Neic, et al., "The impact of wall thickness and curvature on wall stress in patient-specific electromechanical models of the left atrium," *Biomechanics and modeling in mechanobiology*, vol. 19, pp. 1015–1034, 2020. doi:10.1007/s10237-019-01268-5

[16] J. M. Hörmann, C. Bertoglio, A. Nagler, et al., "Multiphysics modeling of the atrial systole under standard ablation strategies." *Cardiovascular engineering and technology*, vol. 8, pp. 205–218, 2017. doi:10.1007/s13239-017-0308-z

[17] C. M. Augustin, A. Neic, M. Liebmann, et al., "Anatomically accurate high resolution modeling of human whole heart electromechanics: a strongly scalable algebraic multigrid solver method for nonlinear deformation," *J. Computat. Phys.*, vol. 305, pp. 622–646, 2016. doi:10.1016/j.jcp.2015.10.045

[18] A. Santiago, M. Zavala-Aké, J. Aguado-Sierra, et al., "Fully coupled fluid-electro-mechanical model of the human heart for supercomputers." *International journal for numerical methods in biomedical engineering*, 2018. doi:10.1002/cnm.3140

[19] M. R. Pfaller, J. M. Hörmann, M. Weigl, et al., "The importance of the pericardium for cardiac biomechanics: from physiology to computational modeling," *Biomechanics and modeling in mechanobiology*, vol. 18, pp. 503–529, 2019.

[20] T. Fritz, C. Wieners, G. Seemann, H. Steen, and O. Dössel, "Simulation of the contraction of the ventricles in a human heart model including atria and pericardium : Finite element analysis of a frictionless contact problem," *Biomechanics and Modeling in Mechanobiology*, vol. 13, pp. 627–641, 2014. doi:10.1007/s10237-013-0523-y

[21] A. J. Prassl, F. Kickinger, H. Ahammer, et al., "Automatically generated, anatomically accurate meshes for cardiac electrophysiology problems." *IEEE transactions on bio-medical engineering*, vol. 56, pp. 1318–30, 2009. doi:10.1109/TBME.2009.2014243

[22] C. Roney, M. Beach, A. Mehta, et al., "Constructing virtual patient cohorts for simulating atrial fibrillation ablation," in *2020 Computing in Cardiology Conference (CinC)*, 2020 Computing in Cardiology Conference (CinC), vol. 47, 2020. doi:10.22489/CinC.2020.117

[23] M. Strocchi, C. M. Augustin, M. A. F. Gsell, et al., "A publicly available virtual cohort of four-chamber heart meshes for cardiac electro-mechanics simulations." *PloS one*, vol. 15, p. e0235145, 2020. doi:10.1371/journal.pone.0235145

[24] C. H. Roney, A. Pashaei, M. Meo, et al., "Universal atrial coordinates applied to visualisation, registration and construction of patient specific meshes." *Medical Image Analysis*, vol. 55, pp. 65–75, 2019. doi:10.1016/j.media.2019.04.004

[25] J. Bayer, A. J. Prassl, A. Pashaei, et al., "Universal ventricular coordinates: A generic framework for describing position within the heart and transferring data." *Medical Image Analysis*, vol. 45, pp. 83–93, 2018. doi:10.1016/j.media.2018.01.005

[26] S. Schuler, N. Pilia, D. Potyagaylo, and A. Loewe, "Cobiveco: Consistent biventricular coordinates for precise and intuitive description of position in the heart - with MATLAB implementation," *Preprint*, 2021.

[27] E. Kovacheva, L. Baron, S. Schuler, T. Gerach, O. Dössel, and A. Loewe, "Optimization framework to identify constitutive law parameters of the human heart," in *Current Directions*

in Biomedical Engineering, vol. 6, no. 3. Leipzig; online Conference: De Gruyter, 2020, pp. 95–98. doi:10.1515/cdbme-2020-3025

[28] L. Marx, J. A. Niestrawska, M. A. F. Gsell, F. Caforio, G. Plank, and C. M. Augustin, "Efficient identification of myocardial material parameters and the stress-free reference configuration for patient-specific human heart models," *Elsevier*, 2021.

[29] S. Pezzuto, F. W. Prinzen, M. Potse, et al., "Reconstruction of three-dimensional biventricular activation based on the 12-lead electrocardiogram via patient-specific modelling," *EP Europace*, 2020. doi:10.1093/europace/euaa330

[30] M. Potse, D. Krause, W. Kroon, et al., "Patient-specific modelling of cardiac electrophysiology in heart-failure patients," *Europace : European Pacing, Arrhythmias, and Cardiac Electrophysiology : Journal of the Working Groups on Cardiac Pacing, Arrhythmias, and Cardiac Cellular Electrophysiology of the European Society of Cardiology*, vol. 16 Suppl 4, pp. iv56–iv61, 2014. doi:10.1093/europace/euu257

[31] K. Gillette, A. Prassl, J. Bayer, E. Vigmond, A. Neic, and G. Plank, "Automatic generation of bi-ventricular models of cardiac electrophysiology for patient specific personalization using non-invasive recordings," in *2018 Computing in Cardiology Conference (CinC)*, 2018 Computing in Cardiology Conference (CinC), vol. 45, 2018. doi:10.22489/CinC.2018.265

[32] W. Kahlmann, E. Poremba, D. Potyagaylo, O. Dössel, and A. Loewe, "Modelling of patient-specific purkinje activation based on measured ECGs," *Current Directions in Biomedical Engineering*, vol. 3, pp. 171–174, 2017. doi:10.1515/cdbme-2017-0177

[33] C. Corrado, S. Williams, R. Karim, G. Plank, M. O'Neill, and S. Niederer, "A work flow to build and validate patient specific left atrium electrophysiology models from catheter measurements." *Medical image analysis*, vol. 47, pp. 153–163, 2018. doi:10.1016/j.media.2018.04.005

[34] T. Grandits, S. Pezzuto, F. S. Costabal, et al., "Learning atrial fiber orientations and conductivity tensors from intracardiac maps using physics-informed neural networks," 2021.

[35] T. Gerach, S. Schuler, J. Fröhlich, et al., "Electro-mechanical whole-heart digital twins: A fully coupled multi-physics approach," *Mathematics*, vol. 9, p. 1247, 2021. doi:10.3390/math9111247

[36] S. Appel, "Parameteroptimierung zur Regulierung der calciumabhängigen Kraftentwicklung in Herzmuskelzellen," Master's thesis, Institut für Biomedizinische Technik, Karlsruher Institut für Technologie (KIT), 2020.

[37] S. Appel, T. Gerach, O. Dössel, and A. Loewe, "Adaptation of the calcium-dependent tension development in ventricular cardiomyocytes," in *Current Directions in Biomedical Engineering*, vol. 7, no. 2, 2021, pp. 251–254. doi:10.1515/cdbme-2021-2064

[38] S. A. Niederer, E. Kerfoot, A. P. Benson, et al., "Verification of cardiac tissue electrophysiology simulators using an n-version benchmark," *Philosophical Transactions of the Royal Society A: Mathematical, Physical and Engineering Sciences*, vol. 369, pp. 4331–4351, 2011. doi:10.1098/rsta.2011.0139

[39] S. Land, V. Gurev, S. Arens, et al., "Verification of cardiac mechanics software: benchmark problems and solutions for testing active and passive material behaviour," *Proceedings. Mathematical, Physical, and Engineering Sciences / the Royal Society*, vol. 471, p. 2015.0641, 2015. doi:10.1098/rspa.2015.0641

[40] T. Gerach, S. Schuler, E. Kovacheva, O. Doessel, and A. Loewe, "Consequences of using an orthotropic stress tensor for left ventricular systole," 2020 Computing in Cardiology Conference (CinC), vol. 47, 2020. doi:10.22489/CinC.2020.246

[41] T. Gerach, S. Appel, J. Wilczek, K. S. Golba, T. Jadczyk, and A. Loewe, "Dyssynchronous left ventricular activation is insufficient for the breakdown of wringing rotation," *Frontiers in Physiology*, vol. 13, 2022.

[42] A. Dasi i Martinez, "Consideration of electromechanical remodelling during heart failure in a 3d in-silico model of dilated cardiomyopathy," Master's thesis, Institute of Biomedical Engineering, Karlsruhe Institute of Technology (KIT), 2020.

[43] J. G. Betts, P. DeSaix, E. Johnson, et al., *Anatomy and physiology*, 2013.

[44] T. Fritz, "Biomechanical modeling of the human heart - modeling of the ventricles, the atria and the pericardium and the inverse problem of cardiac mechanics," PhD thesis, Karlsruhe, 2015.

[45] I. J. LeGrice, B. H. Smaill, L. Z. Chai, S. G. Edgar, J. B. Gavin, and P. J. Hunter, "Laminar structure of the heart: ventricular myocyte arrangement and connective tissue architecture in the dog," *Am. J. Physiol.*, vol. 269, pp. H571–H582, 1995.

[46] I. J. LeGrice, P. J. Hunter, and B. H. Smaill, "Laminar structure of the heart: a mathematical model," *Am. J. Physiol.*, vol. 272, pp. H2466–H2476, 1997.

[47] J. Keener and J. Sneyd, Eds., *Mathematical physology ; i: Cellular physiology*, Interdisciplinary Applied Mathematics ; V. 8, 1. New York: Springer, 2009.

[48] J. Keener and J. Sneyd, Eds., *Mathematical physology ; ii: Systems physiology*, Interdisciplinary Applied Mathematics ; V. 8, 2. New York: Springer, 2009.

[49] N. M. Van Mieghem, J. J. Schreuder, F. Zijlstra, et al., "Invasive left ventricle pressure–volume analysis: overview and practical clinical implications," *European Heart Journal*, vol. 41, pp. 1286–1297, 2020. doi:10.1093/eurheartj/ehz552

[50] A. Quarteroni, T. Lassila, S. Rossi, and R. Ruiz-Baier, "Integrated heart—coupling multiscale and multiphysics models for the simulation of the cardiac function," *Computer Methods in Applied Mechanics and Engineering*, vol. 314, pp. 345–407, 2017. doi:10.1016/j.cma.2016.05.031

[51] L. Dedè, A. Quarteroni, and F. Regazzoni, "Mathematical and numerical models for the cardiac electromechanical function," *Rendiconti Lincei - Matematica e Applicazioni*, vol. 32, pp. 233–272, 2021. doi:10.4171/RLM/935

[52] A. L. Hodgkin and A. F. Huxley, "A quantitative description of membrane current and its application to conduction and excitation in nerve," *Journal of Physiology*, vol. 117, pp. 500–544, 1952.

[53] O. H. Schmitt, "Biological information processing using the concept of interpenetrating domains," pp. 325–331, 1969. doi:10.1007/978-3-642-87086-6_18

[54] D. B. Geselowitz and T. W. Miller, "A bidomain model for anisotropic cardiac muscle," *Annals of Biomedical Engineering*, vol. 11, pp. 191–206, 1983.

[55] P. C. C. Franzone, L. F. Pavarino, and S. Scacchi, "Mathematical cardiac electrophysiology," 2014.

[56] B. Verma, T. Oesterlein, A. Loewe, A. Luik, C. Schmitt, and O. Dössel, "Regional conduction velocity calculation from clinical multichannel electrograms in human atria," *Computers in Biology and Medicine*, vol. 92, pp. 188–196, 2018. doi:10.1016/j.compbiomed.2017.11.017

[57] C. Mendonca Costa, E. Hoetzl, B. Martins Rocha, A. J. Prassl, and G. Plank, "Automatic parameterization strategy for cardiac electrophysiology simulations," in *Computing in Cardiology Conference (CinC), 2013*, 2013, pp. 373–376.

[58] A. Loewe, M. W. Krueger, F. Holmqvist, O. Dössel, G. Seemann, and P. G. Platonov, "Influence of the earliest right atrial activation site and its proximity to interatrial connections on p-wave morphology," *Europace*, vol. 18, pp. iv35–iv43, 2016. doi:10.1093/europace/euw349

[59] D. Durrer, R. T. van Dam, G. E. Freud, M. J. Janse, F. L. Meijler, and R. C. Arzbaecher, "Total excitation of the isolated human heart," *Circulation*, vol. 41, pp. 899–912, 1970.

[60] L. Cardone-Noott, A. Bueno-Orovio, A. Mincholé, N. Zemzemi, and B. Rodriguez, "Human ventricular activation sequence and the simulation of the electrocardiographic QRS complex and its variability in healthy and intraventricular block conditions." *Europace*, vol. 18, pp. iv4–iv15, 2016. doi:10.1093/europace/euw346

[61] K. Gillette, M. A. Gsell, A. J. Prassl, et al., "A framework for the generation of digital twins of cardiac electrophysiology from clinical 12-leads ECGs," *Medical Image Analysis*, p. 102080, 2021. doi:10.1016/j.media.2021.102080

[62] K. Gillette, M. A. F. Gsell, J. Bouyssier, et al., "Automated framework for the inclusion of a his–purkinje system in cardiac digital twins of ventricular electrophysiology," *Annals of Biomedical Engineering*, 2021. doi:10.1007/s10439-021-02825-9

[63] T. Ijiri, T. Ashihara, T. Yamaguchi, et al., "A procedural method for modeling the purkinje fibers of the heart," *The Journal of Physiological Sciences : JPS*, vol. 58, pp. 481–486, 2008. doi:10.2170/physiolsci.RP003208

[64] F. Sahli Costabal, D. E. Hurtado, and E. Kuhl, "Generating purkinje networks in the human heart," *Journal of Biomechanics*, vol. 49, pp. 2455–2465, 2016. doi:10.1016/j.jbiomech.2015.12.025

[65] E. J. Vigmond and C. Clements, "Construction of a computer model to investigate sawtooth effects in the purkinje system," *Biomedical Engineering, IEEE Transactions on*, vol. 54, pp. 389–399, 2007.

[66] E. J. Vigmond and B. D. Stuyvers, "Modeling our understanding of the his-purkinje system." *Progress in Biophysics and Molecular Biology*, vol. 120, pp. 179–88, 2016. doi:10.1016/j.pbiomolbio.2015.12.013

[67] V. Zimmerman, R. Sebastian, B. H. Bijnens, and A. F. Frangi, "Modeling the purkinje conduction system with a non deterministic rule based iterative method," in *Computers in Cardiology*, vol. 36, 2009, pp. 461–464.

[68] F. Barber, P. Langfield, M. Lozano, et al., "Estimation of personalized minimal purkinje systems from human electro-anatomical maps." *IEEE transactions on medical imaging*, 2021. doi:10.1109/TMI.2021.3073499

[69] M. Landajuela, C. Vergara, A. Gerbi, L. Dedè, L. Formaggia, and A. Quarteroni, "Numerical approximation of the electromechanical coupling in the left ventricle with inclusion of the purkinje network," *International Journal for Numerical Methods in Biomedical Engineering*, vol. 34, p. e2984, 2018. doi:10.1002/cnm.2984

[70] R. Sebastian, V. Zimmerman, D. Romero, and A. F. Frangi, "Construction of a computational anatomical model of the peripheral cardiac conduction system," *IEEE Transactions on Biomedical Engineering*, vol. 58, pp. 3479–3482, 2011. doi:10.1109/TBME.2011.2166553

[71] C. Vergara, S. Palamara, D. Catanzariti, et al., "Patient-specific generation of the purkinje network driven by clinical measurements of a normal propagation," *Medical & Biological Engineering & Computing*, vol. 52, pp. 813–826, 2014. doi:10.1007/s11517-014-1183-5

[72] C. Vergara, M. Lange, S. Palamara, T. Lassila, A. F. Frangi, and A. Quarteroni, "A coupled 3d-1d numerical monodomain solver for cardiac electrical activation in the myocardium with

detailed purkinje network," *Journal of Computational Physics*, vol. 308, pp. 218–238, 2016. doi:10.1016/j.jcp.2015.12.016

[73] D. M. Bers, "Excitation-contraction coupling and cardiac contractile force."

[74] C. Kemnitz, G. W. Jenkins, and G. J. Tortora, *Anatomy and physiology: From science to life*. John Wiley & Sons, 2006.

[75] A. M. Katz, *Physiology of the heart*. Lippincott Williams & Wilkins, 2010.

[76] A. V. Hill, "The heat of shortening and the dynamic constants of muscle," *Proc. R. Soc. Lond. B*, vol. 126, pp. 136–195, 1938.

[77] J. C. Kentish, H. E. t. Keurs, L. Ricciardi, J. J. Bucx, and M. I. Noble, "Comparison between the sarcomere length-force relations of intact and skinned trabeculae from rat right ventricle. influence of calcium concentrations on these relations," *Circ. Res*, vol. 58, pp. 755–768, 1986.

[78] D. P. Dobesh, J. P. Konhilas, and P. P. de Tombe, "Cooperative activation in cardiac muscle: impact of sarcomere length," *American Journal of Physiology-Heart and Circulatory Physiology*, vol. 282, pp. H1055–H1062, 2002. doi:10.1152/ajpheart.00667.2001

[79] H. E. ter Keurs, T. Shinozaki, Y. M. Zhang, et al., "Sarcomere mechanics in uniform and non-uniform cardiac muscle: A link between pump function and arrhythmias," *Progress in Biophysics and Molecular Biology*, vol. 97, pp. 312–331, 2008. doi:10.1016/j.pbiomolbio.2008.02.013

[80] F. Regazzoni, L. Dedè, and A. Quarteroni, "Biophysically detailed mathematical models of multiscale cardiac active mechanics," *PLOS Computational Biology*, vol. 16, p. e1008294, 2020. doi:10.1371/journal.pcbi.1008294

[81] J. Bestel, F. Clément, and M. Sorine, "A biomechanical model of muscle contraction," in *Medical Image Computing and Computer-Assisted Intervention MICCAI 2001*, Lecture Notes in Computer Science, W. Niessen and M. Viergever, Eds. Springer Berlin / Heidelberg, 2001, vol. 2208, pp. 1159–1161. doi:10.1007/3-540-45468-3_143

[82] N. Stergiopulos, J. J. Meister, and N. Westerhof, "Determinants of stroke volume and systolic and diastolic aortic pressure." *The American journal of physiology*, vol. 270, pp. H2050–9, 1996. doi:10.1152/ajpheart.1996.270.6.H2050

[83] S. A. Niederer, P. J. Hunter, and N. P. Smith, "A quantitative analysis of cardiac myocyte relaxation: a simulation study." *Biophysical journal*, vol. 90, pp. 1697–722, 2006. doi:10.1529/biophysj.105.069534

[84] S. A. Niederer, G. Plank, P. Chinchapatnam, et al., "Length-dependent tension in the failing heart and the efficacy of cardiac resynchronization therapy." *Cardiovascular research*, vol. 89, pp. 336–43, 2011. doi:10.1093/cvr/cvq318

[85] J. Lumens, T. Delhaas, B. Kirn, and T. Arts, "Three-wall segment (triseg) model describing mechanics and hemodynamics of ventricular interaction." *Annals of biomedical engineering*, vol. 37, pp. 2234–55, 2009. doi:10.1007/s10439-009-9774-2

[86] P. J. Hunter, A. D. McCulloch, and H. E. D. J. t. Keurs, "Modelling the mechanical properties of cardiac muscle," *Prog. Biophys. Mol. Biol.*, vol. 69, pp. 289–331, 1998.

[87] M. V. Razumova, A. E. Bukatina, and K. B. Campbell, "Stiffness-distortion sarcomere model for muscle simulation," *Journal of Applied Physiology*, vol. 87, pp. 1861–1876, 1999. doi:10.1152/jappl.1999.87.5.1861

[88] J. J. Rice, R. L. Winslow, and W. C. Hunter, "Comparison of putative cooperative mechanism in cardiac muscle: length dependence and dynamic responses," *Am J Physiol*, vol. 276, pp. H1734– H1754, 1999.

[89] J. J. Rice, F. Wang, D. M. Bers, and P. P. de Tombe, "Approximate model of cooperative activation and crossbridge cycling in cardiac muscle using ordinary differential equations." *Biophysical journal*, vol. 95, pp. 2368–90, 2008. doi:10.1529/biophysj.107.119487

[90] F. B. Sachse, K. Glänzel, and G. Seemann, "Modeling of protein interactions involved in cardiac tension development," *Int. J. Bifurcation and Chaos*, vol. 13, pp. 3561–3578, 2003.

[91] F. B. Sachse, K. Glänzel, and G. Seemann, "Modeling of electro-mechanical coupling in cardiac myocytes: feedback mechanisms and cooperativity," in *Lecture Notes in Computer Science*, I. e. al, Ed., vol. 2674. Springer-Verlag Berlin Heidelberg, 2003, pp. 62–71.

[92] S. Land, S. A. Niederer, J. M. Aronsen, et al., "An analysis of deformation-dependent electromechanical coupling in the mouse heart." *The Journal of physiology*, vol. 590, pp. 4553–69, 2012. doi:10.1113/jphysiol.2012.231928

[93] S. Land and S. A. Niederer, "A spatially detailed model of isometric contraction based on competitive binding of troponin i explains cooperative interactions between tropomyosin and crossbridges." *PLoS computational biology*, vol. 11, p. e1004376, 2015. doi:10.1371/journal.pcbi.1004376

[94] S. Land, S.-J. Park-Holohan, N. P. Smith, C. G. Dos Remedios, J. C. Kentish, and S. A. Niederer, "A model of cardiac contraction based on novel measurements of tension development in human cardiomyocytes," *Journal of Molecular and Cellular Cardiology*, vol. 106, pp. 68–83, 2017. doi:10.1016/j.yjmcc.2017.03.008

[95] J. Rice, G. Stolovitzky, Y. Tu, and P. Detombe, "Ising model of cardiac thin filament activation with nearest-neighbor cooperative interactions," *Biophysical Journal*, vol. 84, pp. 897–909, 2003. doi:10.1016/S0006-3495(03)74907-8

[96] J. Hussan, P. P. de Tombe, and J. J. Rice, "A spatially detailed myofilament model as a basis for large-scale biological simulations," *IBM Journal of Research and Development*, vol. 50, pp. 583–600, 2006. doi:10.1147/rd.506.0583

[97] T. Washio, J.-i. Okada, A. Takahashi, et al., "Multiscale heart simulation with cooperative stochastic cross-bridge dynamics and cellular structures," *Multiscale Modeling & Simulation*, vol. 11, pp. 965–999, 2013. doi:10.1137/120892866

[98] T. Washio, K. Yoneda, J.-i. Okada, T. Kariya, S. Sugiura, and T. Hisada, "Ventricular fiber optimization utilizing the branching structure," *International Journal for Numerical Methods in Biomedical Engineering*, vol. 32, p. e02753, 2016. doi:10.1002/cnm.2753

[99] F. Regazzoni, L. Dedè, and A. Quarteroni, "Active contraction of cardiac cells: a reduced model for sarcomere dynamics with cooperative interactions." *Biomechanics and modeling in mechanobiology*, 2018. doi:10.1007/s10237-018-1049-0

[100] F. Regazzoni, L. Dedè, and A. Quarteroni, "Machine learning of multiscale active force generation models for the efficient simulation of cardiac electromechanics," *Computer Methods in Applied Mechanics and Engineering*, vol. 370, p. 113268, 2020. doi:10.1016/j.cma.2020.113268

[101] J. Bonet and R. D. Wood, *Nonlinear continuum mechanics for finite element analysis*. Cambridge University Press, 2008.

[102] T. Belytschko, W. K. Liu, B. Moran, and K. Elkhodary, *Nonlinear finite elements for continua and structures*. John wiley & sons, 2014.

[103] J. M. Guccione, A. D. McCulloch, and L. K. Waldman, "Passive material properties of intact ventricular myocardium determined from a cylindrical model." *Journal of biomechanical engineering*, vol. 113, pp. 42–55, 1991. doi:10.1115/1.2894084

[104] J. M. Guccione, K. D. Costa, and A. D. McCulloch, "Finite element stress analysis of left ventricular mechanics in the beating dog heart," *J. Biomechanics*, vol. 28, pp. 1167–1177, 1995.

[105] K. D. Costa, J. W. Holmes, and A. D. McCulloch, "Modelling cardiac mechanical properties in three dimensions," *The integrated heart: modelling cardiac structure and function. Roy Soc of London Phil Tr A*, vol. 359, p. 1233, 2001. doi:10.1098/rsta.2001.0828

[106] T. Usyk, R. Mazhari, and A. McCulloch, "Effect of laminar orthotropic myofiber architecture on regional stress and strain in the canine left ventricle," *Journal of Elasticity*, vol. 61, pp. 143–164, 2000. doi:10.1023/A:1010883920374

[107] G. A. Holzapfel and R. W. Ogden, "Constitutive modelling of passive myocardium: a structurally based framework for material characterization." *Philosophical transactions. Series A, Mathematical, physical, and engineering sciences*, vol. 367, pp. 3445–75, 2009. doi:10.1098/rsta.2009.0091

[108] L. R. Caggiano and J. W. Holmes, "A comparison of fiber based material laws for myocardial scar," *Journal of Elasticity*, vol. 145, pp. 321–337, 2021. doi:10.1007/s10659-021-09845-5

[109] D. Nordsletten, A. Capilnasiu, W. Zhang, et al., "A viscoelastic model for human myocardium," *Acta Biomaterialia*, vol. 135, pp. 441–457, 2021. doi:10.1016/j.actbio.2021.08.036

[110] A. I. Hassaballah, M. A. Hassan, A. N. Mardi, and M. Hamdi, "An inverse finite element method for determining the tissue compressibility of human left ventricular wall during the cardiac cycle," *PLoS ONE*, vol. 8, p. e82703, 2013. doi:10.1371/journal.pone.0082703

[111] H. Liu, J. S. Soares, J. Walmsley, et al., "The impact of myocardial compressibility on organ-level simulations of the normal and infarcted heart." *Scientific reports*, vol. 11, p. 13466, 2021. doi:10.1038/s41598-021-92810-y

[112] D. Ambrosi, G. Arioli, F. Nobile, and A. Quarteroni, "Electromechanical coupling in cardiac dynamics: The active strain approach," *SIAM Journal on Applied Mathematics*, vol. 71, pp. 605–621, 2011. doi:10.1137/100788379

[113] D. Ambrosi and S. Pezzuto, "Active stress vs. active strain in mechanobiology: Constitutive issues," *Journal of Elasticity*, vol. 107, pp. 199–212, 2011. doi:10.1007/s10659-011-9351-4

[114] D. Martonová, D. Holz, J. Seufert, M. T. Duong, M. Alkassar, and S. Leyendecker, "Comparison of stress and stress–strain approaches for the active contraction in a rat cardiac cycle model," *Journal of Biomechanics*, vol. 134, p. 110980, 2022. doi:10.1016/j.jbiomech.2022.110980

[115] M. R. Pfaller, J. M. Hörmann, M. Weigl, et al., "The importance of the pericardium for cardiac biomechanics: from physiology to computational modeling." *Biomechanics and modeling in mechanobiology*, 2018. doi:10.1007/s10237-018-1098-4

[116] M. Strocchi, M. A. Gsell, C. M. Augustin, et al., "Simulating ventricular systolic motion in a four-chamber heart model with spatially varying robin boundary conditions to model the effect of the pericardium," *Journal of Biomechanics*, p. 109645, 2020. doi:10.1016/j.jbiomech.2020.109645

[117] M. Strocchi, C. M. Augustin, M. A. F. Gsell, et al., "The effect of ventricular myofibre orientation on atrial dynamics," vol. 12738, pp. 659–670, 2021. doi:10.1007/978-3-030-78710-3_63

[118] S. Sugiura, T. Washio, A. Hatano, J. Okada, H. Watanabe, and T. Hisada, "Multi-scale simulations of cardiac electrophysiology and mechanics using the University of Tokyo heart simulator," *Progress in Biophysics and Molecular Biology*, vol. 110, pp. 380–389, 2012. doi:10.1016/j.pbiomolbio.2012.07.001

[119] D. Nordsletten, M. McCormick, P. J. Kilner, P. Hunter, D. Kay, and N. P. Smith, "Fluid-solid coupling for the investigation of diastolic and systolic human left ventricular function," *International Journal for Numerical Methods in Biomedical Engineering*, vol. 27, pp. 1017–1039, 2011. doi:10.1002/cnm.1405

[120] T. Arts, T. Delhaas, P. Bovendeerd, X. Verbeek, and F. W. Prinzen, "Adaptation to mechanical load determines shape and properties of heart and circulation: the circadapt model." *American journal of physiology. Heart and circulatory physiology*, vol. 288, pp. H1943–54, 2005. doi:10.1152/ajpheart.00444.2004

[121] S. Paeme, K. T. Moorhead, J. G. Chase, et al., "Mathematical multi-scale model of the cardiovascular system including mitral valve dynamics. application to ischemic mitral insufficiency." *Biomedical engineering online*, vol. 10, p. 86, 2011. doi:10.1186/1475-925X-10-86

[122] G. Guidoboni, L. Sala, M. Enayati, et al., "Cardiovascular function and ballistocardiogram: A relationship interpreted via mathematical modeling." *IEEE transactions on bio-medical engineering*, vol. 66, pp. 2906–2917, 2019. doi:10.1109/TBME.2019.2897952

[123] C. M. Augustin, M. A. Gsell, E. Karabelas, et al., "A computationally efficient physiologically comprehensive 3d–0d closed-loop model of the heart and circulation," *Computer Methods in Applied Mechanics and Engineering*, vol. 386, p. 114092, 2021. doi:10.1016/j.cma.2021.114092

[124] J. Sainte-Marie, D. Chapelle, R. Cimrman, and M. Sorine, "Modeling and estimation of the cardiac electromechanical activity," *Computers & Structures*, vol. 84, pp. 1743–1759, 2006. doi:10.1016/j.compstruc.2006.05.003

[125] R. C. P. Kerckhoffs, M. L. Neal, Q. Gu, J. B. Bassingthwaighte, J. H. Omens, and A. D. McCulloch, "Coupling of a 3d finite element model of cardiac ventricular mechanics to lumped systems models of the systemic and pulmonic circulation," *Annals of Biomedical Engineering*, vol. 35, pp. 1–18, 2007. doi:10.1007/s10439-006-9212-7

[126] V. Gurev, T. Lee, J. Constantino, H. Arevalo, and N. A. Trayanova, "Models of cardiac electromechanics based on individual hearts imaging data: image-based electromechanical models of the heart," *Biomechanics and Modeling in Mechanobiology*, vol. 10, pp. 295–306, 2011. doi:10.1007/s10237-010-0235-5

[127] V. Gurev, P. Pathmanathan, J.-L. Fattebert, et al., "A high-resolution computational model of the deforming human heart." *Biomechanics and modeling in mechanobiology*, vol. 14, pp. 829–49, 2015. doi:10.1007/s10237-014-0639-8

[128] M. Hirschvogel, M. Bassilious, L. Jagschies, S. M. Wildhirt, and M. W. Gee, "A monolithic 3d-0d coupled closed-loop model of the heart and the vascular system: Experiment-based parameter estimation for patient-specific cardiac mechanics." *International journal for numerical methods in biomedical engineering*, vol. 33, p. e2842, 2017. doi:10.1002/cnm.2842

[129] C. M. Augustin, M. A. F. Gsell, E. Karabelas, et al., "Validation of a 3d-0d closed-loop model of the heart and circulation – modeling the experimental assessment of diastolic and systolic ventricular properties," 2020.

[130] S. Schuler, L. Baron, A. Loewe, and O. Dössel, "Developing and coupling a lumped element model of the closed loop human vascular system to a model of cardiac mechanics," in *BMTMedPhys 2017*, vol. 62, no. S1. Dresden: de Gruyter, 2017, p. S69.

[131] S. Schuler, "Developing and coupling a lumped parameter model of the closed loop human vascular system to a model of cardiac mechanics," Master's thesis, Institute of Biomedical Engineering, Karlsruhe Institute of Technology (KIT), 2016.

[132] D. Garcia, P. Pibarot, and L.-G. Durand, "Analytical modeling of the instantaneous pressure gradient across the aortic valve." *Journal of Biomechanics*, vol. 38, pp. 1303–11, 2005. doi:10.1016/j.jbiomech.2004.06.018

[133] J. P. Mynard, M. R. Davidson, D. J. Penny, and J. J. Smolich, "A simple, versatile valve model for use in lumped parameter and one-dimensional cardiovascular models," *International Journal for Numerical Methods in Biomedical Engineering*, vol. 28, pp. 626–641, 2012. doi:10.1002/cnm.1466

[134] C. G. Broyden, "A class of methods for solving nonlinear simultaneous equations," *Mathematics of computation*, vol. 19, pp. 577–593, 1965.

[135] E. Kovacheva, "Model based estimation of the elastomechanical properties of the human heart," PhD thesis, Karlsruher Institut für Technologie (KIT), Karlsruhe, 2021. doi:10.5445/IR/1000135416

[136] G. Balarac, F. Basile, P. Bénard, et al., "TETRAHEDRAL REMESHING IN THE CONTEXT OF LARGE-SCALE NUMERICAL SIMULATION AND HIGH PERFORMANCE COMPUTING," 2021, working paper or preprint. https://hal.sorbonne-universite.fr/hal-03344779

[137] A. Neic, M. A. Gsell, E. Karabelas, A. J. Prassl, and G. Plank, "Automating image-based mesh generation and manipulation tasks in cardiac modeling workflows using meshtool," *SoftwareX*, vol. 11, p. 100454, 2020. doi:10.1016/j.softx.2020.100454

[138] M. Fedele and A. Quarteroni, "Polygonal surface processing and mesh generation tools for the numerical simulation of the cardiac function." *International journal for numerical methods in biomedical engineering*, p. e3435, 2021. doi:10.1002/cnm.3435

[139] C. Geuzaine and J.-F. Remacle, "Gmsh: A three-dimensional finite element mesh generator with built-in pre- and post-processing facilities," *International Journal for Numerical Methods in Engineering*, vol. 79, pp. 1309–1331, 2009. doi:10.1002/nme.2579

[140] L. Geerts, P. Bovendeerd, K. Nicolay, and T. Arts, "Characterization of the normal cardiac myofiber field in goat measured with MR-diffusion tensor imaging," *Am J Physiol Heart Circ Physiol*, vol. 283, p. 139, 2002.

[141] J. D. Bayer, R. C. Blake, G. Plank, and N. A. Trayanova, "A novel rule-based algorithm for assigning myocardial fiber orientation to computational heart models," *Annals of Biomedical Engineering*, vol. 40, pp. 2243–2254, 2012. doi:10.1007/s10439-012-0593-5

[142] R. Doste, D. Soto-Iglesias, G. Bernardino, et al., "A rule-based method to model myocardial fiber orientation in cardiac biventricular geometries with outflow tracts." *International journal for numerical methods in biomedical engineering*, vol. 35, p. e3185, 2019. doi:10.1002/cnm.3185

[143] J. Wong and E. Kuhl, "Generating fibre orientation maps in human heart models using poisson interpolation." *Computer methods in biomechanics and biomedical engineering*, vol. 17, pp. 1217–26, 2014. doi:10.1080/10255842.2012.739167

[144] R. Piersanti, P. C. Africa, M. Fedele, et al., "Modeling cardiac muscle fibers in ventricular and atrial electrophysiology simulations," *Computer Methods in Applied Mechanics and Engineering*, vol. 373, p. 113468, 2021. doi:10.1016/j.cma.2020.113468

[145] A. Wachter, A. Loewe, M. W. Krueger, O. Dössel, and G. Seemann, "Mesh structure-independent modeling of patient-specific atrial fiber orientation," *Current Directions in Biomedical Engineering*, vol. 1, pp. 409–412, 2015. doi:10.1515/cdbme-2015-0099

[146] D. D. Streeter, H. M. Spotnitz, D. P. Patel, R. J. J, and E. H. Sonnenblick, "Fiber orientation in the canine left ventricle during diastole and systole," *Circ. Res.*, vol. 24, pp. 339–347, 1969.

[147] D. D. Streeter and D. L. Bassett, "An engineering analysis of myocardial fiber orientation in pig's left ventricle in systole," *The Anatomical Record*, vol. 155, pp. 503–511, 1966. doi:10.1002/ar.1091550403

[148] S. Schuler, "Kit-ibt/ldrb_fibers," *Zenodo*, 2021. doi:10.5281/zenodo.4606575

[149] H. Lombaert, J. Peyrat, P. Croisille, et al., "Human atlas of the cardiac fiber architecture: Study on a healthy population," *IEEE Transactions on Medical Imaging*, 2012. doi:10.1109/TMI.2012.2192743

[150] A. Loewe, "Modeling human atrial patho-electrophysiology from ion channels to ECG: substrates, pharmacology, vulnerability, and p-waves," PhD thesis, KIT Scientific Publishing, Karlsruhe, 2016. doi:10.5445/KSP/1000054615

[151] J. A. Sethian, *Level set methods and fast marching methods: evolving interfaces in computational geometry, fluid mechanics, computer vision, and materials science*, vol. 3. Cambridge university press, 1999.

[152] G. Peyre, "Toolbox fast marching," *MATLAB Central File Exchange*, 2022. https://www.mathworks.com/matlabcentral/fileexchange/6110-toolbox-fast-marching

[153] S. Schuler, N. Pilia, D. Potyagaylo, and A. Loewe, "Cobiveco: Consistent biventricular coordinates for precise and intuitive description of position in the heart – with MATLAB implementation," *Medical Image Analysis*, vol. 74, p. 102247, 2021. doi:10.1016/j.media.2021.102247

[154] M. D. Cerqueira, N. J. Weissman, V. Dilsizian, et al., "Standardized myocardial segmentation and nomenclature for tomographic imaging of the heart," *Circulation*, vol. 105, pp. 539–542, 2002. doi:10.1161/hc0402.102975

[155] M. Courtemanche, R. J. Ramirez, and S. Nattel, "Ionic mechanisms underlying human atrial action potential properties: insights from a mathematical model." *The American journal of physiology*, vol. 275, pp. H301–21, 1998.

[156] T. O'Hara, L. Virag, A. Varro, and Y. Rudy, "Simulation of the undiseased human cardiac ventricular action potential: model formulation and experimental validation," *PLoS Computational Biology*, vol. 7, p. e1002061, 2011. doi:10.1371/journal.pcbi.1002061

[157] E. Passini, A. Mincholé, R. Coppini, et al., "Mechanisms of pro-arrhythmic abnormalities in ventricular repolarisation and anti-arrhythmic therapies in human hypertrophic cardiomyopathy." *Journal of molecular and cellular cardiology*, vol. 96, pp. 72–81, 2016. doi:10.1016/j.yjmcc.2015.09.003

[158] S. Dutta, A. Mincholé, T. A. Quinn, and B. Rodriguez, "Electrophysiological properties of computational human ventricular cell action potential models under acute ischemic conditions." *Progress in biophysics and molecular biology*, vol. 129, pp. 40–52, 2017. doi:10.1016/j.pbiomolbio.2017.02.007

[159] F. Levrero-Florencio and et al., "Sensitivity analysis of a strongly-coupled human-based electromechanical cardiac model: Effect of mechanical parameters on physiologically relevant biomarkers," *Computer Methods in Applied Mechanics and Engineering*, 2020. doi:10.1016/j.cma.2019.112762

[160] F. Margara, Z. J. Wang, F. Levrero-Florencio, et al., "In-silico human electro-mechanical ventricular modelling and simulation for drug-induced pro-arrhythmia and inotropic risk assessment," *Progress in Biophysics and Molecular Biology*, 2020. doi:10.1016/j.pbiomolbio.2020.06.007

[161] A. Kamkin, I. Kiseleva, K.-D. Wagner, and H. Scholz, "Mechano-electric feedback in the heart: evidence from intracellular microelectrode recordings on multicellular preparations and single cells from healthy and diseased tissue," *Mechanosensitivity in cells and tissues*, 2005.

[162] F. S. Costabal, F. A. Concha, D. E. Hurtado, and E. Kuhl, "The importance of mechano-electrical feedback and inertia in cardiac electromechanics." *Computer methods in applied mechanics and engineering*, vol. 320, pp. 352–368, 2017. doi:10.1016/j.cma.2017.03.015

[163] N. A. Trayanova, "Whole-heart modeling: applications to cardiac electrophysiology and electromechanics," *Circulation Research*, vol. 108, pp. 113–128, 2011. doi:10.1161/CIRCRESAHA.110.223610

[164] F. Guharay and F. Sachs, "Stretch-activated single ion channel currents in tissue-cultured embryonic chick skeletal muscle." *The Journal of physiology*, vol. 352, pp. 685–701, 1984.

[165] W. Niu and F. Sachs, "Dynamic properties of stretch-activated k+ channels in adult rat atrial myocytes," *Progress in Biophysics and Molecular Biology*, vol. 82, pp. 121–135, 2003. doi:10.1016/S0079-6107(03)00010-5

[166] T. Zeng, G. C. Bett, and F. Sachs, "Stretch-activated whole cell currents in adult rat cardiac myocytes." *American journal of physiology. Heart and circulatory physiology*, vol. 278, pp. H548–57, 2000. doi:10.1152/ajpheart.2000.278.2.H548

[167] Y. H. Zhang, J. B. Youm, H. K. Sung, et al., "Stretch-activated and background non-selective cation channels in rat atrial myocytes." *The Journal of physiology*, vol. 523 Pt 3, pp. 607–19, 2000. doi:10.1111/j.1469-7793.2000.00607.x

[168] E. Pueyo, M. Orini, J. F. Rodríguez, and P. Taggart, "Interactive effect of beta-adrenergic stimulation and mechanical stretch on low-frequency oscillations of ventricular action potential duration in humans." *Journal of molecular and cellular cardiology*, vol. 97, pp. 93–105, 2016. doi:10.1016/j.yjmcc.2016.05.003

[169] P. Tavi, C. Han, and M. Weckström, "Mechanisms of stretch-induced changes in [ca2+]i in rat atrial myocytes: role of increased troponin c affinity and stretch-activated ion channels." *Circulation research*, vol. 83, pp. 1165–77, 1998. doi:10.1161/01.res.83.11.1165

[170] P. Kohl and F. Sachs, "Mechanoelectric feedback in cardiac cells," *The integrated heart: modelling cardiac structure and function. Roy Soc of London Phil Tr A*, vol. 359, pp. 1173–1185, 2001. doi:10.1098/rsta.2001.0824

[171] A. Loewe, M. W. Krueger, P. G. Platonov, F. Holmqvist, O. Dössel, and G. Seemann, "Left and right atrial contribution to the p-wave in realistic computational models," vol. 9126, pp. 439–447, 2015. doi:10.1007/978-3-319-20309-6_50

[172] M. W. Krüger, "Personalized multi-scale modeling of the atria : Heterogeneities, fiber architecture, hemodialysis and ablation therapy," PhD thesis, KIT Scientific Publishing, 2013.

[173] S. Klotz, I. Hay, M. L. Dickstein, et al., "Single-beat estimation of end-diastolic pressure-volume relationship: a novel method with potential for noninvasive application." *American journal of physiology. Heart and circulatory physiology*, vol. 291, pp. H403–12, 2006. doi:10.1152/ajpheart.01240.2005

[174] M. Sellier, "An iterative method for the inverse elasto-static problem," *Journal of Fluids and Structures*, vol. 27, pp. 1461–1470, 2011. doi:10.1016/j.jfluidstructs.2011.08.002

[175] J. Bols and et al., "A computational method to assess the in vivo stresses and unloaded configuration of patient-specific blood vessels," *Journal of Computational and Applied Mathematics*, 2013. doi:10.1016/j.cam.2012.10.034

[176] M. K. Rausch, M. Genet, and J. D. Humphrey, "An augmented iterative method for identifying a stress-free reference configuration in image-based biomechanical modeling," *Journal of Biomechanics*, vol. 58, pp. 227–231, 2017. doi:10.1016/j.jbiomech.2017.04.021

[177] J. Chung and G. M. Hulbert, "A time integration algorithm for structural dynamics with improved numerical dissipation: The generalized-α method," *Journal of Applied Mechanics*, vol. 60, p. 371, 1970. doi:10.1115/1.2900803

[178] R. Coppini and et al., "Late sodium current inhibition reverses electromechanical dysfunction in human hypertrophic cardiomyopathy." *Circulation*, 2013. doi:10.1161/CIRCULATIONAHA.112.134932

[179] B. Pieske, M. Sütterlin, S. Schmidt-Schweda, et al., "Diminished post-rest potentiation of contractile force in human dilated cardiomyopathy. functional evidence for alterations in intracellular ca2+ handling." *The Journal of clinical investigation*, vol. 98, pp. 764–76, 1996. doi:10.1172/JCI118849

[180] L. A. Mulieri, G. Hasenfuss, B. Leavitt, P. D. Allen, and N. R. Alpert, "Altered myocardial force-frequency relation in human heart failure." *Circulation*, vol. 85, pp. 1743–50, 1992. doi:10.1161/01.cir.85.5.1743

[181] E. I. Rossman, R. E. Petre, K. W. Chaudhary, et al., "Abnormal frequency-dependent responses represent the pathophysiologic signature of contractile failure in human myocardium." *Journal of molecular and cellular cardiology*, vol. 36, pp. 33–42, 2004. doi:10.1016/j.yjmcc.2003.09.001

[182] K. Brixius, M. Pietsch, S. Hoischen, J. Müller-Ehmsen, and R. H. G. Schwinger, "Effect of inotropic interventions on contraction and ca2+ transients in the human heart," *Journal of Applied Physiology*, vol. 83, pp. 652–660, 1997, pMID: 9262464. doi:10.1152/jappl.1997.83.2.652

[183] M. Flesch, H. Kilter, B. Cremers, et al., "Acute effects of nitric oxide and cyclic GMP on human myocardial contractility." *The Journal of pharmacology and experimental therapeutics*, vol. 281, pp. 1340–9, 1997.

[184] G. Kocabay and et al., "Normal left ventricular mechanics by two-dimensional speckle-tracking echocardiography. reference values in healthy adults." *Revista espanola de cardiologia (English ed.)*, 2014. doi:10.1016/j.rec.2013.12.009

[185] G. Dominguez and H. A. Fozzard, "Effect of stretch on conduction velocity and cable properties of cardiac purkinje fibers," *Am J Physiol*, vol. 237, p. 119, 1979.

[186] D. Sung, R. W. Mills, J. Schettler, S. M. Narayan, J. H. Omens, and A. D. McCulloch, "Ventricular filling slows epicardial conduction and increases action potential duration in an optical mapping study of the isolated rabbit heart," *J Cardiovasc Electrophysiol*, vol. 14, pp. 739–749, 2003.

[187] N. Kuijpers, H. T. Eikelder, P. Bovendeerd, S. Verheule, T. Arts, and P. Hilbers, "Mechano-electric feedback leads to conduction slowing and block in acutely dilated atria: a modeling study of cardiac electromechanics," *Am J Physiol Heart Circ Physiol.*, vol. 292, pp. H2832–H2853, 2007.

[188] R. W. Mills, S. M. Narayan, and A. D. McCulloch, "Mechanisms of conduction slowing during myocardial stretch by ventricular volume loading in the rabbit," *American Journal of Physiology-Heart and Circulatory Physiology*, vol. 295, pp. H1270–H1278, 2008.

[189] K. S. Campbell, "Compliance accelerates relaxation in muscle by allowing myosin heads to move relative to actin." *Biophysical journal*, vol. 110, pp. 661–668, 2016. doi:10.1016/j.bpj.2015.12.024

[190] E. Kovacheva, T. Gerach, S. Schuler, M. Ochs, O. Dössel, and A. Loewe, "Causes of altered ventricular mechanics in hypertrophic cardiomyopathy: an in-silico study," *BioMedical Engineering OnLine*, vol. 20, p. 69, 2021. doi:10.1186/s12938-021-00900-9

[191] F. Regazzoni and A. Quarteroni, "An oscillation-free fully staggered algorithm for velocity-dependent active models of cardiac mechanics," *Computer Methods in Applied Mechanics and Engineering*, vol. 373, p. 113506, 2021. doi:10.1016/j.cma.2020.113506

[192] S. A. Niederer, E. Kerfoot, A. P. Benson, et al., "Verification of cardiac tissue electrophysiology simulators using an N-version benchmark," *Phil. Trans. R. Soc. A*, vol. 369, pp. 4331–4351, 2011. doi:10.1098/rsta.2011.0139

[193] L. A. Woodworth, B. Cansız, and M. Kaliske, "A numerical study on the effects of spatial and temporal discretization in cardiac electrophysiology," *International Journal for Numerical Methods in Biomedical Engineering*, p. e3443, 2021.

[194] K. H. W. J. ten Tusscher and A. V. Panfilov, "Alternans and spiral breakup in a human ventricular tissue model," *American Journal of Physiology. Heart and Circulatory Physiology*, vol. 291, pp. H1088–100, 2006. doi:10.1152/ajpheart.00109.2006

[195] D. Harrild and C. Henriquez, "A computer model of normal conduction in the human atria." *Circulation research*, vol. 87, pp. E25–36, 2000. doi:10.1161/01.res.87.7.e25

[196] B. Andreianov, M. Bendahmane, A. Quarteroni, and R. Ruiz-Baier, "Solvability analysis and numerical approximation of linearized cardiac electromechanics," *Math. Models Methods Appl. Sci.*, vol. 25, pp. 959–993, 2015. doi:10.1142/S0218202515500244

[197] F. Mroue, "Cardiac electromechanical coupling: modeling, mathematical analysis and numerical simulation," Theses, Ecole Centrale de Nantes (ECN) ; Université Libanaise, 2019. https://tel.archives-ouvertes.fr/tel-02395361

[198] P. G. Ciarlet, Ed., *Mathematical elasticity ; volume i. three-dimensional elasticity*, Studies in mathematics and its applications ; v. 20, 27, 29. Amsterdam: North-Holland, 1988.

[199] F. Dorri and et al., "A finite element model of the human left ventricular systole." *Computer methods in biomechanics and biomedical engineering*, 2006. doi:10.1080/10255840600960546

[200] D. H. S. Lin and F. C. P. Yin, "A multiaxial constitutive law for mammalian left ventricular myocardium in steady-state barium contracture or tetanus," *Journal of Biomechanical Engineering*, 1998. doi:10.1115/1.2798021

[201] J. M. Guccione, A. D. McCulloch, and L. Waldman, "Passive material properties of intact ventricular myocardium determined from a cylindrical model," *J. Biomechanical Engineering*, 1991.

[202] A. J. Yezzi and J. L. Prince, "An eulerian PDE approach for computing tissue thickness." *IEEE transactions on medical imaging*, 2003. doi:10.1109/TMI.2003.817775

[203] U. Sechtem and et al., "Regional left ventricular wall thickening by magnetic resonance imaging: Evaluation in normal persons and patients with global and regional dysfunction," *The American Journal of Cardiology*, 1987. doi:10.1016/S0002-9149(87)80088-7

[204] K. Emilsson and et al., "Mitral annulus motion versus long-axis fractional shortening," *Experimental & Clinical Cardiology*, 2006.

[205] S. E. Petersen and et al., "Reference ranges for cardiac structure and function using cardiovascular magnetic resonance (CMR) in caucasians from the UK biobank population cohort." *Journal of cardiovascular magnetic resonance*, 2017. doi:10.1186/s12968-017-0327-9

[206] A. M. S. Omar, S. Vallabhajosyula, and P. P. Sengupta, "Left ventricular twist and torsion: research observations and clinical applications." *Circulation. Cardiovascular imaging*, vol. 8, 2015. doi:10.1161/CIRCIMAGING.115.003029

[207] P. P. Sengupta, V. K. Krishnamoorthy, J. Korinek, et al., "Left ventricular form and function revisited: Applied translational science to cardiovascular ultrasound imaging," *Journal of the American Society of Echocardiography*, vol. 20, pp. 539–551, 2007. doi:10.1016/j.echo.2006.10.013

[208] I. K. Rüssel and M. J. W. Götte, "New insights in LV torsion for the selection of cardiac resynchronisation therapy candidates." *Netherlands heart journal : monthly journal of the Netherlands Society of Cardiology and the Netherlands Heart Foundation*, vol. 19, pp. 386–91, 2011. doi:10.1007/s12471-011-0136-y

[209] S. Sillanmäki, J. A. Lipponen, M. P. Tarvainen, et al., "Relationships between electrical and mechanical dyssynchrony in patients with left bundle branch block and healthy controls," *Journal of Nuclear Cardiology*, vol. 26, pp. 1228–1239, 2018. doi:10.1007/s12350-018-1204-0

[210] A. Paoletti Perini, S. Sacchi, C. D. Votta, et al., "Left ventricular rotational dyssynchrony before cardiac resynchronization therapy," *Journal of Cardiovascular Medicine*, vol. 17, pp. 469–477, 2016. doi:10.2459/JCM.0000000000000391

[211] B. A. Popescu, C. C. Beladan, A. Călin, et al., "Left ventricular remodelling and torsional dynamics in dilated cardiomyopathy: reversed apical rotation as a marker of disease severity," *European Journal of Heart Failure*, vol. 11, pp. 945–951, 2009. doi:10.1093/eurjhf/hfp124

[212] B. M. van Dalen, K. Caliskan, O. I. I. Soliman, et al., "Left ventricular solid body rotation in non-compaction cardiomyopathy: a potential new objective and quantitative functional diagnostic criterion?" *European journal of heart failure*, vol. 10, pp. 1088–93, 2008. doi:10.1016/j.ejheart.2008.08.006

[213] L. E. Sade, Ö. Demir, I. Atar, H. Müderrisoglu, and B. Özin, "Effect of mechanical dyssynchrony and cardiac resynchronization therapy on left ventricular rotational mechanics," *The American Journal of Cardiology*, vol. 101, pp. 1163–1169, 2008. doi:10.1016/j.amjcard.2007.11.069

[214] I. K. Rüssel, M. J. Götte, G. J. de Roest, et al., "Loss of opposite left ventricular basal and apical rotation predicts acute response to cardiac resynchronization therapy and is associated with long-term reversed remodeling," *Journal of Cardiac Failure*, vol. 15, pp. 717–725, 2009. doi:10.1016/j.cardfail.2009.04.007

[215] R. M. Setser, J. M. Kasper, M. L. Lieber, R. C. Starling, P. M. McCarthy, and R. D. White, "Persistent abnormal left ventricular systolic torsion in dilated cardiomyopathy after partial left ventriculectomy," *The Journal of Thoracic and Cardiovascular Surgery*, vol. 126, pp. 48–55, 2003. doi:10.1016/S0022-5223(03)00050-3

[216] C. Leclercq, H. Burri, A. Curnis, et al., "Cardiac resynchronization therapy non-responder to responder conversion rate in the more response to cardiac resynchronization therapy with multipoint pacing (MORE-CRT MPP) study: results from phase i," *European Heart Journal*, vol. 40, pp. 2979–2987, 2019. doi:10.1093/eurheartj/ehz109

[217] I. K. Rüssel, M. J. W. Götte, J. G. Bronzwaer, P. Knaapen, W. J. Paulus, and A. C. van Rossum, "Left ventricular torsion: an expanding role in the analysis of myocardial dysfunction." *JACC. Cardiovascular imaging*, vol. 2, pp. 648–55, 2009. doi:10.1016/j.jcmg.2009.03.001

[218] T. Jadczyk, R. Kurzelowski, K. S. Golba, et al., "Local electromechanical alterations determine the left ventricle rotational dynamics in CRT-eligible heart failure patients," *Scientific Reports*, vol. 11, 2021. doi:10.1038/s41598-021-82793-1

[219] T. F. Oostendorp, A. van Oosterom, and G. Huiskamp, "Interpolation on a triangulated 3d surface," *Journal of Computational Physics*, vol. 80, pp. 331–343, 1989. doi:10.1016/0021-9991(89)90103-4

[220] C. M. Augustin, A. Neic, M. Liebmann, et al., "Anatomically accurate high resolution modeling of human whole heart electromechanics: A strongly scalable algebraic multigrid solver method for nonlinear deformation." *Journal of computational physics*, vol. 305, pp. 622–646, 2016. doi:10.1016/j.jcp.2015.10.045

[221] L. Lehmonen, M. Jalanko, M. Tarkiainen, et al., "Rotation and torsion of the left ventricle with cardiovascular magnetic resonance tagging: comparison of two analysis methods," *BMC Medical Imaging*, vol. 20, 2020. doi:10.1186/s12880-020-00473-4

[222] E. J. Stöhr, R. E. Shave, A. L. Baggish, and R. B. Weiner, "Left ventricular twist mechanics in the context of normal physiology and cardiovascular disease: a review of studies using speckle tracking echocardiography," *American Journal of Physiology-Heart and Circulatory Physiology*, vol. 311, pp. H633–H644, 2016. doi:10.1152/ajpheart.00104.2016

[223] P. P. Sengupta, A. J. Tajik, K. Chandrasekaran, and B. K. Khandheria, "Twist mechanics of the left ventricle," *JACC: Cardiovascular Imaging*, vol. 1, pp. 366–376, 2008. doi:10.1016/j.jcmg.2008.02.006

[224] B. M. van Dalen, W. B. Vletter, O. I. Soliman, F. J. ten Cate, and M. L. Geleijnse, "Importance of transducer position in the assessment of apical rotation by speckle tracking echocardiography," *Journal of the American Society of Echocardiography*, vol. 21, pp. 895–898, 2008. doi:10.1016/j.echo.2008.02.001

[225] B. I. Jugdutt, M. J. Joljart, and M. I. Khan, "Rate of collagen deposition during healing and ventricular remodeling after myocardial infarction in rat and dog models." *Circulation*, vol. 94, pp. 94–101, 1996. doi:10.1161/01.cir.94.1.94

[226] F. Carreras, J. Garcia-Barnes, D. Gil, et al., "Left ventricular torsion and longitudinal shortening: two fundamental components of myocardial mechanics assessed by tagged cine-MRI in normal subjects," *The International Journal of Cardiovascular Imaging*, vol. 28, pp. 273–284, 2011. doi:10.1007/s10554-011-9813-6

[227] M. D. Eggen, C. M. Swingen, and P. A. Iaizzo, "Analysis of fiber orientation in normal and failing human hearts using diffusion tensor mri," in *2009 IEEE international symposium on biomedical imaging: from nano to macro*. IEEE, 2009, pp. 642–645.

[228] I. A. Bollen, E. Ehler, K. Fleischanderl, et al., "Myofilament remodeling and function is more impaired in peripartum cardiomyopathy compared with dilated cardiomyopathy and ischemic heart disease," *The American Journal of Pathology*, vol. 187, pp. 2645–2658, 2017.

[229] G. Hindricks, T. Potpara, N. Dagres, et al., "2020 ESC guidelines for the diagnosis and management of atrial fibrillation developed in collaboration with the european association of cardio-thoracic surgery (EACTS)." *European Heart Journal*, 2020. doi:10.1093/eurheartj/ehaa612

[230] S. P. Thomas, I. A. Nicholson, G. R. Nunn, et al., "Effect of atrial radiofrequency ablation designed to cure atrial fibrillation on atrial mechanical function," *Journal of Cardiovascular Electrophysiology*, vol. 11, pp. 77–82, 2000.

[231] F. Regazzoni and A. Quarteroni, "Accelerating the convergence to a limit cycle in 3d cardiac electromechanical simulations through a data-driven 0d emulator," *Computers in Biology and Medicine*, p. 104641, 2021. doi:10.1016/j.compbiomed.2021.104641

[232] S. M. Shavik, S. Wall, J. Sundnes, et al., "Computational modeling studies of the roles of left ventricular geometry, afterload, and muscle contractility on myocardial strains in heart

failure with preserved ejection fraction." *Journal of cardiovascular translational research*, 2021. doi:10.1007/s12265-021-10130-y

[233] O. Dössel, M. Krueger, F. Weber, M. Wilhelms, and G. Seemann, "Computational modeling of the human atrial anatomy and electrophysiology," *Medical & Biological Engineering & Computing*, vol. 50, pp. 773–799, 2012. doi:10.1007/s11517-012-0924-6

[234] S. R. Jernigan, G. D. Buckner, and J. W. Eischen, "Finite element modeling of the left atrium to facilitate the design of an endoscopic atrial retractor," *Journal of Biomechanical Engineering*, vol. 129, pp. 825–837, 2007. doi:10.1115/1.2801650

[235] E. S. Di Martino, C. Bellini, and D. S. Schwartzman, "In vivo porcine left atrial wall stress: Computational model," *Journal Biomechanics*, vol. 44, pp. 2589–2594, 2011.

[236] E. S. Di Martino, C. Bellini, and D. S. Schwartzman, "In vivo porcine left atrial wall stress: Effect of ventricular tachypacing on spatial and temporal stress distribution," *Journal of Biomechanics*, pp. 2755–2760, 2011.

[237] C. Bellini, E. S. Di Martino, and S. Federico, "Mechanical behaviour of the human atria," *Ann Biomed Eng*, pp. 1–13, 2012.

[238] T.-K. N. Phung, C. B. Moyer, P. T. Norton, J. D. Ferguson, and J. W. Holmes, "Effect of ablation pattern on mechanical function in the atrium," *Pacing and Clinical Electrophysiology*, vol. 40, pp. 648–654, 2017. doi:10.1111/pace.13086

[239] T. Alhogbani, O. Strohm, and M. G. Friedrich, "Evaluation of left atrial contraction contribution to left ventricular filling using cardiovascular magnetic resonance," *Journal of Magnetic Resonance Imaging*, vol. 37, pp. 860–864, 2013.

[240] V. Fuster, L. E. Ryden, D. S. Cannom, et al., "2011 ACCF/AHA/HRS focused updates incorporated into the ACC/AHA/ESC 2006 guidelines for the management of patients with atrial fibrillation: a report of the American College of Cardiology Foundation/American Heart Association Task Force on practice guidelines," *Circulation*, vol. 123, pp. 269–367, 2011.

[241] L.-M. Busch, T. Fritz, M. W. Krueger, G. Seemann, and O. Dössel, "Impact of different ablation patterns on the biomechanics of the human left atrium," in *Biomedizinische Technik. Biomedical Engineering*, vol. 58, no. s1, 2013. doi:10.1515/bmt-2013-4336

[242] J. B. Nielsen, J. T. Kuhl, A. Pietersen, et al., "P-wave duration and the risk of atrial fibrillation: Results from the copenhagen ECG study," *Heart Rhythm : the Official Journal of the Heart Rhythm Society*, vol. 12, pp. 1887–1895, 2015. doi:10.1016/j.hrthm.2015.04.026

[243] S. Y. Ng, C. K. Wong, and S. Y. Tsang, "Differential gene expressions in atrial and ventricular myocytes: insights into the road of applying embryonic stem cell-derived cardiomyocytes for future therapies," *American Journal of Physiology-Cell Physiology*, vol. 299, pp. C1234–C1249, 2010. doi:10.1152/ajpcell.00402.2009

[244] M. Krueger, W. Schulze, K. Rhode, R. Razavi, G. Seemann, and O. Dössel, "Towards personalized clinical in-silico modeling of atrial anatomy and electrophysiology," *Medical & Biological Engineering & Computing*, vol. 51, pp. 1251–1260, 2013.

[245] Y. Takahashi, M. D. O'Neill, M. Hocini, et al., "Effects of stepwise ablation of chronic atrial fibrillation on atrial electrical and mechanical properties," 2007. doi:10.1016/j.jacc.2006.11.033

[246] P. B. Sparks, H. G. Mond, J. K. Vohra, S. Jayaprakash, and J. M. Kalman, "Electrical remodeling of the atria following loss of atrioventricular synchrony," *Circulation*, vol. 100, pp. 1894–1900, 1999. doi:10.1161/01.CIR.100.18.1894

[247] P. B. Sparks, H. G. Mond, J. K. Vohra, A. G. Yapanis, L. E. Grigg, and J. M. Kalman, "Mechanical remodeling of the left atrium after loss of atrioventricular synchrony," *Circulation*, vol. 100, pp. 1714–1721, 1999. doi:10.1161/01.CIR.100.16.1714

[248] M. Allessie, J. Ausma, and U. Schotten, "Electrical, contractile and structural remodeling during atrial fibrillation," *Cardiovascular Research*, vol. 54, pp. 230–246, 2002.

[249] J. L. Jefferies and J. A. Towbin, "Dilated cardiomyopathy," *The Lancet*, vol. 375, pp. 752–762, 2010.

[250] G. W. Dec and V. Fuster, "Idiopathic dilated cardiomyopathy," *New England Journal of Medicine*, vol. 331, pp. 1564–1575, 1994.

[251] E. M. McNally and L. Mestroni, "Dilated cardiomyopathy: genetic determinants and mechanisms," *Circulation Research*, vol. 121, pp. 731–748, 2017.

[252] H.-P. Schultheiss, D. Fairweather, A. L. Caforio, et al., "Dilated cardiomyopathy," *Nature Reviews Disease Primers*, vol. 5, pp. 1–19, 2019.

[253] J. F. Gomez, K. Cardona, L. Romero, J. M. Ferrero Jr, and B. Trenor, "Electrophysiological and structural remodeling in heart failure modulate arrhythmogenesis. 1d simulation study," *PloS one*, vol. 9, 2014.

[254] A. Ahmad Bakir, A. Al Abed, M. C. Stevens, N. H. Lovell, and S. Dokos, "A multiphysics biventricular cardiac model: Simulations with a left-ventricular assist device," *Frontiers in Physiology*, vol. 9, p. 1259, 2018.

[255] C. von Deuster, E. Sammut, L. Asner, et al., "Studying dynamic myofiber aggregate reorientation in dilated cardiomyopathy using in vivo magnetic resonance diffusion tensor imaging," *Circulation: Cardiovascular Imaging*, vol. 9, p. e005018, 2016.

[256] B. T. Chan, E. Lim, K. H. Chee, and N. A. A. Osman, "Review on cfd simulation in heart with dilated cardiomyopathy and myocardial infarction," *Computers in Biology and Medicine*, vol. 43, pp. 377–385, 2013.

[257] E. A. Perez Alday, D. G. Whittaker, A. Benson, and M. A. Colman, "Effects of heart rate and ventricular wall thickness on non-invasive mapping: an in silico study," *Frontiers in Physiology*, vol. 10, p. 308, 2019.

[258] A. Grosberg and M. Gharib, "Modeling the macro-structure of the heart: healthy and diseased," *Medical & Biological Engineering & Computing*, vol. 47, pp. 301–311, 2009.

[259] F. Scardulla, A. Rinaudo, S. Pasta, and C. Scardulla, "Evaluation of ventricular wall stress and cardiac function in patients with dilated cardiomyopathy," *Proceedings of the Institution of Mechanical Engineers, Part H: Journal of Engineering in Medicine*, vol. 230, pp. 71–74, 2016.

[260] J. Constantino, Y. Hu, and N. A. Trayanova, "A computational approach to understanding the cardiac electromechanical activation sequence in the normal and failing heart, with translation to the clinical practice of crt," *Progress in Biophysics and Molecular Biology*, vol. 110, pp. 372–379, 2012.

[261] A. K. Heikhmakhtiar, A. J. Ryu, E. B. Shim, K.-S. Song, N. A. Trayanova, and K. M. Lim, "Influence of lvad function on mechanical unloading and electromechanical delay: a simulation study," *Medical & Biological Engineering & Computing*, vol. 56, pp. 911–921, 2018.

[262] D. Zeng, J. Wu, S.-S. Wu, H.-H. Lin, and H. Chen, "Three-dimensional echocardiographic comparison of left ventricular geometry and systolic function between dilated cardiomyopathy and mitral regurgitation with similar left ventricular dilation," *Journal of Clinical Ultrasound*, vol. 48, pp. 29–37, 2020.

[263] N. Dusturia, S. W. Choi, K. S. Song, and K. M. Lim, "Effect of myocardial heterogeneity on ventricular electro-mechanical responses: a computational study," *Biomedical Engineering Online*, vol. 18, p. 23, 2019.

[264] M. T. Mora, J. M. Ferrero, L. Romero, and B. Trenor, "Sensitivity analysis revealing the effect of modulating ionic mechanisms on calcium dynamics in simulated human heart failure," *PloS one*, vol. 12, p. e0187739, 2017.

[265] V. MALTSEV and A. UNDROVINAS, "A multi-modal composition of the late na+ current in human ventricular cardiomyocytes," *Cardiovascular Research*, vol. 69, pp. 116–127, 2006. doi:10.1016/j.cardiores.2005.08.015

[266] E. Pueyo, M. Orini, J. F. Rodríguez, and P. Taggart, "Interactive effect of beta-adrenergic stimulation and mechanical stretch on low-frequency oscillations of ventricular action potential duration in humans," *Journal of Molecular and Cellular Cardiology*, vol. 97, pp. 93–105, 2016.

[267] A. Gayazzi, R. De Maria, G. Renosto, et al., "The spectrum of left ventricular size in dilated cardiomyopathy: clinical correlates and prognostic implications," *American Heart Journal*, vol. 125, pp. 410–422, 1993.

[268] Y. Mishiro, T. Oki, H. Yamada, T. Wakatsuki, and S. Ito, "Evaluation of left ventricular contraction abnormalities in patients with dilated cardiomyopathy with the use of pulsed tissue doppler imaging," *Journal of the American Society of Echocardiography*, vol. 12, pp. 913–920, 1999.

[269] A. Junker, P. Thayssen, B. Nielsen, and P. Andersen, "The hemodynamic and prognostic significance of echo-doppler-proven mitral regurgitation in patients with dilated cardiomyopathy," *Cardiology*, vol. 83, pp. 14–20, 1993.

[270] J. Carroll, S. Shroff, P. Wirth, M. Halsted, S. Rajfer, et al., "Arterial mechanical properties in dilated cardiomyopathy. aging and the response to nitroprusside." *The Journal of Clinical Investigation*, vol. 87, pp. 1002–1009, 1991.

[271] J. Malcolm, M. Arnold, G. E. Marchiori, et al., "Large artery function in patients with chronic heart failure," *Circulation*, 1991.

[272] C. J. Pepine, W. W. Nichols, and C. R. Conti, "Aortic input impedance in heart failure." *Circulation*, vol. 58, pp. 460–465, 1978.

[273] T. O'Hara, L. Virág, A. Varró, and Y. Rudy, "Simulation of the undiseased human cardiac ventricular action potential: model formulation and experimental validation," *PLoS Comput Biol*, vol. 7, p. e1002061, 2011.

[274] S. Land, S.-J. Park-Holohan, N. P. Smith, C. G. dos Remedios, J. C. Kentish, and S. A. Niederer, "A model of cardiac contraction based on novel measurements of tension development in human cardiomyocytes," *Journal of Molecular and Cellular Cardiology*, vol. 106, pp. 68–83, 2017.

[275] K. Brixius, M. Pietsch, S. Hoischen, J. Müller-Ehmsen, and R. H. Schwinger, "Effect of inotropic interventions on contraction and ca2+ transients in the human heart." *Journal of applied physiology (Bethesda, Md. : 1985)*, vol. 83, pp. 652–60, 1997. doi:10.1152/jappl.1997.83.2.652

[276] P. Alter, H. Rupp, M. Rominger, K. Klose, and B. Maisch, "A new methodological approach to assess cardiac work by pressure–volume and stress–length relations in patients with aortic valve stenosis and dilated cardiomyopathy," *Pflügers Archiv-European Journal of Physiology*, vol. 455, pp. 627–636, 2008.

[277] M. H. Kim, W. H. Devlin, S. K. Das, J. Petrusha, D. Montgomery, and M. R. Starling, "Effects of β-adrenergic blocking therapy on left ventricular diastolic relaxation properties in patients with dilated cardiomyopathy," *Circulation*, vol. 100, pp. 729–735, 1999.

[278] D. R. Warriner, A. G. Brown, S. Varma, et al., "Closing the loop: modelling of heart failure progression from health to end-stage using a meta-analysis of left ventricular pressure-volume loops," *PLoS One*, vol. 9, p. e114153, 2014.

[279] I. S. Wittstein, D. A. Kass, P. H. Pak, W. L. Maughan, B. Fetics, and J. M. Hare, "Cardiac nitric oxide production due to angiotensin-converting enzyme inhibition decreases beta-adrenergic myocardial contractility in patients with dilated cardiomyopathy," *Journal of the American College of Cardiology*, vol. 38, pp. 429–435, 2001.

[280] P. Radau, Y. Lu, K. Connelly, G. Paul, A. Dick, and G. Wright, "Evaluation framework for algorithms segmenting short axis cardiac mri," *The MIDAS Journal-Cardiac MR Left Ventricle Segmentation Challenge*, vol. 49, 2009.

[281] J. E. Hall, *Guyton and hall textbook of medical physiology e-book*. Elsevier Health Sciences, 2010.

[282] H. Zhan, J. Zhang, A. Jiao, and Q. Wang, "Stretch-activated current in human atrial myocytes and na+ current and mechano-gated channels' current in myofibroblasts alter myocyte mechanical behavior: a computational study," *Biomedical Engineering Online*, vol. 18, pp. 1–15, 2019.

[283] K. Narayanan, K. Reinier, C. Teodorescu, et al., "Left ventricular diameter and risk stratification for sudden cardiac death," *Journal of the American Heart Association*, vol. 3, p. e001193, 2014.

[284] M. Strocchi, C. M. Augustin, M. A. Gsell, et al., "A publicly available virtual cohort of four-chamber heart meshes for cardiac electro-mechanics simulations," *PLoS One*, vol. 15, p. e0235145, 2020.

[285] W. T. Abraham, W. G. Fisher, A. L. Smith, et al., "Cardiac resynchronization in chronic heart failure," *New England Journal of Medicine*, vol. 346, pp. 1845–1853, 2002.

[286] C. Linde, W. T. Abraham, M. R. Gold, et al., "Randomized trial of cardiac resynchronization in mildly symptomatic heart failure patients and in asymptomatic patients with left ventricular dysfunction and previous heart failure symptoms," *Journal of the American College of Cardiology*, vol. 52, pp. 1834–1843, 2008.

[287] J. B. Young, W. T. Abraham, A. L. Smith, et al., "Combined cardiac resynchronization and implantable cardioversion defibrillation in advanced chronic heart failure: the miracle icd trial," *Jama*, vol. 289, pp. 2685–2694, 2003.

[288] A. M. Maceira, J. Cosín-Sales, M. Roughton, S. K. Prasad, and D. J. Pennell, "Reference right atrial dimensions and volume estimation by steady state free precession cardiovascular magnetic resonance," *Journal of Cardiovascular Magnetic Resonance*, vol. 15, pp. 1–10, 2013.

[289] J. D. Bayer, R. C. Blake, G. Plank, and N. A. Trayanova, "A novel rule-based algorithm for assigning myocardial fiber orientation to computational heart models," *Annals of Biomedical Engineering*, vol. 40, pp. 2243–2254, 2012.

[290] G. A. Holzapfel and R. W. Ogden, "Constitutive modelling of passive myocardium: a structurally based framework for material characterization," *Philosophical Transactions of the Royal Society A: Mathematical, Physical and Engineering Sciences*, vol. 367, pp. 3445–3475, 2009.

[291] P. A. Helm, L. Younes, M. F. Beg, et al., "Evidence of structural remodeling in the dyssynchronous failing heart," *Circulation Research*, vol. 98, pp. 125–132, 2006.

[292] H. Ashikaga, J. H. Omens, and J. W. Covell, "Time-dependent remodeling of transmural architecture underlying abnormal ventricular geometry in chronic volume overload heart failure," *American Journal of Physiology-Heart and Circulatory Physiology*, vol. 287, pp. H1994–H2002, 2004.

[293] H. Finsberg, C. Xi, J. L. Tan, et al., "Efficient estimation of personalized biventricular mechanical function employing gradient-based optimization," *International Journal for Numerical Methods in Biomedical Engineering*, vol. 34, p. e2982, 2018.

[294] M. Tokuda and Y. Sawaki, *Numerical simulator for left-ventricular functions*, K. Hayashi and H. Ishikawa, Eds. Tokyo: Springer Japan, 1996.

[295] J. Constantino, Y. Hu, A. C. Lardo, and N. A. Trayanova, "Mechanistic insight into prolonged electromechanical delay in dyssynchronous heart failure: a computational study," *American Journal of Physiology-Heart and Circulatory Physiology*, vol. 305, pp. H1265–H1273, 2013.

[296] Y. Wu, S. P. Bell, K. Trombitas, et al., "Changes in titin isoform expression in pacing-induced cardiac failure give rise to increased passive muscle stiffness," *Circulation*, vol. 106, pp. 1384–1389, 2002.

[297] A. C. Hueb, F. B. Jatene, L. F. P. Moreira, P. M. Pomerantzeff, E. Kallás, and S. A. de Oliveira, "Ventricular remodeling and mitral valve modifications in dilated cardiomyopathy: new insights from anatomic study," *The Journal of Thoracic and Cardiovascular Surgery*, vol. 124, pp. 1216–1224, 2002.

[298] I. Adeniran, D. H. MacIver, J. C. Hancox, and H. Zhang, "Abnormal calcium homeostasis in heart failure with preserved ejection fraction is related to both reduced contractile function and incomplete relaxation: an electromechanically detailed biophysical modeling study," *Frontiers in Physiology*, vol. 6, p. 78, 2015.

[299] K. Tran, N. P. Smith, D. S. Loiselle, and E. J. Crampin, "A metabolite-sensitive, thermodynamically constrained model of cardiac cross-bridge cycling: implications for force development during ischemia," *Biophysical Journal*, vol. 98, pp. 267–276, 2010.

[300] P. Lafortune, R. Arís, M. Vázquez, and G. Houzeaux, "Coupled electromechanical model of the heart: Parallel finite element formulation." *International journal for numerical methods in biomedical engineering*, vol. 28, pp. 72–86, 2012. doi:10.1002/cnm.1494

[301] E. L. Wilson, *Three dimensional static and dynamic analysis of structures: a physical approach with emphasis on earthquake engineering*. Computers and Structures Incorporated, 1998.

[302] E. Heiberg, J. Sjögren, M. Ugander, M. Carlsson, H. Engblom, and H. Arheden, "Design and validation of segment-freely available software for cardiovascular image analysis," *BMC medical imaging*, vol. 10, pp. 1–13, 2010.

List of Publications and Supervised Theses

Journal Articles

- **T. Gerach**, S. Appel, J. Wilczek, K. S. Golba, T. Jadczyk and A. Loewe, *Dyssynchronous Left Ventricular Activation is Insufficient for the Breakdown of Wringing Rotation*, Frontiers in Physiology, vol. 13, 2022
- **T. Gerach**, S. Schuler, J. Fröhlich, L. Lindner, E. Kovacheva, R. Moss, E. M. Wülfers, G. Seemann, C. Wieners, and A. Loewe, *Electro-Mechanical Whole-Heart Digital Twins: A Fully Coupled Multi-Physics Approach*, Mathematics, vol. 9(11) , pp. 1247, 2021
- E. Kovacheva, **T. Gerach**, S. Schuler, M. Ochs, O. Dössel, and A. Loewe, *Causes of altered ventricular mechanics in hypertrophic cardiomyopathy: an in-silico study*, BioMedical Engineering OnLine, vol. 20(1) , pp. 69, 2021
- J. Brenneisen, A. Daub, **T. Gerach**, E. Kovacheva, L. Huetter, B. Frohnapfel, O. Dössel, and A. Loewe, *Sequential Coupling Shows Minor Effects of Fluid Dynamics on Myocardial Deformation in a Realistic Whole-Heart Model*, Frontiers in Cardiovascular Medicine, vol. 8, 2021
- L. Gassner, **T. Gerach**, T. Hertweck, and T. Bohlen, *Seismic characterization of submarine gas-hydrate deposits in the Western Black Sea by acoustic full-waveform inversion of ocean-bottom seismic data*, Geophysics, vol. 84, 2019

Preprints/Manuscripts under review

- **T. Gerach**, S. Schuler, A. Wachter, A. Loewe, *The Impact of Standard Ablation Strategies for Atrial Fibrillation on Cardiovascular Performance in a Four-Chamber Heart Model*, arXiv preprint, 2022

Refereed Conference Articles

- S. Appel, **T. Gerach**, O. Dössel and A. Loewe, *Adaptation of the Calcium-dependent Tension Development in Ventricular Cardiomyocytes*, Current Directions in Biomedical Engineering, vol. 7, no. 2, 2021
- J. Brenneisen, S. Schuler, E. Kovacheva, **T. Gerach**, O. Dössel and A. Loewe, *Influence of Geometrical Properties for the Calculation of a Pressure-Free Whole Heart Geometry*, WCCM-ECCOMAS, 2020
- E. Kovacheva, L. Baron, S. Schuler, **T. Gerach**, O. Dössel and A. Loewe. *Optimization Framework to Identify Constitutive Law Parameters of the Human Heart*, Current Directions in Biomedical Engineering, vol. 6, no. 3, 2020
- **T. Gerach**, S. Schuler, E. Kovacheva, O. Dössel and A. Loewe, *Consequences of Using an Orthotropic Stress Tensor for Left Ventricular Systole*, Computing in Cardiology (CinC), vol. 47, 2020
- **T. Gerach**, D. Weiß, O. Dössel and A. Loewe, *Observation Guided Systematic Reduction of a Detailed Human Ventricular Cell Model*, Computing in Cardiology (CinC), vol. 46, 2019

Refereed Conference Abstracts

- J. Brenneisen, A. Daub, E. Kovacheva, **T. Gerach**, L. Hütter, B. Frohnapfel, O. Dössel and A. Loewe, *A sequential coupling approach for fluid-structure interaction in a patient specific whole heart geometry*, iHEART Congress – Modelling the Cardiac Function, 2021
- J. Brenneisen, E. Kovacheva, **T. Gerach**, A. Daub, L. Hütter, B. Frohnapfel, O. Dössel and A. Loewe, *Characterization of the Fluid Dynamic Pressure Field in the Human Heart as a Basis for Coupled Fluid-Structure Simulations*, 54th Annual Conference of the German Society for Biomedical Engineering, 2020
- **T. Gerach** and E. Kovacheva, O. Dössel, and A. Loewe, *A Bidirectionally Coupled Model of Electrophysiology and Elastomechanics of the Human Heart*, Towards an integrated numerical heart model: Coupling the relevant physics the right way, 2019
- E. Kovacheva, S. Schuler, **T. Gerach**, O. Dössel, and A. Loewe, *A Method for Pressure-Volume-Based Parameter Identification for a Passive Constitutive Model of Myocardium*, RISM Congress: iHEART–Modelling the Cardiac Function, 2019
- **T. Gerach**, O. Dössel, and A. Loewe, *Identification of structurally non-identifiable and sloppy parameters of a detailed ventricular myocyte model*, 52nd annual conference of the German Society for Biomedical Engineering (poster), 2018

Supervised Student Projects

- Larissa Hütter, *Ein Integriertes Herzmodel: Aspekte der Kopplung der Fluid Dynamik, Mechanik und Elektrophysiologie*, Master Thesis, Institute of Biomedical Engineering, Karlsruhe Institute of Technology (KIT), 2019
- Stephanie Appel, *Parameter Optimization fot the Regulation of Calcium-dependent Tension Development in Cardiomyocytes*, Bachelor Thesis, Institute of Biomedical Engineering, Karlsruhe Institute of Technology (KIT), 2020
- Albert Dasí i Martinez, *Simulating Heart Failure in an Electromechanically Coupled Model*, Master Thesis, Institute of Biomedical Engineering, Karlsruhe Institute of Technology (KIT), 2020
- Stephanie Appel, *Discrimination of Left Ventricular Rotation During Heart Failure Using the NOGA System*, Student Research Project, Institute of Biomedical Engineering, Karlsruhe Institute of Technology (KIT), 2021

Awards & Grants

- Semi-Finalist, Rosanna Degani Young Investigators Award
  Tobias Gerach, Steffen Schuler, Ekaterina Kovacheva, Olaf Dössel, Axel Loewe, *Consequences of Using an Orthotropic Stress Tensor for Left Ventricular Systole*, Computing in Cardiology, Rimini (Italy), 2020